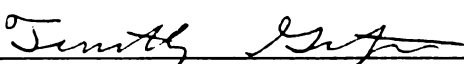This is to certify that the
dissertation entitled

MINIATURE MICROWAVE PLASMAS OF HYDROGEN AND
ARGON INVESTIGATED USING OPTICAL EMISSION
SPECTROSCOPY

presented by

DAVID STORY

has been accepted towards fulfillment
of the requirements for the

___PHD___   degree in   ___ELECTRICAL ENGINEERING___

_____
Major Professor's Signature

___May 26, 2006___

Date

PLACE IN RETURN BOX to remove this checkout from your record.
TO AVOID FINES return on or before date due.
MAY BE RECALLED with earlier due date if requested.

DATE DUE	DATE DUE	DATE DUE

MINIATURE MICROWAVE PLASMAS OF HYDROGEN AND ARGON
INVESTIGATED USING OPTICAL EMISSION SPECTROSCOPY

By

David Story

A DISSERTATION

Submitted to

Michigan State University

in partial fulfillment of the requirements

for the degree of

DOCTOR OF PHILOSOPHY

Department of Electrical Engineering

2006

Abstract

MINIATURE MICROWAVE PLASMAS OF HYDROGEN AND ARGON
INVESTIGATED USING OPTICAL EMISSION SPECTROSCOPY

By

David Story

Research on miniature microwave plasmas is motivated in part by the interest in generating on-chip plasma sources for applications such as miniature spectroscopy, sterilization of on-chip laboratories, and local area plasma-assisted etching and chemical vapor deposition.

The goal of this work is to determine the properties of miniature plasma discharges generated by microwave energy. Specifically, small discharges of argon and hydrogen with volumes of less than 1 cubic centimeter are investigated. Various properties of the plasma discharges are measured including plasma gas temperature, electron density, and internal plasma electromagnetic field strength.

The discharges are measured across a wide pressure range from 0.1 Torr to over 100 Torr using non-invasive optical emission spectroscopy techniques. Specific optical emission diagnostic techniques utilized includes Stark broadening of atomic hydrogen emissions to determine electron density, molecular hydrogen rotational temperature, Zeeman splitting in molecular hydrogen emissions to determine both the microwave magnetic field strength and the plasma temperature.

Modeling of the plasma discharges is also done using particle and energy balance equations.

ACKNOWLEDGMENTS

Table of Contents

List of Tables

List of Figures

Chapter 1 Introduction

The creation and characterization of miniature microwave plasma sources is a relatively new and under-investigated field. Some miniature plasma sources have been developed for the pixel cells in flat panel displays, as well as to investigate the possibility of bringing mass spectrometry and optical emission spectroscopy functions to the computer processor unit (CPU). However, none of the previously mentioned sources are created with microwave power, which allows for more flexible geometries and a wider range of pressure variations.

The first objective of this investigation is to establish the operating conditions for a microwave plasma source that allows the creation of miniature discharges, and then to measure the properties of the resulting plasma discharges. An additional objective is to develop a predictive understanding of miniature microwave plasma behavior by using plasma global models, and by comparing model results to the measured plasma properties. The overall goal is to add to the scientific understanding and engineering design principles for miniature microwave discharges.

To this end, investigations are performed in both noble and molecular gases (argon and hydrogen) across a range of pressure and microwave powers. The investigation includes the implementation of instrumentation for non-invasive optical emission spectroscopy. The plasma discharge properties focused on in this investigation include discharge shape and size, plasma power density, plasma electron density, plasma gas temperature, and electric and magnetic field strength in the plasma.

In this investigation, hydrogen and argon plasmas are formed at pressures ranging from 0.1-100 Torr, and at powers from 5-60 W. To obtain both high optical emission sensitivity and spectral resolution a special optical system is designed to bring lenses to within 5 mm of the plasma center. The optical system permits non-invasive measurements of the intense plasma discharges.

Argon discharges are analyzed experimentally to determine plasma density and plasma discharge power density. Two techniques are compared to determine the electron density from argon discharges.

Analysis of hydrogen data was extensive, including plasma discharge size and shape, plasma power density, plasma electron density, plasma gas temperature, and electric and magnetic field strength in the plasma. Optical spectrum measurements reveal peaks in the diatomic hydrogen rotation spectrum used to estimate rotational temperature. Higher resolution measurements of the sub-band structure of diatomic hydrogen were used to determine resident magnetic fields consistent with Zeeman splitting. This suggests hydrogen plasmas have a partially discrete or constant magnitude magnetic field component, which varies with pressure.

Atomic hydrogen spectroscopic readings demonstrated sub-band structure as well. Peaks within the hydrogen alpha, beta, and gamma bands were consistent with energy level splitting seen in the Stark effect. As a result, the magnitude of the resident electric field was estimated across the pressure regime.

Chapter 2 provides a background for the study of miniature microwave plasma sources by presenting the current state of miniature plasma sources.

Chapter 3 presents the experimental set-up. The experimental set-up includes designs and builds for both the plasma system and the diagnostic system, a multi-channel fiber optic feed-through. The diagnostic set-up required the build of a new optics system to penetrate the reactor and focus on the center of the plasma discharge. Chapter 3 concludes with test results for both the plasma reactor system and fiber optic feed-through.

Chapter 4 presents the global model, a theory that describes the plasma physics of monotonic gases such as argon. Low to medium pressure plasmas can be described accurately with the global model. The global model is found ineffective at higher pressures; this was substantiated on preliminary test sets made during initial system testing.

Chapter 5 presents the spectroscopic theory for diatomic molecules and for single electron atoms. Both sets of theory are directly applicable to hydrogen plasmas.

Chapter 6 applies spectroscopic theory from Chapter 5 to predict the peak amplitude and splitting in atomic and rotational spectra associated with hydrogen. Chapter 6 introduces spectral theory specific to hydrogen-like (Rydberg) atoms, without which determination of the Stark spectrum would be impossible.

Chapter 7 accumulates the experimental results, and makes direct comparisons between the experimental results and predictions made by the global model in Chapter 4 and the spectroscopy theory developed in Chapter 5 and Chapter 6. Chapter 7 records experimental results for diatomic and atomic hydrogen spectra, and matches these results to the Zeeman and Stark effects developed in Chapter 5 and Chapter 6.

Chapter 8 summarizes project results, and lays the groundwork for future experiments aimed to get at the root of plasma behavior. Chapter 8 also suggests future experimental techniques to provide more insight into the nature of the hydrogen plasma behavior, specifically high-pressure contraction.

Chapter 2 Background

The current research activity in miniature plasma sources and microwave plasma sources is presented in the following two subchapters. The miniature microwave plasma source designed for this project is detailed in Chapter 3. The miniature microwave plasma source design is similar to larger microwave plasma sources, but requires fundamental knowledge of miniature source operation to be successful.

2.1 *Miniature Plasma Sources*

This brief overview presents the current state of miniature plasma sources. The following plasma sources will be discussed in the proceeding paragraphs: Micro-cell plasma display panels, micro-strip line sources, capacitive sources, inductive sources, torch and arc discharges, and micro-hollow cathode tubes.

2.1.1 Micro-Cell Plasma Display Panels

Micro-cell plasma display pixel cells consist of two parallel glass plates fitted with electrodes on their surfaces, as shown in Figure 1 [1]. Each electrode is covered by thin dielectric layer and coated with MgO. The cell is filled with various combinations of Xenon, Neon, Helium, and trace amounts of Argon. The cell is sealed; the cell pressure can vary from 100 torr to 500 torr, depending on other cell parameters including gas mixture and excitation frequency. The cell is approximately 1 mm cubed in dimension.

The MgO layer produces secondary electrons on impact by electrons, greatly multiplying the number of electrons in the plasma and the number of collisions that
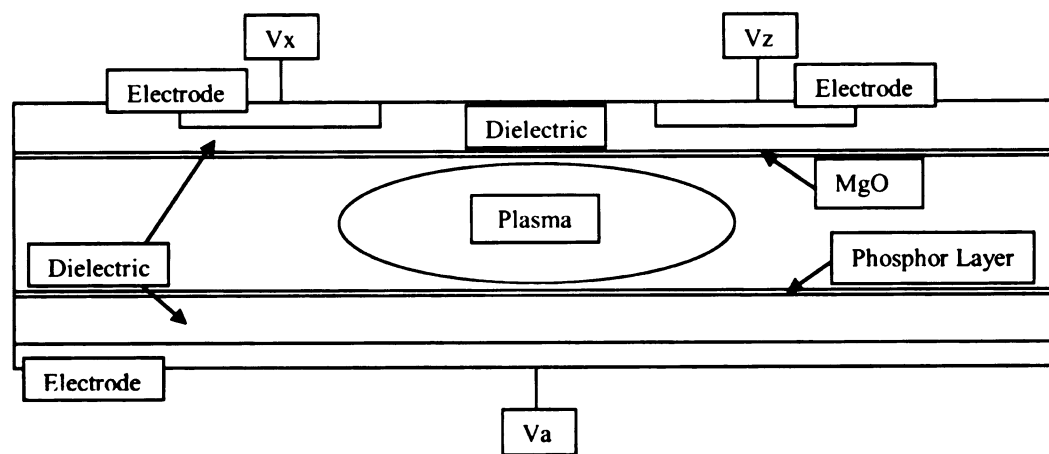
Figure 1 Micro-Cell Plasma Display Panels.

generate excited radicals. In fact, secondary electron emission is by far the main source of electrons in micro-cell plasma displays. The MgO layer provides a high secondary electron emission rate, and hence increases the cell efficiency rate. The cell efficiency rate is defined as the ratio of the power absorbed per unit volume that produces excited states of Xenon to the total power absorbed per unit volume.

The breakdown voltage, or the voltage necessary to ignite the plasma, and the self-sustaining voltage are a function of the ionization energy of the fill gas, the frequency, the cell capacitance, lifetimes for each of the gas species, and the secondary electron emission rate of the MgO layer. The typical breakdown voltage for a cell is approximately 300 volts. During self-sustaining operation, at a frequency of 50 kHz, the plasma electron density is approximately 10^{11}-10^{12} electrons per cubic centimeter [2].

Application of a high voltage pulse across the electrodes initiates the plasma discharge. The energetic free electrons excite Xenon atoms through atomic collision. Excited Xenon atoms release photons as electrons fall from higher energy states (resonant, excimer, and metastable states) to the ground state. The photons are emitted in the ultraviolet range. The ultraviolet radiation reacts with the phosphor coating on the cell walls, which converts the ultraviolet light into visible light- red, green, or blue, depending on the type of phosphor coating.

Investigation shows that the mixtures relatively lean in Xenon produce the lowest breakdown voltages while still delivering high ionization rates. Neon-Xenon and Helium-Xenon ratios of 95%-5% reduce the breakdown voltage from 300 volts, necessary for 100% Xenon cells, to approximately 125 volts. Xenon efficiency rates peak at 90% for 100% Xenon cells, and drop-off moderately to approximately 70% as the

Xenon concentration is reduced to 5%. Cell efficiency rates are higher for Neon-Xenon mixtures than for Helium-Xenon mixtures in all concentrations. The effect of Argon as an additive is negligible [3].

Researchers have also studied the optimum shape and operating frequency of these plasmas. Two-dimensional modeling of the plasma cell predicts that much higher cell efficiency rates and electron densities can be achieved with a cylindrically shaped cell operating at radio frequencies (13.56 MHz) [4]. The cylindrical shape geometry allows for greater plasma volume for a given surface area. As a result, the cell can be made smaller, and the necessary breakdown voltage and self-sustaining voltage reduced.

The advantages of smaller size cannot be realized if the frequency is not increased as well. Although much less mobile than the electrons, ionized Helium still has enough time to pass through the sheath to the walls at relatively low frequencies. Applying radio frequency voltage helps trap the Helium ions in the reduced plasma volume. As a result, plasma electron densities can be increased by a factor of five to ten, reaching 1.0×10^{13} electrons per cubic centimeter.

2.1.2 Micro-Strip Line Sources

Miniature microwave frequency plasma sources are targeted for on-chip applications, including micro-strip line technology. Micro-strip line sources, as shown in Figure 2 [5], consist of approximately one-millimeter square channels in fused silica dielectrics, or simply 0.3-1 mm silica tubes, and the corresponding ground plane and microwave matching elements formed on the top and bottom of the channel. Argon is flowed through the channel; the plasma is ignited with a piezoelectric sparking device and sustained with approximately 15 Watts of microwave power at 2.45 GHz.

8

Gas Feed

Coaxial Connector

Ground Plane

Microstrip Line

Dielectric Layer

Ignition Point

Plasma/Gas Channel
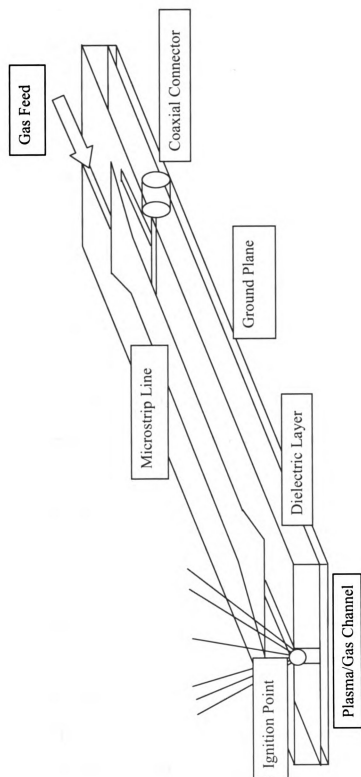
Figure 2 Micro-Stripe Line Sources.

The resulting plasma is very bright as viewed looking into the open-ended channel. The micro-strip line plasma has been demonstrated at one atmosphere, allowing contaminants to be introduced from the environment, and hypothetically, detected by matching the contaminant to its atomic emission spectra. The benefit of a source of this type is an on-chip optical emission or atomic emission spectrometer.

2.1.3 Capacitive Sources

A simple plasma source geometry is that of the capacitive source. In general, a high DC, rf (13.56 MHz) or microwave (2.45 GHz) voltage is set up across parallel plates. The resulting electric field ionizes neutrals, producing ions and free electrons. The free electrons accelerate under the influence of the electric field, and collide with neutrals and ions. If the free electrons are given sufficient energy, these collisions generate more free electrons, and the plasma becomes self-sustaining.

In DC discharges, electron acceleration is strictly a function of the applied electric field and the mean free path of the electron, which is a function of pressure. In an RF or microwave power discharge, the effective mean free paths can be made shorter if collisions reverse the electron momentum at a frequency roughly equal to the frequency of the applied electric field. Optimal coupling occurs when the frequency of the applied power matches the electron collision frequency, which occurs at a pressure of approximately 5 torr for an applied RF power at 13.56 MHz.

One specific capacitive source application is the miniature mass spectrometer, as shown in Figure 3 [6]. The plasma is coupled to the incoming gas by accelerating plasma electrons through a two-grid electrode system. The plasma electrons are focused into a narrow beam as they enter the sample gas ionization chamber to keep the ion

Gas Flow

Ionized Gas

Ion Deflector

V-accel

Free Electrons

Plasma

HF-Source
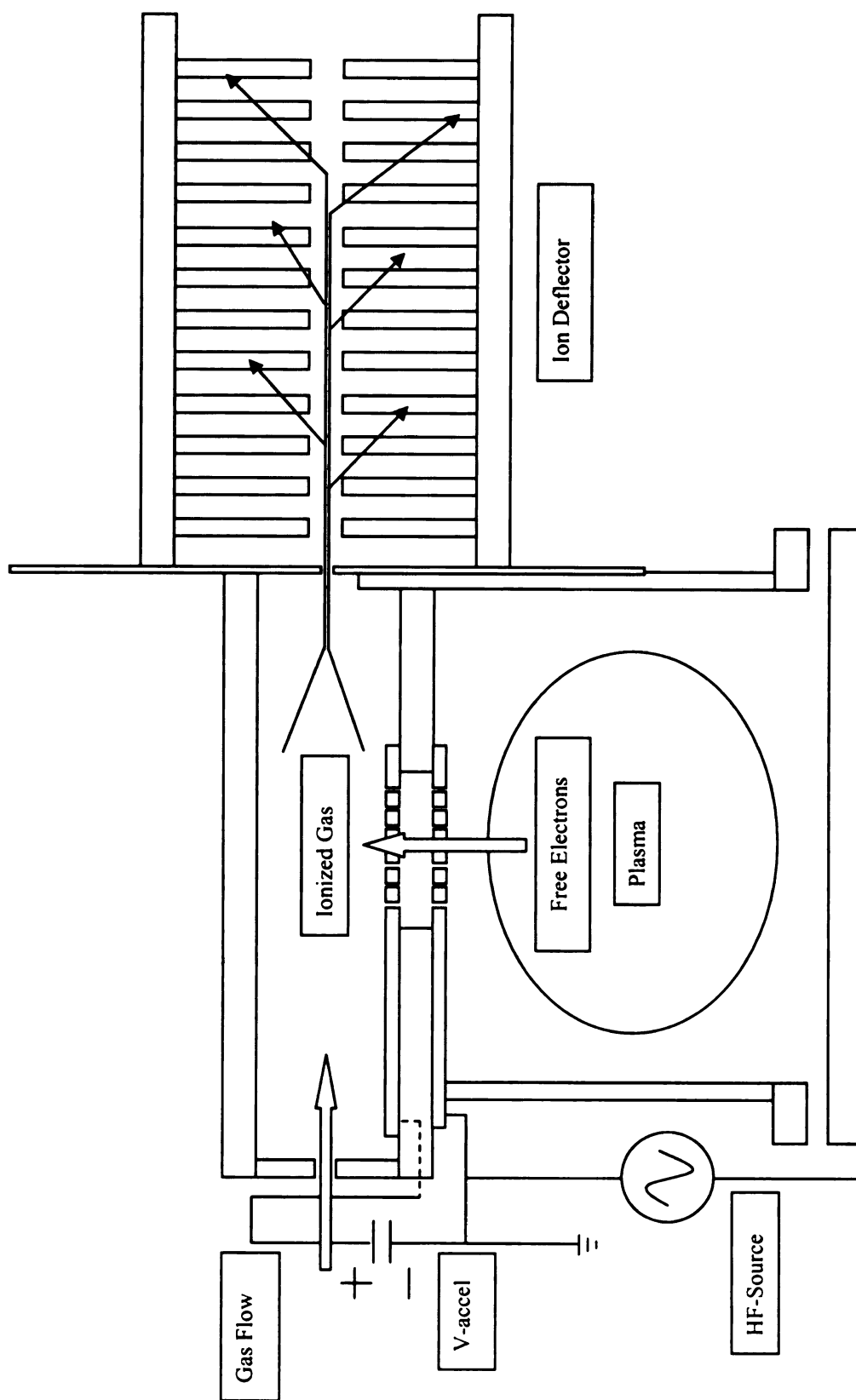
Figure 3 Miniature Mass Spectrometer (Capacitive).

11

energy distribution as narrow as possible. The electrons ionize the gas sample; the ions are then accelerated and deflected as they travel along the mass spectrometer channel by a series of alternating voltage pulses synchronized to periodically spaced terminals.

Microwave power is the preferred source for two reasons. Firstly, sputter damage to the plasma cell walls is reduced as the plasma ions are trapped by the high frequency electric fields. Secondly, and more importantly, the high frequency electric fields used to generate the plasma discharge have a negligible effect on the heavy ions in the mass spectrometer channel. Obviously, since the theory of operation for the mass spectrometer is the ionization, acceleration, deflection, and accurate deflection detection of the gas species, spurious electric fields must be avoided or the entire system will be compromised.

Technically, the micro-cell plasma display discussed in section 2.1.1 is a capacitive plasma source. Also, the micro-strip line plasma source presented in the previous section can be generated as a capacitve discharge or a surface wave discharge.

2.1.4 Inductive Sources

Large-scale inductive sources dominate the microchip fabrication landscape. Miniature inductive plasma sources could be used as part of a microprocessor based emission spectrometer or mass spectrometer, or could be the basis for thrust generation in ion beam drives for space propulsion. Recent work has demonstrated the ability to create 5 mm, 10 mm, and 15 mm diameter planar inductively coupled plasmas (ICPs) at pressures below 10 torr, powered by 1-20 Watts RF power between 13.56 MHz-500 MHz.

Miniature planar ICPs, as shown in Figure 4 [7], are constructed by masking off a 20-turn spiral pattern, 15 mm in diameter for the largest of the three sources. The planar spiral is fixed directly above a 1.8-mm glass window, which contains the plasma. Two high-Q capacitors are placed in series with the helix to adjust the tuning; the tuning is effected by the inter-winding capacitance. The plasma containment vessel is filled with Argon or air, and operated at pressures between 0.01 torr and 10 torr.

The miniature ICP sources accurately follows the same trends for plasma potential, electron temperature (when the plasma sheath is correctly removed from the calculation), and ignition frequency (electron elastic collision frequency equals rf source frequency) as do large-scale ICPs. But, both experimental Langmuir probe and interferometer measurements (35 GHz) yield electron densities (approximately 1.0×10^{10} to 1.0×10^{11} electrons per cm^3) which are an order of magnitude lower than that predicted by global plasma models. This discrepancy is thought to be a function of wall recombination, resulting from the relatively low volume to surface area ratio. Similar effects were mentioned previously in the low frequency micro-cell plasma display cell.

2.1.5 Microwave Torch and Arc Discharges

Torch and arc discharges have been investigated for over four decades. In present torch and arc configurations, gas is forced through a small (~1mm) diameter nozzle supersonically, and ignited by microwave power. The resulting plasma can take two forms in general, corona and torch. The plasma forms as the high electric field at the electrode or nozzle tip accelerates electrons into neutrals at a high enough velocity to ionize the neutrals. This form is known as the corona, and is concentrated at the very tip of the nozzle.

13
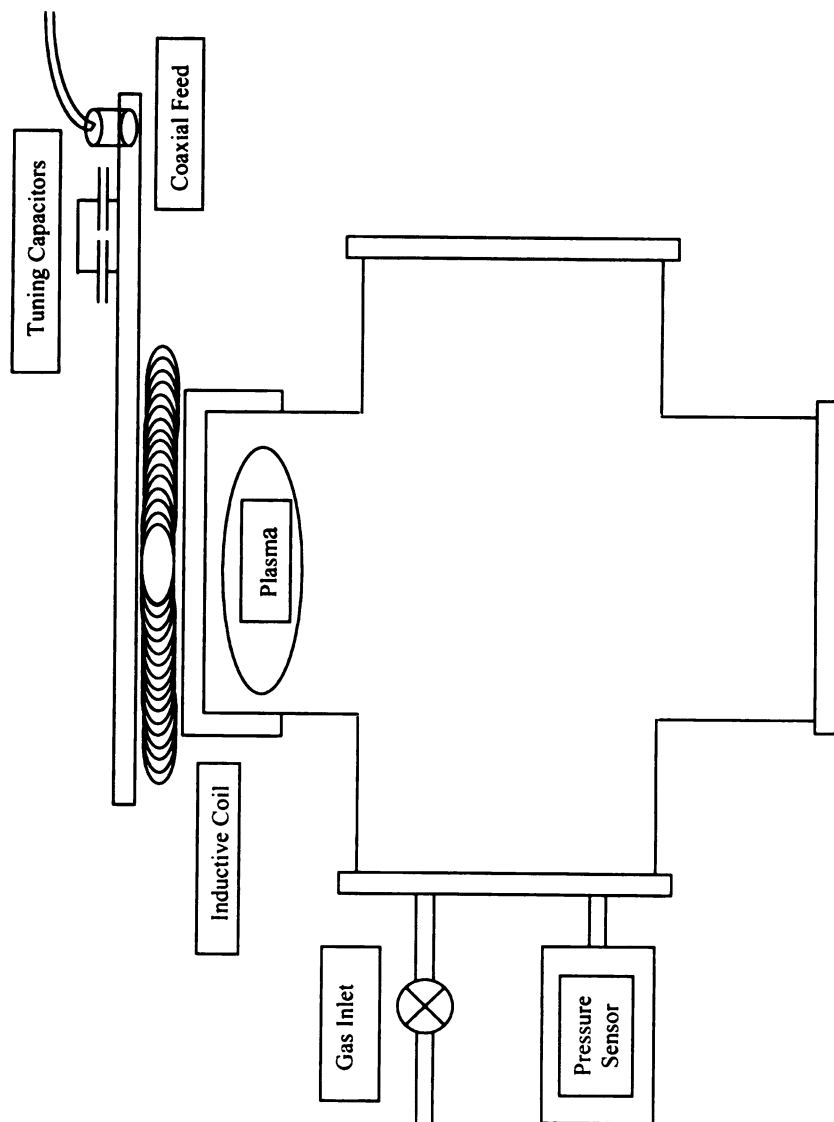
Figure 4 Inductive Sources.

Tuning Capacitors

Coaxial Feed

Inductive Coil

Plasma

Gas Inlet

Pressure Sensor

As the plasma slowly begins to absorb more power, the vibration energy and translation energy in the gas increases, as well as the ionization. This reduces the effective electric field near the nozzle, gradually extinguishing the corona form of the plasma near the nozzle, but exciting the working gas that is farther from the nozzle. The plasma appears as a flame, with a hollowed center where the corona discharge is extinguished. This form of the plasma is called the torch. The electric field present when the corona discharge forms is approximately 14,000 volts per centimeter; the electric field in the torch discharge is approximately 300 volts per centimeter [8]. Electron temperatures in the range of 5000-5200K have been recorded for similar experimental sets [9].

As the gas flow rate is increased, the gas will flow around the torch, and the vibration temperature and translation temperature of the gas will be reduced due to gas cooling. The torch effectively runs out of fuel, the microwave energy again begins to accelerate electrons near the tip, and the corona form of the plasma returns as the torch appears to be blown out.

When the microwave power dissipated in the torch discharge increases above a critical point, the sharp electrode edge is heated to produce thermionic electron emission. The resulting plasma looks more like a controlled arc than a torch, and is referred to as an arc torch discharge. The thermionic emission provides enough electrons to prohibit the return of the corona plasma form, stabilizing the discharge.

Another attempt to stabilize the torch discharge is the introduction of a conical nozzle that contains, or redirects the working gas such that the plasma consumes nearly all of the flowed reactant. Typical electron densities, as measured by the resonant

15

frequency and bandwidth shift, registered approximately 1.0×10^9 to 1.0×10^{11} cm^{-3} for this form of the plasma torch, operating at one atmosphere. This variation of the torch discharge is shown in Figure 5 [10].

Torch or arc torch discharges have been developed for pressures ranging from 0.5 torr up to one atmosphere. Torch discharges have been used for surface treatment and cleaning, and for thin film depositions on internal cavity walls, holes, vias, and on substrates of complex shape.

A variation of the torch or arc torch is the microwave powered plasma pencil [11]-[13]. The experimental set-up is similar to that given for the microwave torch and arc discharge. The difference is that the plasma pencil utilizes the gas delivery tube as a hollow cathode to supply the microwave power. Research in this area includes attempts to focus the plasma beam with a high-current magnetic lens system. This is similar to the focusing achieved in modern microscopy, such as the electron microscope. Plasma diagnostics of the plasma pencil yielded electron temperatures from 5200K to 5800K, with gas temperatures on the order of 700K to 950K, operating at one atmosphere [13].

2.1.6 Micro-Hollow Cathode Tubes

The micro-hollow cathode tube refers to a structure, as shown in Figure 6 [14], in which the plasma forms between a hollow cathode and an arbitrarily shaped anode. The micro-hollow cathode tube is characterized by an initial pre-discharge. The initial pre-discharge plasma is shaped by the electric field. As the applied DC voltage and current are increased, the pre-discharge forms a column extending from the hollow cathode to the anode.
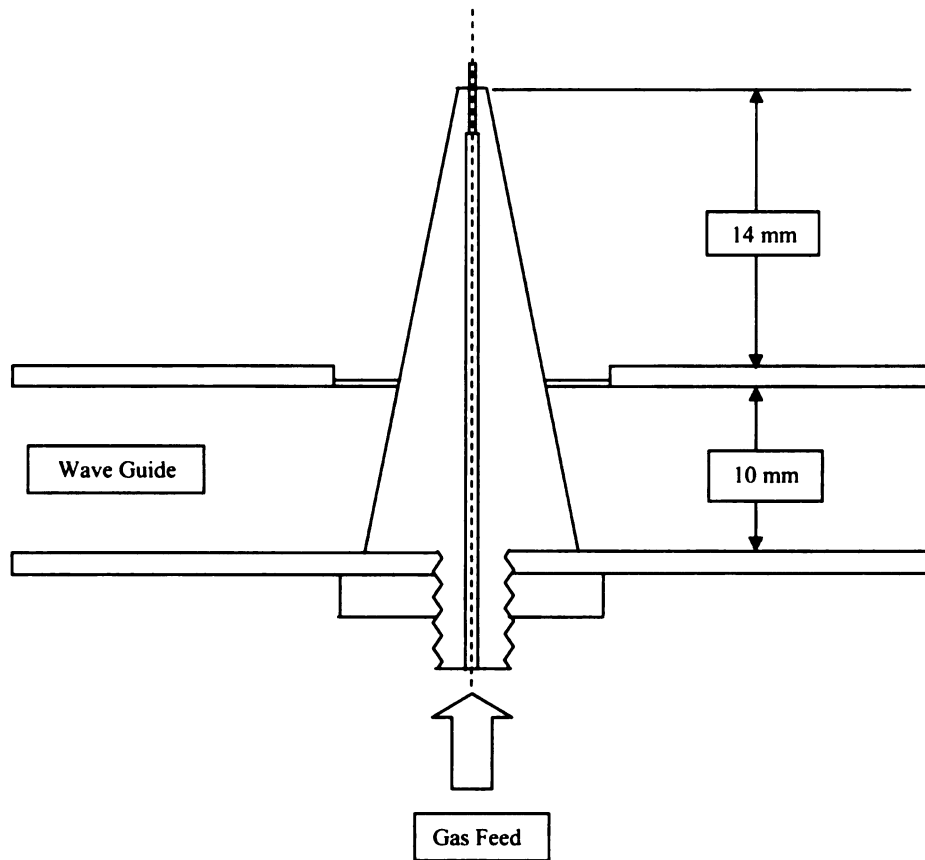
Figure 5 Torch and Arc Discharges.

14 mm

10 mm

Wave Guide

Gas Feed
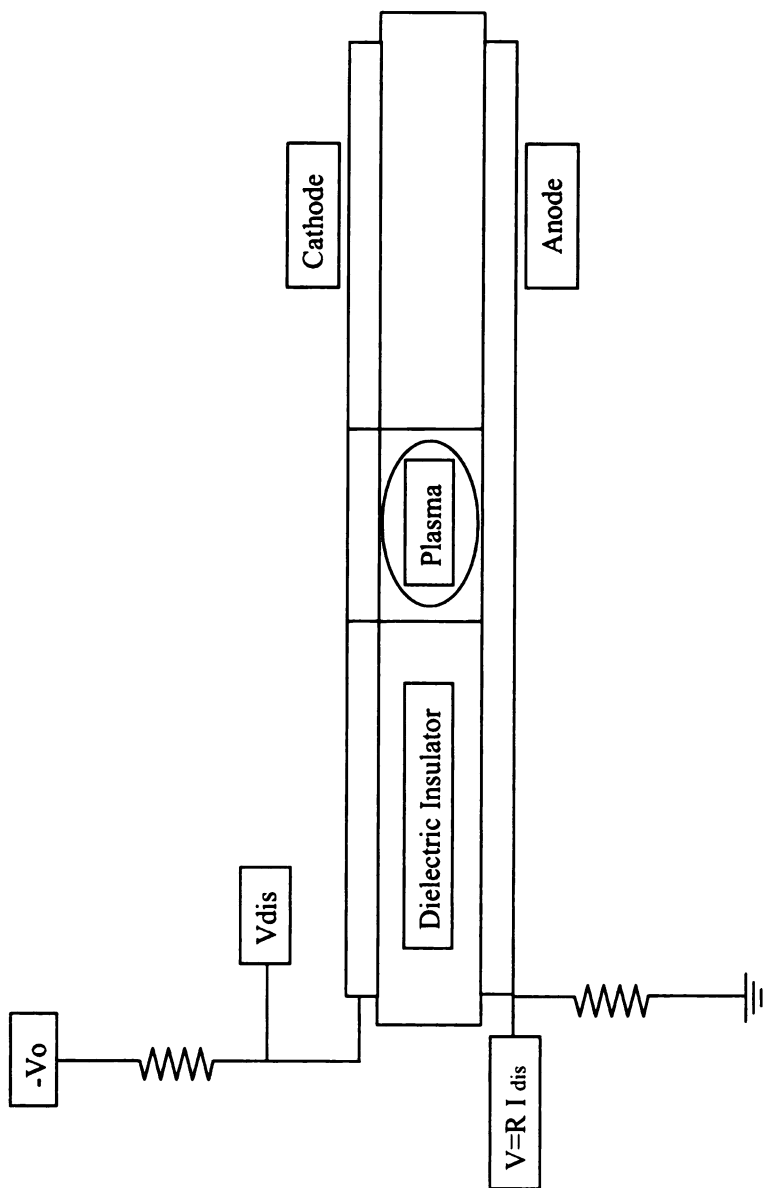
Figure 6 Micro-Hollow Cathode Tubes.

18

The pre-discharge potential is pinned to the anode. As a result, the electrons follow electric field lines and accelerate radially inward. When the pressure is such that the mean free path of the electrons closely matches the diameter of the hollow tube, the electrons (fast electrons) gain enough energy to ionize the gas species and form a negative potential discharge within the hollow cathode tube. The electrons (fast electrons) oscillate between the negative discharge and negative cathode [15].

The electrons (fast electrons) generate ions and electrons on collision with the gas species. Ions and electrons follow field lines axially along the hollow cathode tube. As a result of these interactions, the plasma potential drops as the current through the plasma increases. This regime, where the effective resistance of the plasma is negative, is the normal operating regime and referred to as the 'hollow cathode discharge'.

The hollow cathode discharge often has a spherical shape, confined by the hollow cathode and the anode. With increasing current, the voltage begins to increase, and the plasma breaks into filaments, as commonly seen in high-voltage discharges between small, sharp-edged gaps.

The critical discharge figure of merit for the hollow cathode discharge is pD; the plasma pressure (p) multiplied by the diameter (D) of the hollow cathode. The hollow cathode discharge forms for pD values from a fraction of a torr-cm to 10-20 torr-cm. Electron energies, determined by spectroscopy, are greater than 10 eV [14].

The anode and cathode are made from molybdenum [14], and separated by a 250-micron mica layer. Argon gas is flowed through the hollow cathode tube. Hollow cathode discharges have been formed with hole diameters as small as 200 microns, and at pressures approaching 900 torr (17.9 torr-cm).

2. 2 *Microwave Plasma Sources*

This study focuses on microwave plasma sources. Microwave plasma sources offer several advantages over plasma sources driven at lower frequencies. First, when microwave energy is focused in a resonator cavity, the electric field strength, which is a function of potential and wavelength, is strong enough to excite a discharge. Second, the microwave energy can propagate through dielectric media; hence, the microwave probe does not need to come in contact with the plasma itself, making the discharge electrodeless. This is not true with low frequency discharges, which require putting the electrodes in direct contact with the plasma. Potential damage to or contamination from metal electrodes by collisions with high-energy plasma species is eliminated.

A second advantage to higher frequencies is seen in miniature plasmas. The fast electric field reversal maintains the electrons in the center of the discharge, reducing the number of collisions with the container wall. By trapping the electrons, fewer electrons are lost to the walls and more energy is absorbed by the electrons, resulting in greater ionization. This effect was discussed in section 2.1.1 when examining micro-cell plasma displays, which were dominated by secondary electron emission, in contrast to direct ionization within the plasma itself.

In general, microwave plasmas operate with smaller plasma potentials, thus reducing the plasma sheath potential, which affects the energy at which the gas species exit the plasma. Such reduced gas species energy is necessary for the success of many surface reactions involved in plasma-assisted chemical vapor deposition (PACVD).

The literature covering microwave plasma sources is extensive. The following subsections examine three common designs: the 2.45 GHz microwave plasma cavity

20

resonator, the surface wave plasma reactor, and the electron cyclotron resonance (ECR) reactor.

2.2.1 2.45 GHz Microwave Plasma Cavity Resonator

A common microwave plasma source design, developed at Michigan State University, is the 2.45 GHz microwave plasma cavity resonator, shown in Figure 7 [16]. Microwave power is introduced to a cylindrical cavity through a coaxial probe, penetrating the cavity axially from the top or the side. The height of the cavity and the probe depth are adjusted for cavity microwave field resonance with the applied microwave frequency. In one design, the cavity diameter is 17.8 cm, and the height is adjusted to 21 cm. The resulting resonant mode is TM 013. Microwave power levels range from 500W-5kW. Operating pressures run from 5 torr to 180 torr. Such systems have been developed for PACVD of diamond.

The plasma discharge forms within a sealed quartz dome, mounted at the base of the cylindrical reactor. The discharge is initiated by the electric field focused in the quartz dome. The reactant gases are injected from the base plate of the reactor with high velocity, mixing in the quartz dome before ignition. Premixing the gases improves deposition uniformity in plasma assisted chemical vapor deposition (PACVD) reactions. Uniform deposition can be maintained on wafers up to four inches in diameter.

The substrate holder is interchangeable and adjustable in height, to better interact with the plasma formed above it. In high-pressure experiments, the substrate holder has been water-cooled to better facilitate deposition. The system has been scaled up to accommodate 915 MHz power supplies. The 915 MHz reactor is 45 cm in diameter; the
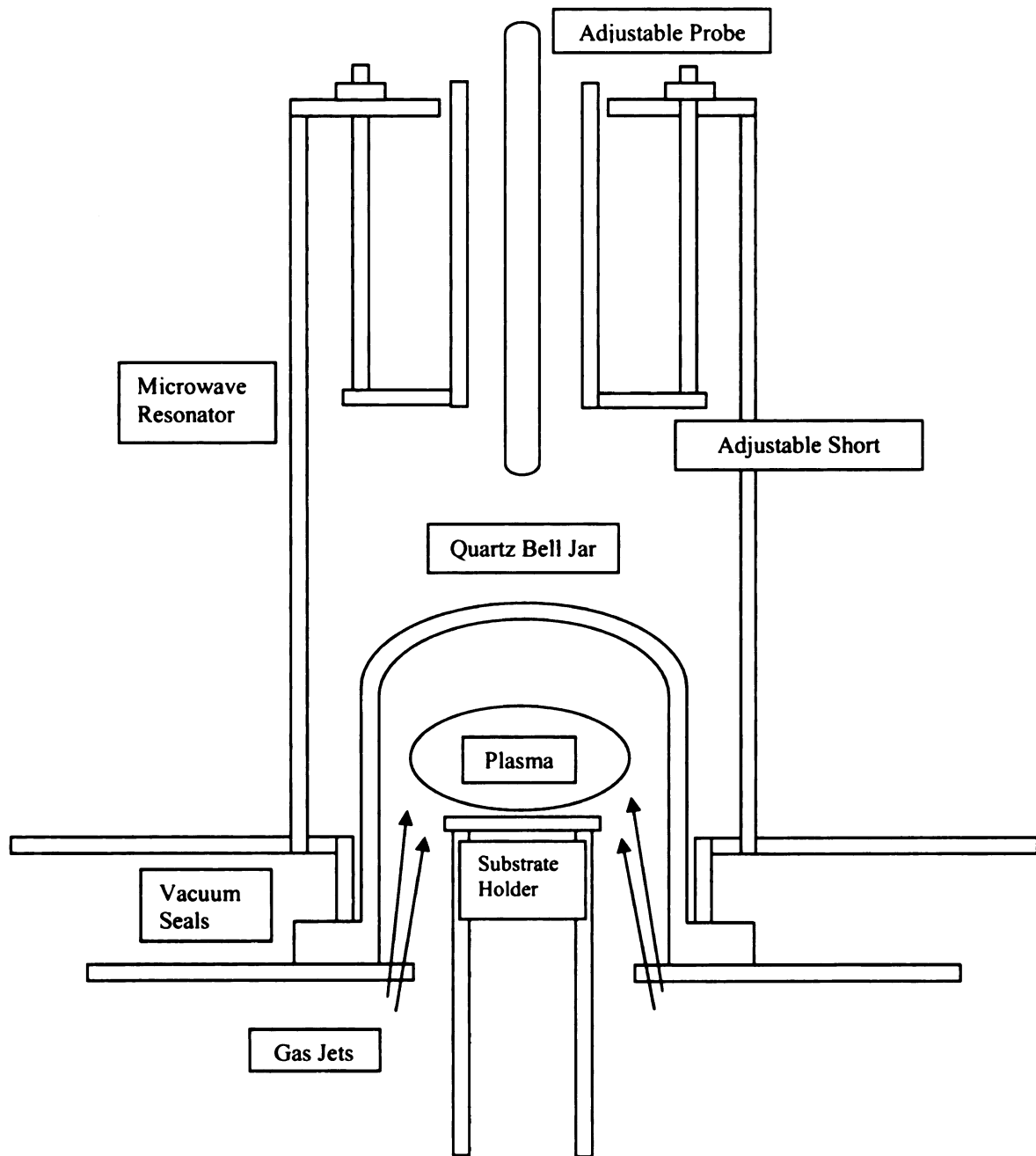
Figure 7 2.45 GHz Microwave Plasma Assisted CVD Reactor.

largest possible substrate size is 33 cm. The 915 MHz reactor power requirement is 8kW-18kW.

2.2.2 Surface Wave Plasma Reactor

The surface wave plasma reactor's geometry is completely different from that of the 2.45 GHz-microwave plasma cavity. In the surface wave reactor, the microwave power is transmitted from the waveguide through a sealed 2.5-cm diameter quartz tube, into a waveguide surfatron, which functions as a double-stub tuner. The quartz tube is filled with reactant gases; the pressure can be adjusted from 1-60 torr. The surface wave reactor uses 1 kW microwave power at 2.45 GHz. The surface wave plasma reactor schematic is given in Figure 8 [17].

The plasma fills the quartz tube, and distends several centimeters below the waveguide structure at low pressures. The plasma excitation along the plasma column is facilitated by the propagation of microwave energy along the column via surface waves that travel along the boundary of the plasma. Below the waveguide structure, the quartz tube diameter can be increased to accommodate substrates up to 8 cm in diameter. The plasma expands to fill the quartz tube below the waveguide, allowing for complete coverage of the substrate during deposition.

2.2.3 Electron Cyclotron Resonance (ECR) Reactor

The electron cyclotron resonance (ECR) reactor is similar in geometry to the 2.45 GHz-microwave plasma cavity, however the nature of the plasma is quite different. In the ECR reactor, electron heating -motion and collision- is a result of the electron
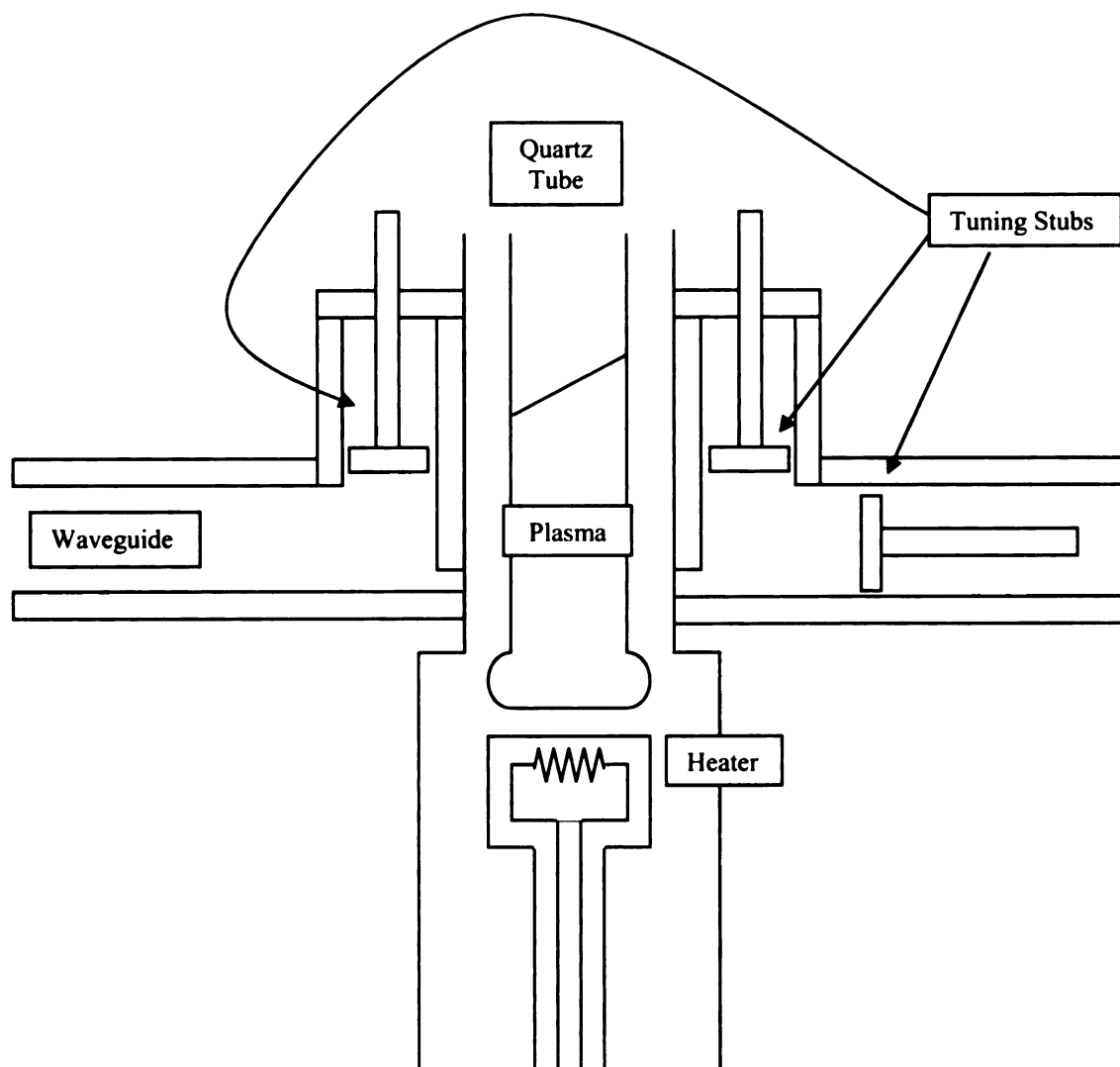
Figure 8 Surface-Wave Microwave Plasma Assisted CVD Reactor.

cyclotron effect; the force imposed on charged particles that results from an oscillating electric field in the presence of a permanent magnetic field (875 gauss).

In the reactors described previously, the most efficient heating occurs at pressures where the mean free path of the electrons give rise to a collision frequency that matches the microwave frequency. At the point of collision with an atom, the electron momentum is randomized. At the same instant, the electric field reverses to accelerate the electron, increasing its average velocity with each field reversal and collision, until the electron has enough energy to ionize the atom or molecule.

In ECR reactors operating at resonance frequency, the electron revolves around the magnetic field lines with an angular rate equal to the frequency of the applied microwave power. Each field reversal accelerates the electron for one-half revolution before the next reversal. The electron will ionize an atom upon collision if it has been given enough time to build up sufficient energy.

A specific example of an ECR source is the compact ion and free radical model #610 plasma source developed at Michigan State University, shown in Figure 9 [18]. The reactor is a stainless steel cylinder with 5.8-cm outer diameter. The front half of the cylinder is the coaxial microwave power feed, terminated with a loop antenna. The back half is filled with a 3.6-cm x 3.0-cm quartz reaction vessel. The operating pressure is kept between 0.1 mtorr and 3.0 mtorr, much lower than the operating pressure for the 2.45-GHz microwave plasma cavity resonator described in section 2.2.1. Microwave power levels range from 50W-200W.
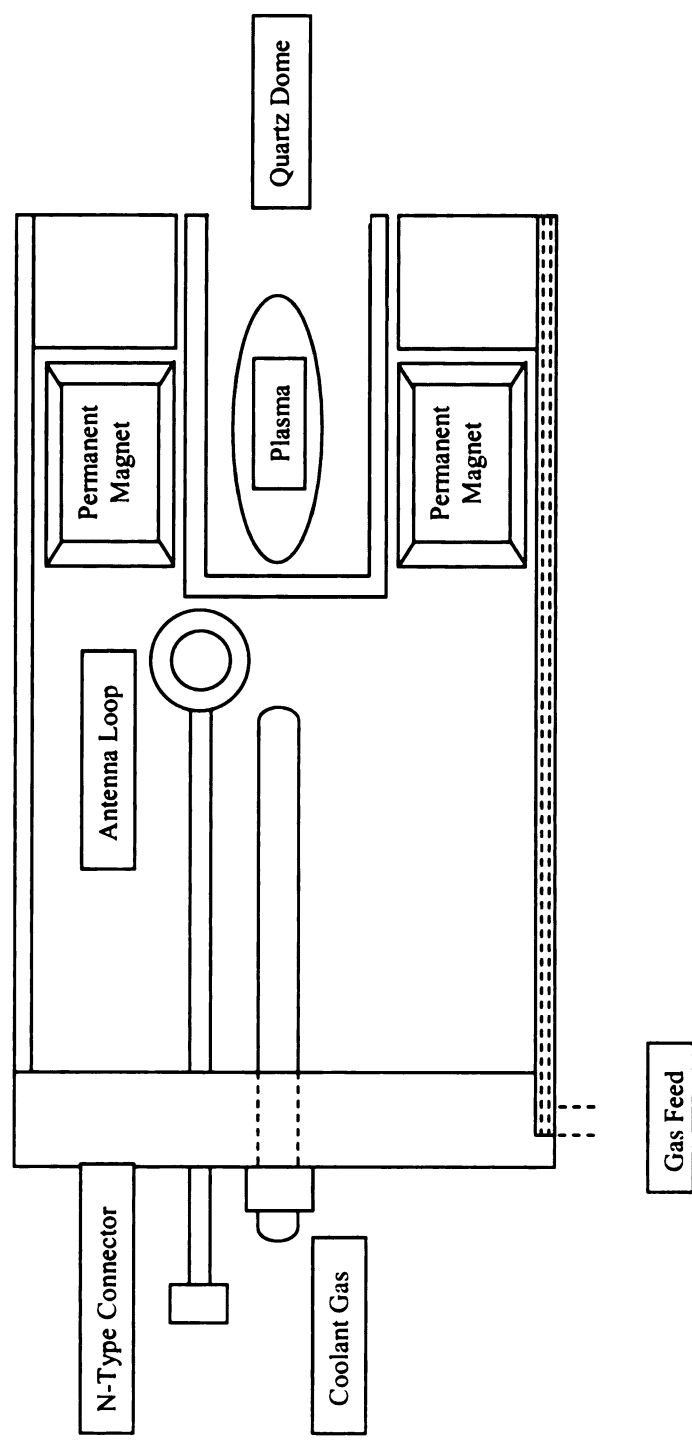
Figure 9 Electron Cyclotron Resonance CVD Reactor.

Quartz Dome

Permanent Magnet

Plasma

Permanent Magnet

Antenna Loop

N-Type Connector

Coolant Gas

Gas Feed

Chapter 3 Experimental Setup

The primary research objective is to quantify the operating characteristics of miniature microwave plasmas with sizes ranging from 0.25-10mm. To this end, a new microwave plasma system must be built that can create miniature plasmas in the specified range at controlled pressures. Additionally, it should allow for multiple gas feeds at controllable flow rates. It should be safe, affordable, run at low power, and ideally, portable.

Plasma diagnostics must be investigated and developed. Diagnostics must provide the following plasma characteristics: electron density, gas temperature, and plasma power density. Diagnostics should also be portable, requiring only standard laptop computer interface.

The following section describes the design, construction, operation, test, and function of the miniature microwave plasma reactor and system designed specifically for this investigation. The next section describes the plasma diagnostic set, and the extra design work that was necessary to extract the required plasma characteristics from such a small, low-power source.

Section 3.3 provides valuable initial test data from the plasma system, giving insight into plasma ignition and plasma operating conditions that drive diagnostic and theoretical development decisions.

3. 1 *Miniature Microwave Plasma System*

A miniature microwave plasma source and experimental system was designed, built, and tested at Michigan State University. The experimental system, as shown in

Figure 10, consists of the plasma source, vacuum chamber, microwave power system, pressure control system, and gas delivery system. The microwave plasma source, shown in Figure 11, is a 6.5-cm outer diameter coaxial waveguide, with 10-mm diameter center probe. The waveguide is terminated with an adjustable short. The center probe can be adjusted to vary the center conductor gap, where the plasma is formed. The distance from the short to the center conductor gap is adjusted to approximately one-half the wavelength of the applied microwave power (2.45 GHz). A quartz tube slips over the center probe, surrounding the gap and enclosing the plasma.

The plasma source is connected to a 100 W microwave power supply (2.45 GHz) through a circulator and a series of directional couplers and terminators or loads. The circulator is fixed to the microwave source output to protect its magnetron from reflected power. Thermistors convert transmitted and reflected microwave power into current, which drives the associated power meters.

The pressure control system functions to stabilize the system pressure. It consists of two Baratron pressure sensors (20 torr and 1000 torr), a 2-atmosphere pressure gauge, manual pressure sensor selector, three independent pressure control setting channels, two digital pressure display units, and automatic pressure control feedback circuitry to fix pressures from 1 mtorr to 1000 torr. The pressure control feedback drives a throttle valve, which determines the rate the reactant gas is evacuated from the system. An impeller pump (Alcatel, 40 liter/min) develops the vacuum.

The automatic pressure control circuitry receives signals from the manually selected Baratron pressure sensors. The 20 torr head measures pressure accurate to 1 mtorr, for pressures less than 10 torr. The 1000 torr head measures pressure accurate to

28
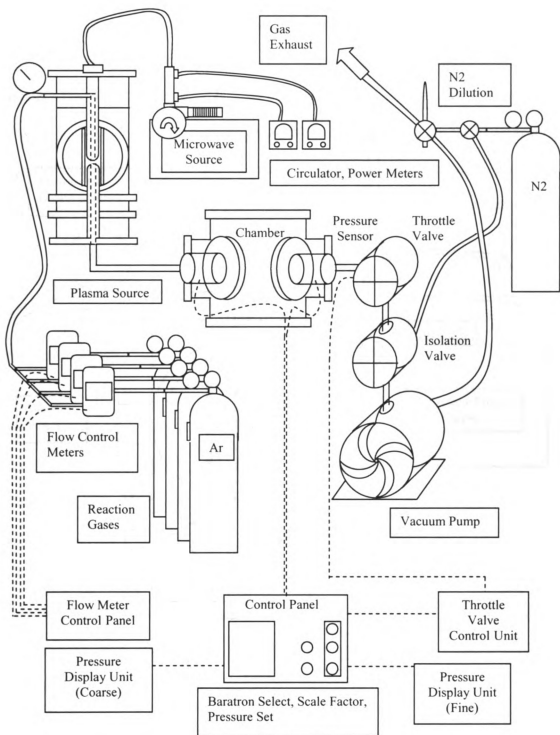
Figure 10 Experimental System.
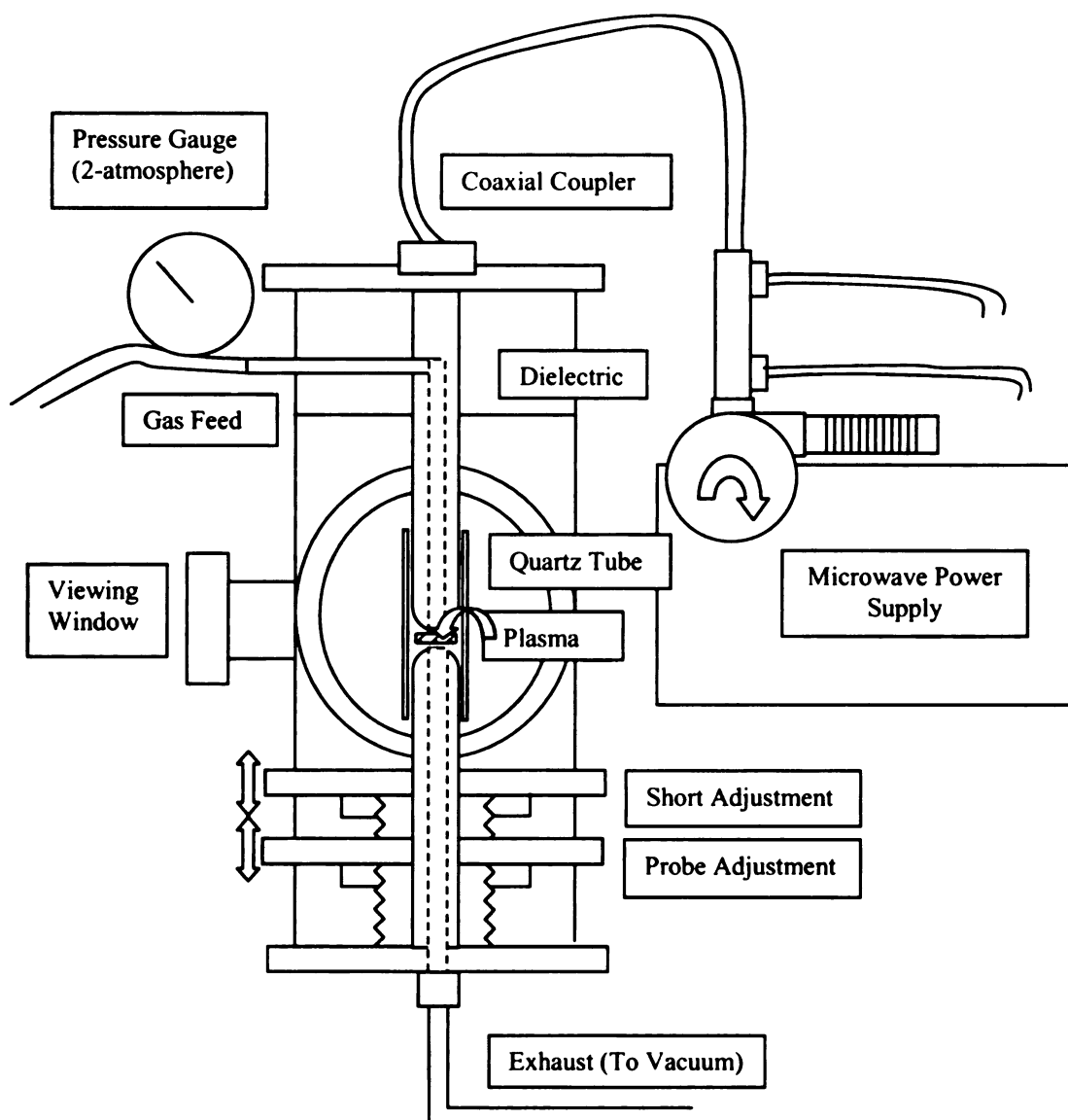
Figure 11 Plasma Source.

0.1 torr, up to pressures of 1000 torr. The pressure controller compares the Baratron input to that of the selected pressure setting, and drives the throttle valve to converge to the control setting. The pressure and target pressures are registered on the digital displays.

The gas delivery system includes a 4-channel bank of gas flow meters (Hastings: model #CPR-4A, MKS: Type 247). Three flow meters are rated for flows up to 1000-standard cubic centimeters per minute (sccm); the fourth flow meter is limited to 10-sccm, and as a result, provides the highest resolution. The 4-channel flow control unit actuates all four flow meters. The controller drives the flow meters with the difference between the selected flow rate and the flow rate feedback from the flow meters. The flow rate through each of the four flow meters is registered on controller digital displays. Each gas channel is connected to 2500-psi gas cylinders, regulated to 15 psi. The gas cylinders are secured to the side of the plasma source system. The gas channels and gas canisters are completely interchangeable. This allows for experiments using any combination of up to four gases.

The experimental system is sealed by metal-to-metal fittings (VCR seals, 64 total seals). The base pressure is less than 1 mtorr under normal operation (impeller pump only); the base pressure drops to less than 1.0×10^{-7} torr during leak tests, which requires the addition of an auxiliary turbo pump (Alcatel, 100 liter/min). Leak tests consistently register leaks less than 1 mtorr for 16-hour intervals. The system volume is 78 liters.

To reduce contamination and water vapor accumulation, the system is closed during system purge. Argon, regulated to just under one atmosphere, brings the system back up to pressure when the experiment is complete.

The following chart summarizes the current state of the miniature microwave plasma source and experimental system. The system specifications include the plasma source, vacuum chamber, microwave power system, pressure control system, and gas delivery system.

- Base pressure (roughing pump): < 1mtorr

- Base pressure (turbo pump): < 10^{-7} torr

- Leak rate (w/o reactor): < 1mtorr/16 hrs

- Plasma ignition power: 10W

- Power meters:

    1 forward power meter following 50/50 splitter
    1 reflected power meter following circulator

- Gas channels:

    3 1000-sccm channels
    1 10-sccm channel

- Pressure heads:

    1 1000-torr Baratron transducer
    1 20-torr Baratron transducer
    1 2-atmosphere head

- Pressure display for each pressure head:

    Digital display: Baratron heads
    Analog display: 2-atmosphere head

- Automatic pressure control select between 1000-torr and 20-torr Baratron heads

- Accurate automatic pressure control from 1 mtorr to 1000 torr

- Three pressure control setting channels

- Automatic Argon system purge to 1 atmosphere with adjustable pressure regulator

- Additional air valve isolation from roughing pump

32

- Manual equalization valve to bring roughing pump to 1 atmosphere

- Nitrogen vent to roof:

    Adjustable Nitrogen flow rate
    Shut-off valve to prevent backflow from neighboring DLC system

- All seals metal-to-metal (VCR) fittings

    In summary, the following input parameters can be controlled and monitored:

1. Pressure: 0.5 torr-2 atmospheres

2. Power: 0.5-100 W

3. Probe diameter (plasma diameter): 0.2-10mm

4. Plasma height: 0.2mm-20mm

5. Gas flow: 1.25-1000sccm (velocity function of nozzle size)

6. Gas species: Argon, Nitrogen, Hydrogen, Air, Hydrogen/Methane mixture

The flexibility in design allows for plasma investigation at a wide range of pressures, at different discharge aspect ratios, at power levels from 0.5 W to 100 W, and with reconfiguration capability on all four-gas channels.

3.2 *Plasma Diagnositics*

The plasma diagnostics proposed to investigate miniature microwave plasmas created by the plasma source built for this investigation are limited to spectroscopy due to the configuration of the source. The following sections describe the diagnostic set up for the optical emission spectrometer.

3.2.1 Optical Emission Spectroscopy

Optical plasma diagnostic techniques include plasma-induced emission and laser-induced fluorescence [19]-[20]. Other radiation based non-intrusive techniques include

optogalvanic, infrared, spontaneous and stimulated Raman, and multi-photon spectroscopy [21]. Optical diagnostic techniques, specifically plasma-induced emission, will be used to estimate electron density, electron temperature, and gas temperature in this investigation. The experimental set up for plasma-induced emission, or optical emission spectroscopy (OES), is given in Figure 12.

Line broadening is seen in high-density plasmas where high local electric fields are present, which result from localized charge imbalances. This effect is called Stark broadening, or electric field broadening. Estimates can be made from Stark broadening for translation temperature and electron density.

Stark broadening of the Hydrogen Balmer series (H_α, H_β) as a function of electron temperature has been computed by Griem [22]. Electron density and temperature determine the broadening for purely Stark broadened H_α lines. Deconvolving the Stark shape from the total spectrum line leaves a Doppler broadened H_α curve, and gives an estimate for Hydrogen translation energy and electron density (assuming a Maxwell distribution) [23]-[24].

Gas temperature is measured using the optical emission lines corresponding to H_2 and N_2 rotational temperature; molecular Hydrogen electronic configurations and rotational energy levels and transitions are shown in Figures 13 -14 [25].

Rotational temperature transitions within the same electronic configuration and vibration energy produce line intensities in accordance with the Boltzmann distribution.

$$I = Kv^4 S_{J'J''} \exp\left(-\frac{Bv'J'(J'+1)hc}{kT_r}\right)$$

(3.1)
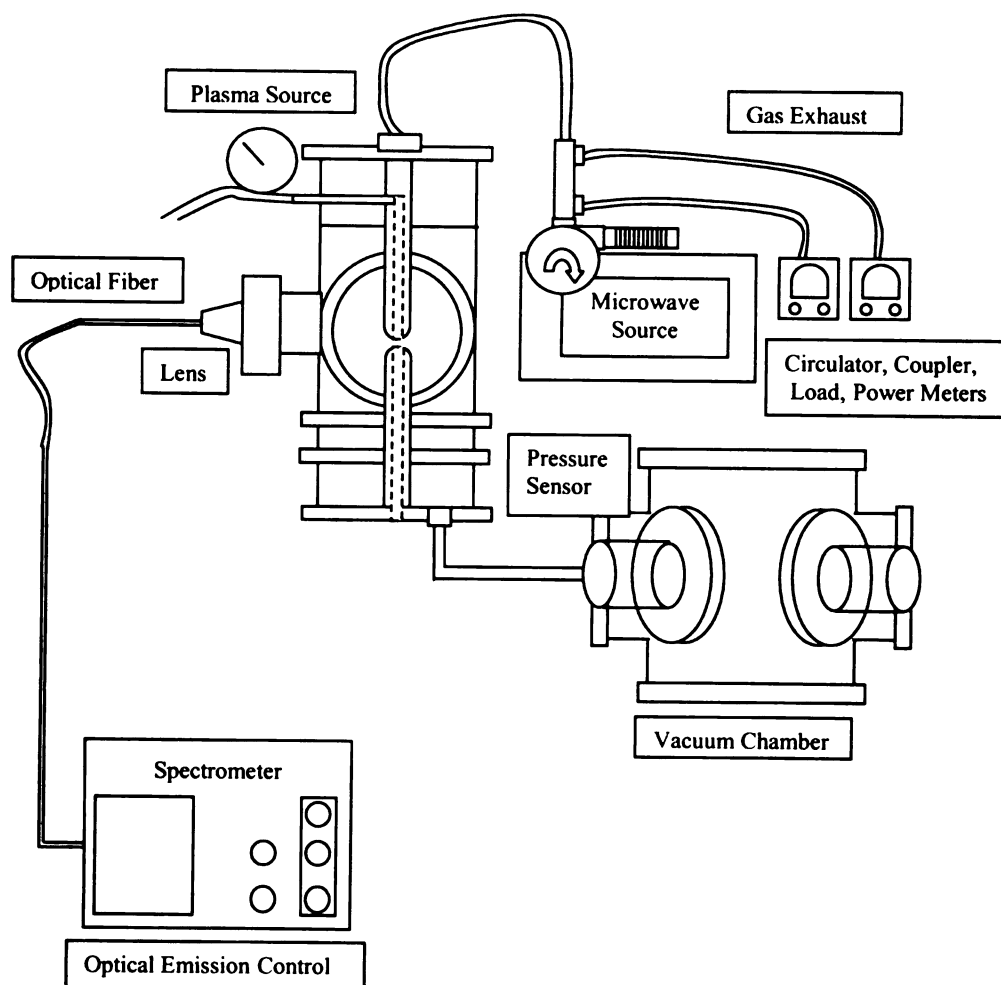
Figure 12 Optical Emission Diagnostics.

Labels in figure:
- Plasma Source
- Gas Exhaust
- Optical Fiber
- Microwave Source
- Circulator, Coupler, Load, Power Meters
- Lens
- Pressure Sensor
- Vacuum Chamber
- Spectrometer
- Optical Emission Control
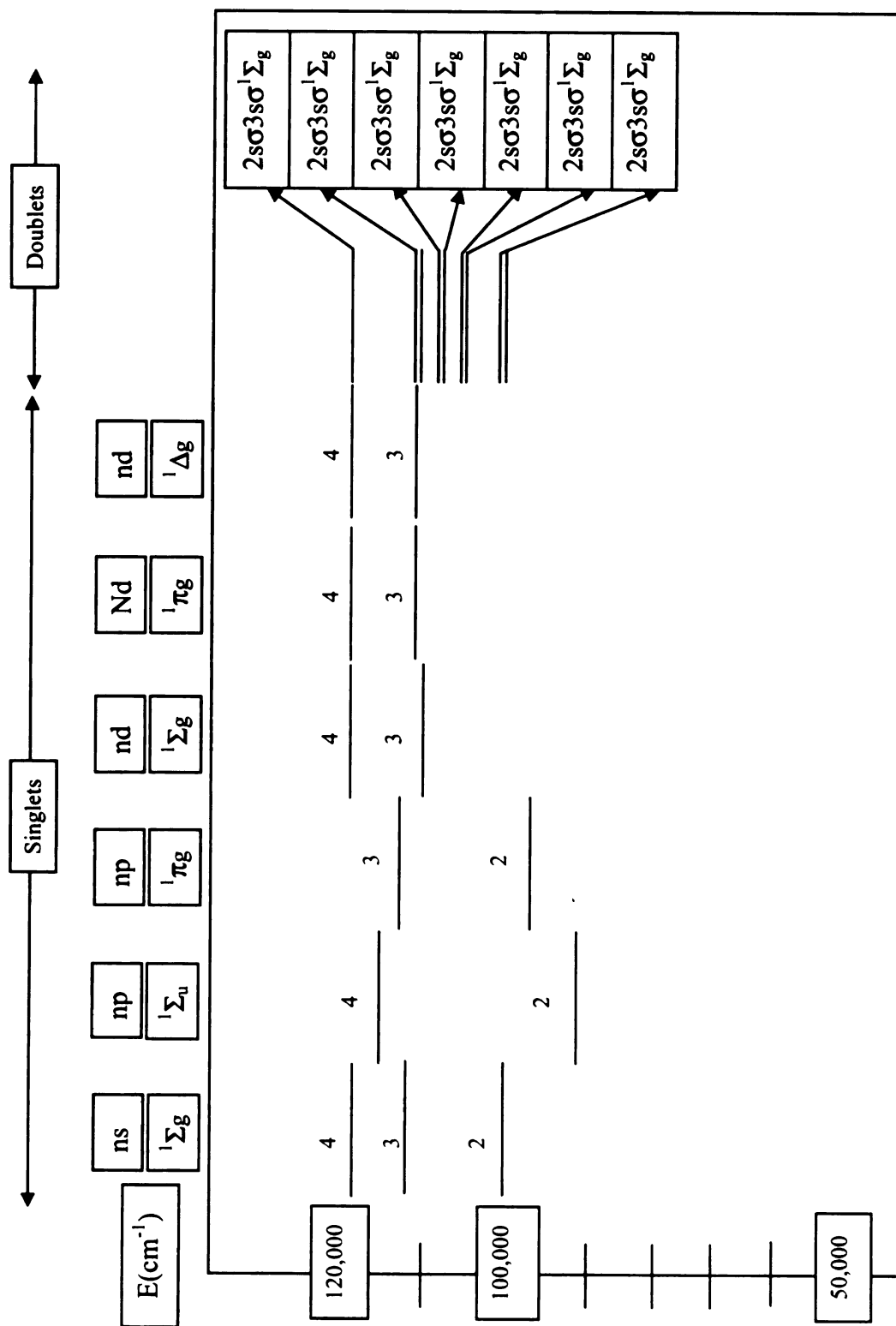
Figure 13 Observed Electronic States (H_2).
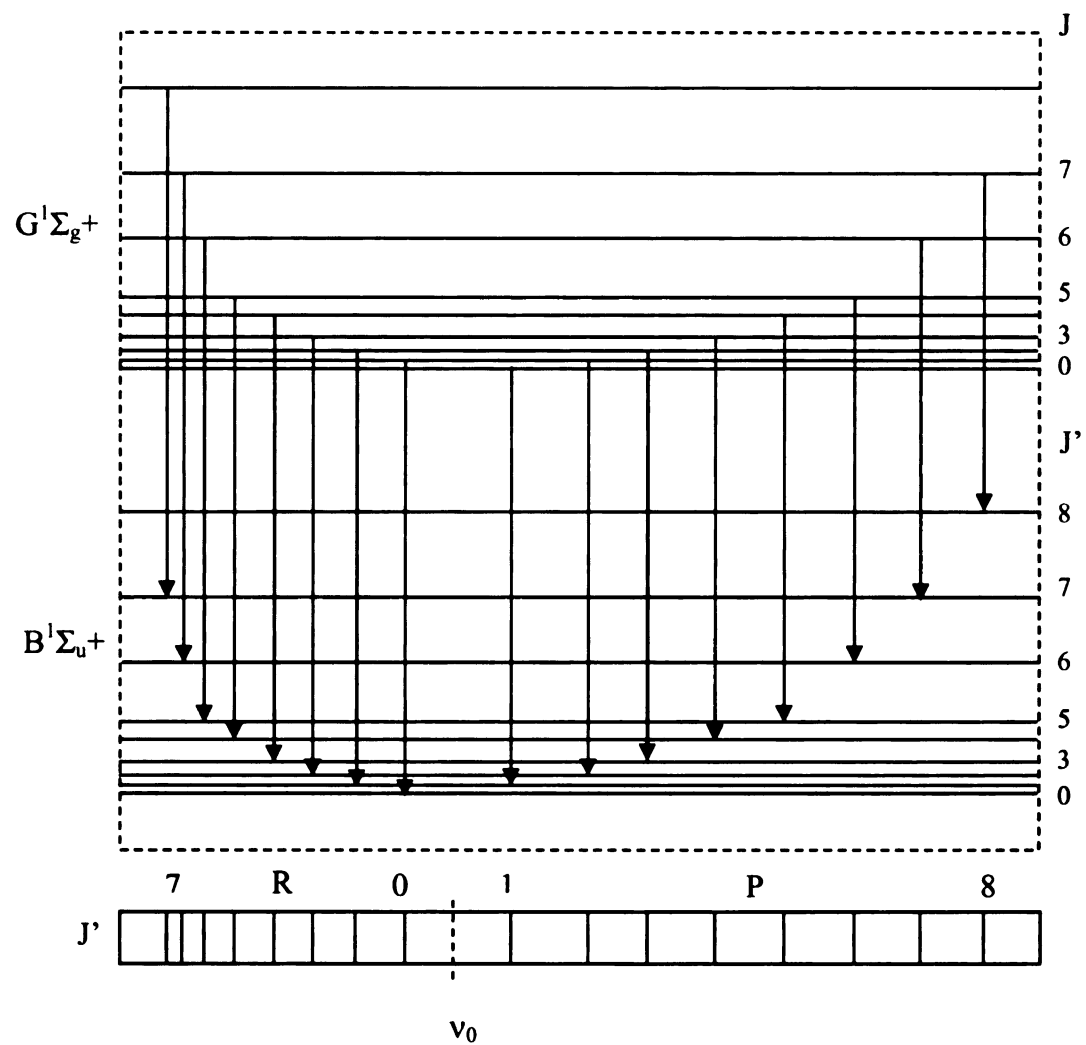
Figure 14 Rotation Temperature (Gas).

Where:

K	$\equiv$ Constant for same electron configuration and vibration level
v	$\equiv$ Frequency of radiation
$S_{J'J''}$	$\equiv$ Hoal-London factor
$B_{v'}$	$\equiv$ Molecular rotation constant
J'	$\equiv$ Rotation quantum number
h	$\equiv$ Planck's constant
c	$\equiv$ Speed of light
k	$\equiv$ Boltzmann's constant
T_r	$\equiv$ Rotation temperature

3.2.2 Optical Emission Spectroscopy Design

The intensity of the light that was gathered by the optical emission spectrometer from plasma emission was found to be so weak in preliminary testing that virtually no signal could be detected by the optical emission spectrometer. The plasma light intensity itself was well above any detectable threshold, very visible to the naked eye in all cases. However, the simple lens and fiber optic system used to focus the light into the McPherson model 216.5 optical emission spectrometer was insufficient. This preliminary design is shown in Figure 15.

In an attempt to increase the emission intensity, the lens system was plunged into the plasma reactor, focusing the plasma emission on an array of optical fibers inside the reaction chamber. The vacuum was sealed with a double O-ring feed-through, similar to seals used in electron microscopy. Light was focused into the fibers, and collimated at the end of the fibers, by specially designed and cut spherical lenses. The collimated light at the end of the fibers was refocused into the McPherson 216.5 optical emission spectrometer. Figures 16-18 detail the diagnostic setup, fiber feed-through design, and spherical lens specifications, respectively.
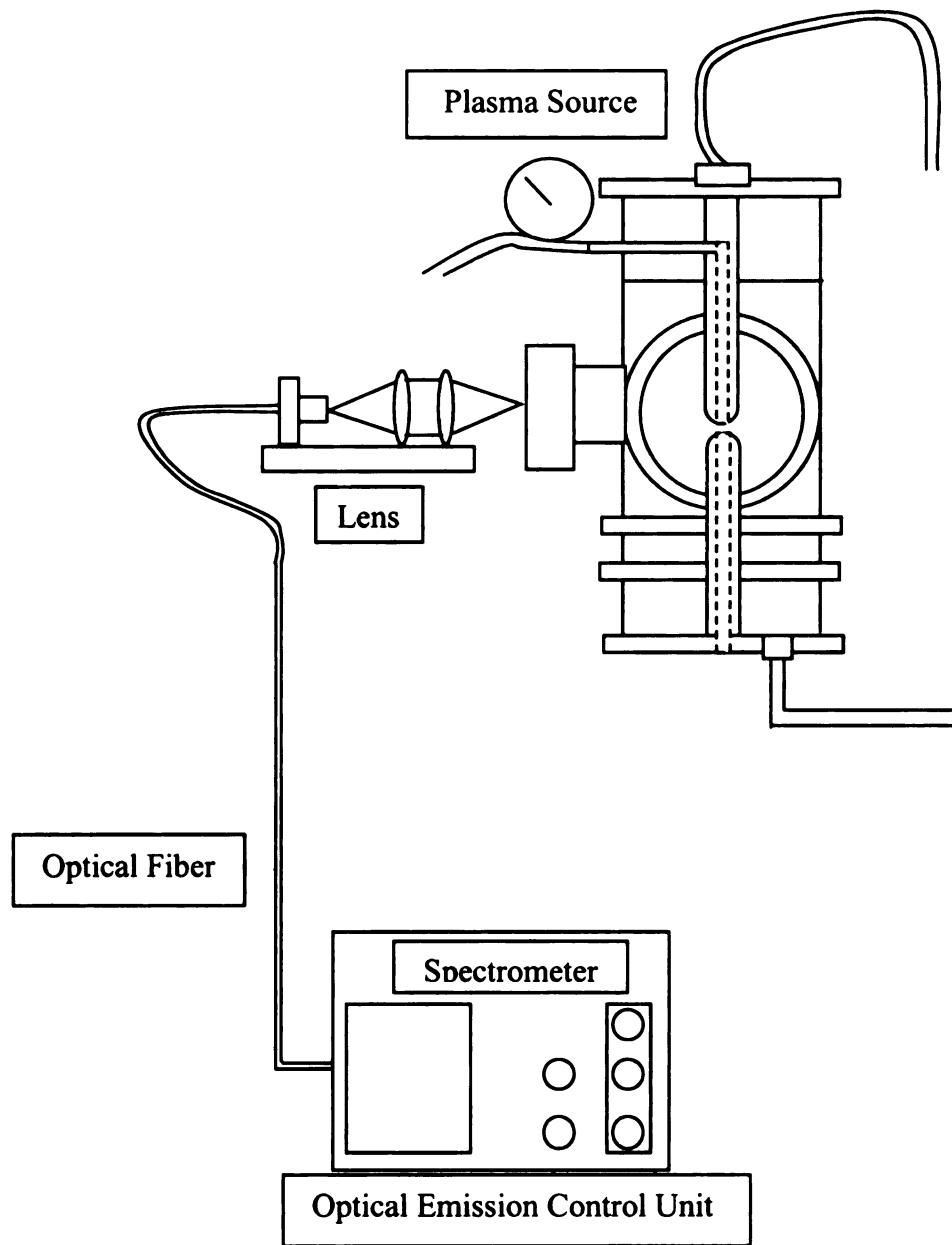
Figure 15 Optical Emission Preliminary Design.

39
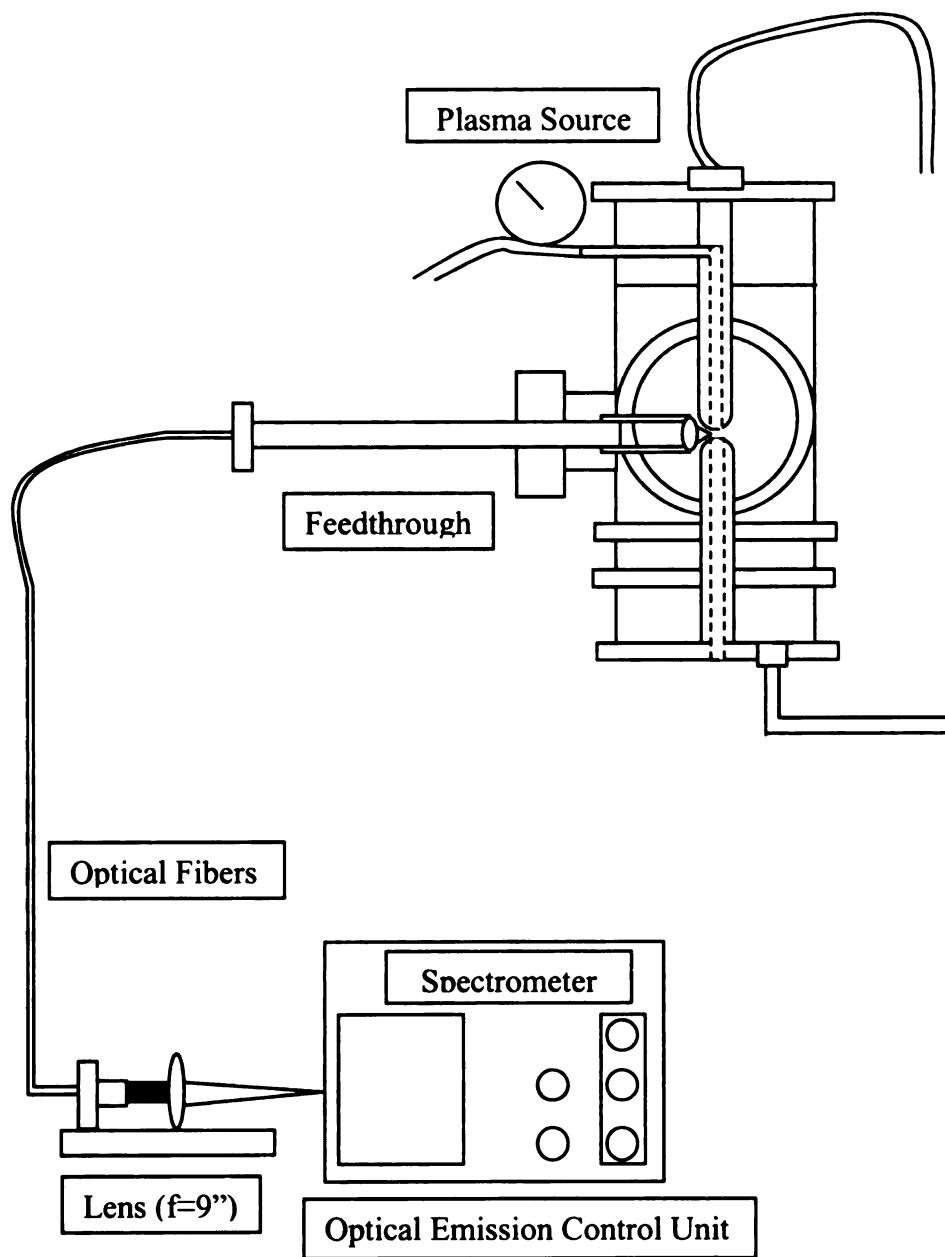
Figure 16 Optical Emission Spectroscopy Design.

BK7 Coupling Lenses (13)

Fiber Focus Lens

Fiber Seals

Fiber Optic Array
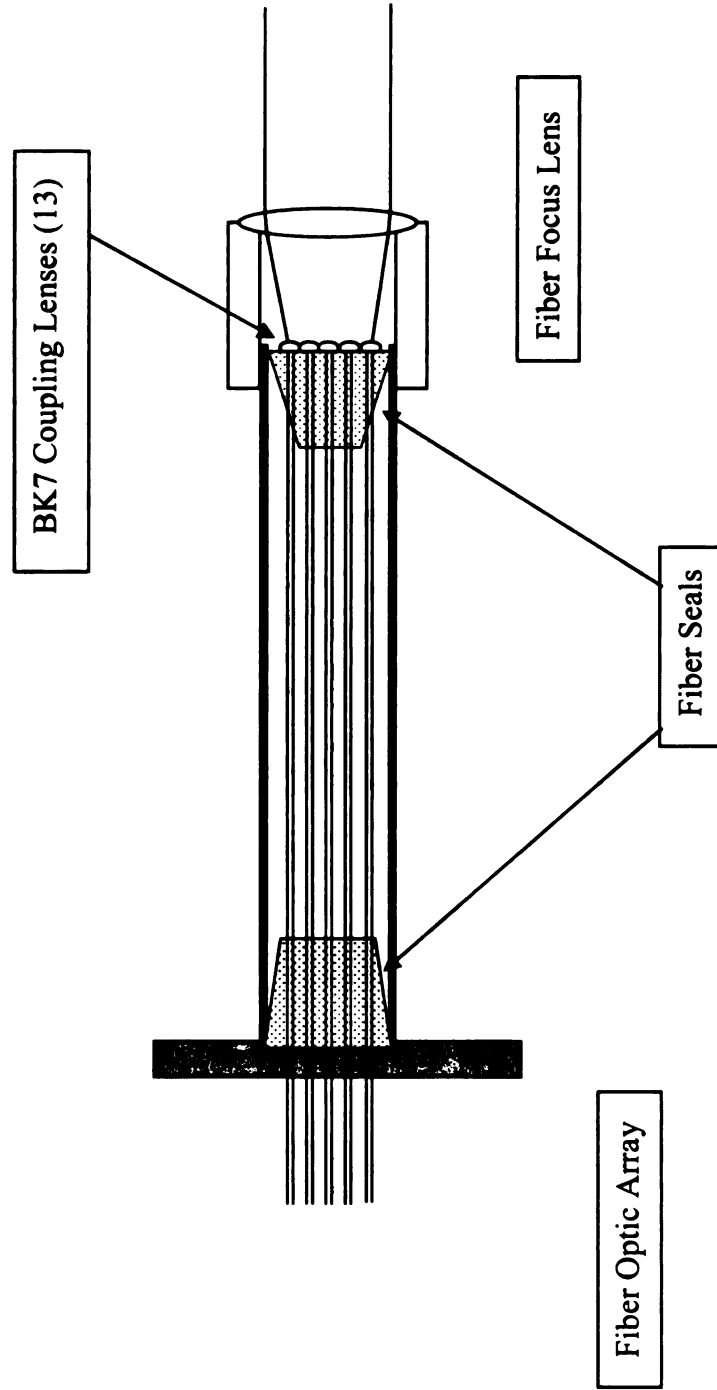
Figure 17 Optical Emission Feed-through.

41

NA=0.55

Radius=1.25 mm

0.88 mm
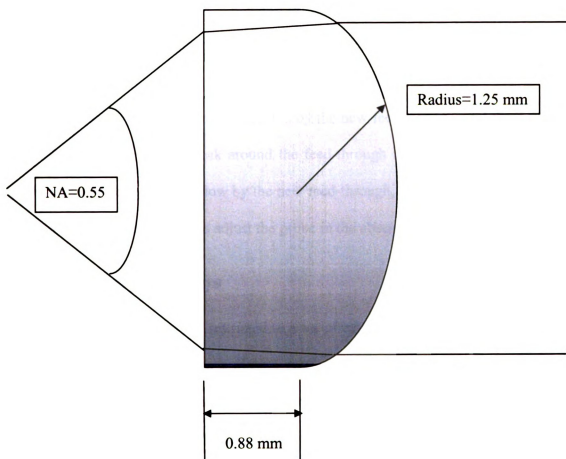
Figure 18 Spherical Lens Design.

3.2.3 Optical Emission Spectroscopy Test

Initial test results for the optical emission spectroscopy design are given in Figure 19. Photomultiplier tube currents in excess of 200 nA were recorded for the H_β line with an accelerating voltage of -900V. Vacuum pressures were unaffected by the new feed-through; there was no discernable difference in leak rate after the feed-through installation.

The plasma formation was unaffected by the new feed-through, and there was no detectable microwave energy leak around the feed-through mount. To compensate the light blocked at the reactor window by the new feed-through, its unused fibers were used to channel light into the cavity to adjust the probe in the absence of the plasma.

3.3 Preliminary Findings

Preliminary findings are restricted to a set of experiments conducted immediately following the miniature microwave plasma system build (June-August, 2001). The first set of experiments tested the miniature microwave system functions, such as leak rate, base pressure, pressure control, flow control, and microwave power measurement. The second set of experiments was concerned with plasma formation and stability. In the second set of experiments, Argon plasmas were formed at pressures ranging from 1 mtorr-760 torr (1 atmosphere). These experiments were conducted to verify that plasmas could be formed, controlled, and operated safely over the required pressure range.

The miniature microwave system leak rate registered less than 1 mtorr over a period of 16 hours. Base system pressure measured less than 9.0×10^{-8} torr while pumping with an auxiliary turbo pump. System pressure was monitored to 0.1 mtorr.
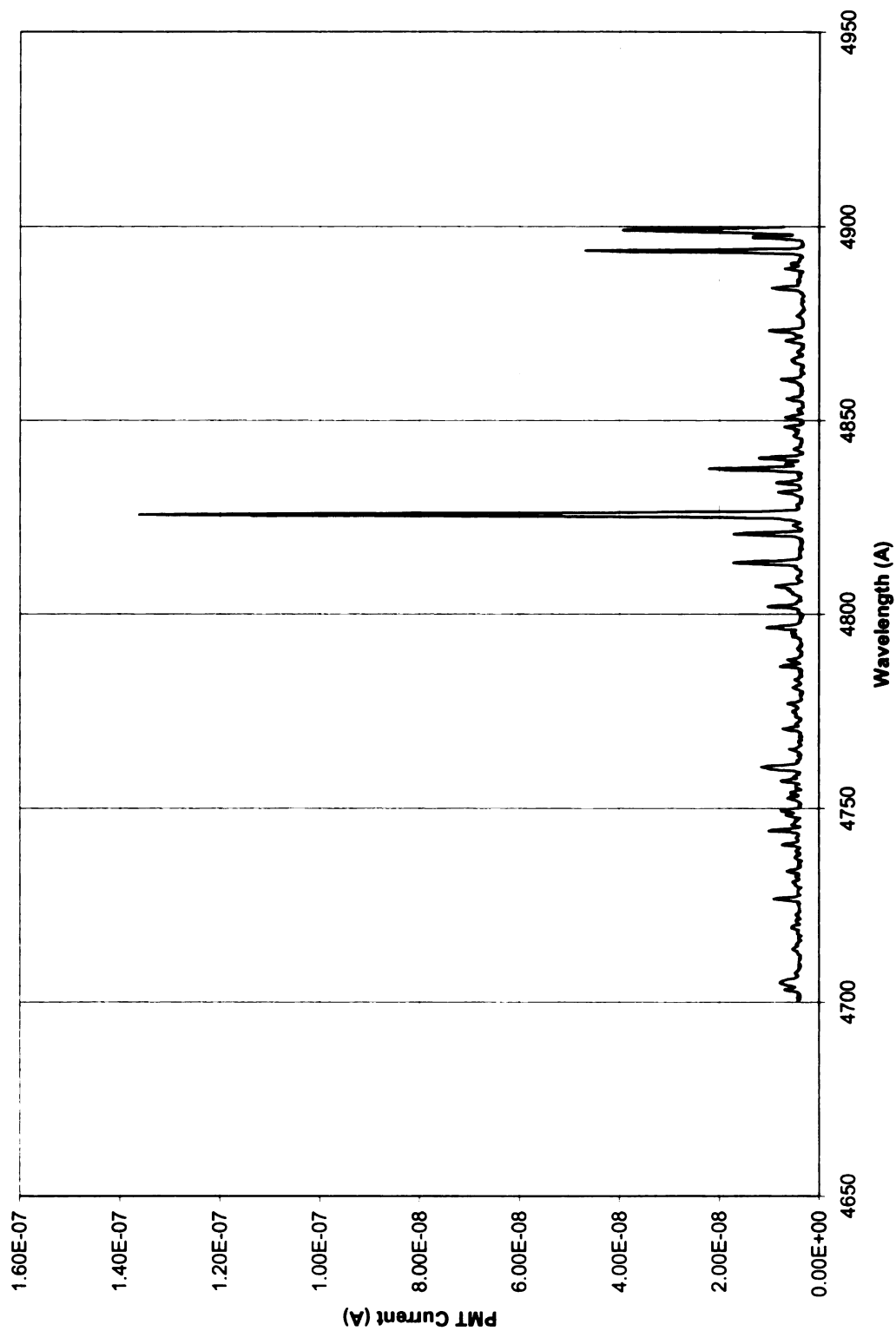
Figure 19 H_β (100 mT) Optic Test.

System pressure could be stabilized with no gas flow at pressures as low as 1 mtorr. System pressure could be stabilized with gas flow at pressures approaching 10 mtorr. The pressure at which the miniature microwave system pressure can be stabilized is limited by the resolution of the flow meters, not the throttle valve feedback control loop.

Argon plasmas were ignited at pressures between 5 torr-10 torr. The microwave power (2.45 GHz) necessary for ignition was approximately 30W-40W. The microwave power necessary for a self-sustaining plasma was as small as 0.2 W for pressures less than 100 torr.

3.3.1 Preliminary Experiments

Preliminary experiments concentrated on Argon plasmas and their characteristics. Argon plasmas are easily formed, as monotonic gases ionize more readily. Plasmas were ignited at pressures between 10 torr-15 torr. Pressure settings were adjusted such that stable plasmas were formed at pressures from 1 mtorr-1000 torr.

Argon plasmas formed at pressures below 1 torr diffused through the gaps in the quartz tube, filling the entire reactor. Plasmas formed at pressures greater than 400 torr began to collapse, pulling away from the quartz tube. Plasmas greater than 800 torr were spherical. In general, higher pressure Argon plasmas formed discharge filaments when the plasma impedance was not matched to the impedance of the microwave power circuit.

3.3.2 Preliminary Diagnostic Results

Preliminary diagnostics were restricted to plasma size, shape, and power density, as recorded by digital imaging. Measurements for plasma size and shape were taken

directly from the digital image. Microwave power meters recorded transmitted and reflected microwave power. The resulting data is summarized in the series of plots given in Figures 20-21, first published June 15, 2001 [26].

Specifically, power density is recorded for pressures from 100 torr-760 torr for the Argon plasma, and plotted in Figure 20. The power density, calculated from the diagnostic data, is used in section 7.2.1 to calculate electron density and temperature using the global model. Ignition power was recorded for pressures from 5 mtorr-760 torr, and is plotted in figure 21.
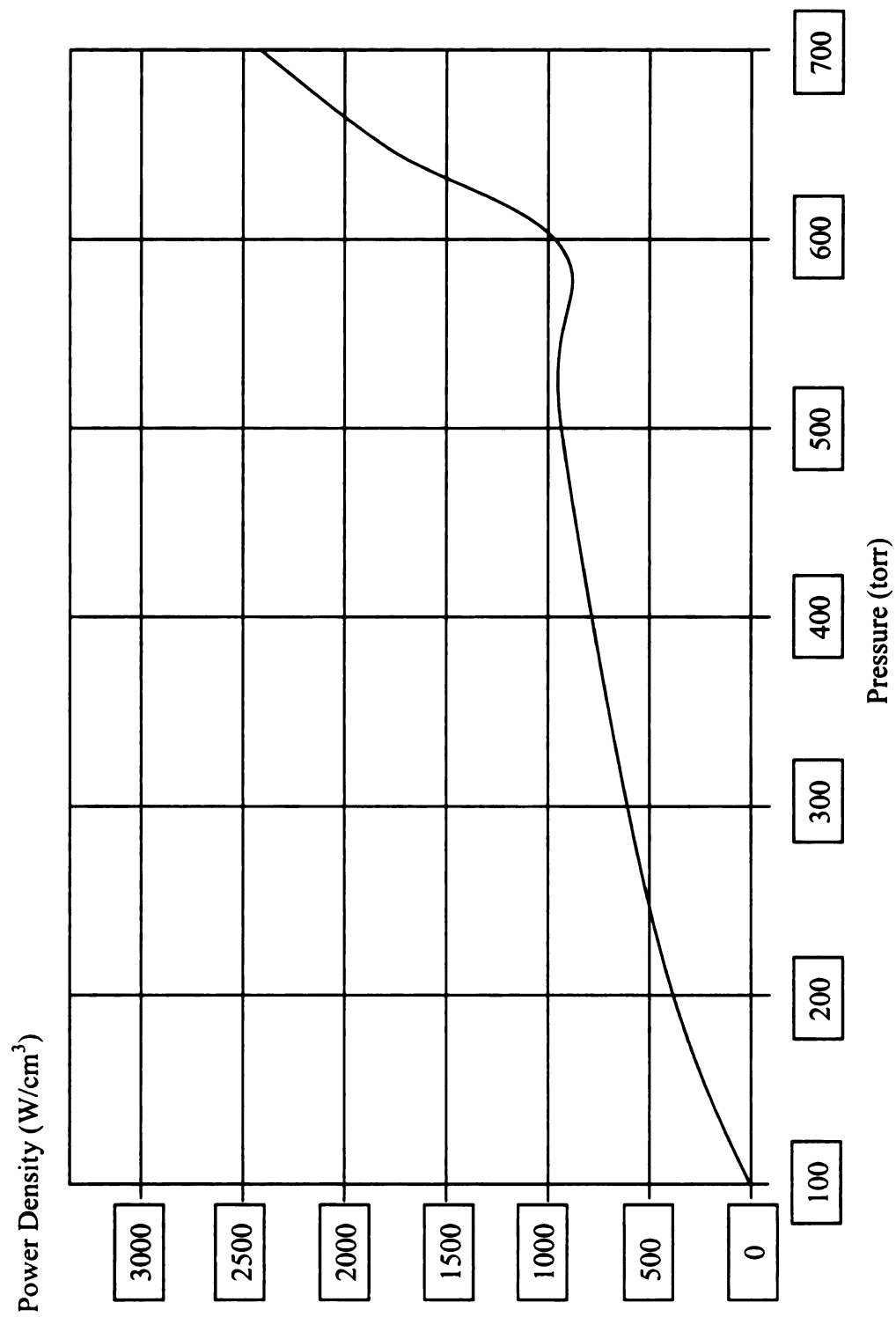
Figure 20 Power Density in Argon Plasma.
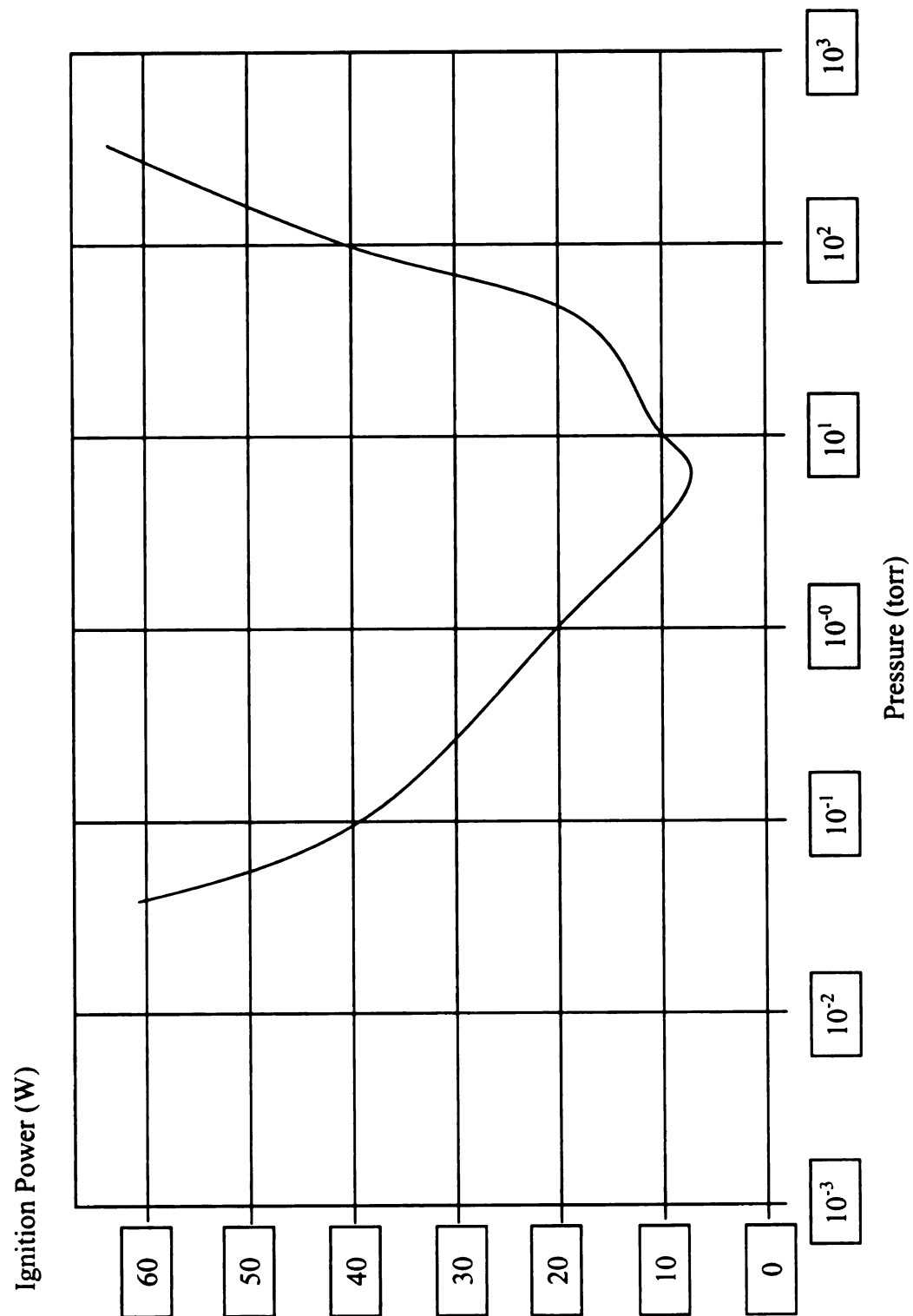
Figure 21 Experimental Argon Ignition Power.

48

Chapter 4 Global Model Theory

To complete the characterization of the miniature microwave plasma, it is necessary to model the plasma mathematically. Several models have been proposed for low-pressure plasmas [27]-[29], moderate pressure plasmas [30], and high-pressure plasmas (~1 atmosphere) [31]-[32]. Matching these models to the diagnostic estimates is necessary to prove the validity of these models, such that these models can be used in the future for miniature plasma source design.

Global models for non-equilibrium plasmas calculate electron density (n) and electron temperature (T_e) as a function of input power (P_{abs}), pressure (P), gas concentrations and plasma reactor geometry.

Briefly, global models require species balance, momentum balance, and energy balance in the Boltzmann transport equations. Conservation of these three quantities are commonly referred to as the zero, first, and second moment Boltzmann equations. The global models balance these equations macroscopically, as opposed to other finite difference analysis techniques [33] that balance these equations for each small volume element included in the microwave reactor system. Global models can incorporate chemical reactions and reaction rates for specific species.

Global models do not consider convective flow dominated conditions, as found at higher pressures (> 100 torr).

4. 1 *Global Model*

The global model development begins with the general Boltzmann transport equations. This set of equations can be simplified by limiting the plasma behavior.

Pinning the plasma boundary conditions to the edge of a collisionless sheath reduces the equation set further. The resulting set of equations require pressure dependent relationships, valid over limited pressure regimes. The global model, in its final form, combines Boltmann transport particle, momentum, and energy balance equations, matched at the edge of a collisionless sheath. Solved iteratively, the global model predicts electron and ion densities, electron temperatures, and electron and ion flux. The mathematical development proceeds directly from texts by Bittencourt [34], Lieberman [35], Goldston [36], Bird [37], and Chen [38].

The global model requires balancing zero (mass/species), first (momentum), and second (energy) moments of the Boltzmann transport equations. More complicated mathematical models require balancing higher order Boltzmann transport equations; for example, heat transfer through convective flows requires balancing the third moment Boltzmann transport equation. These equations are critical in developing mathematical models. The zero moment Boltzmann equation is given as follows:

$$\frac{\partial \rho_{m\alpha}}{\partial t} + \vec{\nabla} \bullet (\rho_{m\alpha} \vec{u}_\alpha) = S_\alpha$$

(4.1)

$$S_\alpha = \left. \frac{\partial \rho_{m\alpha}}{\partial t} \right|_{collision} = m_e (K_i n_e - k_r n_e^2 - k_a n_e)$$

$\rho_{mu} \equiv \alpha$ density
$\vec{u}_\alpha \equiv \alpha$ average velocity
$S_\alpha \equiv \alpha$ ionization rate
$m_e \equiv$ electron mass
$\eta_e \equiv$ electron number density
$K_i, k_r, k_a \equiv$ ionization, recombination, attachment rates

50

Equation 4.1 is called the continuity equation, and represents the conservation of mass. Physically, the difference between the rate at which particles α flow from a differential volume (dV) and the rate the particles are generated (S_α) is equal to the time rate of change of the particles α within the differential volume. The first moment Boltzmann equation is given as,

$$\rho_{m\alpha} \frac{D\vec{u}_\alpha}{Dt} = n_\alpha q_\alpha (\vec{E} + \vec{u}_\alpha x\vec{B}) + \rho_{m\alpha}\vec{g} - \vec{\nabla}P_\alpha + \vec{A}_\alpha$$

(4.2)

$$\vec{A}_\alpha = \frac{\partial(\rho_{m\alpha}\vec{u}_\alpha)}{\partial t}\bigg|_{collision}$$

$\vec{g} \equiv acceleration\ due\ to\ gravity$

$\vec{P}_\alpha \equiv \alpha\ partial\ pressure$

$\vec{A}_\alpha \equiv \alpha\ momentum\ collision\ rate$

Equation 4.2 is referred to as the equation of motion, and represents the conservation of momentum. Physically, as expected, the mass density times the time derivative of the average velocity is equal to the sum of the forces. In Equation 4.2, the forces are composed of the Lorentz force and forces resulting from gravity and pressure. The additional term, $\vec{A}_\alpha$, represents the mean momentum change with respect to time of the α particles as a result of collisions within the plasma.

The second moment Boltzmann equation is given as,

$$\frac{D}{Dt}\left(\frac{3P_\alpha}{2}\right) + \left(\frac{3P_\alpha}{2}\right)(\vec{\nabla} \bullet \vec{u}_\alpha) + (\vec{\nabla}P_\alpha \bullet \vec{\nabla}) \bullet \vec{u}_\alpha + \vec{q}_\alpha = M_\alpha - \vec{u}_\alpha \bullet \vec{A}_\alpha + (u_\alpha{}^2/2)S_\alpha$$

$$M_\alpha = \left.\frac{\partial(\rho_{m\alpha} <v^2>_\alpha /2)}{\partial t}\right|_{collision}$$

$$M_\alpha \equiv \alpha \text{ energy collision rate} \tag{4.3}$$

Equation 4.3 is called the energy transport equation, and represents the conservation of energy. The first term represents the total thermal energy rate of change of a differential volume moving with average velocity u. The second term represents the thermal energy entering and leaving the differential volume. The third term represents the work performed on the species within the unit volume by the forces (pressure) on the surface. The fourth term represents the heat flux through the differential volume. The terms on the right side of the equation represent the energy change as a result of particle collisions.

The global model follows directly from the first three Boltzmann moment equations. Approximations to the Boltzmann moment equations can be made, given the plasma pressure regime. Sections 4.1.1-4.1.3 examines approximations made for the low, moderate, and high-pressure regimes, respectively. In each pressure regime, the plasma is assumed to be in steady state operation.

4.1.1 Low Pressure, Steady-State Approximations

The Boltzmann transport equations can be simplified dramatically by assuming no change in state in the plasma over time; that is, the plasma density function is constant in phase space, both distance and velocity, at every point in the plasma. At low-pressure, electron diffusion immediately counteracts the effects of internal forces, such as electric field. As a result, there is no net electron acceleration in the plasma, and the total derivative with respect to time is set equal to zero in Equation 4.2, when considering electrons. Ion diffusion is much slower; drift due to the electric field dominates diffusion. For ions, given a constant state, the partial derivative with respect to time is set equal to zero in Equation 4.2. Thus,

$$m\eta_e \frac{D}{Dt}\vec{u}_e = e\eta_e \vec{E} + \vec{\nabla}P_e = -e\eta_e \vec{\nabla}\phi + \vec{\nabla}P_e = 0; \quad where: \quad \vec{E} = -\vec{\nabla}\phi$$

$$\vec{\nabla}P_e = kT_e\vec{\nabla}\eta_e \quad isothermal \ plasma \tag{4.4}$$

$$\Rightarrow \eta_e = \eta_0 e^{\phi/T_e} \quad Boltsmann \ distribution \ formula$$

$$M\frac{D}{Dt}\vec{u}_i = M\left(\frac{\partial}{\partial t}\vec{u}_i + \vec{u}_i \bullet \nabla\vec{u}_i\right) = M\vec{u}_i \bullet \nabla\vec{u}_i = e\,\vec{E} - \left(\frac{\vec{\nabla}P_i}{\eta_i}\right)$$

$$\Rightarrow \frac{1}{2}Mu_i^2 + e\,\phi_i + \left(P_i/\eta_i\right) = 0 \tag{4.5}$$

$$\Rightarrow \frac{1}{2}Mu_i^2 + e\,\phi_i = 0; \quad for: \quad P_i \cong 0$$

53

Solving Equations 4.4 and 4.5 for u_i, and substituting into Equation 4.1 gives:

$$\vec{\nabla} \bullet (\vec{u}\eta) = \vec{\nabla} \bullet \left[\left(-\frac{2eT_e}{M} \ln \frac{\eta}{\eta_0} \right)^{1/2} \eta \right] = v_{iz} \eta$$

$$\eta = \eta_e = \eta_i$$

$$\eta_s/\eta_0 \cong 0.425 \qquad\qquad\qquad\qquad\qquad\qquad (4.6)$$

$$\lambda_i < (R, L)$$

$\lambda_i \equiv$ *mean free path*

$\eta_s \equiv$ *density at edge of collisionless sheath*

$\eta_0 \equiv$ *bulkdensity*

The solution to Equation 4.6 can be found in closed-form. The ratio of the density at the edge of the plasma sheath to the bulk density is a constant. Combining Equations 4.4 and 4.5 with Poisson's equation, that is,

$$\eta_e = \eta_0 e^{\phi/T_e}$$

$$\frac{1}{2} M u_B^2 = \frac{1}{2} M u^2 + e\phi$$

$u_B \equiv$ *Bohm velocity* (*velocity at sheath edge*)

$M \equiv$ *ion mass* $\qquad\qquad\qquad\qquad\qquad\qquad (4.7)$

$$\nabla^2 \phi = \frac{e}{\varepsilon_0}(\eta_e - \eta_i)$$

Poisson's equation

54

$$\Rightarrow \nabla^2 \phi = \frac{e\eta_s}{\varepsilon_0} \left[e^{\varphi/T_e} - \left(1 - \frac{\phi}{\varepsilon_s}\right)^{-1/2} \right]$$

<div align="right">(4.8)</div>

$$e\varepsilon_s = \frac{1}{2} M u_s^2$$

$$\Rightarrow u_B = \left(\frac{eT_e}{M}\right)^{1/2}$$

<div align="right">(4.9)</div>

The Bohm velocity (u_B) is defined as the velocity on the edge of the plasma sheath, when the sheath is collisionless. In the global model development, the plasma sheath is always considered collisionless; the Bohm velocity development is valid for each of the pressure regions considered in this study.

4.1.2 Intermediate Pressure, Steady-State Approximations

Intermediate pressures are defined as pressures in which ion motion is still dominated by drift. However, the mean free path is less than the plasma reactor dimensions. Therefore, the collision term in Equation 4.2 must be included at intermediate pressures. Thus,

$$v_m = u_i / \lambda_i$$

$$\mu_i = \frac{2e\lambda_i}{\pi M u_i}$$

<div align="right">(4.10)</div>

$$u_i = \mu_i E$$

$v_m \equiv$ *momentum reversal rate,* $\lambda_i \equiv$ *ion mean free path*
$\mu_i \equiv$ *ion mobility*

Equations 4.10, taken with the Boltzmann distribution function and the time invariant continuity equation, Equation 4.1, gives the following non-linear differential equation:

$$u_B \left(\frac{2\lambda_i}{\pi} \right)^{1/2} \frac{d}{dx} \left(-\eta \frac{d\eta}{dx} \right)^{1/2} = v_{iz} \eta \qquad (4.11)$$

The analytic solution to Equation 4.11 does not converge to the low-pressure analytic solution in section 4.1.1, as the mean free path goes to infinity. Godyak found an approximate solution that does converge to the low-pressure solution. According to Godyak, the following ratios are to be used to relate plasma density at the sheath edge to plasma density in the bulk, given a cylindrical discharge with radius R and length L:

$$h_L = \frac{\eta_L}{\eta_0} \cong 0.86 \left[3 + \frac{L}{2\lambda_i} \right]^{-1/2} \qquad (4.12)$$

$$h_R = \frac{\eta_R}{\eta_0} \cong 0.80 \left[4 + \frac{R}{\lambda_i} \right]^{-1/2} \qquad (4.13)$$

And the ionization rate is given as:

$$v_{iz} = \frac{\eta_L}{\eta_0} \cong 2.2 \frac{u_B}{R} \left[4 + \frac{R}{\lambda_i} \right]^{-1/2} \qquad (4.14)$$

The density ratios are used in the global model to find the ratio of the plasma volume to the effective plasma area; that is,

$$d_{eff} = \frac{1}{2} \frac{RL}{Rh_L + Lh_R}$$

$$\eta_s A = \eta_0 A_{eff}$$

(4.15)

$d_{eff} \equiv$ *volume / effective area*

$\eta_s \equiv$ *density at sheath edge*

$A_{eff} \equiv$ *effective area*

In both low and intermediate pressure regimes, the plasma density is constant, or nearly constant, through the bulk of the plasma, and sharply driven to zero in the sheath between the bulk plasma and reactor walls. The flat distribution is due to the uneven diffusion rates of the two charged species, electrons and ions. At higher pressures, the ion diffusion rate is not negligible, and the bulk plasma density is no longer constant. Returning to Equation 4.1, given constant densities:

$$\oint_S \vec{\Gamma} \cdot d\vec{S} = \int_{vol} K_{iz}\eta_g\eta \, dvol; \quad where: K_{iz}\eta_g \equiv v_{iz}, \eta_g \equiv neutral \ gas \ densities$$

$$u_B\eta_0\left(h_R \, 2\pi RL + h_L \, 2\pi R^2\right) = K_{iz}\eta_g\eta_0\left(\pi R^2 L\right)$$

(4.16)

$$\frac{K_{iz}}{u_B} = \frac{1}{d_{eff}\,\eta_g}$$

Equation 4.16 is solved iteratively for T_e, as both K_{iz} and u_B are functions of T_e. The ratio d_{eff} is used in the global model as part of the global model power balance equation. A description of the power balance equation can be found at the end of section 4.1.3. The relationship between $n_g d_{eff}(T_e)$ and T_e for Argon in the low to moderate

57

pressure regime is shown in Figure 22 [19]. Figure 22 also gives $n_g d_{eff}(T_e)$ as a function of T_e in the high pressure regime, which is addressed in section 4.1.3.

4.1.3 High Pressure, Steady-State Approximations

High-pressures are defined as pressures in which the ion diffusion rate is not dominated by ion drift. That is, ion diffusion and electron diffusion, and the resulting drift due to internal electric fields, must balance such that ion density and ion flux is equal to electron density and flux at every point in the plasma. Accordingly, in steady-state, Equation 4.2 and the isothermal assumption gives:

$$\Gamma_\alpha = \frac{e}{m_\alpha v_{m\alpha}} \eta_\alpha E - \frac{kT_\alpha}{m_\alpha v_{m\alpha}} \nabla \eta_\alpha = \mu_\alpha \eta_\alpha E - D_\alpha \nabla \eta_\alpha$$

$$\eta_i = \eta_e = \eta$$

$$\Gamma_i = \Gamma_e = \Gamma \Rightarrow \eta_i u_i = \eta_e u_e = \eta u \tag{4.17}$$

$\alpha \equiv$ *ions, electrons*
$D_\alpha \equiv \alpha$ *diffusion*

$$\Gamma = \eta u = -\frac{\mu_i D_e + \mu_e D_i}{\mu_i + \mu_e} \nabla \eta \equiv -D \nabla \eta \tag{4.18}$$

$D \equiv$ *ambipolar diffusion coeff*

Substituting Equation 4.18 into the continuity equation, Equation 4.1, gives the following second—order differential equation:

$$-D \nabla^2 \eta = v_{iz} \eta \tag{4.19}$$

Electron Temperature (eV)
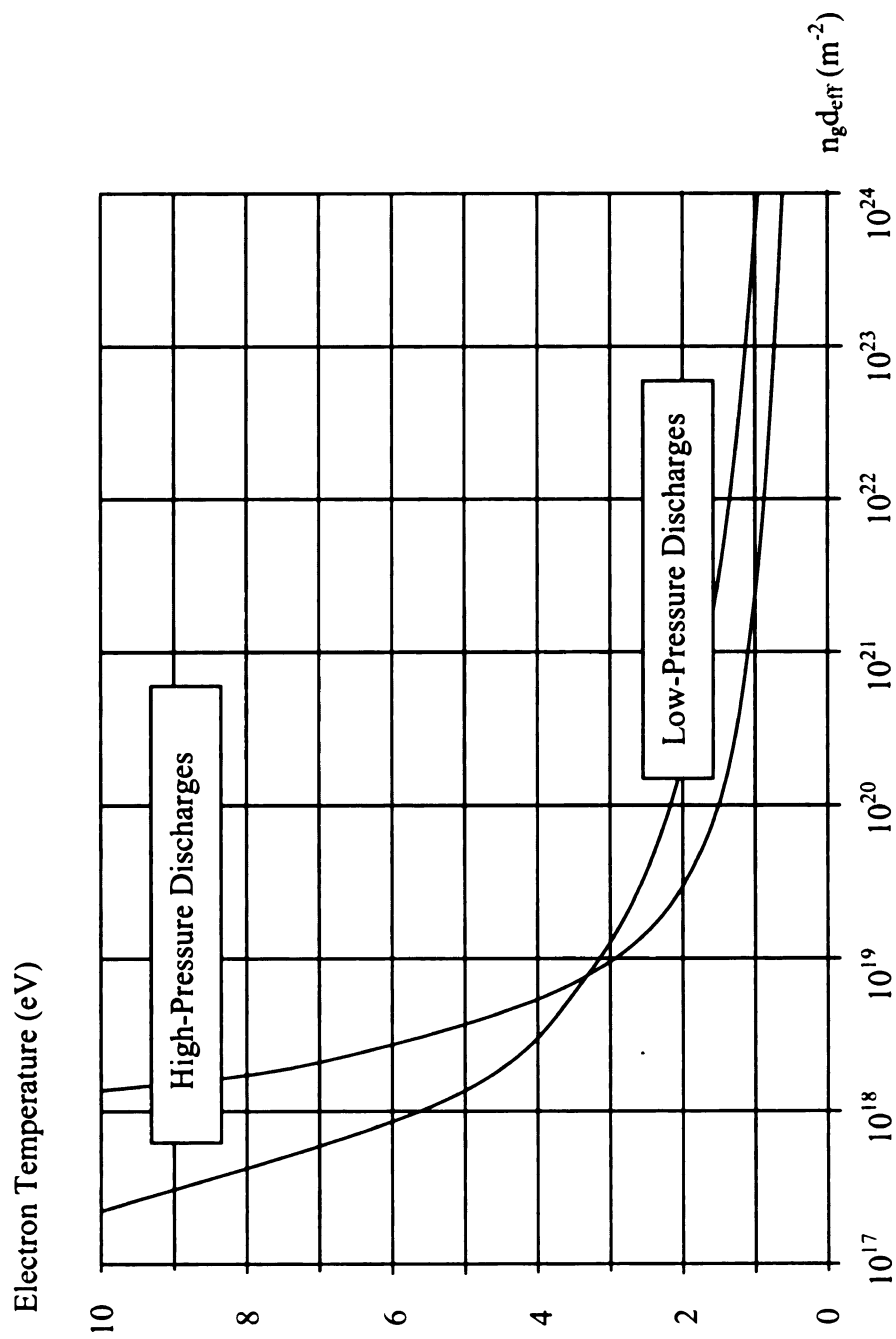
Figure 22 $n_g d_{eff}$ vs. Te for Maxwell Electrons in Argon.

Solving Equation 4.19 in cylindrical coordinates gives the following solution set:

$$\eta = \eta_0 J_0\left(\frac{X_{01}r}{R}\right)\cos\left(\frac{\pi z}{L}\right) \qquad : \quad X_{01} = 2.405 \ (1st \ zero \ of \ J_0)$$

$$\Gamma_{iz} = -D\frac{\partial \eta}{\partial z} = \frac{\pi D}{L}\eta_0 J_0\left(\frac{X_{01}r}{R}\right) \qquad : \quad \Gamma_{iz} \equiv z - flux \ at \ r$$

(4.20)

$$\Gamma_{ir} = -D\frac{\partial \eta}{\partial r} = \frac{X_{01}D}{R}\eta_0 J_1(X_{01})\cos\left(\frac{\pi z}{L}\right) \quad : \quad \begin{array}{l} \Gamma_{ir} \equiv r - flux \ at \ z \\[6pt] J_1(X_{01}) = 0.519 \end{array}$$

Returning to the steady-state continuity equation, integrating with respect to volume, and applying Green's theorem gives:

$$\oint_S \vec{\Gamma} \bullet dS = \int_{vol} v_{iz}\,\eta(r,z)\,dvol$$

(4.21)

Integrals on the right and left side of Equation 4.21 can be found in closed-form with the relationships given in Equations 4.20. Setting the right and left side of Equation 4.21 equal gives the following:

$$\frac{v_{iz}}{D\eta_g} = \frac{K_{iz}}{D} = \frac{\left(\dfrac{X_{01}}{R}\right)^2 + \left(\dfrac{\pi}{L}\right)^2}{\eta_g} \equiv \frac{1}{d_{eff}^{\,2}\eta_g}$$

(4.22)

$$K_{iz}\eta_g\eta_e \equiv v_{iz}\eta_e$$

60

Equation 4.22 is of the same form as Equation 4.16, with $D(T_e)$ replacing $u_B(T_e)$. Equation 4.22 is solved iteratively for T_e, with the aid of the Figure 22 [39], which gives $n_g d_{eff}(T_e)$ as a function of T_e in the high pressure regime.

The energy conservation equation, Equation 4.3, is simplified by assuming relatively constant differential volumes, and by neglecting convection. These assumptions eliminate the third and fourth terms in equation 4.3. The assumption that the plasma is steady-state requires the partial derivative of thermal energy with respect to time to be zero. Applying the chain rule to the total derivative and gradient:

$$\frac{D}{Dt}\left(\frac{3P_\alpha}{2}\right) = \frac{\partial}{\partial t}\left(\frac{3P_\alpha}{2}\right) + \frac{3}{2}\vec{u}\bullet\vec{\nabla}P_\alpha$$

$$(4.23)$$

$$\vec{\nabla}\bullet\left(\frac{3}{2}P_\alpha\vec{u}\right) = \frac{3}{2}P_\alpha\vec{\nabla}\bullet\vec{u} + \frac{3}{2}\vec{u}\bullet\vec{\nabla}P_\alpha$$

$$\frac{D}{Dt}\left(\frac{3P_\alpha}{2}\right) + \frac{3}{2}P_\alpha\vec{\nabla}\bullet\vec{u} = \vec{\nabla}\bullet\left(\frac{3}{2}P_\alpha\vec{u}\right) + \frac{\partial}{\partial t}\left(\frac{3}{2}P_\alpha\right) = \vec{\nabla}\bullet\left(\frac{3}{2}P_\alpha\vec{u}\right) \qquad (4.24)$$

The derivative with respect to time on the left side of Equation 4.24 is equal to the total power absorbed in the plasma volume, defined as S_{abs}, less the power lost in electron-neutral collisions that ionize neutrals. The gradient on the right side of Equation 4.24 is equal to the thermal energy flux to the reactor walls. Specifically:

$$S_{abs} = e(\varepsilon_e + \varepsilon_i)\oint_S \bar{\Gamma} \cdot dS + e\varepsilon_c \int_{vol} K_{iz}\eta_g\eta_e \, dvol$$

$$\oint_S \bar{\Gamma} \cdot dS = 4\pi D\eta_0 J_1(X_{01})\left[\frac{L}{\pi}X_{01} + \frac{\pi}{L}\frac{R^2}{X_{01}}\right]$$

(4.25)

$$\int_{vol} K_{iz}\eta_g\eta_e \, dvol = 4\pi K_{iz}\eta_g\eta_0 \frac{L}{\pi}\frac{R^2}{X_{01}} J_1(X_{01})$$

$\varepsilon_e, \varepsilon_i, \varepsilon_c$ are loss terms

Where the integrals in Equation 4.25 are exactly the same integrals found in Equations 4.20-4.22. The loss terms represent thermal energy lost in the electrons and ions as they diffuse to the reactor walls, and ionization collisions in the plasma bulk, respectively. Combining Equations 4.25 with Equation 4.21 gives:

$$\eta_0 = \frac{S_{abs}}{e D \hat{A}_{eff} \varepsilon_T}$$

$$\hat{A}_{eff} = 4\pi J_1(X_{01})\left(\frac{L}{\pi}X_{01} + \frac{\pi}{L}\frac{R^2}{X_{01}}\right)$$

(4.26)

$$\varepsilon_T = \varepsilon_e + \varepsilon_i + \varepsilon_c$$

Equation 4.26 is also valid for low and intermediate pressure regimes, with u_B replacing D, and the effective area given in Equations 4.15. Note the effective area in Equation 4.26 has units of distance.

The collection of equations in section 4.1.1, section 4.1.2, and section 4.1.3 provide the global model equation set. Solving the continuity equation gives the electron temperature; solving the power balance, or energy conservation equation, yields electron

and ion density. To complete the equation set, it is necessary to determine the power loss terms, ε_e, ε_i, and ε_c. The electron density distribution, f, is critical in finding these terms. The global model places only one restriction on the electron energy distribution; that is, electron-ion collisions are elastic. As a result:

$$\int_v \frac{1}{2}mv^2 f\, dv + \int_v \phi f\, dv = \frac{3}{2}kT_e$$

(4.27)

for monotonic gases (normalized)

Therefore, the maximum entropy of the distribution function f, constrained by Equation 4.27, sets the electron energy distribution function equal to the Maxwell distribution. The average energy flux for the electron, given a Maxwell distribution, is $2eT_e$; the average velocity is given by:

$$< v_e >= \left(\frac{8T_e}{\pi m_e} \right)^{1/2}$$

(4.28)

Assuming only elastic collisions, the ions pass from the plasma bulk to the reactor wall with no change in energy. The difference between the bulk plasma potential and the reactor wall potential is equal to the energy flux per ion. The potential difference is found in two parts. Firstly, from the plasma bulk to the sheath edge; secondly, from the sheath edge to the reactor wall. The former potential (a) is found by invoking energy conservation from the center of the discharge to the sheath edge; the latter potential (b) is found by balancing electron and ion flux to the reactor wall. Thus,

$$(a)\ e\phi_e = \frac{1}{2}Mu_B^2 = \frac{1}{2}M\left(\sqrt{\frac{eT_e}{M}}\right)^2 \Rightarrow \varphi_e = \frac{T_e}{2}$$

$$(b)\ \Gamma_e = \Gamma_i \Rightarrow \frac{1}{4}\eta_s e^{\phi_W/T_e} <v_e> = \eta_s u_B$$

$$(4.29)$$

$$\Rightarrow \frac{1}{4}\eta_s e^{\phi_W/T_e}\left(\frac{8Te}{\pi m}\right)^{1/2} = \eta s\left(\frac{eT_e}{M}\right)^{1/2} \Rightarrow -\phi_W = \frac{T_e}{2}\ln\left(\frac{M}{2\pi m}\right)$$

$$(c)\varepsilon_i = \phi_p - \phi_W = \frac{T_e}{2}\left[1 + \ln\left(\frac{M}{2\pi m}\right)\right]$$

And,

$$\varepsilon_T = \varepsilon_e + \varepsilon_i + \varepsilon_c = 2T_e + \frac{Te}{2}\left[1 + \ln\left(\frac{M}{2\pi m}\right)\right] + \varepsilon_c(T_e)$$

$$(4.30)$$

The rate energy is lost per unit volume per ionization collision is a function of electron temperature, and is given by the curve presented in Figure 23. Calculations of electron density and temperature for experimental data are given in chapter 7.
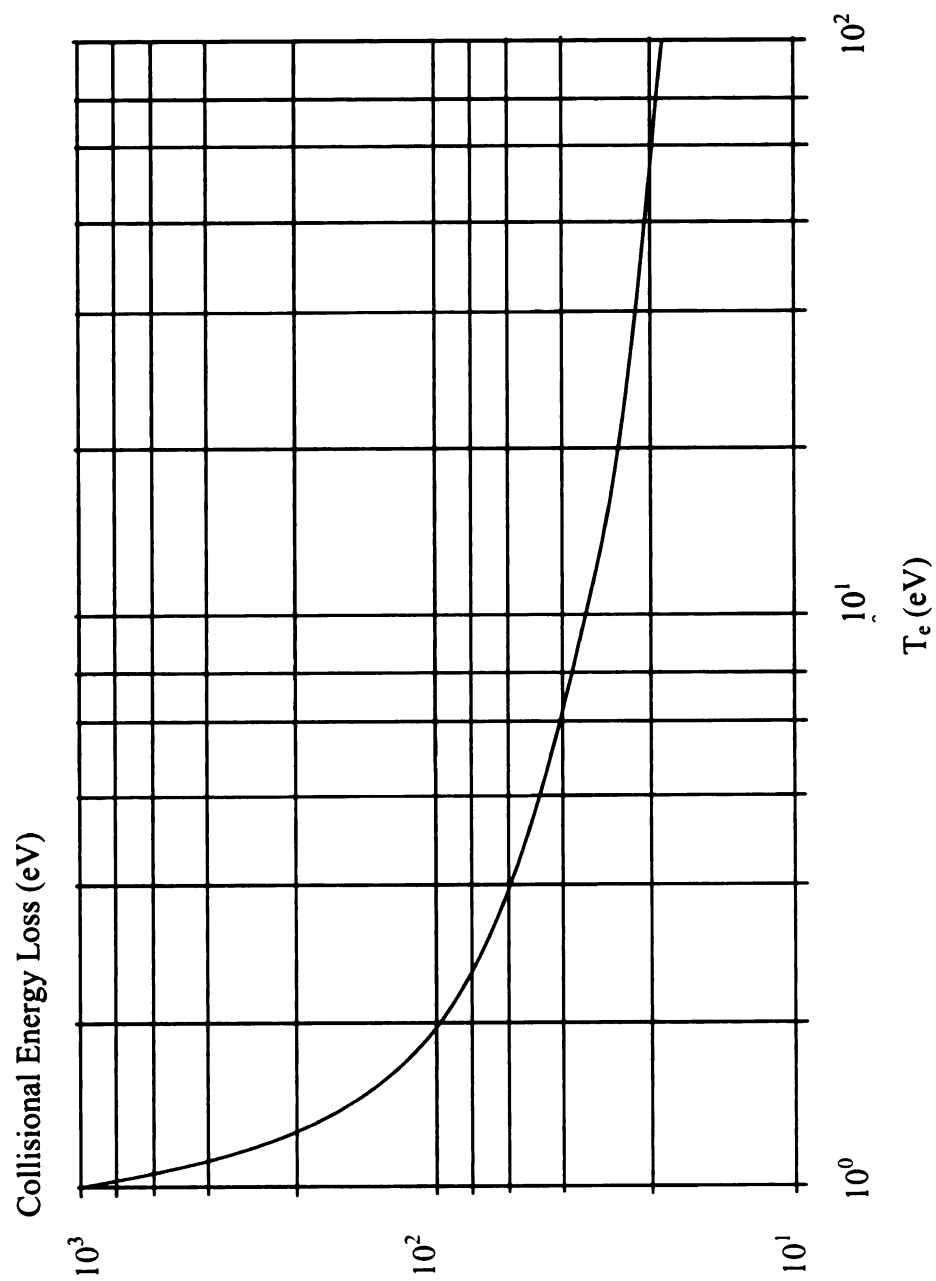
Figure 23 Collisional Energy Loss vs. Te in Argon.

65

Chapter 5 Spectroscopy Theory: Zeeman Effect

Extracting information from spectroscopy results requires an understanding of Quantum Theory. Bohr-Sommerfeld Theory adequately explains simple atomic spectra classically, with given ad hoc quantization rules. For example, the Balmer formula, a direct result of Bohr-Sommerfeld, accurately accounts for the principle peaks in the visible atomic Hydrogen spectrum. The theory also accounts for the quantization of angular momentum, and applies to the vibration and rotation spectrum of simple molecules, and the normal Zeeman effect.

However, Quantum Theory is necessary to explain complex atomic spectra, the anomalous Zeeman effect, and fine structure. Quantum Theory is necessary to formulate angular momentum coupling (spin-orbit) and coupling to magnetic moments. Quantum theory is necessary to address relativistic effects (Thomas Precession, Darwin Shift) and multi-body effects (Lamb Shift); effects that are pronounced in atomic Hydrogen spectra. Additionally, a systematic analysis of spectral data is not possible without the constructs of Quantum Theory.

The first two sections introduce Quantum Theory fundamentals, followed by sections that describe the quantum effects of fields on particles. In a plasma, these quantum interactions effect changes in spectral lines. Specifically, the effects that contribute to spectral peak splitting found in atomic and diatomic hydrogen are discussed in the final sections.

5. 1 Introduction: Quantum Theory

One starting point for Quantum Theory is the Schrodinger equation, proposed by E. Schrodinger in 1925. The Schrodinger equation defines the wave function state; that is, the wave function position and momentum. Classically, the equations of motion are found by following the stationary path defined by the action integral (Maupertuis, Hamilton). In Quantum Theory, the equations of motion –the Schrodinger equation- is found by following all possible paths. In 1948, R. Feynman developed the Schrodinger equation formally by summing all possible paths constrained by the action integral and uncertainty in conjagate state variables position and momentum. The Schrodinger equation is given as follows:

$$-\frac{\hbar^2}{2m}\nabla^2\psi(x,t) + V\psi(x,t) = j\hbar\frac{\partial}{\partial t}\psi(x,t) \qquad (5.1)$$

Setting the potential energy term (V) to the energy stored in the near parabolic energy well of an atomic bond, the Schrodinger equation yields Hermite polynomials as the wave function (Ψ) solution for the harmonic oscillator. Setting the potential energy term to the potential that results from a central potential, the Schrodinger equation yields spherical harmonic functions (associated Legendre polynomials) as the wave function solution for a single electron orbiting the nucleus.

It should be noted that the wave function solutions for the harmonic oscillator and the central charge can both be constructed without the use of the Schrodinger equation.

Dirac constructed eigenvectors and developed solutions for the harmonic oscillator based strictly on the constructs of Hilbert space and conjugate relations. Born, Heisenberg, and Jordan did the same with angular momentum operators to solve for the angle dependent solutions to a central potential.

For the purpose of studying spectroscopy peaks, the Schrodinger equation will be temporarily set aside. First, the eigenvector equations and operator functions for the harmonic oscillator and central charge will be briefly illustrated. This tact will demonstrate the powerful nature of the eigenvector technique, particularly for spectroscopy, where the only results needed are the corresponding eigenvalues, which set the energy levels of the system.

The eigenvector approach will introduce the angular momentum operators that are used to determine degenerate energy levels in central charge potentials. These operators will then be used to find the energy levels and degeneracies in coupled angular momentum problems. Perturbation theory will show how these energy levels split –the degeneracies are removed- with the effect of applied magnetic fields (Zeeman effect). Results will be applied to the hydrogen rotational spectrum.

The Schrodinger equation will be used to address effects caused by changes made to the potential energy of the system. Perturbation theory is needed to calculate energy shifts that result from magnetic fields (Zeeman) and electric fields (Stark). The Schrodinger equation must be modified to account for the interaction of the electron spin with the orbital angular momentum of the electron. Also, the Schrodinger equation must be adjusted to account for the relativistic mass of the electron. Results will be applied to the diatomic and atomic hydrogen spectrums; the complete energy spectrum for diatomic

hydrogen is given in Chapter 6; the complete energy spectrum for atomic hydrogen (H_α, H_β, H_γ) is given in Chapter 7.

5. 2 Eigenvectors

Mathematically, the eigenvector equation is given by the following:

$$A \mid x\rangle = \lambda \mid x\rangle \tag{5.2}$$

Where A is a vector operator, x is a set of eigenvectors or eigenfunctions, and λ is the eigenvalue diagonal matrix. Physically, the linear algebra terms observability and projection space mean the physical quantity or operator (A) can be observed and measured (λ) if the object (x) can be projected without distortion.

An example is a microscope. The microscope objective lens operates (A) on the light reflected from the object (x -LHS) to create an image projected onto the focal plane (x –RHS) of the eyepiece. In this case, the operation of the objective lens is observable if the image is clear; that is, x-RHS = x-LHS. The eigenvalue for the microscope is simply its magnification.

Operators that commute can be observed by the same set of eigenfunctions. This can be seen for operators A and B in the following:

$$A \mid x \rangle = \lambda \mid x \rangle$$

$$A \mid x' \rangle = \lambda' \mid x' \rangle$$

$$\langle x' \mid AB \mid x \rangle = \lambda' \langle x' \mid B \mid x \rangle$$

(5.3)

$$\langle x' \mid BA \mid x \rangle = \lambda \langle x' \mid B \mid x \rangle$$

$$\langle x' \mid [A,B] \mid x \rangle = (\lambda' - \lambda) \langle x' \mid B \mid x \rangle$$

$$[A,B] = 0 \Rightarrow \langle x' \mid B \mid x \rangle = 0 \Rightarrow B \mid x \rangle = \lambda_b x$$

For the microscope example, a compound objective lens commutes; it does not matter whether the higher magnification occurs first or second. The next two sections describe the operators for the harmonic oscillator and central potential.

5.2.1 Harmonic Oscillator

The infinitesimal translator operator changes the wave function position argument as follows:

$$T(\partial x) = 1 - \partial x' \cdot \frac{\partial}{\partial x} = 1 - j \cdot -j\hbar \frac{\partial}{\partial x} \cdot \frac{\partial x'}{\hbar} = 1 - j \cdot p \cdot \frac{\partial x'}{\hbar}$$

(5.4)

Where p is the momentum operator, and is Hermitian. The Hamiltonian –the energy operator- is given by:

70

$$\frac{1}{\hbar\omega}H = \frac{1}{2}\left(P^2 + Q^2\right)$$ (5.5)

Where:

$$x = \sqrt{\frac{\hbar}{m\omega}}Q$$

$$p = \sqrt{m\hbar\omega}P$$ (5.6)

$$\left(m\omega^2 = k\right)$$

And $m\omega^2$ is the spring constant (k) of the system. Q and P represent derivative position and momentum operators, which like true momentum operators p and q, do not commute.

$$[Q,P] = j$$ (5.7)

The one-dimensional harmonic oscillator potential energy is a function of compression- or translation -which can be discretized; allowed transitions increase or decrease compression by one unit. Operators that change the energy of the wave function are commonly called "ladder operators".

Creation and annihilation operators [40] for the one-dimensional harmonic oscillator are given in the following. These operators are unitless, and represent the infinitesimal energy change that results from the infinitesimal translation, given in Equation 5.4.

71

$$a = \frac{1}{\sqrt{2}}(Q + jP)$$

(5.8)

$$a^+ = \frac{1}{\sqrt{2}}(Q - jP)$$

And,

$$[a, a^+] = 1$$

(5.9)

Now,

$$\frac{1}{\hbar\omega}H = \frac{1}{2}(P^2 + Q^2) = \frac{1}{2}(aa^+ + a^+a) = N + \frac{1}{2}$$

(5.10)

Where,

$$N = a^+ a$$

(5.11)

Returns the original wave function as the eigenvector, with eigenvalue equal to the number of units of energy stored in compression (n). In eigenvector notation:

$$N \mid n \rangle = n \mid n \rangle$$

(5.12)

And with,

$$[N, a] = [a^+a, a] = a^+[a, a] + [a^+, a]a = -a$$

(5.13)

$$[N, a^+] = [a^+a, a^+] = a^+[a, a^+] + [a^+, a^+]a = a^+$$

It is clear that,

$$Na \mid n\rangle = ([N,a] + aN) \mid n\rangle = (n-1)a \mid n\rangle$$

$$(5.14)$$

$$Na^+ \mid n\rangle = ([N,a^+] + a^+ N) \mid n\rangle = (n+1)a^+ \mid n\rangle$$

Which implies a+|n> and a|n> are also eigenvectors of N, with eigenvalues n+1 and n-1, respectively. Relating Equations 5.13 and 5.14, it follows that:

$$a \mid n\rangle = \sqrt{n} \mid n-1\rangle$$

$$(5.15)$$

$$a^+ \mid n\rangle = \sqrt{n+1} \mid n+1\rangle$$

Returning to the Hamiltonian,

$$H \mid n\rangle = \hbar\omega\left(N + \frac{1}{2}\right) \mid n\rangle = \hbar\omega(n+1/2) \mid n\rangle \qquad (5.16)$$

Therefore, the energy levels for the one-dimensional harmonic oscillator are given by the eigenvalues:

$$E_n = \hbar\omega(n+1/2) \qquad (5.17)$$

5.2.2 Central Potential

Understanding the central charge potential requires a thorough understanding of the angular momentum component, which contains the most interesting spectral information —that of degenerate peaks that split in the presence of an applied electric or magnetic field. The angular momentum component and angular momentum operators will be covered in the next section. The central potential Hamiltonian will be presented in the following section.

5.2.2.1 Angular Momentum Operators

The infinitesimal rotation operator changes the wave function position argument as follows [41]:

$$
R_z(\partial\phi) = -r\partial\phi' \cdot \frac{\partial}{\partial\phi} = 1 - \partial\phi'\left(x\frac{\partial}{\partial y} - y\frac{\partial}{\partial x} \right)
$$

$$
= 1 - j \cdot \left(x \cdot -j\hbar\frac{\partial}{\partial y} - y \cdot -j\hbar\frac{\partial}{\partial x} \right)\partial\phi'\!\!\Big/_{\!\hbar} = 1 - j \cdot J_z \cdot \partial\phi'\!\!\Big/_{\!\hbar}
$$

(5.18)

This is exactly analogous to the infinitesimal translation operator presented in the previous section. The second order expansion of the infinitesimal rotation operator leads directly to the angular momentum commutation relations:

74

$$R_z(\partial\phi) = R_z(\partial\varphi'/2)R_z(\partial\varphi'/2)$$

$$= \left(1 - j\cdot J_z \cdot \frac{\partial\phi'}{2\hbar}\right)\left(1 - j\cdot J_z \cdot \frac{\partial\phi'}{2\hbar}\right) \qquad (5.19)$$

$$= 1 - j\cdot J_z \cdot \frac{\partial\phi'}{\hbar} - J_z^2\left(\frac{\partial\phi'}{2\hbar}\right)^2$$

And,

$$R_x(\partial\phi')R_y(\partial\phi') - R_y(\partial\phi')R_x(\partial\phi') = R_z\left(\partial\phi'^2\right) - 1 \qquad (5.20)$$

Which implies,

$$\left[1 - j\cdot J_x \cdot \frac{\partial\phi'}{\hbar} - J_x^2\left(\frac{\partial\phi'}{2\hbar}\right)^2\right]\left[1 - j\cdot J_y \cdot \frac{\partial\phi'}{\hbar} - J_y^2\left(\frac{\partial\phi'}{2\hbar}\right)^2\right]$$

$$-\left[1 - j\cdot J_y \cdot \frac{\partial\phi'}{\hbar} - J_y^2\left(\frac{\partial\phi'}{2\hbar}\right)^2\right]\left[1 - j\cdot J_x \cdot \frac{\partial\phi'}{\hbar} - J_x^2\left(\frac{\partial\phi'}{2\hbar}\right)^2\right]$$

$$\qquad (5.21)$$

$$= \left(J_y J_x - J_x J_y\right)\left(\frac{\partial\phi'}{\hbar}\right) = -j\cdot J_z \cdot \left(\partial\phi'^2\right)/\hbar$$

$$\Rightarrow [J_x, J_y] = j\hbar J_z$$

And, in general,

$$[J_i, J_j] = j\hbar\varepsilon_{ijk}J_k \qquad (5.22)$$

75

The angular momentum components J_x, J_y, and J_z do not commute. Likewise, orbital angular momentum operators L_x, L_y, and L_z do not commute. Recasting the components of L in spherical coordinates, as shown in Figure 24:

$$L_h' = L_\pm' = L_x' \pm jL_y' = \left[\pm \frac{\partial}{\partial\theta} + j\cot\theta \frac{\partial}{\partial\phi} \right]$$

$$L_z = \frac{1}{j}\frac{\partial}{\partial\phi}$$

(5.23)

Where the primed coordinates are body-axis coordinates. Now, raising the operator dimension by one gives the horizontal component of the angular momentum magnitude, in both body-axis and inertial frame:

$$L_h^2 = L_h^{2'} = \frac{1}{2}\left(L_+' L_-' + L_-' L_+' \right) = -\left[\frac{1}{\sin\theta}\frac{\partial}{\partial\theta}\sin\theta\frac{\partial}{\partial\theta} + \cot^2\theta\frac{\partial^2}{\partial\phi^2} \right]$$

(5.24)

$$[L_h, L_z] = 0$$

Here it is clear that L_h^2 and L_z commute. Therefore, L^2 and L_z commute and have the same eigenfunctions. L^2 is identical to the Laplacian operator in spherical coordinates, and is given by:

$$L^2 = -\left[\frac{1}{\sin\theta}\frac{\partial}{\partial\theta}\sin\theta\frac{\partial}{\partial\theta} + \frac{1}{\sin^2\theta}\frac{\partial^2}{\partial\phi^2} \right]$$

(5.25)

76

Figure 24 Angular Momentum Operator: Spherical Coordinates.

L_z is periodic about the z axis. Its eigenvector equation must be the following:

$$L_z \mid Y_l^m \rangle = m \mid Y_l^m \rangle$$

(5.26)

$$\Rightarrow Y_l^m(\theta,\phi) = F(\theta)e^{jm\phi}$$

The eigenvector equation for L^2 is different for each m. For m = 1, the eigenvector equation is:

$$L^2 \mid Y_l^l \rangle = -\left[\frac{1}{\sin\theta}\frac{\partial}{\partial\theta}\sin\theta\frac{\partial}{\partial\theta} + \frac{l^2}{\sin^2\theta}\right] \mid Y_l^l \rangle$$

(5.27)

$$L^2 \mid \sin^l\theta \rangle = l(l+1) \mid \sin^l\theta \rangle$$

Where the corresponding eigenfunction and eigenvalue are $\sin^l\theta$ and $l(l+1)$. The angular momentum ladder operators are the infinitesimal angular momentum operators from Figure 24 and Equation 5.23. More succinctly, they are given as:

$$L_\pm = L_x \pm jL_y = \left[\pm\frac{\partial}{\partial\theta} - m\cot\theta\right]$$

(5.28)

Where m is the eigenvalue for L_z. Physically, m is the dimension of the divergence operator ($\nabla\bullet$), and depends on the dimension −or eigenvalue- of the wave function.

Commutator relations are as follows:

$$[L_z, L_+] = L_+$$

$$[L_z, L_-] = -L_- \tag{5.29}$$

$$[L_+, L_-] = 2L_z$$

With Equation 5.24:

$$L^2 = L_h^2 + L_z^2 = \frac{1}{2}(L_-L_+ + L_+L_-) + L_z^2$$

$$L_-L_+ = L^2 - L_z(L_z + 1) \tag{5.30}$$

$$L_+L_- = L^2 - L_z(L_z - 1)$$

And,

$$[L^2, L_i] = 0 \Rightarrow [L^2, L_+] = [L^2, L_-] = 0 \tag{5.31}$$

So,

$$L^2 L_\pm \mid l, m\rangle = L_\pm L^2 \mid l, m\rangle = l(l+1)L_\pm \mid l, m\rangle$$

$$L_z L_\pm \mid l, m\rangle = L_\pm (L_z \pm 1) \mid l, m\rangle = (m \pm 1)L_\pm \mid l, m\rangle \tag{5.32}$$

$$\Rightarrow L_\pm \mid l, m\rangle = c_\pm \mid l, m \pm 1\rangle$$

Equation 5.32 implies $L_{\pm}|l,m\rangle$ are both eigenvectors of L^2 and L_z, with eigenvalues $l(l+1)$ and $m\pm1$, respectively. Further, $L_{\pm}$ are ladder operators, analogous to the ladder operators for the harmonic oscillator found in Equation 5.15. Using Equation 5.30, and the fact the ladder operators are Hermitian:

$$c_+^2 = \left| L_+ \mid l,m\rangle \right|^2 = \langle l,m \mid L_- L_+ \mid l,m\rangle = [l(l+1) - m(m+1)]\langle l,m \mid l,m\rangle$$

$$c_-^2 = \left| L_- \mid l,m\rangle \right|^2 = \langle l,m \mid L_+ L_- \mid l,m\rangle = [l(l+1) - m(m-1)]\langle l,m \mid l,m\rangle$$

(5.33)

$$\Rightarrow c_\pm = \sqrt{l(l+1) - m(m\pm1)}$$

$$L_\pm \mid l,m\rangle = \sqrt{l(l+1) - m(m\pm1)} \mid l, m\pm1\rangle \Rightarrow -l \le m \le +l$$

Before leaving this introduction, it is useful to see that the results given in Equation 5.33 can be arrived at be restricting oneself to the physical interpretation of the operators. The operators can be written as successive gradient/divergence operators, each changing the dimension of the waveform by one. As seen in Equation 5.30, the anti-commutation of L_+ and L_- yields the Laplacian for the horizontal-plane component of angular momentum. Using the identity in Equation 5.28 for a given m:

$$L_h^2 = \frac{1}{2}\left(L_- L_+ + L_+ L_-\right)$$

$$L_- L_+ = -\frac{1}{\sin^{+(m+1)}\theta}\frac{\partial}{\partial\theta}\sin^{+(m+1)}\cdot\frac{1}{\sin^{-m}\theta}\frac{\partial}{\partial\theta}\sin^{-m}\theta$$

(5.34)

$$L_+ L_- = -\frac{1}{\sin^{-(m-1)}\theta}\frac{\partial}{\partial\theta}\sin^{-(m-1)}\cdot\frac{1}{\sin^{+m}\theta}\frac{\partial}{\partial\theta}\sin^{+m}\theta$$

80

Ladder operators applied to the RHS of L_h^2 increase (decrease) the dimension by one; that is, the exponent on the sin function (m) increases (decreases) to reflect the dimension of the wavefunction. Starting with m = 1, $L_z \mid Y_l' \rangle = l \mid Y_l' \rangle$, and applying the L. operator s times, $m \rightarrow m - s$, and the new wavefunction that satisfies Equation 5.34 is given by:

$$L_-^s L_z \mid Y_l' \rangle = L_z L_-^s \mid Y_l' \rangle = (l - s) \mid \left(\frac{1}{\sin^{+m}\theta} \frac{\partial}{\partial\theta} \sin^{+m}\theta \right) Y_l' \rangle \qquad (5.35)$$

The spherical harmonic function, $Y_l^m(\theta,\phi)$, is multiplied by the radial wave function component to complete the wave function. The complete central potential Hamiltonian and radial wave function component are covered briefly in the next section.

Finally, the angular momentum operator can be connected to the harmonic oscillator (Schwinger) [42] by mixing the fields of uncoupled harmonic oscillators, each with independent commutation relations. One operator (L+) creates one unit of $+\hbar/2$ angular momentum (L_z) and annihilates one unit of $-\hbar/2$ angular momentum. Likewise, its conjugate (L.) annihilates one unit of $+\hbar/2$ angular momentum and creates one unit of $-\hbar/2$ angular momentum. This connection reinforces the results from the Clebsch-Gordan calculation in section 5.4.1.

5.2.2.2 Central Potential Hamiltonian

Returning to the Schrodinger equation, the central potential Hamiltonian (hydrogen atom) is given in spherical coordinates as:

$$H = \frac{p_r^2}{2m} + \frac{L^2}{2mr^2} + V(r)$$

$$p_r = \frac{\hbar}{j}\frac{1}{r}\frac{\partial}{\partial r}r$$

(5.36)

$$L^2 = -\hbar^2\left[\frac{1}{\sin\theta}\frac{\partial}{\partial\theta}\sin\theta\frac{\partial}{\partial\theta} + \frac{1}{\sin^2\theta}\frac{\partial^2}{\partial\phi^2}\right]$$
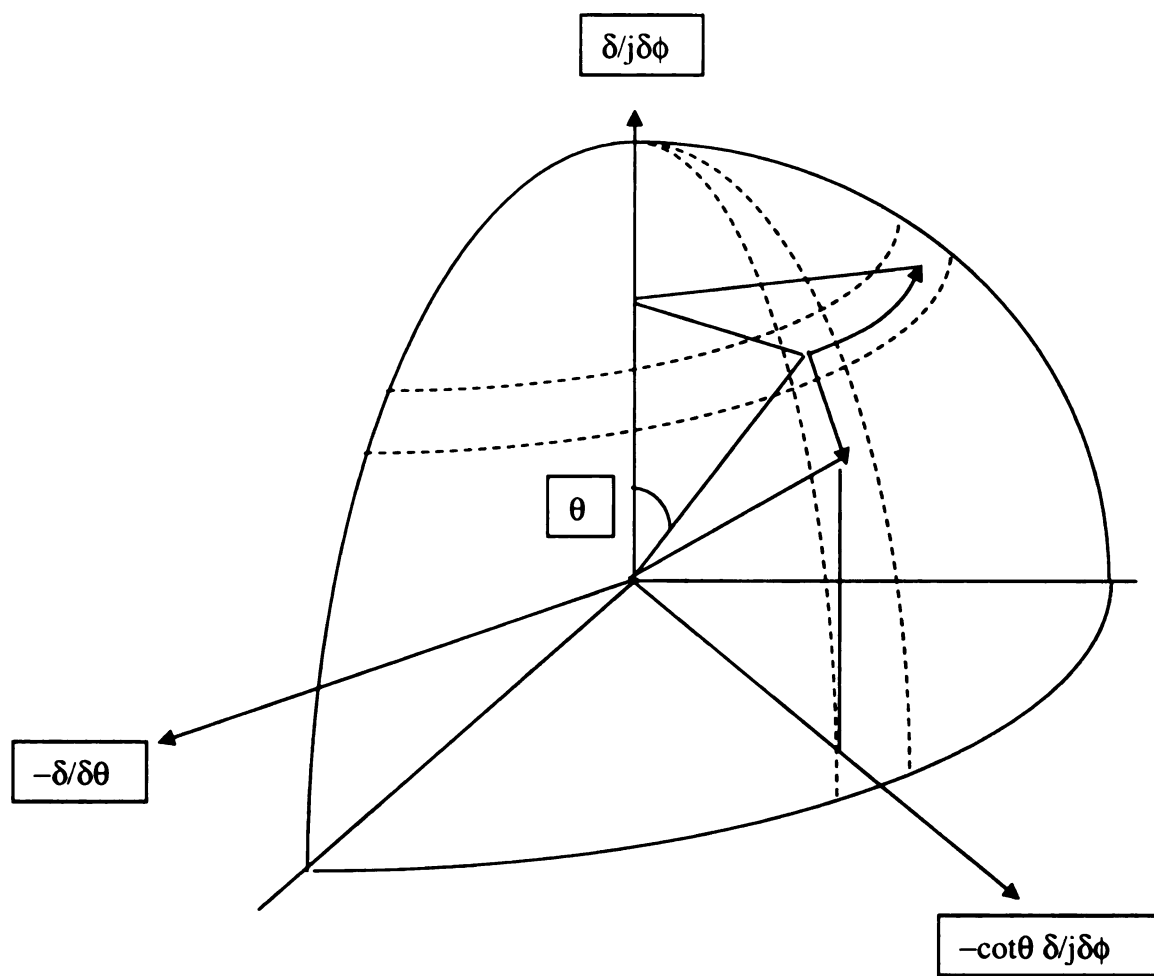
$$V(r) = -\frac{e^2}{r}$$

And,

$$H\,|\psi\rangle = E\,|\psi\rangle$$

(5.37)

Substituting as follows:

$$\chi = \frac{\sqrt{-2mE}}{\hbar}; x = 2\chi r$$

$$v = \frac{e^2}{\hbar c}\sqrt{\frac{mc^2}{-2E}} \qquad (5.38)$$

$$r\psi = x^{l+1}e^{-\frac{1}{2}x}v_l$$

Equation 5.37 can be rewritten:

$$\left[x\frac{d^2}{dx^2} + (2l+2-x)\frac{d}{dx} - (l+1-v)\right]v_l = 0 \qquad (5.39)$$

Solving by Taylor series expansion gives [43]-[44]:

$$v_l = F(l+1-v, 2l+2; x) = \sum_{p=0}^{\infty} \frac{\Gamma(l+1+p-v)}{\Gamma(l+1-v)}\frac{(2l+1)!}{(2l+1+p)!}\frac{x^v}{p!} \xrightarrow[x\to\infty]{} x^{-l-1-v}e^x$$

$$\Rightarrow r\psi \xrightarrow[x\to\infty]{} x^{-v}e^{\frac{1}{2}x}$$

$$(5.40)$$

Which does not converge for large r. However, rψ in Equation 5.38 does

converge if the polynomial is finite, that is:

$$l+1-v = 0, -1, -2, -3, \ldots \Rightarrow v = n : n - (l+1) = 0, 1, 2, 3, \ldots$$

$$(5.41)$$

$$\Rightarrow \begin{cases} n = 1,2,3,\ldots \\ l = 0,1,2\ldots n-1 \\ -l \le m \le +l \end{cases} \Rightarrow \begin{cases} H \mid \psi\rangle = n \mid \psi\rangle \\ L^2 \mid \psi\rangle = l(l+1) \mid \psi\rangle \\ L_z \mid \psi\rangle = m \mid \psi\rangle \end{cases}$$

Where (n, l(l+1), m) are the eigenvalues –or quantum numbers- for a central potential. The principle quantum number, n, defines the energy level, l(l+1) the rotational energy (angular momentum), and m, bounded in Equation 5.33, the magnetic moment.

5. 3 Electron Spin

Electron spin follows the eigenfunction precepts detailed for orbital momentum. However, spin is a more elusive concept. In 1922, O. Stern and W. Gerlach carried out a series of experiments in Frankfurt (Stern-Gerlach Experiments) that illustrated just how illusive a concept spin is [42]. Randomly oriented electrons were ejected from a collimating slit, passed through a gradient magnetic field, and recorded on a screen. Two peaks were observed, corresponding to spin up and spin down orientations. These peaks were identified as S_z^+ and S_z^-.

Then, S_z^+ is passed through a second gradient magnetic field, perpendicular to the first. Again, two peaks result, identified as S_x^+ and S_x^-. The S_x^+ beam of electrons was then passed through a third gradient magnetic field, oriented identically to the first. The result: both spin up and spin down peaks were observed (S_z^+, S_z^-), even though S_z^- had been removed in the first step of the experiment.

The conclusion is that the S_x^+ measurement –or filtering- restores the missing S_z^- spin. Mathematically, this can be seen with the following operator set:

$$S_x = \frac{\hbar}{2}[(|+\rangle\langle-|)+(|-\rangle\langle+|)]$$

$$S_y = \frac{\hbar}{2}[-j(|+\rangle\langle-|)+j(|-\rangle\langle+|)] \tag{5.42}$$

$$S_z = \frac{\hbar}{2}[(|+\rangle\langle+|)-(|-\rangle\langle-|)]$$

Physically, an exact measurement of $S_x{}^+$ means that there is no certainty to the measurement of S_z -that $S_z{}^+$ and $S_z{}^-$ are equally likely- as S_x and S_z do not commute. This relationship is analogous to the relationship between position and momentum.

Spin commutator relationships are identical to those of the orbital angular momentum commutators, given in Equation 5.22.

$$[S_i, S_j] = j\hbar\varepsilon_{ijk}S_k \tag{5.43}$$

In addition, spin has the following anti-commutator relationships:

$$\{S_i, S_j\} = \frac{1}{2}\hbar^2\delta_{ij} \Rightarrow S^2 = \left(\frac{1}{4}+\frac{1}{4}+\frac{1}{4}\right)\hbar^2 = \frac{3}{4}\hbar^2 \tag{5.44}$$

And spin ladder operators are given by:

$$[S_z, S_+] = \frac{\hbar}{2}S_+$$

$$[S_z, S_-] = -\frac{\hbar}{2}S_- \tag{5.45}$$

$$[S_+, S_-] = 2\frac{\hbar}{2}S_z$$

Where:

$$S_{\pm} \mid s,m\rangle = \sqrt{s(s+1)-m(m\pm1)} \mid s,m\pm1\rangle \Rightarrow -\frac{1}{2} \le m \le +\frac{1}{2} \qquad (5.46)$$

For a system of two spins,

$$S = S_1 + S_2$$

$$S^2 \mid \chi\rangle = (S_1 + S_2)^2 \mid \chi\rangle = s(s+1)\hbar^2 \mid \chi\rangle$$

$$(5.47)$$

$$S_{iz} \mid \chi\rangle = m_i\hbar \mid \chi\rangle$$

$$S_z \mid \chi\rangle = (S_{1z} + S_{2z}) \mid \chi\rangle = (m_1 + m_2) \mid \chi\rangle = m \mid \chi\rangle$$

The full eigenfunction –or wavefunction– solution for the central potential problem is simply the product of the spatial and spin wavefunctions:

$$\psi(r,t) = \phi(x,t)\chi(1,2)$$

$$(5.48)$$

$$\begin{cases} \psi_3 = (\phi(x_1,x_2) - \phi(x_2,x_1))\chi_3(1,2) \\ \\ \psi_1 = (\phi(x_1,x_2) + \phi(x_2,x_1))\chi_1(1,2) \end{cases}$$

The Pauli Exclusion Principle excludes two identical particles from the same state (position, momentum) [45]; therefore, the wavefunction must be anti-symmetric. The first wavefunction (ψ_3) is anti-symmetric in space, symmetric in spin; there are three

configurations of spin (triplets) that satisfy the symmetry condition. The second wavefunction (ψ_1) is symmetric in space, anti-symmetric in spin; there is only one configuration of spin (singlet) that satisfies the anti-symmetry condition.

In diatomic molecules, the triplet wavefunction density is lower between atoms than that of the singlet; that is, the inner product term in the square (exchange density) is smaller. The triplets represent anti-bonding orbitals, set at a higher energy than the singlet bonding orbitals.

Triplet and singlet states can be built from individual spin states, using ladder operators and the orthogonality principle, as shown in the following.

$$
\left\{
\begin{aligned}
&|s=1,m=1\rangle = |++\rangle \\[2ex]
&|s=1,m=0\rangle = S_- \,|s=1,m=1\rangle = \left(S_{1-} + S_{2-}\right)|s=1,m=1\rangle \\[2ex]
&\Rightarrow \sqrt{1(1+1)-1(1-0)}\,|s=1,m=0\rangle = \sqrt{\frac{1}{2}(\frac{1}{2}+1)-\frac{1}{2}(\frac{1}{2}-1)}(|-+\rangle+|+-\rangle) \\[2ex]
&\Rightarrow |s=1,m=0\rangle = \frac{1}{\sqrt{2}}(|-+\rangle+|-+\rangle) \\[2ex]
&|s=1,m=-1\rangle = S_- \,|s=1,m=0\rangle = \left(S_{1-} + S_{2-}\right)|s=1,m=0\rangle \\[2ex]
&\Rightarrow \sqrt{1(1+1)-0(0+1)}\,|s=1,m=0\rangle = \sqrt{\frac{1}{2}(\frac{1}{2}+1)-\frac{1}{2}(\frac{1}{2}-1)}\sqrt{2}(|--\rangle+|--\rangle) \\[2ex]
&\Rightarrow |s=1,m=-1\rangle = |--\rangle
\end{aligned}
\right.
\tag{5.49}
$$

And,

$$| s = 0, m = 0 \rangle = \sqrt{2} (| {-}{+} \rangle - | {+}{-} \rangle)$$

$$\tag{5.50}$$

$$\Rightarrow \langle s = 0, m = 0 \mid s = 1, m = 0 \rangle = \langle \sqrt{2}(| {-}{+} \rangle - | {+}{-} \rangle) \mid \sqrt{2}(| {-}{+} \rangle + | {+}{-} \rangle) \rangle = 0$$

Equations 5.49 and 5.50 convert individual spins to total spin. The total angular momentum is energy degenerate, but not so under the influence of a magnetic field. Total spin and total magnetic moment are needed to calculate this interaction. The next section shows how to combine angular momentum terms, spin and otherwise.

5. 4 Angular Momentum Addition: Clebsch-Gordan Coefficients

The addition of angular momentum requires the conversion from the $|l_1, m_1; l_2, m_2 \rangle$ (L_1^2, L_{1z}; L_2^2, L_{2z}) representation to the $|j_1, j_2; j, m \rangle$ (J_1^2, J_2^2; J^2, J_z) representation. The elements in the square matrix that perform this transformation are called the Clebsch-Gordan coefficients.

The representation transformation is important in spectral analysis. All four elements in both representations commute for spherically symmetric groups. For groups that are cylindrically symmetric, but not spherically symmetric, only the latter representation commutes. Specifically, for diatomic molecules such as hydrogen, $L \bullet L_z$ does not commute with L_{1z} or L_{2z}. In spin-orbit coupling found in atomic hydrogen, $L \bullet S$ does not commute with L_z or S_z. But in both cases, they do commute with all the elements in the latter representation; therefore, that representation is observable and complete.

Equations 5.49 and 5.50 are an example of Clebsch-Gordan coefficients; in this case, transforming from (S_1^2, S_{1z}; S_2^2, S_{2z}) to (S_1^2, S_2^2; S^2, S_z) representations. For

diatomic hydrogen in the ground state (Σ_g, Σ_u) –that is, no orbital angular momentum-two electron spins couple with the molecular angular momentum (R) to give the total angular momentum, as shown in Figure 25. For atomic hydrogen, one electron spin couples with its orbital angular momentum (spin-orbit coupling). These two cases are examined in the next two sections.
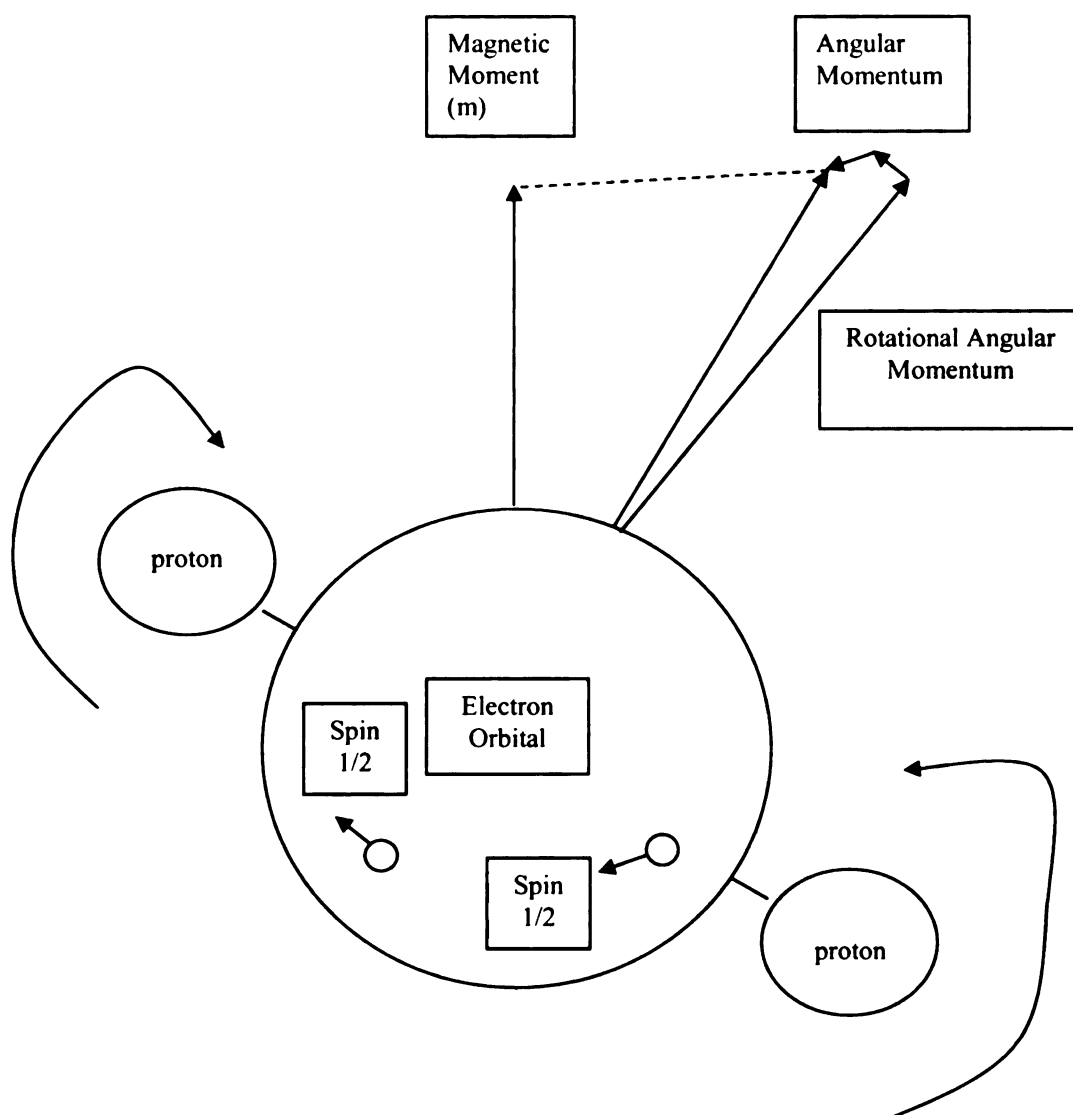
Figure 25 Angular Momentum Diatomic Hydrogen.

5.4.1 Diatomic Hydrogen: Clebsch-Gorden Coefficients

Special attention will be given to the portion of the rotational spectrum of diatomic hydrogen where electrons fall from the charge-transfer excited state (Σ_u) molecular orbital to the ground (Σ_g) molecular orbital. Each peak represents a transition from an angular momentum state one unit higher, lower, or equal to the final state [46].

Both Σ_u and Σ_g are degenerate in orbital angular momentum. Although they are both s-orbitals, and spherically symmetric, the angular momentum eigenvalue is unity (l=1); this is a result of the rotation about the axis perpendicular to the internuclear axis (m_l = +1, 0, -1), as shown in Figure 25 [47]. The spin degeneracy for two electrons, as described in section 5.3, accounts for an additional degeneracy in each of the orbital momentum states. Represented in triplet and singlet form, the spin degeneracy is unity (S=1). The total degeneracy in each ground state is equal to (2l+1)(2S+1) = 9.

Equations 5.49 and 5.50 are a simple example of the Clebsch-Gordan coefficients; the angular momentum (s) and magnetic moment (s_z) of individual electrons are added to give the total angular momentum (S) and magnetic moment (S_z). The Clebsch-Gordan coefficients summing electron spins were found by applying operators S^+ and S^-. In general, Clebsch-Gordan coefficients summing angular momentum are found with the following recursion relationships, from application of the ladder operators J^+ and J^-.

$$\sqrt{(j \mp m)(j \pm m + 1)}\langle j_1, j_2; m_1, m_2 \mid j_1, j_2; j, m \pm 1\rangle$$

$$= \sqrt{(j_1 \mp m_1)(j_1 \pm m_1 + 1)}\langle j_1, j_2; m_1 \mp 1, m_2 \mid j_1, j_2; j, m\rangle \tag{5.51}$$

$$+ \sqrt{(j_2 \mp m_2)(j_2 \pm m_2 + 1)}\langle j_1, j_2; m_1, m_2 \mp 1 \mid j_1, j_2; j, m\rangle$$

Adding the diatomic hydrogen orbital angular momentum eigenvector to one electron spin eigenvector gives:

$$| j = l + \frac{1}{2}, m \rangle = \sqrt{\frac{l + m + \frac{1}{2}}{2l + 1}} \, | m_l = m - \frac{1}{2}, m_s = \frac{1}{2} \rangle \qquad (5.52)$$

$$+ \sqrt{\frac{l - m + \frac{1}{2}}{2l + 1}} \, | m_l = m + \frac{1}{2}, m_s = -\frac{1}{2} \rangle$$

$$| j = l - \frac{1}{2}, m \rangle = -\sqrt{\frac{l - m + \frac{1}{2}}{2l + 1}} \, | m_l = m - \frac{1}{2}, m_s = \frac{1}{2} \rangle \qquad (5.53)$$

$$+ \sqrt{\frac{l + m + \frac{1}{2}}{2l + 1}} \, | m_l = m + \frac{1}{2}, m_s = -\frac{1}{2} \rangle$$

Equations 5.52 and 5.53 can be rewritten as a rotation matrix.

$$\begin{bmatrix} | j = l + \frac{1}{2}, m \rangle \\ | j = l - \frac{1}{2}, m \rangle \end{bmatrix} = \begin{bmatrix} \sqrt{\frac{l + m + \frac{1}{2}}{2l + 1}} & \sqrt{\frac{l - m + \frac{1}{2}}{2l + 1}} \\ -\sqrt{\frac{l - m + \frac{1}{2}}{2l + 1}} & \sqrt{\frac{l + m + \frac{1}{2}}{2l + 1}} \end{bmatrix} \begin{bmatrix} | m_l = m - \frac{1}{2}, m_s = +\frac{1}{2} \rangle \\ | m_l = m + \frac{1}{2}, m_s = -\frac{1}{2} \rangle \end{bmatrix} \qquad (5.54)$$

Addition of the second electron spin gives the following 3x4 matrix as the sum of orbital angular momentum and two electron spins:

$$
\begin{bmatrix} |l+1,m\rangle \\ \\ |l,m\rangle \\ \\ |l-1,m\rangle \end{bmatrix} = \begin{bmatrix} M_{l+1,++} & M_{l+1,+-} & M_{l+1,-+} & M_{l+1,--} \\ M_{l,++} & M_{l,+-} & M_{l,-+} & M_{l,--} \\ M_{l-1,++} & M_{l-1,+-} & M_{l-1,-+} & M_{l-1,--} \end{bmatrix} \begin{bmatrix} |m-1;+\frac{1}{2},+\frac{1}{2}\rangle \\ |m;+\frac{1}{2},-\frac{1}{2}\rangle \\ |m;-\frac{1}{2},+\frac{1}{2}\rangle \\ |m+1;-\frac{1}{2},-\frac{1}{2}\rangle \end{bmatrix} \qquad (5.55)
$$

An identical 3x4 Clebsch-Gordan coefficient matrix exists with m replaced by negative m. These two matrices are coupled for diatomic molecules. P. Zeeman discovered and explained the coupling physically in 1902. Simultaneous forward (m) and reverse rotations (-m) rotations sum to a single vibration, which precesses in the presence of a magnetic field [48]-[49], as shown in Figure 26. As a result, nine distinct degeneracies are present for each total angular momentum >0; three for rotation (+, 0, -), and three spin (+, 0, -) for each rotation.
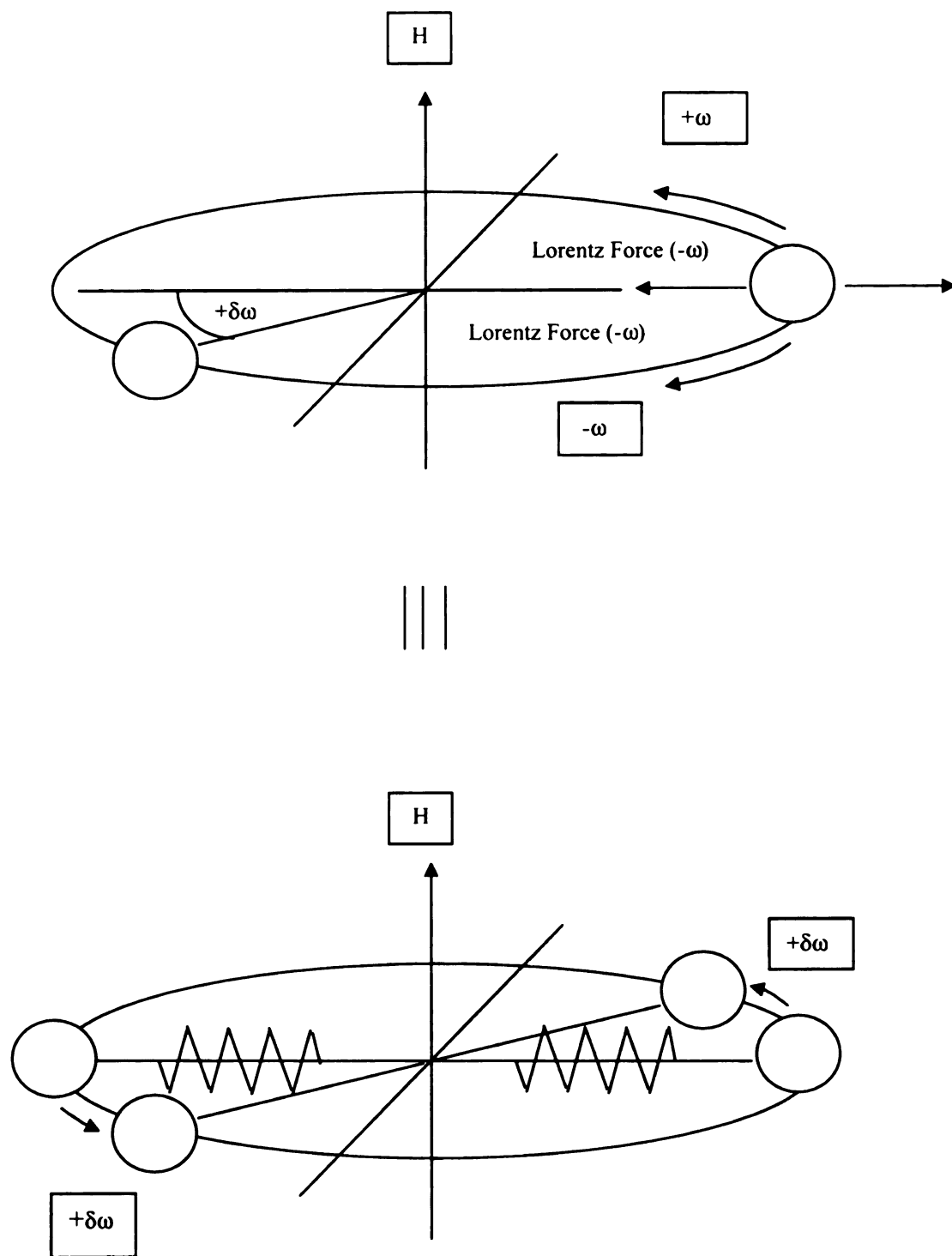
Figure 26 Precession of Vibrating Diatomic.

94

The following lists the matrix elements for the rotation matrix in Equation 5.55.

$$M_{l+1,++} = \langle m_l - 1, +\tfrac{1}{2}, +\tfrac{1}{2} \mid l+1, m \rangle = \sqrt{\frac{l+m}{2l+1}}\sqrt{\frac{l+m+1}{2l+2}}$$

$$M_{l+1,+-} = \langle m_l, +\tfrac{1}{2}, -\tfrac{1}{2} \mid l+1, m \rangle = \sqrt{\frac{l+m+1}{2l+1}}\sqrt{\frac{l-m+1}{2l+2}}$$

$$M_{l+1,-+} = \langle m_l, -\tfrac{1}{2}, +\tfrac{1}{2} \mid l+1, m \rangle = \sqrt{\frac{l+m+1}{2l+1}}\sqrt{\frac{l-m+1}{2l+2}}$$

$$M_{l+1,--} = \langle m_l + 1, -\tfrac{1}{2}, -\tfrac{1}{2} \mid l+1, m \rangle = \sqrt{\frac{l-m}{2l+1}}\sqrt{\frac{l-m+1}{2l+2}}$$

$$M_{l,++} = \langle m_l - 1, +\tfrac{1}{2}, +\tfrac{1}{2} \mid l, m \rangle = -\sqrt{\frac{l-m+1}{2l+1}}\left(\sqrt{\frac{l+m}{2l}} + \sqrt{\frac{l+m}{2l+2}}\right)$$

$$M_{l,+-} = \langle m_l, +\tfrac{1}{2}, -\tfrac{1}{2} \mid l, m \rangle = -\sqrt{\frac{l-m}{2l}}\sqrt{\frac{l-m}{2l+1}} + \sqrt{\frac{l+m+1}{2l+1}}\sqrt{\frac{l+m+1}{2l+2}}$$

$$M_{l,-+} = \langle m_l, -\tfrac{1}{2}, +\tfrac{1}{2} \mid l, m \rangle = \sqrt{\frac{l+m}{2l}}\sqrt{\frac{l+m}{2l+1}} - \sqrt{\frac{l-m+1}{2l+1}}\sqrt{\frac{l-m+1}{2l+2}}$$

$$M_{l,--} = \langle m_l + 1, -\tfrac{1}{2}, -\tfrac{1}{2} \mid l, m \rangle = \sqrt{\frac{l+m+1}{2l+1}}\left(\sqrt{\frac{l-m}{2l}} + \sqrt{\frac{l-m}{2l+2}}\right)$$

$$(5.56)$$

$$M_{l-1,++} = \langle m_l - 1, +\tfrac{1}{2}, +\tfrac{1}{2} \mid l-1, m \rangle = \sqrt{\frac{l-m}{2l}}\sqrt{\frac{l-m+1}{2l+1}}$$

$$M_{l-1,+-} = \langle m_l, +\tfrac{1}{2}, -\tfrac{1}{2} \mid l-1, m \rangle = -\sqrt{\frac{l+m}{2l}}\sqrt{\frac{l-m}{2l+1}}$$

$$M_{l-1,-+} = \langle m_l, -\tfrac{1}{2}, +\tfrac{1}{2} \mid l-1, m \rangle = -\sqrt{\frac{l+m}{2l}}\sqrt{\frac{l-m}{2l+1}}$$

$$M_{l-1,--} = \langle m_l + 1, -\tfrac{1}{2}, -\tfrac{1}{2} \mid l-1, m \rangle = \sqrt{\frac{l+m}{2l}}\sqrt{\frac{l+m+1}{2l+1}}$$

Entries in the matrix for Equations 5.55-5.56 are the Clebsch-Gordan coefficients for the sum of orbital angular momentum and two electron spins for a diatomic molecule, such as hydrogen. These coefficients are combined to find rotation and spin degeneracies.

5.4.2 Atomic Hydrogen: Clebsch-Gorden Coefficients

The total angular momentum and magnetic moment for atomic hydrogen can be found by the addition of one unit of orbital angular moment and one electron spin, as given in Equation 5.54 in the previous section. These coefficients are necessary to find the energy change as a result of spin-orbit coupling, a result that follows from perturbation theory.

5. 5 *Perturbation Theory*

Perturbation theory allows additional operators to be included in the Hamiltonian to account for small changes in energy. Energy changes result from applied fields, and energy corrections can be made for the relativistic mass of the electron and spin-orbit coupling. Energy changes caused by electric (Stark) and magnetic (Zeeman) fields remove orbital and spin degeneracies.

In general, the Hamiltonian can be appended with additional energy operators. The set of equations on the following page summarize the perturbation mathematics for non-degenerate energy levels, such as those found in the fine structure of atomic hydrogen. Further development later in this section allows for the perturbation of degenerate energy levels, found in the mixing of atomic wave functions.

$$H_0 \mid n_0 \rangle = E_0 \mid n_0 \rangle$$

$$\left(H_0 + \lambda V\right) \mid n_0 \rangle = E_0 \mid \left(n_0 + \overline{n_0}\right)\rangle$$

$$n = n_0 + \overline{n_0}, \langle n_0 \mid \overline{n_0} \rangle = 0$$

$$\left(E_0 - H_0\right) \mid n \rangle = \left(\lambda V - \Delta_n\right) \mid n \rangle$$

$$\langle n_0 \mid \left(E_0 - H_0\right) \mid n \rangle = \langle n_0 \mid \left(\lambda V - \Delta_n\right) \mid n \rangle = 0$$

$$\Rightarrow \begin{cases} \left(\lambda V - \Delta_n\right) \mid n \rangle \varepsilon \overline{n_0} \\[2ex] \Delta_n \mid n >= \lambda \langle n_0 \mid V \mid n \rangle \mid n > \end{cases} \tag{5.57}$$

That is, the change in energy along the nth eigenvector is the projection of the potential operating on $|n_0\rangle$. Finding $|n\rangle$ should be as easy as applying $(E_0\text{-}H_0)^{-1}$ to both sides of Equation 5.57, and it is. But, $(E_0\text{-}H_0)$ maps $|n_0\rangle$ to 0, so $(E_0\text{-}H_0)^{-1}$ is ill-defined for n. However, $(E_0\text{-}H_0)^{-1}$ is not ill-defined for $\overline{n}_0$, which is orthogonal to n. Defining Φ_n orthogonal to n results in the following:

$$\Phi_n \mid n \rangle = \left(1 - \mid n_0 \rangle\langle n_0 \mid\right) \mid n \rangle \varepsilon \overline{n_0}$$

$$\tag{5.58}$$

$$\Rightarrow \begin{cases} \mid n \rangle \equiv \mid n \rangle + \mid \overline{n_0} \rangle = \mid n_0 \rangle + \dfrac{\Phi_n}{\left(E_0 - H_0\right)}\left(\lambda V - \Delta_n\right) \mid n \rangle \\[3ex] \Delta_n = \lambda \langle n_0 \mid V \mid n \rangle \end{cases}$$

Equation 5.58 can be solved iteratively for eigenvectors $|n\rangle$; eigenvectors $|n_i\rangle$ will be combinations of eigenvectors orthogonal to $n_0\rangle$, the set of eigenvectors for the

unperturbed Hamiltonian. Given the notation, the first and second order perturbations for

energy level and eigenfunctions are given in the following two sets of equations [42]:

$$V_{kl} = \langle n_k \mid V \mid n_l \rangle$$

$$\Delta_n^0 = 0$$

(5.59)

$$\Delta_n^1 = \langle n_0 \mid \lambda V \mid n_0^0 \rangle = \lambda V_{nn}$$

$$\Delta_n^2 = \langle n_0 \mid V \mid n_0^1 \rangle = \langle n_0 \mid \lambda V \frac{\Phi_n}{(E_0 - H_0)} \lambda V \mid n_0^0 \rangle = \lambda V_{nn} + \lambda^2 \sum_{k \neq n} \frac{V_{nk} V_{kn}}{(E_n - E_k)}$$

$$V_{kl} = \langle n_k \mid V \mid n_l \rangle$$

$$n_0^0 \rangle = \mid n_0 \rangle$$

$$n_0^1 \rangle = \mid n_0^0 \rangle + \frac{\Phi_n}{(E_0 - H_0)} \lambda V \mid n_0^0 \rangle = \mid n_0 \rangle + \lambda \sum_{k \neq n} \frac{V_{kn}}{(E_n - E_k)} \mid k \rangle$$

$$n_0^2 \rangle = \mid n_0^0 \rangle + \frac{\Phi_n}{(E_0 - H_0)} \lambda V \mid n_0^1 \rangle$$

$$= \mid n_0^0 \rangle + \frac{\Phi_n}{(E_0 - H_0)} \lambda V \mid n_0^0 \rangle + \frac{\Phi_n}{(E_0 - H_0)} \lambda V \mid \frac{\Phi_n}{(E_0 - H_0)} \lambda V \mid n_0^0 \rangle$$

$$= \mid n_0^0 \rangle + \lambda \sum_{k \neq n} \frac{V_{kn}}{(E_n - E_k)} \mid k \rangle$$

(5.60)

$$+ \lambda^2 \left(\sum_{k \neq n} \sum_{l \neq n} \frac{V_{kl} V_{ln}}{(E_n - E_k)(E_n - E_l)} \mid k \rangle - \sum_{k \neq n} \frac{V_{nn} V_{kn}}{(E_n - E_k)} \mid k \rangle \right)$$

Intuitively, Equations 5.59-5.60 state that the first order perturbation is the projection back to the zero order eigenvectors of λV, which operates on the zero order eigenvector set. The second order perturbation operates and projects a second time. On convergence, $\lambda V|n>$ projects back onto $|n>$, returning exactly the eigenvector equation.

Equations 5.59-5.60 are predicated on the fact that $E_n \neq E_k$ for $k \neq n$; that is, the energy levels are non-degenerate. For degenerate energy levels, Equations 5.59-5.60 fail to produce perturbed energy levels and wave functions.

However, degenerate energy levels allow the freedom to mix eigenfunctions within a given level. The new eigenfunction representation can be composed such that the inner product terms V_{kn} go to zero for each $E_n = E_k$ where $k \neq n$. Returning to Equations 5.57-5.60:

$$P_m = \sum_{i=0}^{I} | m_i >< m_i |$$

$$| l_j >= P_m | l_j >= \sum_{i=0}^{I} | m_i >< m_i | l_j >$$

(5.61)

$$0 = \langle m_j^0 | (E_0 - H_0) | l_j^0 \rangle = \langle m_j^0 | (\lambda V - \Delta_m) | l_j^0 \rangle$$

$$\Rightarrow \sum_{i=0}^{I} \langle m_j^0 | \lambda V | m_i^0 >< m_i^0 | l_j^0 \rangle = \sum_{i=0}^{I} \lambda V_{ij} < m_i^0 | l_j^0 \rangle = \Delta_m < m_i^0 | l_j^0 \rangle$$

Equation 5.61 transforms the wave function representation into one in which the new inner product term matrix (V_{kn}) is diagonal; that is, $V_{kn}=0$ for all $k \neq n$. The

eigenvalues for Equation 5.61 are the perturbed energy levels; the eigenvectors for Equation 5.61 are the linear transform coefficients mapping |m> to |l>. Equations 5.59-5.60 are now valid for degenerate energy levels; summation is over all remaining non-degenerate states, all states with unique, non-zero eigenvalues.

The next three sections look at spin-orbit coupling in atomic hydrogen, the relativistic mass correction for atomic hydrogen, and the anomalous Zeeman effect. Each of these effects can be accurately approximated by perturbation theory.

5.5.1 Spin-Orbit Interaction

A magnetic field will interact with the orbital angular momentum and electron spin of an atom, splitting the energy lines in the visible spectrum. This effect is called the anomalous Zeeman effect. But first, it is important to look at just the interaction of the orbital angular momentum with the electron spin –the spin-orbit interaction.

The central potential in the Schrodinger equation is not strictly a central potential due to the shape of the electron cloud surrounding the nucleus. A moving electron accelerates radially in response to a field gradiant just as it would to an applied magnetic field, namely:

$$V = e\Phi(r)$$

(5.62)

$$B = -\frac{v}{c} \times E = \frac{v}{ec} \times \nabla V$$

The electron spin couples with B; the energy correction operator represents the work done to rotate the electron spin away from the magnetic field.

Thus,

$$\mu = \frac{eS}{m_e c}$$

$$H_{LS} = -\mu \bullet B = \frac{1}{m_e^2 c^2}\left[S \bullet \left(\vec{p} \times -\vec{r}\frac{1}{r}\frac{dV}{dr}\right)\right] = \left(\frac{1}{2}\right)\frac{1}{m_e^2 c^2}\frac{1}{r}\frac{dV}{dr}(L \bullet S)$$

Where the extra multiplicative constant ½ is due to Thomas precession [50]. $(L \bullet S)$ does not commute with L_z or S_z, but does commute with total angular momentum J^2 and J_z. There are two total angular momentum terms, from section 5.4.1:

$$L \bullet S = \frac{1}{2}\left(J^2 - L^2 - S^2 \right)$$

$$\langle Y_l^{j=l\pm 1/2,m} \mid H_{LS} \mid Y_l^{j=l\pm 1/2,m}\rangle = \frac{\hbar^2}{2}\left(j(j+1) - l(l+1) - \frac{3}{4}\right)\langle Y_l^{j=l\pm 1/2,m} \mid Y_l^{j=l\pm 1/2,m}\rangle$$

$$\langle Y_l^{j=l\pm 1/2,m} \mid H_{LS} \mid Y_l^{j=l\pm 1/2,m}\rangle = \begin{cases} \dfrac{l}{2}\hbar^2; & j = l+1/2 \\[2mm] -\dfrac{l+1}{2}\hbar^2; & j = l-1/2 \end{cases}$$

$$\Delta_{nlm} = \frac{1}{2m_e^2 c^2}\left\langle \frac{1}{r}\frac{dV}{dr}\right\rangle_{nl} \langle Y_l^{j=l\pm 1/2,m} \mid H_{LS} \mid Y_l^{j=l\pm 1/2,m}\rangle$$

$$\Delta_{nlm} = \frac{1}{2m_e^2 c^2}\left\langle \frac{1}{r}\frac{dV}{dr}\right\rangle_{nl}\begin{cases} \dfrac{l}{2}\hbar^2; & j = l+1/2 \\[2mm] -\dfrac{l+1}{2}\hbar^2; & j = l-1/2 \end{cases}$$

Equation 5.64 is Lande's interval rule [42]. Referencing Equations 5.36-5.41, the potential gradient term can be found in steps:

$$\langle \Psi_{nl} \mid r \nabla V \mid \Psi_{nl} \rangle = 2E_n = -\frac{1}{n^2}\frac{e^2}{a_0}$$

$$\Rightarrow \langle \Psi_{nl} \mid \frac{1}{r} \mid \Psi_{nl} \rangle = \frac{1}{n^2}\frac{1}{a_0}$$

$$\langle \Psi_{nl} \mid \frac{\partial}{\partial l} H \mid \Psi_{nl} \rangle = \frac{2}{n^3}\frac{e^2}{a_0}$$

$$\Rightarrow \langle \Psi_{nl} \mid \frac{1}{r^2} \mid \Psi_{nl} \rangle = \frac{4}{(2l+1)n^3}\frac{m_e e^2}{\hbar^2 a_0} = \frac{4}{(2l+1)n^3}\frac{1}{a_0^2}$$

$$\langle \Psi_{nl} \mid \frac{\partial}{\partial r} H \mid \Psi_{nl} \rangle = \langle \Psi_{nl} \mid -\frac{2l(l+1)\hbar^2}{m_e r^3} + \frac{e^2}{r^2} \mid \Psi_{nl} \rangle = 0$$

$$\Rightarrow \langle \Psi_{nl} \mid \frac{1}{r^3} \mid \Psi_{nl} \rangle = \frac{m_e e^2}{\hbar^2}\frac{1}{2l(l+1)}\langle \Psi_{nl} \mid \frac{1}{r^2} \mid \Psi_{nl} \rangle = \frac{2}{l(l+1)(l+2)n^3}\frac{1}{a_0^3} \quad (5.65)$$

$$\Rightarrow \langle \Psi_{nl} \mid \frac{1}{r}\frac{\partial}{\partial r} V \mid \Psi_{nl} \rangle = \frac{2}{l(l+1)(l+2)n^3}\frac{e^2}{a_0^3}$$

102

The ratio of the energy shift for atomic hydrogen to the Balmer intervals is on the order of $\alpha^2 = 1/137^2$ [42], that is:

$$a_0 = \frac{\hbar^2}{m_e e^2}$$

$$\alpha = \frac{e^2}{\hbar c} = \frac{1}{137} \tag{5.66}$$

$$\frac{\Delta^1_{nlm}}{\frac{e^2}{2a_0}} = \frac{\frac{\hbar^2}{2m_e^2 c^2}\left\langle \frac{1}{r}\frac{dV}{dr}\right\rangle_{nl}}{\frac{e^2}{2a_0}} \sim \frac{\frac{\hbar^2}{2m_e^2 c^2} \cdot \frac{e^2}{a_0^3}}{\frac{e^2}{2a_0}} = \left(\frac{e^2}{\hbar c}\right)^2 = \frac{1}{137}^2$$

Which means Δ^1_{nlm} can be written as:

$$\Delta^1_{nlm} = \frac{e^2}{2a_0}\alpha^2 \frac{1}{l(l+1)(l+2)n^3}
\begin{cases}
\dfrac{l}{2}; & j = l+1/2 \\[2mm]
-\dfrac{l+1}{2}; & j = l-1/2
\end{cases}$$

$$\tag{5.67}$$

$$= m_e c^2 \frac{\alpha^4}{2n^4} \frac{1}{l(l+1)(l+2)}
\begin{cases}
\dfrac{nl}{2}; & j = l+1/2 \\[2mm]
-\dfrac{n(l+1)}{2}; & j = l-1/2
\end{cases}$$

This expression will be combined with the relativistic mass correction in the next section.

5.5.2 Relativistic Mass Correction

The perturbation operator for relativistic mass comes directly from the relativistic energy term:

$$E_{nl}^2 = m_e^2 c^4 + p^2 c^2$$

(5.68)

$$\frac{p^2}{2m_e} \rightarrow E_{nl} - m_e c^2 = m_e c^2 \left(\sqrt{1 + \frac{p^2}{m_e^2 c^2}} - 1 \right) \approx \frac{p^2}{2m_e} - \frac{1}{2m_e c^2} \left(\frac{p^2}{2m_e} \right)^2$$

Solving for Δ_{nl}^1:

$$\Delta_{nl}^1 = -\frac{1}{2m_e c^2} \langle \Psi_{nl} | \left(\frac{p^2}{2m_e} \right)^2 | \Psi_{nl} \rangle = -\frac{1}{2m_e c^2} \langle E_n + \frac{e^2}{r} | E_n + \frac{e^2}{r} \rangle$$

$$= -\frac{1}{2m_e c^2} \left(E_n^2 + 2 E_n e^2 \langle \frac{1}{r} \rangle + e^2 \langle \frac{1}{r^2} \rangle \right)$$

(5.69)

$$= E_n \frac{\alpha^2}{n} \left(\frac{2}{2l+1} - \frac{3}{4n} \right)$$

$$= m_e c^2 \frac{\alpha^4}{2n^4} \left(\frac{2n}{2l+1} - \frac{3}{4} \right)$$

Now, adding the spin-orbit interaction to the relativistic mass correction, with total angular momentum j substituted for orbital angular momentum l:

$$\Delta_{nlm}^1 = -m_e c^2 \frac{\alpha^4}{2n^4} \left(\frac{n}{j + \frac{1}{2}} - \frac{3}{4} \right)$$

(5.70)

And the total energy, including rest mass, is [50]:

$$E_{nj} = m_e c^2 \left[1 - \frac{\alpha^2}{2n^2} - \frac{\alpha^4}{2n^4} \left(\frac{n}{j + \frac{1}{2}} - \frac{3}{4} \right) + ... \right] \qquad (5.71)$$

Briefly, an additional correction term –the Darwin term [51]- allows for s orbital (l=0) corrections in Equation 5.69. Both the Darwin term and Lamb Shift evolve from the relativistic quantum field equation –the Dirac equation. The Lamb shift makes a very small correction to remove the degeneracies in orbital angular momentum [42]. Its effect is nearly negligible for this set of experiments, and will not be pursued here.

Equation 5.71 completely describes the energy levels associated with the fine structure of atomic hydrogen. The fine structure of atomic hydrogen, and nominal transition intensities, are addressed further in sections 5.7 and 5.8.

5.5.3 Anomalous Zeeman Effect

Degeneracies in the spin-orbit interaction are lifted with an applied magnetic field. This effect is the anomalous Zeeman effect. The perturbation term enters as the electron momentum interacts with the field momentum, the field that produces the magnetic moment.

Thus, for a relatively weak magnetic field,

$$A = \frac{1}{2}(B \times r) \Rightarrow A = -\frac{1}{2}(\hat{x}By - \hat{y}Bx)$$

$$p \rightarrow p - \frac{eA}{c} \Rightarrow H = \frac{p^2}{2m_e} + V - \frac{e}{2m_e c}(p \bullet A + A \bullet p) + \frac{e^2 A^2}{2m_e c^2}$$

(5.72)

$$p \bullet A = A \bullet p - j\hbar \nabla \bullet A = A \bullet p + 0 = A \bullet p = \frac{1}{2}B(-yp_x + xp_y) = \frac{1}{2}BL_z$$

$$A^2 = A \bullet A = \frac{1}{4}B^2(x^2 + y^2)$$

Ignoring the smaller quadratic term:

$$H = \frac{p^2}{2m_e} + V - \frac{eB}{2m_e c}(L_z + 2S_z)$$

(5.73)

Where the factor of two on the spin term is due to the g-factor of the electron [50].

To summarize:

$$H_0 = \frac{p^2}{2m_e} + V$$

$$H_{LS} = \frac{1}{2m_e^2 c^2}\frac{1}{r}\frac{dV}{dr}(L \bullet S)$$

(5.74)

$$H_B = -\frac{eB}{2m_e^2 c}(L_z + 2S_z) = -\frac{eB}{2m_e^2 c}(J_z + S_z)$$

The transformation to total angular momentum and total magnetic moment is given in Equation 5.54 (Clebsch-Gordan coefficients), namely:

$$| \, j = l \pm \frac{1}{2}, m \rangle = \pm \sqrt{\frac{l \pm m + \frac{1}{2}}{2l+1}} \; | \, m_l = m - \frac{1}{2}, m_s = \frac{1}{2} \rangle$$

$$+ \sqrt{\frac{l \mp m + \frac{1}{2}}{2l+1}} \; | \, m_l = m + \frac{1}{2}, m_s = -\frac{1}{2} \rangle \qquad (5.75)$$

Therefore, the first order energy perturbation is:

$$\Delta_B^1 = -\frac{eB}{2m_e c} \langle j = l \pm \frac{1}{2}, m \, | \, (J_z + S_z) \, | \, j = l \pm \frac{1}{2}, m \rangle$$

$$\Delta_B^1 = -\frac{eB}{2m_e c} \left[m\hbar \left(\frac{l \pm m + \frac{1}{2}}{2l+1} + \frac{l \mp m + \frac{1}{2}}{2l+1} \right) + \frac{\hbar}{2} \left(\frac{l \pm m + \frac{1}{2}}{2l+1} - \frac{l \mp m + \frac{1}{2}}{2l+1} \right) \right] \qquad (5.76)$$

$$= -\frac{eB}{2m_e c} m\hbar \left[1 \pm \frac{1}{2l+1} \right]$$

For a stronger field, J_z no longer commutes; only L^2, S^2, L_z and S_z remain as commuting operators.

As a result,

$$\Delta_B^1 = -\frac{eB}{2m_e c}\langle j = l \pm \frac{1}{2}, m \mid (L_z + 2S_z) \mid j = l \pm \frac{1}{2}, m\rangle$$

$$= -\frac{eB}{2m_e c}\hbar(m_l + 2m_s) \tag{5.77}$$

$$\Delta_{LS}^1 = -\frac{m_l m_s \hbar^2}{2m_e c^2}\left\langle \frac{1}{r}\frac{\partial}{\partial r}V \right\rangle$$

Not all degeneracies are removed in a strong magnetic field; m_l, m_s combinations yield the same first order energy correction. Line splitting where the applied magnetic field effect exceeds that of the spin-orbit interaction is called the Paschen-Back limit.

5. 6 *Rotational Spectrum for Diatomic Hydrogen*

The intraband rotational spectrum, the series of peaks for a constant vibration eigenvalue and single angular momentum transition, becomes evident as the applied magnetic field removes the degeneracies on orbital and spin angular momentum. Figure 27 shows the energy level diagram for the Σ_u–Σ_g transition [52]. Each of the fifteen transitions is associated with a unique energy difference; the reason: the energy split in orbital angular momentum is approximately 50 percent larger (28.4/20) for Σ_u than Σ_g [53] due to the higher rotational inertia of the charge-transfer orbitals.

Zeeman splitting for a free electron ($_g\Sigma_{BB}$) in an applied magnetic field of 5 T is approximately 4.7 cm-1 (0.2 A/T at 4627.66 A) [54]. Accordingly, the magnetic field in the plasma can be calculated by tracking the intraband peak separation in the rotational
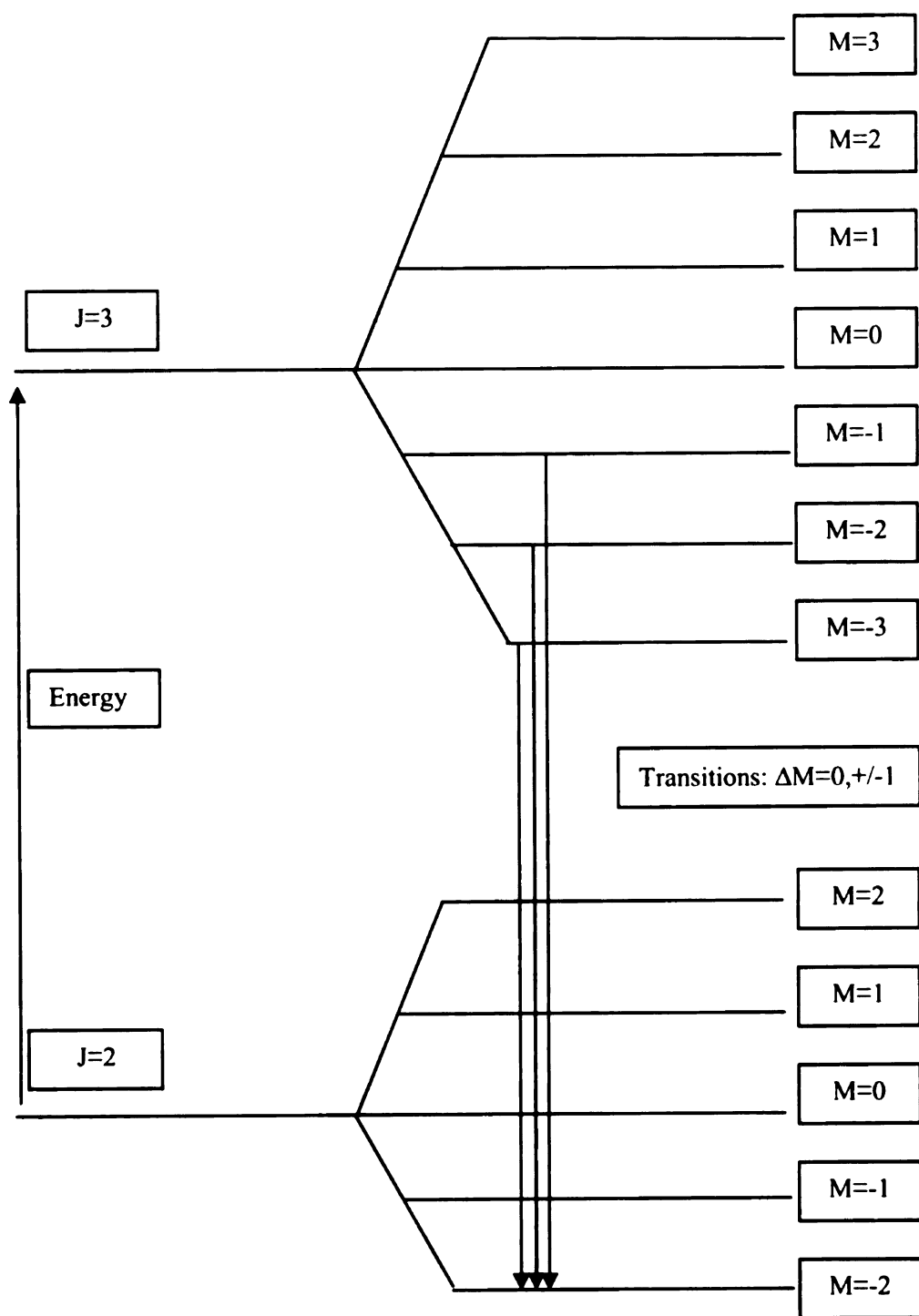
Figure 27 Zeeman Energy Levels.

109

hydrogen spectrum. Peak intensities are a function of the Clebsch-Gordan coefficients, given in Equation 5.54, and energy state population, which is approximately a Boltzmann distribution. Over a narrow energy band, the Boltzmann distribution is linear, with slope $1/kT$. Plasma magnetic field calculations and temperature estimates from experimental rotational spectra are found in Chapter 7.

5.7 *Fine Structure of Atomic Hydrogen*

The fine structure of the atomic hydrogen spectrum is composed of the assembly of corrections formulated in section 5.5, and specified for H_α and H_β in Figures 28 [50]-29. Degeneracies are removed by the energy corrections. However, the fine structure of atomic hydrogen is further mixed upon application of an electric field. It is this additional separation in peaks that complicate the atomic hydrogen spectrum in low to medium electric fields ($\sim$1000 V/cm-5000 V/cm). Calculations for the electric field directly from the Stark shifted spectrum are summarized in the following chapter.

5.8 *Nominal Fine Structure Transition Intensity*

H_α nominal atomic hydrogen fine structure line intensity ratios are given in Figure 30. Fine structure line intensity ratios are a product of the Clebsch-Gordan coefficients that construct the fine structure energy levels, and the overlap integrals that connect these energy levels. The inner product of the angular waveforms relies on the following identity [55]:

$$\cos\theta \cdot Y_{l,m} = \sqrt{\frac{(l+m+1)(l-m+1)}{(2l+1)(2l+3)}}Y_{l+1,m} + \sqrt{\frac{(l+m)(l-m)}{(2l+1)(2l-1)}}Y_{l-1,m} \qquad (5.78)$$

Figure 28 Hα Fine Structure Transitions [50].

111

M=5/2

M=3/2

N=4

M=1/2

M=3/2

N=3

M=1/2

| 0.046 | 0.015 | | 0.305 | | 0.046 |

ΔE=20,570.502 cm-1
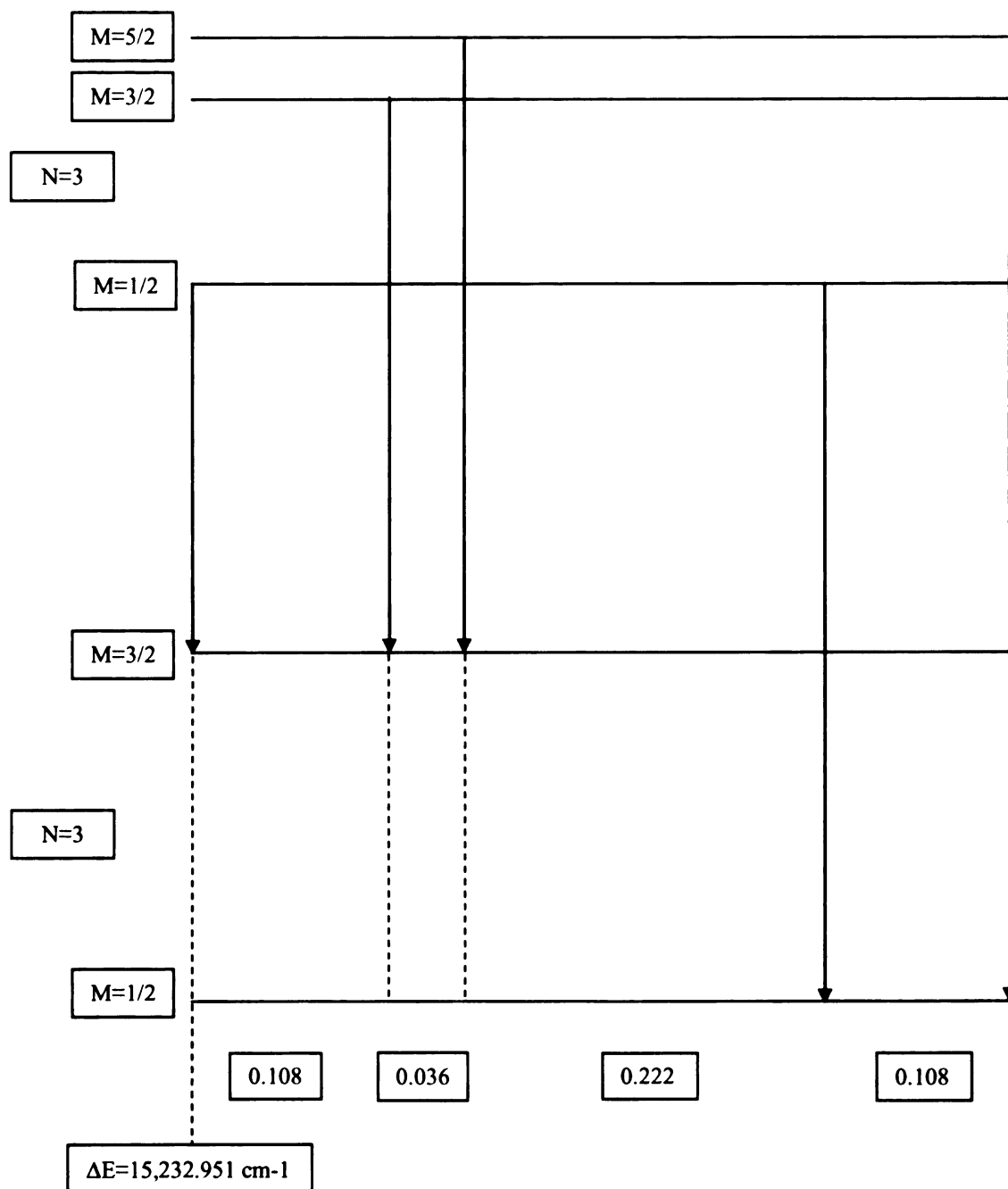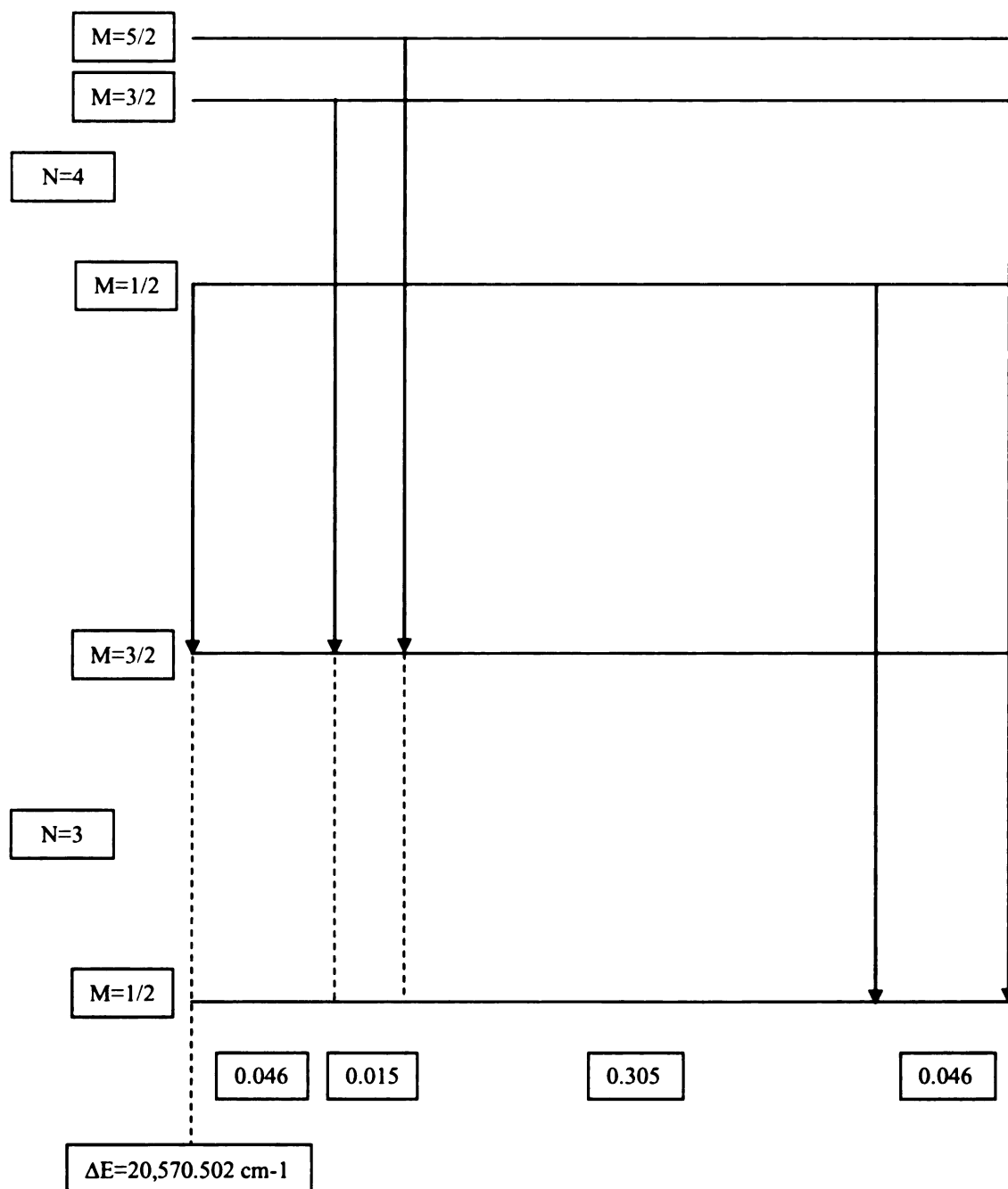
Figure 29 H$_\beta$ Fine Structure Transitions.

112

5/2>3/2

3/2>1/2

1/2>1/2

3/2>3/2

1/2>3/2

0.108

0.036

0.222

0.108

ΔE=15,232.951 cm-1
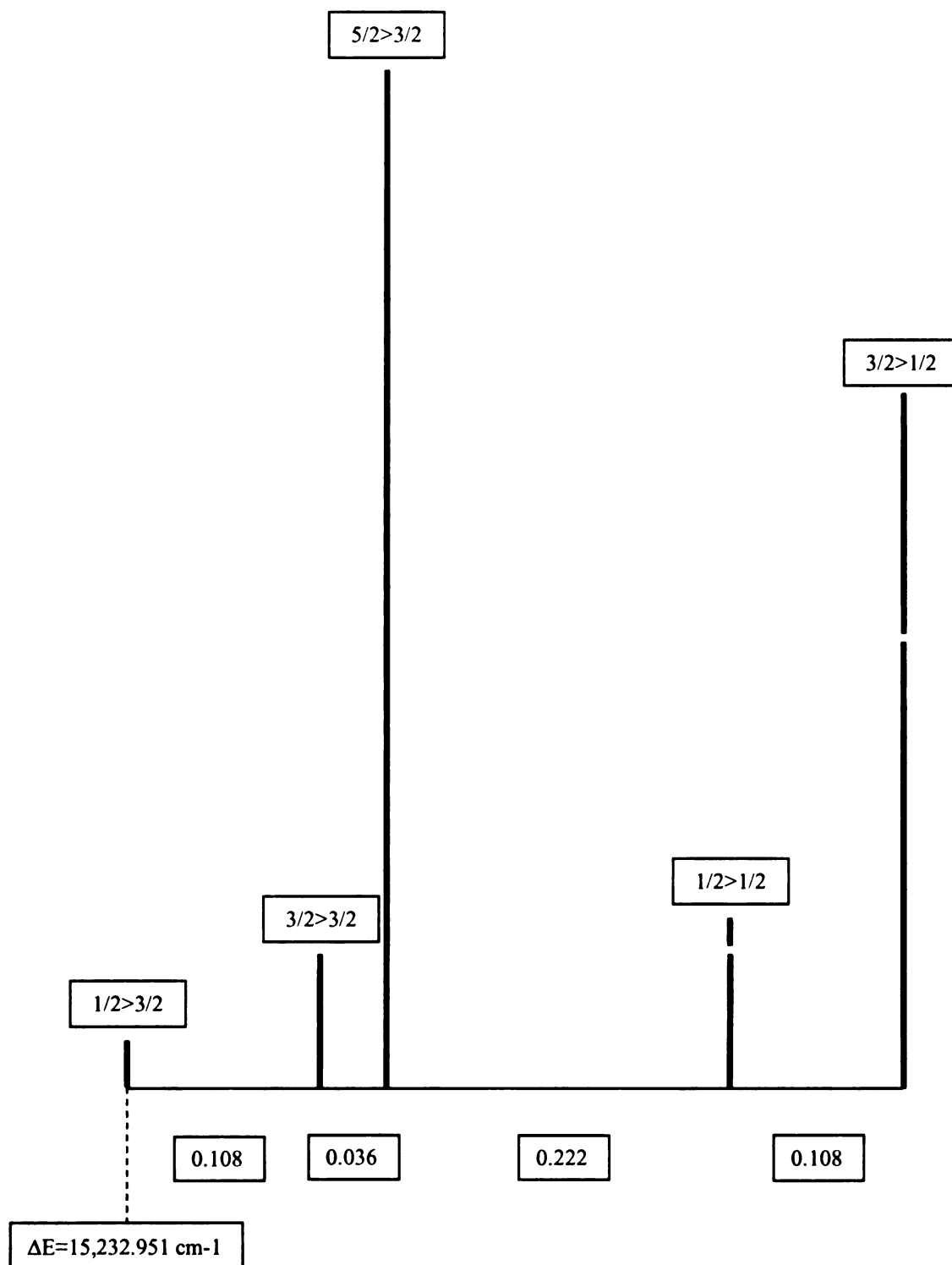
Figure 30 Hα Fine Structure Relative Transition Intensity.

113

And the orthogonality of the waveforms. As a result,

$$< Y^*_{j-1/2,m\pm1/2} \mid \cos\theta \mid Y_{j+1/2,m\pm1/2} > = \frac{1}{2}\sqrt{\frac{(j \mp m)(j \pm m + 1)}{j(j+1)}} \qquad (5.79)$$

Using the identity given in Equation 5.78, the transitional wave functions can be summarized by the expressions,

$$u_{n,j,m} = \begin{cases} + R_{n,j+1/2}\sqrt{\dfrac{j-m+1}{2(j+1)}} Y_{j+1/2,m-1/2} \Rightarrow (5.81) \\[3ex] - R_{n,j+1/2}\sqrt{\dfrac{j+m+1}{2(j+1)}} Y_{j+1/2,m+1/2} \Rightarrow (5.82) \\[3ex] + R_{n,j-1/2}\sqrt{\dfrac{j+m}{2j}} Y_{j-1/2,m-1/2} \Rightarrow (5.83) \\[3ex] + R_{n,j-1/2}\sqrt{\dfrac{j-m}{2j}} Y_{j-1/2,m+1/2} \Rightarrow (5.84) \end{cases} \qquad (C-G) \qquad (5.80)$$

Where:

$$Y_{j+1/2,m-1/2}\cos\theta = \begin{cases} \sqrt{\dfrac{(j+m+1)(j-m+2)}{4(j+1)(j+2)}} Y_{j+3/2,m-1/2} \\[3ex] + \\[3ex] \sqrt{\dfrac{(j+m)(j-m+1)}{4j(j+1)}} Y_{j-1/2,m-1/2} \end{cases} \qquad (5.81)$$

114

$$Y_{j+1/2,m+1/2} \cos\theta = \begin{cases} \sqrt{\dfrac{(j-m+1)(j+m+2)}{4(j+1)(j+2)}} Y_{j+3/2,m+1/2} \\[2mm] + \\[2mm] \sqrt{\dfrac{(j-m)(j+m+1)}{4j(j+1)}} Y_{j-1/2,m+1/2} \end{cases} \qquad (5.82)$$

$$Y_{j-1/2,m-1/2} \cos\theta = \begin{cases} \sqrt{\dfrac{(j+m)(j-m+1)}{4j(j+1)}} Y_{j+1/2,m-1/2} \\[2mm] + \\[2mm] \sqrt{\dfrac{(j-m)(j+m-1)}{4j(j-1)}} Y_{j-3/2,m-1/2} \end{cases} \qquad (5.83)$$

$$Y_{j-1/2,m+1/2} \cos\theta = \begin{cases} \sqrt{\dfrac{(j-m)(j+m+1)}{4j(j+1)}} Y_{j+1/2,m+1/2} \\[2mm] + \\[2mm] \sqrt{\dfrac{(j+m)(j-m-1)}{4j(j-1)}} Y_{j-3/2,m+1/2} \end{cases} \qquad (5.84)$$

The notation $u_{n,j,m}$ represents both the initial and final wave functions, with fine structure quantum numbers n,j,m as given in section 5.5. The relative amplitude of transitions between energy levels is given by:

$$z_{n,j}^{n',j'} = |<\phi_{n,j} \mid z \mid \phi_{n',j'}>|^2 = \sum_{m;j,j'} \left|<u_{n,j,m} \mid R \mid u_{n',j',m}>\right|^2 \qquad (5.85)$$

115

Where Equation 5.85 specifies the inner products of radial wave functions in Equations 5.81-84. These inner products are only a subset of all possible transitions, limited by the orthogonality property of spherical harmonics.

Specifically, the H_α fine structure transition amplitudes are given by the following, with allowable transitions limited to $\Delta J = 0, +/-1$.

$$z_{2,S1/2}^{3,P1/2} = \sum_{m=1/2} |< R_{3,1} \mid R \mid R_{2,0} >|^2 *$$

$$\left[\sqrt{\frac{(1/2-m+1)}{2(1/2+1)}} \sqrt{\frac{(1/2+m)(1/2-m+1)}{4 \cdot 1/2(1/2+1)}} \sqrt{\frac{(1/2+m)}{2 \cdot 1/2}} \right.$$

$$\left. + \sqrt{\frac{(1/2-m+1)}{2(1/2+1)}} \sqrt{\frac{(1/2+m)(1/2-m+1)}{4 \cdot 1/2(1/2+1)}} \sqrt{\frac{(1/2+m)}{2 \cdot 1/2}} \right]^2 \qquad (5.86)$$

$$= 1.04$$

$$z_{2,P1/2}^{3,S1/2} = \sum_{m=1/2} |< R_{3,0} \mid R \mid R_{2,1} >|^2 *$$

$$\left[\sqrt{\frac{(1/2+m)}{2 \cdot 1/2}} \sqrt{\frac{(1/2-m+1)}{2(1/2+1)}} \sqrt{\frac{(1/2+m)(1/2-m+1)}{4 \cdot 1/2(1/2+1)}} \right.$$

$$\left. + \sqrt{\frac{(1/2-m)}{2 \cdot 1/2}} \sqrt{\frac{(1/2+m+1)}{2(1/2+1)}} \sqrt{\frac{(1/2-m)(1/2+m+1)}{4 \cdot 1/2(1/2+1)}} \right]^2 \qquad (5.87)$$

$$= 0.10$$

116

$$z_{2,S1/2}^{3,P3/2} = \sum_{m=1/2} |< R_{3,1} \mid R \mid R_{2,0} >|^2 *$$

$$\left[\sqrt{\frac{(3/2+m)}{2\cdot3/2}} \sqrt{\frac{(3/2-m)(3/2+m-1)}{4\cdot3/2(3/2-1)}} \sqrt{\frac{(1/2+m)}{2\cdot1/2}} \right.$$

$$\left. + \sqrt{\frac{(3/2-m)}{2\cdot3/2}} \sqrt{\frac{(3/2+m)(3/2-m-1)}{4\cdot3/2(3/2-1)}} \sqrt{\frac{(1/2-m)}{2\cdot1/2}} \right]^2 \tag{5.88}$$

$$= 2.08$$

$$z_{2,P1/2}^{3,D3/2} = \sum_{m=1/2} |< R_{3,2} \mid R \mid R_{2,1} >|^2 *$$

$$\left[\sqrt{\frac{(3/2-m+1)}{2(3/2+1)\cdot}} \sqrt{\frac{(1/2-m+1)}{2(1/2+1)}} \sqrt{\frac{(1/2+m+1)(1/2-m+2)}{4(1/2+1)(1/2+2)}} \right.$$

$$\left. + \sqrt{\frac{(3/2+m+1)}{2(3/2+1)}} \sqrt{\frac{(1/2+m+1)}{2(1/2+1)}} \sqrt{\frac{(1/2-m+1)(1/2+m+2)}{4(1/2+1)(1/2+2)}} \right]^2 \tag{5.89}$$

$$= 5.01$$

$$z_{2,P3/2}^{3,S1/2} = \sum_{m=1/2} |< R_{3,0} \mid R \mid R_{2,1} >|^2 *$$

$$\left[\sqrt{\frac{(1/2+m)}{2\cdot1/2}} \sqrt{\frac{(3/2+m)}{2\cdot3/2}} \sqrt{\frac{(3/2-m)(3/2+m-1)}{4\cdot3/2(3/2-1)}} \right.$$

$$\left. + \sqrt{\frac{(1/2-m)}{2\cdot1/2}} \sqrt{\frac{(3/2-m)}{2\cdot3/2}} \sqrt{\frac{(3/2+m)(3/2-m-1)}{4\cdot3/2(3/2-1)}} \right]^2 \tag{5.90}$$

$$= 0.20$$

$$z_{2,P3/2}^{3,D3/2} = \sum_{m=1/2,3/2} |< R_{3,2} \mid R \mid R_{2,1} >|^2 *$$

$$\left[\sqrt{\frac{(3/2-m+1)}{2(3/2+1)}} \sqrt{\frac{(3/2+m)(3/2-m+1)}{4\cdot 3/2(3/2+1)}} \sqrt{\frac{(3/2+m)}{2\cdot 3/2}} \right.$$

$$\left. - \sqrt{\frac{(3/2+m+1)}{2(3/2+1)}} \sqrt{\frac{(3/2-m)(3/2+m+1)}{4\cdot 3/2(3/2+1)}} \sqrt{\frac{(3/2-m)}{2\cdot 3/2}} \right]^2$$

(5.91)

$$= 1.00$$

$$z_{2,P3/2}^{3,D5/2} = \sum_{m=1/2,3/2} |< R_{3,2} \mid R \mid R_{2,1} >|^2 *$$

$$\left[\sqrt{\frac{(5/2+m)}{2\cdot 5/2}} \sqrt{\frac{(5/2-m)(5/2+m-1)}{4\cdot 5/2(5/2-1)}} \sqrt{\frac{(3/2+m)}{2\cdot 3/2}} \right.$$

$$\left. + \sqrt{\frac{(5/2-m)}{2\cdot 5/2}} \sqrt{\frac{(5/2+m)(5/2-m-1)}{4\cdot 5/2(5/2-1)}} \sqrt{\frac{(3/2-m)}{2\cdot 3/2}} \right]^2$$

(5.92)

$$= 9.02$$

118

Where the pertinent normalized radial wave functions are given as [56]:

$$R_{2,0} = \frac{1}{\sqrt{8}}(2-R)e^{-R/2}$$

$$R_{2,1} = \frac{1}{\sqrt{24}}\mathrm{Re}^{-R/2}$$

$$R_{3,0} = \frac{1}{\sqrt{4920.75}}(27-18R+2R^2)e^{-R/3} \tag{5.93}$$

$$R_{3,1} = \frac{1}{\sqrt{2460.375}}(6-R)\mathrm{Re}^{-R/3}$$

$$R_{3,2} = \frac{1}{\sqrt{12,301.875}}R^2 e^{-R/3}$$

In a plasma discharge, fine structure line intensities vary dramatically as a function of electron density [57]-[58]. For example, peak 1/2>1/2 in Figure 30, barely detectable in the nominal case, becomes as strong or stronger than peaks 5/2>3/2 and 3/2>1/2 at electron densities >10^{14} cm^{-3} [42]. Figures 31 [59]-32 [60] demonstrate fine structure peak ratios in experimental conditions closer to experiments run for this study. Both are taken from low-pressure gas discharges. However, electron densities are not recorded for either experiment. As evident, the characteristic shape of the fine structure peaks can be used as a signature for identifying Stark effect splitting in hydrogen plasmas.

119
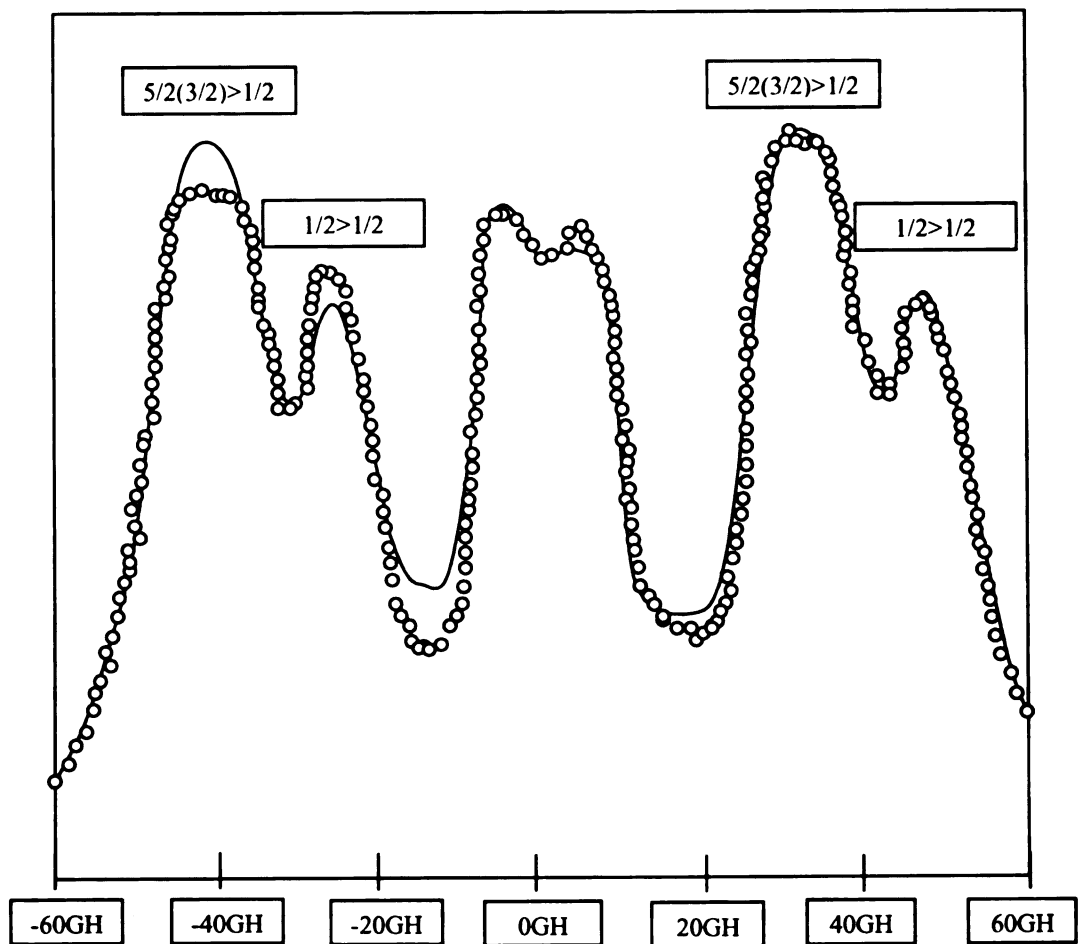
Figure 31 Hα Fine Structure Peaks Near Band Center [59].

120
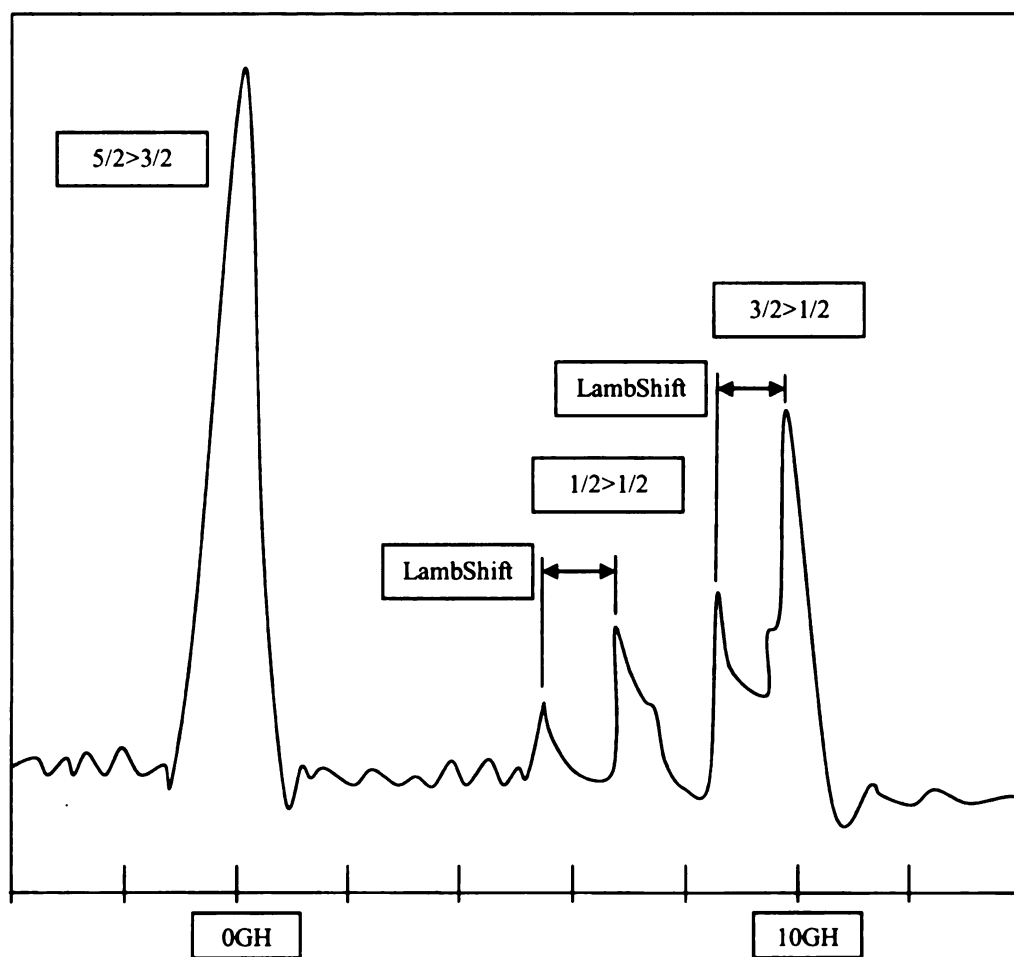
Figure 32 Hα Fine Stucture: Absorption Spectroscopy, Pulsed Dye Laser [60].

121

Chapter 6 Atomic Hydrogen: Stark Effect

Chapter 5 covers Zeeman splitting in the rotation spectrum of molecular hydrogen, and the fine structure of atomic hydrogen. Each of these effects are completely described in spherical coordinates. Chapter 6 addresses Stark splitting in atomic hydrogen. Stark splitting can be expressed in spherical coordinates as well, but spherical coordinates limit spectral analysis of atomic hydrogen when considering the gross structure splitting in combination with fine structure splitting. The gross structure waveforms mix so thoroughly that initiating fine structure points is intractable.

Chapter 6 addresses this shortcoming. The following sections first solve for the Stark effect splitting in spherical coordinates, then the problem is moved to parabolic and semi-parabolic coordinates to better match the symmetry of atomic hydrogen. Wave functions that result from a coulombic central force, such as that found in atomic hydrogen, have an additional degree of freedom when expressed in parabolic coordinates. The additional freedom represents an additional symmetry that was hidden –and not necessary- in spherical coordinates.

As a result, the Stark effect does not mix the resulting waveforms in parabolic coordinates, and the gross structure is predictable in the presence of fine structure splitting.

Sections on Stark fine structure splitting immediately follow the treatment of Stark splitting in parabolic coordinates. For both gross and fine structure splitting, transition amplitudes are included with experimental spectral data in Chapter 7.

122

6. 1 *Stark Splitting: Spherical Coordinates*

The wave functions for atomic hydrogen are developed in spherical coordinates in section 5.2.2.2. The next two sections address the Stark effect for atomic hydrogen in the spherical coordinate system. The first section solves the Schroedinger equation by direct application of perturbation theory, developing the perturbation –or overlap- matrices associated with the given potential operator. Then, solves for the eigenvalues of the perturbation matrices, which immediately give the Stark shifted atomic hydrogen energy levels. The second section details the Stark shifted spectrum for atomic hydrogen.

6.1.1 Perturbation Matrix

The perturbation matrix is composed of all possible wave function overlap integrals; that is, the integrals of each pair of degenerate wave functions and the applicable potential energy operator. The potential energy operator for the Stark effect is related to the applied electric field as follows:

$$V_{Stark} = \begin{cases} eEz & ; Linear Polarization \\ eE(x \pm jy); Circular Polarization \end{cases} \qquad (6.1)$$

Due to reactor geometry, the polarization of the electric field for this set of experiments is strictly linear. First-order approximations to energy level shifts are the eigenvalues of the perturbation matrix.

Spherical wave functions of atomic hydrogen associated with electronic energy levels two through four are given on the following pages [56],[61].

$n = 2$:

$$\psi_{2,0,0} = \frac{1}{\sqrt{2\pi \cdot 16}} \sqrt{\frac{Z^3}{a_0^3}} (2 - \rho) e^{-\rho/2}$$

$$\psi_{2,1,-1} = \frac{1}{\sqrt{2\pi \cdot 32}} \sqrt{\frac{Z^3}{a_0^3}} \rho e^{-\rho/2} \sin\theta \cdot e^{-j\phi} \qquad (6.2)$$

$$\psi_{2,1,0} = \frac{1}{\sqrt{2\pi \cdot 16}} \sqrt{\frac{Z^3}{a_0^3}} \rho e^{-\rho/2} \cos\theta$$

$$\psi_{2,1,+1} = \frac{1}{\sqrt{2\pi \cdot 32}} \sqrt{\frac{Z^3}{a_0^3}} \rho e^{-\rho/2} \sin\theta \cdot e^{+j\phi}$$

$n = 3$:

$$\psi_{3,0,0} = \frac{1}{\sqrt{2\pi \cdot 9841.5}} \sqrt{\frac{Z^3}{a_0^3}} (2 - \rho) e^{-\rho/2}$$

$$\psi_{3,1,-1} = \frac{1}{\sqrt{2\pi \cdot 1640.25}} \sqrt{\frac{Z^3}{a_0^3}} (6 - \rho) \rho e^{-\rho/3} \sin\theta \cdot e^{-j\phi} \qquad (6.3)$$

$$\psi_{3,1,0} = \frac{1}{\sqrt{2\pi \cdot 1640.25}} \sqrt{\frac{Z^3}{a_0^3}} (6 - \rho) \rho e^{-\rho/3} \cos\theta$$

$$\psi_{3,1,+1} = \frac{1}{\sqrt{2\pi \cdot 1640.25}} \sqrt{\frac{Z^3}{a_0^3}} (6 - \rho) \rho e^{-\rho/3} e^{-\rho/2} \sin\theta \cdot e^{+j\phi}$$

$$\psi_{3,2,-2} = \frac{1}{\sqrt{2\pi \cdot 6561}} \sqrt{\frac{Z^3}{a_0^3}} \rho^2 e^{-\rho/3} \sin^2\theta \cdot e^{-j2\phi}$$

$$\psi_{3,2,-1} = \frac{1}{\sqrt{2\pi \cdot 1640.25}} \sqrt{\frac{Z^3}{a_0^3}} \rho^2 e^{-\rho/3} \sin\theta \cos\theta \cdot e^{-j\phi}$$

$$\psi_{3,2,0} = \frac{1}{\sqrt{2\pi \cdot 19683}} \sqrt{\frac{Z^3}{a_0^3}} \rho^2 e^{-\rho/3} \left(3\cos^2\theta - 1\right)$$

$$\psi_{3,2,+1} = \frac{1}{\sqrt{2\pi \cdot 1640.25}} \sqrt{\frac{Z^3}{a_0^3}} \rho^2 e^{-\rho/3} \sin\theta \cos\theta \cdot e^{+j\phi}$$

$$\psi_{3,2,+2} = \frac{1}{\sqrt{2\pi \cdot 6561}} \sqrt{\frac{Z^3}{a_0^3}} \rho^2 e^{-\rho/3} \sin^2\theta \cdot e^{+j2\phi}$$

$n = 4:$

$$\psi_{4,0,0} = \frac{1}{\sqrt{2\pi \cdot 1179648}} \sqrt{\frac{Z^3}{a_0^3}} \left(192 - 144\rho + 24\rho^2 - \rho^3\right) e^{-\rho/4}$$

$$\psi_{4,1,-1} = \frac{1}{\sqrt{2\pi \cdot 1310720}} \sqrt{\frac{Z^3}{a_0^3}} \left(80 - 20\rho + \rho^2\right) e^{-\rho/4} \sin\theta \cdot e^{-j\phi} \tag{6.4}$$

$$\psi_{4,1,0} = \frac{1}{\sqrt{2\pi \cdot 655360}} \sqrt{\frac{Z^3}{a_0^3}} \left(80 - 20\rho + \rho^2\right) e^{-\rho/4} \cos\theta$$

$$\psi_{4,1,-1} = \frac{1}{\sqrt{2\pi \cdot 1310720}} \sqrt{\frac{Z^3}{a_0^3}} \left(80 - 20\rho + \rho^2\right) e^{-\rho/4} \sin\theta \cdot e^{+j\phi}$$

$$\psi_{4,2,-2} = \frac{1}{\sqrt{2\pi \cdot 3145728}} \sqrt{\frac{Z^3}{a_0^3}} (12 - \rho)\rho^2 e^{-\rho/4} \sin^2\theta \cdot e^{-j2\phi}$$

$$\psi_{4,2,-1} = \frac{1}{\sqrt{2\pi \cdot 786432}} \sqrt{\frac{Z^3}{a_0^3}} (12 - \rho)\rho^2 e^{-\rho/4} \sin\theta\cos\theta \cdot e^{-j\phi}$$

$$\psi_{4,2,0} = \frac{1}{\sqrt{2\pi \cdot 4718592}} \sqrt{\frac{Z^3}{a_0^3}} (12 - \rho)\rho^2 e^{-\rho/4} \left(3\cos^2\theta - 1\right)$$

$$\psi_{4,2,+1} = \frac{1}{\sqrt{2\pi \cdot 786432}} \sqrt{\frac{Z^3}{a_0^3}} (12 - \rho)\rho^2 e^{-\rho/4} \sin\theta\cos\theta \cdot e^{+j\phi}$$

$$\psi_{4,2,+2} = \frac{1}{\sqrt{2\pi \cdot 3145728}} \sqrt{\frac{Z^3}{a_0^3}} (12 - \rho)\rho^2 e^{-\rho/4} \sin^2\theta \cdot e^{+j2\phi}$$

$$\psi_{4,3,-3} = \frac{1}{\sqrt{2\pi \cdot 18874368}} \sqrt{\frac{Z^3}{a_0^3}} \rho^3 e^{-\rho/4} \sin^3\theta \cdot e^{-j3\phi}$$

$$\psi_{4,3,-2} = \frac{1}{\sqrt{2\pi \cdot 3145728}} \sqrt{\frac{Z^3}{a_0^3}} \rho^3 e^{-\rho/4} \sin^2\theta\cos\theta \cdot e^{-j2\phi}$$

$$\psi_{4,3,-1} = \frac{1}{\sqrt{2\pi \cdot 31457280}} \sqrt{\frac{Z^3}{a_0^3}} \rho^3 e^{-\rho/4} \sin\theta\left(5\cos^2\theta - 1\right) \cdot e^{-j\phi}$$

$$\psi_{4,3,0} = \frac{1}{\sqrt{2\pi \cdot 2621440}} \sqrt{\frac{Z^3}{a_0^3}} \rho^3 e^{-\rho/4} \left(5/3\cos^3\theta - \cos\theta\right)$$

$$\psi_{4,3,+1} = \frac{1}{\sqrt{2\pi \cdot 31457280}} \sqrt{\frac{Z^3}{a_0^3}} \rho^3 e^{-\rho/4} \sin\theta\left(5\cos^2\theta - 1\right) \cdot e^{+j\phi}$$

$$\psi_{4,3,+2} = \frac{1}{\sqrt{2\pi \cdot 3145728}} \sqrt{\frac{Z^3}{a_0^3}} \rho^3 e^{-\rho/4} \sin^2\theta\cos\theta \cdot e^{+j2\phi}$$

$$\psi_{4,3,+3} = \frac{1}{\sqrt{2\pi \cdot 18874368}} \sqrt{\frac{Z^3}{a_0^3}} \rho^3 e^{-\rho/4} \sin^3\theta \cdot e^{+j3\phi}$$

The non-zero elements of the perturbation matrices for each energy level can be summarized in the following:

$n = 2$:

$a_2 = <\psi_{2,0,0} \mid z \mid \psi_{4,1,0}> = 3.00a_0$

$n = 3$:

$a_3 = <\psi_{3,0,0} \mid z \mid \psi_{3,1,0}> = 7.35a_0$
$b_3 = <\psi_{3,1,-1} \mid z \mid \psi_{3,2,-1}> = 4.50a_0$
$c_3 = <\psi_{3,1,0} \mid z \mid \psi_{3,2,0}> = 5.20a_0$
$d_3 = <\psi_{3,1,+1} \mid z \mid \psi_{3,2,+1}> = 4.50a_0$

$n = 4$:

$a_4 = <\psi_{4,0,0} \mid z \mid \psi_{4,1,0}> = 13.42a_0$
$b_4 = <\psi_{4,1,-1} \mid z \mid \psi_{4,2,-1}> = 9.30a_0$
$c_4 = <\psi_{4,1,0} \mid z \mid \psi_{4,2,0}> = 10.73a_0$
$d_4 = <\psi_{4,1,+1} \mid z \mid \psi_{4,2,+1}> = 9.30a_0$
$e_4 = <\psi_{4,2,-2} \mid z \mid \psi_{4,3,-2}> = 6.00a_0$
$f_4 = <\psi_{4,2,-1} \mid z \mid \psi_{4,3,-1}> = 7.59a_0$ \hfill (6.5)
$g_4 = <\psi_{4,2,0} \mid z \mid \psi_{4,3,0}> = 8.05a_0$
$h_4 = <\psi_{4,2,+1} \mid z \mid \psi_{4,3,+1}> = 7.59a_0$
$i_4 = <\psi_{4,2,+2} \mid z \mid \psi_{4,3,+2}> = 6.00a_0$

Where the perturbation -or overlap- matrices are expressed by the following for each of the electronic energy levels two through four:

$$H_2' = \begin{bmatrix} 0 & 0 & a_2 & 0 \\ 0 & 0 & 0 & 0 \\ a_2 & 0 & 0 & 0 \\ 0 & 0 & 0 & 0 \end{bmatrix}$$

$$H_3' = \begin{bmatrix} 0 & 0 & a_3 & 0 & 0 & 0 & 0 & 0 & 0 \\ 0 & 0 & 0 & 0 & 0 & b_3 & 0 & 0 & 0 \\ a_3 & 0 & 0 & 0 & 0 & 0 & c_3 & 0 & 0 \\ 0 & 0 & 0 & 0 & 0 & 0 & 0 & d_3 & 0 \\ 0 & 0 & 0 & 0 & 0 & 0 & 0 & 0 & 0 \\ 0 & b_3 & 0 & 0 & 0 & 0 & 0 & 0 & 0 \\ 0 & 0 & c_3 & 0 & 0 & 0 & 0 & 0 & 0 \\ 0 & 0 & 0 & d_3 & 0 & 0 & 0 & 0 & 0 \\ 0 & 0 & 0 & 0 & 0 & 0 & 0 & 0 & 0 \end{bmatrix} \qquad (6.6)$$

$$H_4' = \begin{bmatrix} 0 & 0 & a_4 & 0 & 0 & 0 & 0 & 0 & 0 & 0 & 0 & 0 & 0 & 0 & 0 & 0 \\ 0 & 0 & 0 & 0 & 0 & b_4 & 0 & 0 & 0 & 0 & 0 & 0 & 0 & 0 & 0 & 0 \\ a_4 & 0 & 0 & 0 & 0 & 0 & c_4 & 0 & 0 & 0 & 0 & 0 & 0 & 0 & 0 & 0 \\ 0 & 0 & 0 & 0 & 0 & 0 & 0 & d_4 & 0 & 0 & 0 & 0 & 0 & 0 & 0 & 0 \\ 0 & 0 & 0 & 0 & 0 & 0 & 0 & 0 & 0 & 0 & e_4 & 0 & 0 & 0 & 0 & 0 \\ 0 & b_4 & 0 & 0 & 0 & 0 & 0 & 0 & 0 & 0 & 0 & f_4 & 0 & 0 & 0 & 0 \\ 0 & 0 & c_4 & 0 & 0 & 0 & 0 & 0 & 0 & 0 & 0 & 0 & g_4 & 0 & 0 & 0 \\ 0 & 0 & 0 & d_4 & 0 & 0 & 0 & 0 & 0 & 0 & 0 & 0 & 0 & h_4 & 0 & 0 \\ 0 & 0 & 0 & 0 & 0 & 0 & 0 & 0 & 0 & 0 & 0 & 0 & 0 & 0 & i_4 & 0 \\ 0 & 0 & 0 & 0 & 0 & 0 & 0 & 0 & 0 & 0 & 0 & 0 & 0 & 0 & 0 & 0 \\ 0 & 0 & 0 & 0 & e_4 & 0 & 0 & 0 & 0 & 0 & 0 & 0 & 0 & 0 & 0 & 0 \\ 0 & 0 & 0 & 0 & 0 & f_4 & 0 & 0 & 0 & 0 & 0 & 0 & 0 & 0 & 0 & 0 \\ 0 & 0 & 0 & 0 & 0 & 0 & g_4 & 0 & 0 & 0 & 0 & 0 & 0 & 0 & 0 & 0 \\ 0 & 0 & 0 & 0 & 0 & 0 & 0 & h_4 & 0 & 0 & 0 & 0 & 0 & 0 & 0 & 0 \\ 0 & 0 & 0 & 0 & 0 & 0 & 0 & 0 & i_4 & 0 & 0 & 0 & 0 & 0 & 0 & 0 \\ 0 & 0 & 0 & 0 & 0 & 0 & 0 & 0 & 0 & 0 & 0 & 0 & 0 & 0 & 0 & 0 \end{bmatrix}$$

The characteristic equation and solution for each of the electronic energy levels is given by the following:

$n = 2$:

$$\lambda^2\left(\lambda^2 - a_2^2\right) = 0$$

$$\lambda = \begin{cases} 0,0 \\ \pm a_2 \end{cases}$$

$n = 3$:

$$\lambda^3\left(\lambda^2 - a_3^2 - c_3^2\right)\left(\lambda^2 - b_3^2\right)\left(\lambda^2 - d_3^2\right) = 0$$

$$\lambda = \begin{cases} 0,0,0 \\ \pm b_3 \\ \pm d_3 \\ \pm\sqrt{a_3^2 + c_3^2} \end{cases}$$

$n = 4$:

$$\lambda^4\left(\lambda^2 - \left(b_4^2 + f_4^2\right)\right)\left(\lambda^2 - \left(d_4^2 + h_4^2\right)\right)\left(\lambda^2 - e_4^2\right)\left(\lambda^2 - i_4^2\right)\left[\left(\lambda^2 - a_4^2\right)\left(\lambda^2 - g_4^2\right) - c_4^2\lambda^2\right] = 0$$

$$\lambda = \begin{cases} 0,0,0,0 \\ \pm e_4 \\ \pm j_4 \\ \pm\sqrt{b_4^2 + f_4^2} \\ \pm\sqrt{d_4^2 + h_4^2} \\ \pm\sqrt{\dfrac{1}{2}\left(a_4^2 + g_4^2 + c_4^2\right) \pm \dfrac{1}{2}\sqrt{\left(a_4^2 + g_4^2 + c_4^2\right) - 4a_4^2 g_4^2}} \end{cases}$$

$$(6.7)$$

Substituting from Equation 6.5 gives the following Stark energy level shifts in electronic energy levels two through four for linearly polarized electric fields:

$n = 2$:

$$\delta E = \begin{cases} 0 \\ \pm 3ea_0E \end{cases}$$

$n = 3$:

$$\delta E = \begin{cases} 0 \\ \pm 4.5ea_0E \\ \pm 9.0ea_0E \end{cases}$$

$n = 4$:

$$\delta E = \begin{cases} 0 \\ \pm 6.0ea_0E \\ \pm 12.0ea_0E \\ \pm 18.0\varepsilon ea_0E \end{cases}$$

(6.8)

Which can be summarized easily by the following equation:

$$\delta E = ea_0E \cdot \frac{3}{2}ni$$

(6.9)

$0 \le i < n$

Where n is the electronic quantum number.

6.1.2 Stark Energy Spectrum: Spherical Coordinates

Figures 33-34 are diagrams of the Stark shifted energy levels for atomic hydrogen transitions H_α and H_β, respectively. Each figure is specific to an electric field that is linearly polarized. Transition lines are left out of Figures 33-34, and transition amplitudes are not addressed.

In spherical coordinates, allowable transitions in a linearly polarized electric field are limited to those in which quantum numbers $\Delta l = +/-1$ and $\Delta m = 0$. However, Stark shifted wave functions assigned to each energy level can no longer be expressed as spherical harmonics; rather, they are linear combinations of spherical harmonics, and the mixing that results from the applied electric field is not trivial. As a result, the allowed transitions and transition amplitudes are extremely difficult to generate in spherical coordinates.

Following mixing, each eigenfunction is generated from the eigenvalues of the perturbation matrices, and the perturbation matrices themselves. The presence of degenerate eigenvalues (e.g. multiple zeroes) requires very complicated operators to generate the eigenfunctions, or wave functions. These operators turn out to be the ladder operators associated with a new, cylindrically symmetric coordinate system. Instead of working through the ladder operators, it is far simpler to solve the Schroedinger equation for atomic hydrogen in the new coordinate system, that of parabolic coordinates.

6. 2 Parabolic Coordinates

The application of an electric field destroys the symmetry in the radial component of the generalized central force problem; it is now cylindrically symmetric. As a result,
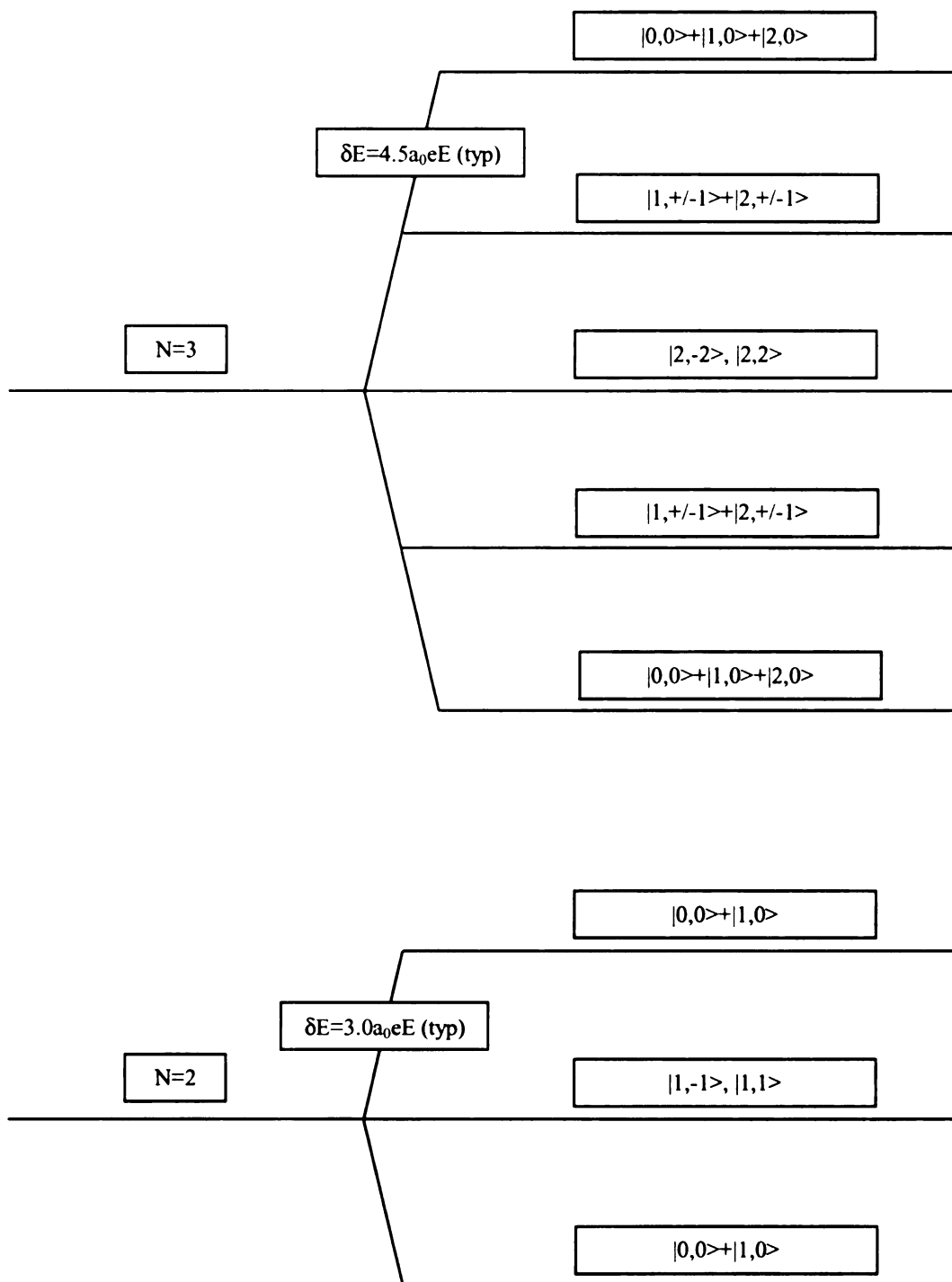
$|0,0> + |1,0> + |2,0>$

$\delta E = 4.5 a_0 e E$ (typ)

$|1,+/-1> + |2,+/-1>$

N=3

$|2,-2>, |2,2>$

$|1,+/-1> + |2,+/-1>$

$|0,0> + |1,0> + |2,0>$

$|0,0> + |1,0>$

$\delta E = 3.0 a_0 e E$ (typ)

N=2

$|1,-1>, |1,1>$

$|0,0> + |1,0>$

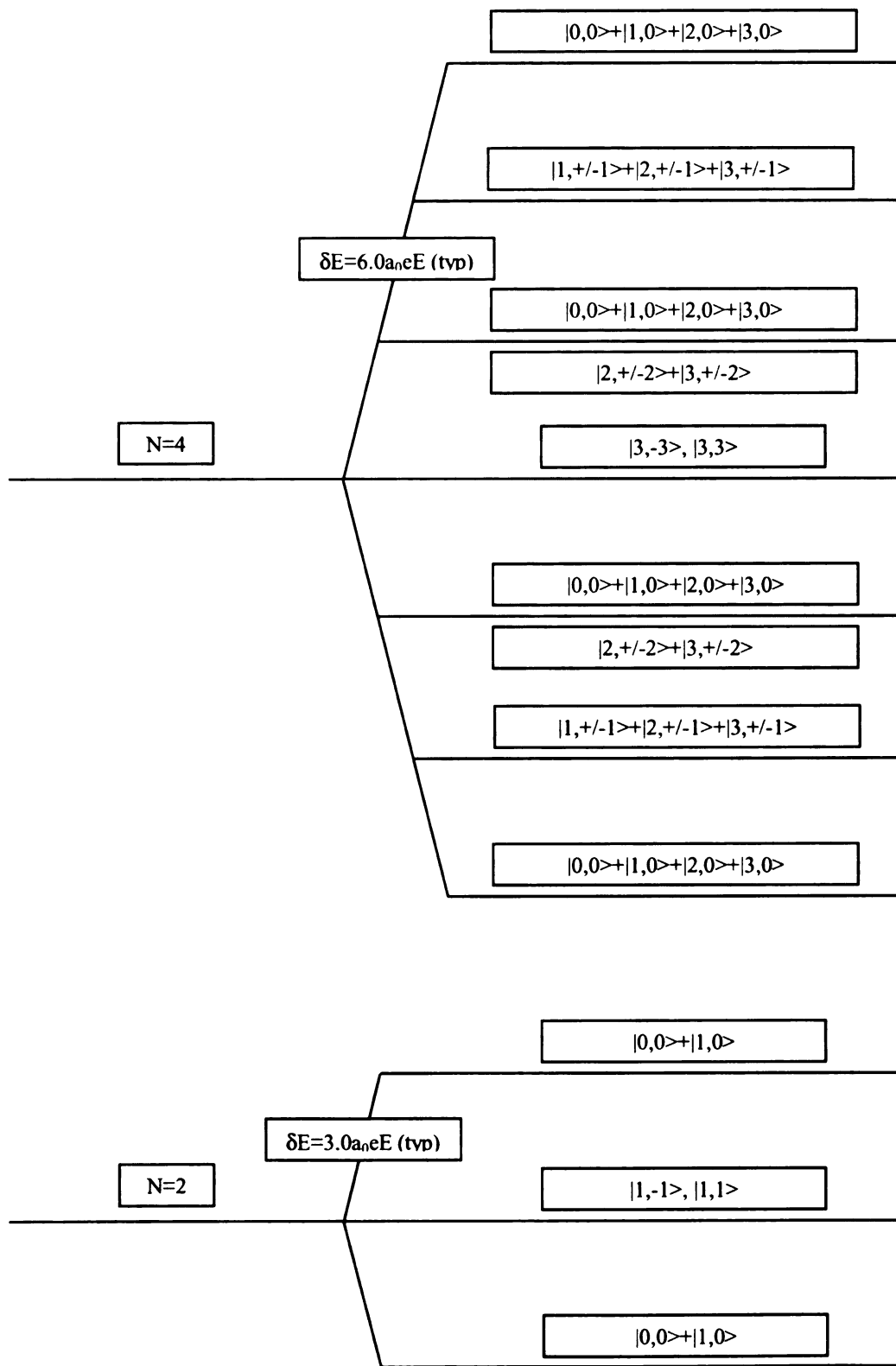**Figure 33** Hα Stark Energy Spectrum: Spherical Coordinates.

132

Figure 34 H_β Stark Energy Spectrum: Spherical Coordinates.

the orbital wave functions are no longer separable in spherical coordinates. More importantly, the mixing of the wave functions that results from perturbation analysis makes ferreting out the spherical harmonic components associated with each energy level very difficult. Both issues are resolved by moving to a new coordinate system that matches the symmetries of the problem.

6.2.1 Parabolic Transform

Cylindrical symmetry is retained when folding up R^3 space in such a way that the x-y plane forms a right circular cone about the z axis, and each additional plane with constant z folds into hyperboloid sheets, as shown in Figure 35. Every plane intersects the infinite set of hyperboloid sheets to form circles, ellipses, parabolas, and hyperbolas; conic sections that define the dynamics associated with a central force proportional to 1/R. (Each conic section is actually a geodesic with respect to rotated SO(2,1) space, or Lorentzian measure [62]). The inverse map of this three-dimensional folding is the parabolic transformation.

The parabolic transform map is shown in Figure 36; this map generates the parabolic coordinate system [63]. Using complex variables:

$$q = \frac{1}{2}w^2 = \frac{1}{2}(\xi + j\eta)^2 = \frac{1}{2}\left(\xi^2 - \eta^2\right) + j\xi\eta$$

$$z = \frac{1}{2}\left(\xi^2 - \eta^2\right) \tag{6.10}$$

$$R = \sqrt{\left[\frac{1}{2}\left(\xi^2 - \eta^2\right)\right]^2 + (\xi\eta)^2} = \frac{1}{2}\left(\xi^2 + \eta^2\right)$$
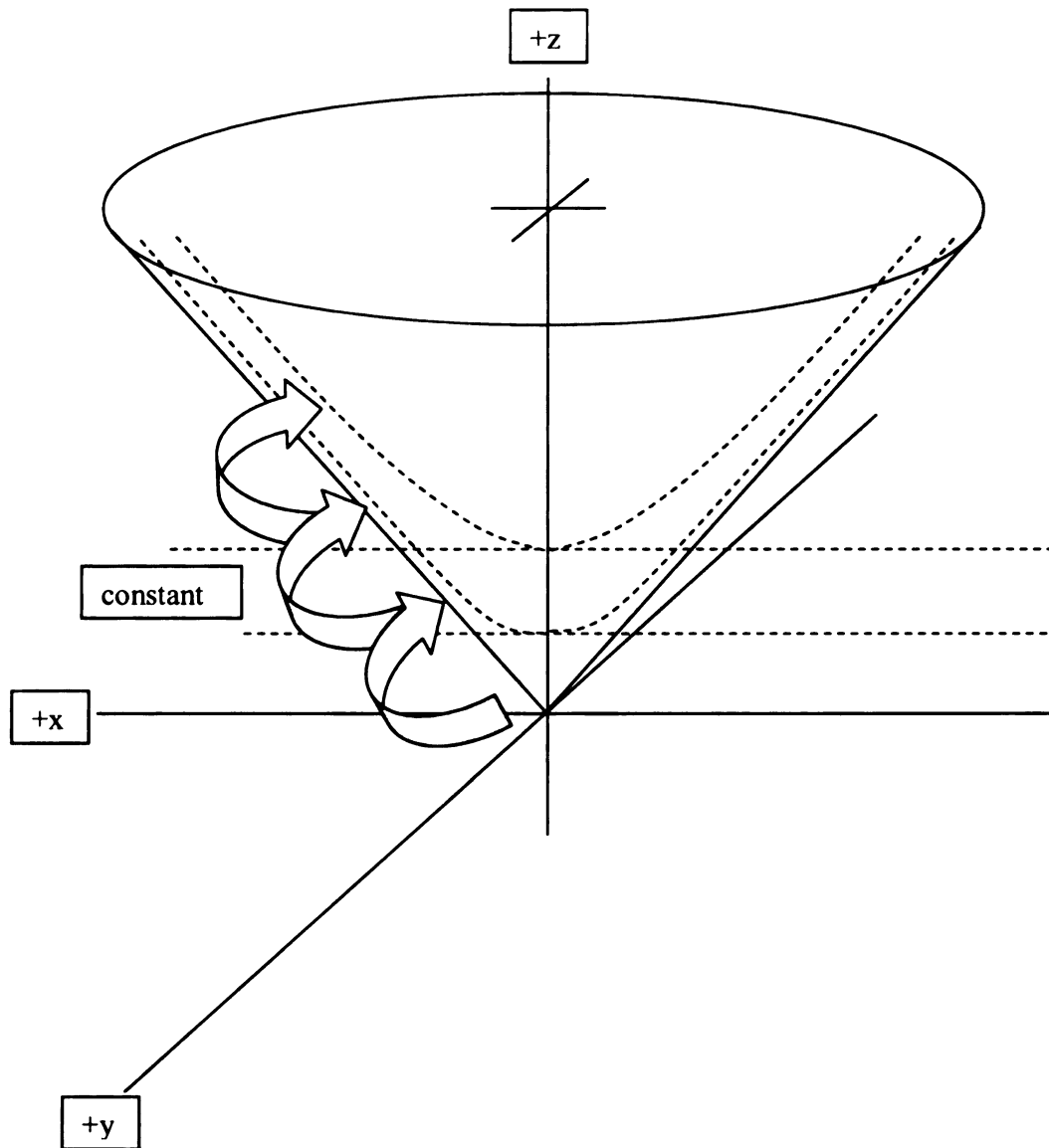
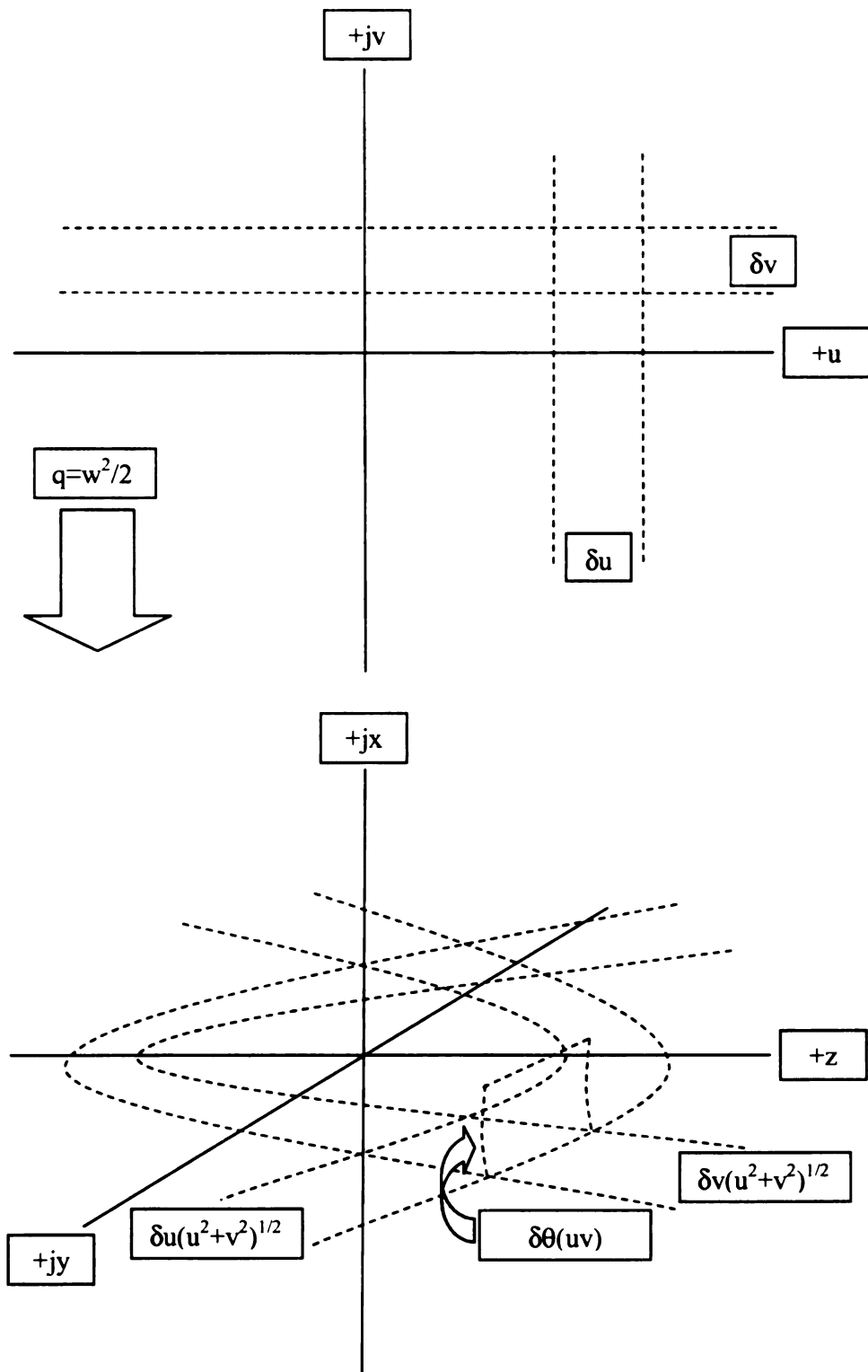**Figure 35** Hyperbolic Transform of Constant z Surfaces.

135

Figure 36 Parabolic Transform in the Complex Plane.

136

Now, Rz is separable as the difference of fourth-order terms. Further, the Laplacian can be found directly from the differentials generated by the map [64].

$$\nabla^2 = \frac{1}{\delta Vol}\left\{\partial\left(\delta A_{\eta\theta}\cdot\frac{\partial}{\partial S_\xi}\right)+\partial\left(\delta A_{\xi\theta}\cdot\frac{\partial}{\partial S_\eta}\right)+\partial\left(\delta A_{\xi\eta}\cdot\frac{\partial}{\partial S_\theta}\right)\right\}$$

(6.11)

$$\nabla^2 = \frac{1}{\xi\eta(\xi^2+\eta^2)}\left\{\frac{\partial}{\partial\xi}\left(\xi\eta\frac{\partial}{\partial\xi}\right)+\frac{\partial}{\partial\eta}\left(\xi\eta\frac{\partial}{\partial\eta}\right)\right\}+\frac{1}{\xi^2\eta^2}\frac{\partial^2}{\partial\theta^2}$$

With a change of variables,

$$\xi = \sqrt{u}$$

(6.12)

$$\eta = \sqrt{v}$$

The Laplacian can be expressed as,

$$\nabla^2 = \frac{4}{u+v}\left\{\frac{\partial}{\partial u}\left(u\frac{\partial}{\partial u}\right)+\frac{\partial}{\partial v}\left(v\frac{\partial}{\partial v}\right)\right\}+\frac{1}{uv}\frac{\partial^2}{\partial\theta^2}$$

(6.13)

And,

$$z = \frac{1}{2}(u-v)$$

(6.14)

$$R = \frac{1}{2}(u+v)$$

Consequently, the Schroedinger equation in parabolic coordinates, with a coulombic central force and applied electric field, is written as,

$$\left(-\frac{\hbar^2}{2m}\nabla^2 + V\right)\psi = E\psi$$

$$\frac{\hbar^2}{2m}\left[\frac{4}{u+v}\left\{\frac{\partial}{\partial u}\left(u\frac{\partial}{\partial u}\right) + \frac{\partial}{\partial v}\left(v\frac{\partial}{\partial v}\right)\right\} + \frac{1}{uv}\frac{\partial^2}{\partial\theta^2}\right]\psi \qquad (6.15)$$

$$+\left(\frac{Ze^2}{\frac{1}{2}(u+v)} + eE\frac{1}{2}(u-v)\right)\psi = W\psi$$

Where Z is the number of protons of the single electron atom (Rydberg atom), which is equal to one in the case of hydrogen. The energy term (W) must match the electronic energy found in spherical coordinates. Equation 6.15 is separable into the following independent equations:

$$\left\{\frac{\hbar^2}{2m}\left[\frac{\partial}{\partial u}\left(u\frac{\partial}{\partial u}\right) - \frac{1}{4}\left(\frac{m^2}{u}\right)\right] - \frac{1}{4}Wu + \frac{1}{2}Z_u e^2 + \frac{1}{8}eEu^2\right\}U = 0$$

$$\left\{\frac{\hbar^2}{2m}\left[\frac{\partial}{\partial v}\left(v\frac{\partial}{\partial v}\right) - \frac{1}{4}\left(\frac{m^2}{v}\right)\right] - \frac{1}{4}Wv + \frac{1}{2}Z_v e^2 - \frac{1}{8}eEv^2\right\}V = 0 \qquad (6.16)$$

$$Z = Z_u + Z_v = 1$$

138

The separation of equations in u and v requires the existence of an additional invariant of motion, covered in the next section. The inability to make this further separation in spherical coordinates is the reason that spherical harmonics remain mixed after solving for the eigenfunctions of the Stark shifted energy levels. The Stark effect perturbation matrices for both equations in u and v, on the other hand, are diagonal. This will be demonstrated in section 6.2.3.

6.2.2 Runge-Lenz Vector

Figure 37 illustrates an additional constant of motion, the Runge-Lenz vector, particular to dynamics where the central potential is proportional to 1/R. A classical development for the procedure follows:

$$mR^2 = \vec{L}$$

$$mR^2\left(\hat{R} \times \hat{\phi} \times \hat{R}\right) = \vec{L}$$

$$-mk\left(\hat{R} \times \hat{\phi} \times \hat{R}\right) \times \hat{R} = \vec{L} \times -\frac{k}{R^2}\hat{R} = \vec{L} \times \hat{p} \qquad (6.17)$$

$$-mk\left(\hat{R} - \hat{R}_0\right) = \vec{L} \times \left(\vec{p} - \vec{p}_0\right)$$

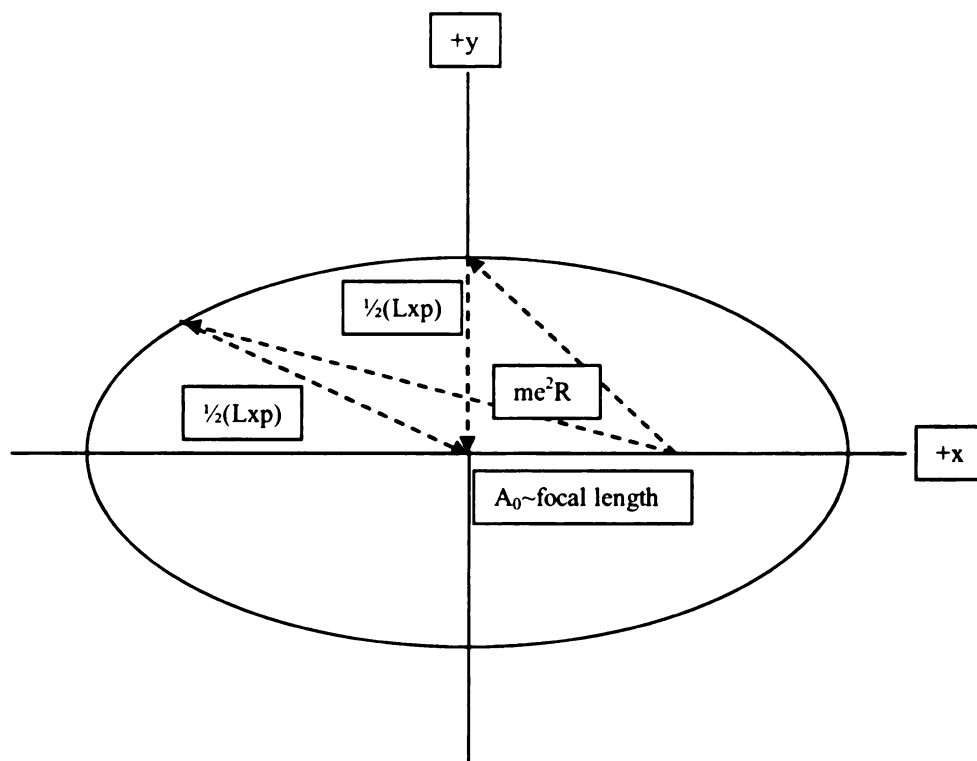$$\vec{A}_0 = \vec{L} \times \vec{p} + mk\hat{R} = \vec{L} \times \vec{p}_0 + mk\hat{R}_0$$

Figure 37 Classical Relationships for Runge-Lenz Vector.

The quantum mechanics form of the Runge-Lenz vector is [65]:

$$\vec{A} = \frac{1}{2}\left(\vec{L} \times \vec{p} - \vec{p} \times \vec{L}\right) + me^2 \hat{R} \tag{6.18}$$

Where,

$$\vec{R} \bullet \vec{A} = \vec{R} \bullet \left[\frac{1}{2}\left(\vec{L} \times \vec{p} - \vec{p} \times \vec{L}\right) + me^2 \hat{R}\right]$$

$$- AR\cos\phi = -\vec{L} \bullet (\vec{R} \times \vec{p}) + me^2 R = -L^2 + me^2 R \tag{6.19}$$

$$\frac{1}{R} = \frac{me^2}{L^2}\left[1 + \frac{A}{me^2}\cos\phi\right] = \frac{me^2}{L^2}[1 + \alpha\cos\phi]$$

$$\alpha \equiv \frac{A}{me^2}$$

Therefore, the Runge-Lenz invariant fixes the eccentricity of the orbital trajectory. Section 6.3.1 and 6.3.3 use Equation 6.19 to develop operators that connect elliptical paths of constant energy, but differing eccentricity.

The Runge-Lenz vector is not independent of the other two invariants, angular momentum and energy. The operator relationships are given as follows:

$$\vec{A} \bullet \vec{L} = 0$$

$$A^2 = 2W(L^2 + 1) + 1 \tag{6.20}$$

141

With units of electron mass and charge, and c=1. The Runge-Lenz vector does not commute with angular momentum L, but upon rescaling:

$$\vec{a} = \frac{1}{\sqrt{-2W}} \vec{A}$$

$$[a_i, a_j] = j\varepsilon_{ijk} L_k$$

$$[L_i, L_j] = j\varepsilon_{ijk} L_k \tag{6.21}$$

$$[L_i, a_j] = j\varepsilon_{ijk} a_k$$

Now, let:

$$J_{1,2} = \frac{1}{2}(L \pm a) \tag{6.22}$$

Equation 6.22 gives,

$$[J_{\alpha,i}, J_{\beta,j}] = j\delta_{\alpha\beta}\varepsilon_{ijk} J_{\alpha,k} \tag{6.23}$$

Linear combinations of the invariants angular momentum and the scaled Runge-Lenz vector yield two uncoupled, commuting angular momenta (J_1, J_2). As a result,

$$J_{1,2}^2 = \frac{1}{4}\left(L^2 \pm L \bullet A \pm A \bullet L + a^2\right)$$

$$= \frac{1}{4}\left(L^2 + a^2\right) = \frac{1}{4}\left(L^2 + \frac{1}{-2W}A^2\right) \tag{6.24}$$

$$= \frac{1}{4}\left(\frac{1}{2W} - 1\right) = \frac{1}{4}(n^2 - 1)$$

Where W is discrete energy, with principle quantum number n. Now, each angular momentum satisfies the previously derived central potential relationships. That is,

$$J_i^2 \mid j_i m_i >= j_i(j_i + 1) \mid j_i m_i >= \frac{1}{2}(n-1)(n+1) \mid j_i m_i >$$

$$J_{z,i} \mid j_i m_i >= m_i \mid j_i m_i > \tag{6.25}$$

$$- j_i \leq m_i \leq j_i$$

6.2.3 Parabolic Energy Levels and Wave Functions

Removing the quadratic Stark effect, solutions to Equations 6.16 are identical. Each equation is equivalent to the Schroedinger equation in spherical coordinates, with m/2 replacing angular momentum l. With the following substitutions:

$$U = e^{-\frac{1}{2}nu} u^{\frac{m}{2}} f_u(u), x = \frac{1}{\sqrt{-2W}} u$$

$$\tag{6.26}$$

$$V = e^{-\frac{1}{2}nv} v^{\frac{m}{2}} f_v(v), y = \frac{1}{\sqrt{-2W}} v$$

The two differential equations can be written as functions of x and y as:

$$\left[x\frac{\partial^2}{\partial x^2} + (m+1-x)\frac{\partial}{\partial x} + \left(\frac{1}{\sqrt{-2W}}Z_u - \frac{1}{2}(m+1) \right) \right] f_u = 0$$

(6.27)

$$\left[y\frac{\partial^2}{\partial y^2} + (m+1-y)\frac{\partial}{\partial y} + \left(\frac{1}{\sqrt{-2W}}Z_v - \frac{1}{2}(m+1) \right) \right] f_v = 0$$

Where Equations 6.27 are of exactly the same form as the reduced differential equation for the radial component of the wave function in spherical coordinates, given in Equation 5.38. As a result, the solutions are:

$$f_u = F(-n_u, m+1, x) = \sum_{p=0}^{\infty} \frac{\Gamma(-n_u + p)}{\Gamma(-n_u)} \frac{\Gamma(m)}{\Gamma(m+p)} \frac{x^p}{p!} \xrightarrow[x \to \infty]{} x^{-n_u - m - 1} e^x$$

$$f_v = F(-n_v, m+1, x) = \sum_{p=0}^{\infty} \frac{\Gamma(-n_v + p)}{\Gamma(-n_v)} \frac{\Gamma(m)}{\Gamma(m+p)} \frac{x^p}{p!} \xrightarrow[x \to \infty]{} x^{-n_v - m - 1} e^x$$

(6.28)

$$n_u = \frac{1}{\sqrt{-2W}}Z_u - \frac{1}{2}(m+1) = nZ_u - \frac{1}{2}(m+1)$$

$$n_v = \frac{1}{\sqrt{-2W}} - \frac{1}{2}(m+1) = nZ_u - \frac{1}{2}(m+1)$$

144

Where the last equality for n_u and n_v holds for the zero perturbation case. Now, $f_{u,v}$ converges if the polynomial is finite, that is:

$$-n_{u,v} = 0,-1,-2,-3,\dots \Rightarrow n_{u,v} = 0,1,2,3,\dots$$

(6.29)

$$\Rightarrow n(Z_u + Z_v) = n = n_u + n_v + m + 1$$

The energy levels in parabolic coordinates are discrete and degenerate, defined by two electric quantum numbers, n_u and n_v, which replace the angular momentum quantum number l found in spherical coordinates. Wave functions in parabolic coordinates are of the same form as the radial component of the wave function in spherical coordinates, both generated by the same differential equation form. The radial component in spherical coordinates and the parabolic wave function are given in the following. The radial component in spherical coordinates is taken directly from Equations 5.37 and 5.39; the parabolic wave function is taken directly from Equations 6.26 and 6.28.

$$R_{n,l} = c_r \rho^l e^{-\frac{1}{2}\rho} F(-(n-l-1),2l+2,\rho)$$

$$\psi_{n_u,n_v,m} = UV$$

(6.30)

$$U = c_p^u u^{\frac{m}{2}} e^{-\frac{1}{2}u} F(-n_u, m+1, u)$$

$$V = c_p^v v^{\frac{m}{2}} e^{-\frac{1}{2}v} F(-n_v, m+1, v)$$

Now, the orthogonality of the radial wave function,

$$\int dr\, r^2 R_{n_i,l_i} R_{n_j,l_j} = \delta_{ij} \tag{6.31}$$

Implies the following inner product relationship for the parabolic wave functions:

$$\begin{cases} \int du\, u^2 U_{n_u^i,m}\, U_{n_v^j,m} = \delta_{ij} \\[4mm] \int dv\, v^2 V_{n_u^i,m}\, V_{n_v^j,m} = \delta_{ij} \end{cases} \tag{6.32}$$

Therefore, the perturbation matrix is diagonal in parabolic coordinates, and the eigenfunctions, or wave functions, do not mix; the parabolic manifold is unchanged [66]. As a result, the allowed transitions and transition amplitudes are tractable.

6.3 *Stark Effect Perturbation*

The linear Stark effect perturbation removes degeneracy from the parabolic wave functions, and further mixes the fine structure of atomic hydrogen in response to the application of a constant value electric field. The next two sections address the Stark effect with respect to both parabolic wave functions (gross structure) and the fine structure of atomic hydrogen, and develop the transition intensities for both gross and fine structure that govern H_α and H_β bands of the atomic hydrogen spectrum. For comparison, transition intensity bar charts are included along side experimental spectra results in Chapter 7.

146

6.3.1 Stark Effect: Parabolic Wave Functions

From the previous sections, specifically Equations 6.16, 6.28, 6.30, and 6.32, the

perturbation matrix elements can be calculated as follows:

$$\delta Z_{n_u,m} = \frac{1}{4}eE \cdot \frac{1}{-2W}\frac{n_u!}{(n_u+m)!^3} \int du\, u^2 \cdot u^m e^{-u}\left[L_{n_u+m}^m(u)\right]^2$$

$$= +\frac{1}{4}eE \cdot \frac{1}{-2W}\left(6n_u^2 + 6n_u m + m^2 + 6n_u + 3m + 2\right)$$

$$\delta Z_{n_v,m} = \frac{1}{4}eE \cdot \frac{1}{-2W}\frac{n_v!}{(n_v+m)!^3} \int dv - v^2 \cdot v^m e^{-v}\left[L_{n_v+m}^m(v)\right]^2 \tag{6.33}$$

$$= -\frac{1}{4}eE \cdot \frac{1}{-2W}\left(6n_v^2 + 6n_v m + m^2 + 6n_v + 3m + 2\right)$$

$$L_{n_u+m}^m(u) = (-1)^m(n_u+m)!\binom{n_u+m}{m}F(-n_u,m+1,u)$$

Where the last equation gives the relationship between the Lagurre polynomials

and the hypergeometric function [67]. Summing Z terms from Equations 6.28 and 6.33,

$$1 = \sqrt{-2W}\left(n_u + \frac{1}{2}(m+1)\right) + \sqrt{-2W}\left(n_v + \frac{1}{2}(m+1)\right)$$

$$+\frac{1}{4}eE \cdot \frac{1}{-2W}\left(6n_u^2 + 6n_u m + m^2 + 6n_u + 3m + 2\right) \tag{6.34}$$

$$-\frac{1}{4}eE \cdot \frac{1}{-2W}\left(6n_v^2 + 6n_v m + m^2 + 6n_v + 3m + 2\right)$$

Which, for small δW, gives [68],

$$1 = \sqrt{-2W} \, n + \frac{3}{2} eEn^2 \cdot n(n_u - n_v)$$

(6.35)

$$\Rightarrow \begin{cases} W = -\dfrac{1}{2n^2} + \dfrac{3}{2} eE \cdot n(n_u - n_v) \\[2mm] n_{u,v} = 0,1,2,3,... \\[2mm] n = n_u + n_v + m + 1 \end{cases}$$

The Stark energy levels in parabolic coordinates exactly match the eigenvalues for spherical coordinates, found in Equation 6.9. Figures 38-39 illustrate the Stark shifted energy levels for atomic hydrogen bands H_α and H_β, and transitions resulting from linear and circular polarization [69].

Wave functions associated with the shifted energy levels are not mixed in parabolic coordinates. Transition amplitudes can be found from direct integration of the unperturbed eigenfunctions. Gordon [70] determines atomic hydrogen transition amplitudes resulting from linear polarization, as represented in parabolic coordinates, in the following:
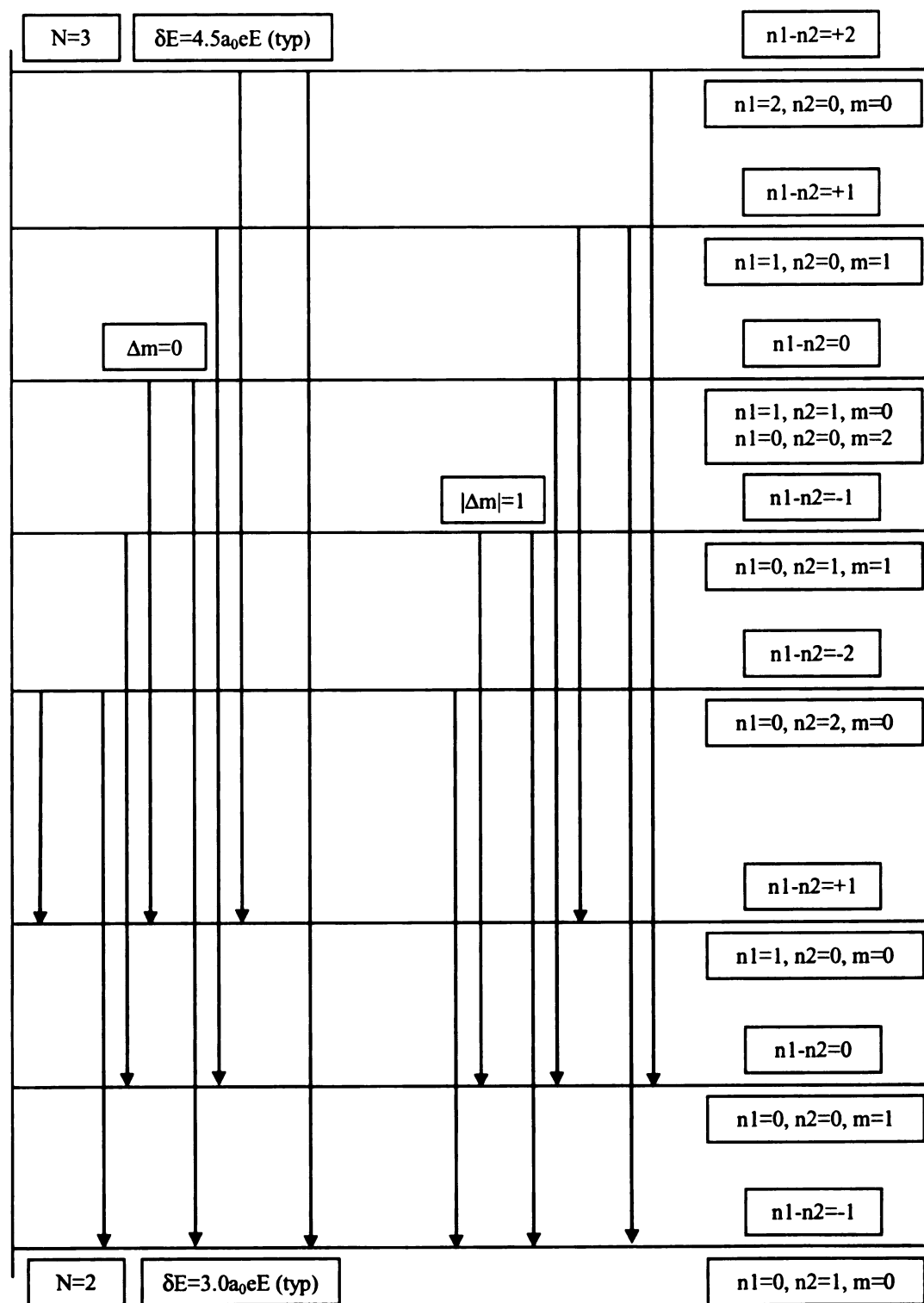
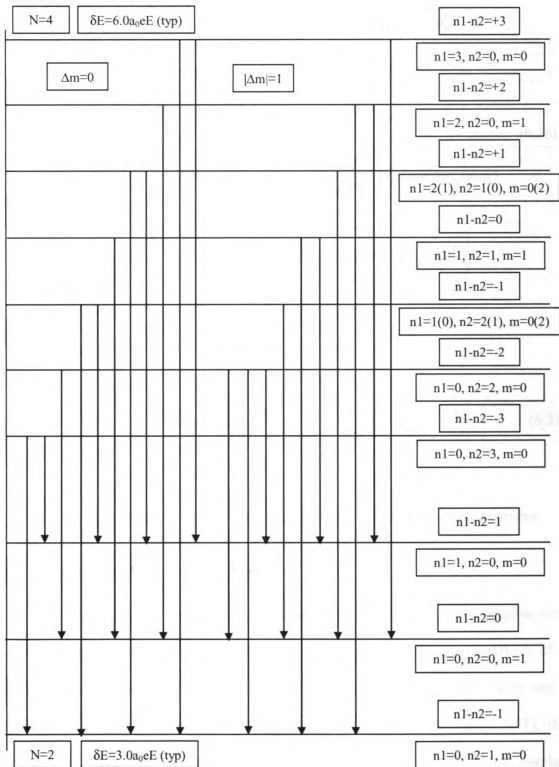**Figure 38** Hα Stark Effect Transitions: Parabolic Coordinates.

149

Figure 39 H$_\beta$ Stark Effect Transitions: Parabolic Coordinates.

150

$$z_{n_u,n_v,m}^{n_u',n_v',m} = (-1)^{n_u'+n_v'} \frac{2a_0}{4m!^2} \sqrt{\frac{(n_u+m)!}{n_u!} \frac{(n_v+m)!}{n_v!} \frac{(n_u'+m)!}{n_u'!} \frac{(n_v'+m)!}{n_u'!}}$$

$$\times \left(\frac{4nn'}{(n-n')^2} \right)^{m+2} \left(\frac{n-n'}{n+n'} \right)^{n+n'}$$

$$\qquad\qquad\qquad\qquad\qquad\qquad\qquad\qquad\qquad\qquad (6.36)$$

$$\times \left\{ \left[(n_1' - n_2') \frac{n^2 + n'^2}{(n+n')^2} - (n_1 - n_2) \frac{2nn'}{(n+n')^2} \right] \psi_m(n_1 n_1') \psi_m(n_1 n_1') \right.$$

$$\left. - [n_1' \psi_m(n_1 n_1' - 1) \psi_m(n_2 n_2') - n_2' \psi_m(n_1 n_1') \psi_m(n_2 n_2' - 1)] \right\}$$

Where,

$$\psi_m(n_i n_i') = F\left(-n_i, -n_i', m+1, \frac{-4nn'}{(n-n')^2} \right) = 1 + \frac{(-n_i)(-n_i')}{(m+1)} \frac{1}{1!} \left[\frac{-4nn'}{(n-n')^2} \right]^1 + \dots \quad (6.37)$$

Figure 63 and Figure 69 in Chapter 8 give the H_α and H_β transition intensities.

6.3.2 Stark Effect: Fine Structure

The Stark effect on the fine structure of atomic hydrogen, which is negligible with respect to Stark splitting in high external fields, is important under conditions of a relatively low applied electric fields (<1000 V/cm) [60]. Energy level shifts are a function of the atomic hydrogen non-degenerate fine structure (Equation 5.71), the associated Clebsch-Gordan coefficients (Equation 5.53), and results from overlap integrals similar to those calculated in section 6.1.1 (Equation 6.5). Calculating the energy perturbation elements for states defined by total angular momentum (njm):

$$\partial E = <\psi_{n,j-1/2,m} \mid z \mid \psi_{n,j+1/2,m}>$$

$$=<R_{n,j-1/2} \mid R \mid R_{n,j+1/2}> \qquad (6.38)$$

$$\cdot \left\{ \begin{array}{l} < \dfrac{\sqrt{j+m}}{\sqrt{2j}} Y^*_{j-1/2,m-1/2} \mid \cos\theta \mid \dfrac{\sqrt{j-m+1}}{\sqrt{2j+2}} Y_{j+1/2,m-1/2} > \\[4mm] < \dfrac{\sqrt{j-m}}{\sqrt{2j}} Y^*_{j-1/2,m+1/2} \mid \cos\theta \mid \dfrac{-\sqrt{j+m+1}}{\sqrt{2j+2}} Y_{j+1/2,m+1/2} > \end{array} \right.$$

The inner product of the radial waveforms can be found in closed form with the use of the generating function for Laguerre polynomials, namely:

$$\dfrac{(-1)^r}{(1-t)^{r+1}} e^{-\frac{xt}{1-t}} = \sum_{k=r}^{\infty} L^r_k(x) \dfrac{t^{k-r}}{k!} \qquad (6.39)$$

Where the radial waveforms are given by,

$$R_{n,l}(R) = \sqrt{\dfrac{(n-l-1)!}{(n+l)!^3 (2n)}} \left(\dfrac{2}{n}\right)^{3/2} e^{-R/n} \left(\dfrac{2R}{n}\right)^l L^{2l+1}_{n+l}\left(\dfrac{2R}{n}\right)$$

$$\qquad (6.40)$$

$$R_{n,l-1}(R) = \sqrt{\dfrac{(n-l)!}{(n+l-1)!^3 (2n)}} \left(\dfrac{2}{n}\right)^{3/2} e^{-R/n} \left(\dfrac{2R}{n}\right)^l L^{2l-1}_{n+l-1}\left(\dfrac{2R}{n}\right)$$

Substituting,

$$L_{n+l}^{2l+1}(\rho) = \frac{(n+l)!}{(n-l-1)!} \frac{d^{n-l-1}}{d\alpha^{n-l-1}} \left[\frac{e^{-\rho\frac{\alpha}{1-\alpha}}}{(1-\alpha)^{2l+2}} \right]_{\alpha=0}$$

(6.41)

$$L_{n+l-1}^{2l-1}(\rho) = \frac{(n+l-1)!}{(n-l)!} \frac{d^{n-l}}{d\beta^{n-l}} \left[\frac{e^{-\rho\frac{\beta}{1-\beta}}}{(1-\beta)^{2l}} \right]_{\beta=0}$$

Which gives,

$$< R_{n,l-1} | R | R_{n,l} > = \frac{1}{4} \frac{\sqrt{n^2-l^2}}{(n+l)!(n-l)!} \cdot$$

$$\cdot \int_{\rho=0}^{\infty} d\rho \rho^{2l+2} e^{-\rho} \frac{d^{n-l-1}}{d\alpha^{n-l-1}} \left[\frac{e^{-\rho\frac{\alpha}{1-\alpha}}}{(1-\alpha)^{2l+2}} \right]_{\alpha=0} \cdot \frac{d^{n-l}}{d\beta^{n-l}} \left[\frac{e^{-\rho\frac{\beta}{1-\beta}}}{(1-\beta)^{2l}} \right]_{\beta=0}$$

$$= \frac{1}{4} \frac{\sqrt{n^2-l^2}}{(n+l)!(n-l)!} \cdot \frac{d^{n-l-1}}{d\alpha^{n-l-1}} \frac{d^{n-l}}{d\beta^{n-l}} \frac{\int_{\rho=0}^{\infty} d\rho \rho^{2l+2} e^{-\rho\left(1+\frac{\alpha}{1-\alpha}+\frac{\beta}{1-\beta}\right)}}{(1-\alpha)^{2l+2}(1-\beta)^{2l}}$$

$$= \frac{1}{4} \frac{\sqrt{n^2-l^2}}{(n+l)!(n-l)!} (2l+2)! \frac{d^{n-l-1}}{d\alpha^{n-l-1}} \frac{d^{n-l}}{d\beta^{n-l}} \left[\frac{(1-\alpha)(1-\beta)^3}{(1-\alpha\beta)^{2l+3}} \right]_{\alpha=\beta=0}$$

(6.42)

153

Now, using differentials of the geometric series,

$$\frac{1}{N!}\frac{d^N}{d(\alpha\beta)^N} = \frac{1}{(1-\alpha\beta)^{N+1}} = \sum_{i=0}^{\infty}\frac{(N+i)!}{N!i!}(\alpha\beta)^i \tag{6.43}$$

Equation 6.42 is reduced to:

$$< R_{n,l-1} \mid R \mid R_{n,l} >= \frac{1}{4}\frac{\sqrt{n^2-l^2}}{(n+l)!(n-l)!} \cdot$$

$$\cdot \sum_{i=0}^{\infty}\frac{(2l+2+i)!}{i!}\frac{d^{n-l-1}}{d\alpha^{n-l-1}}\left[\alpha^i(1-\alpha)\right]_{\alpha=0} \cdot \frac{d^{n-l}}{d\beta^{n-l}}\left[\beta^i(1-\beta)^3\right]_{\beta=0} \tag{6.44}$$

$$= -\frac{3}{2}n\sqrt{n^2-l^2}$$

And,

$$< R_{n,j-1/2} \mid R \mid R_{n,j+1/2} >= -\frac{3}{2}n\sqrt{n^2-(j+1/2)^2} \tag{6.45}$$

The inner product of the angular waveforms relies on the identity given in Equation 5.78, and repeated here:

$$\cos\theta \cdot Y_{l,m} = \sqrt{\frac{(l+m+1)(l-m+1)}{(2l+1)(2l+3)}}Y_{l+1,m} + \sqrt{\frac{(l+m)(l-m)}{(2l+1)(2l-1)}}Y_{l-1,m} \tag{6.46}$$

154

And the orthogonality of the waveforms. As a result,

$$< Y^*_{j-1/2,m\pm1/2} \,|\cos\theta|\, Y_{j+1/2,m\pm1/2} > = \frac{1}{2}\sqrt{\frac{(j \mp m)(j \pm m + 1)}{j(j+1)}} \qquad (6.47)$$

Using Equations 6.38, 6.45, and 6.47, the fine structure perturbation matrix elements connecting each orbital pair (njm) can be expressed explicitly by the following [70]:

$$\partial E_{njm} = < \psi_{n,j-1/2,m} \,|\, z \,|\, \psi_{n,j+1/2,m} >$$

$$\partial E_{njm} = eEa_0 \cdot \frac{\frac{3}{2}n\sqrt{n^2-(j+1/2)^2}}{2\sqrt{j(j+1)}} \frac{[(j+m)(j-m+1)-(j-m)(j+m+1)]}{2\sqrt{j(j+1)}} \qquad (6.48)$$

$$= eEa_0 \cdot \frac{3}{4}\frac{\sqrt{n^2-(j+1/2)^2}}{j(j+1)} nm$$

Thus, each fine structure energy level is split into 2j+1 equally spaced energy levels, identified by magnetic quantum number m, where $- j \le m \le +j$. The uppermost energy level in each fine structure element (j=n-1/2) remains degenerate. The Stark effect energy level shifts in the atomic hydrogen H_α fine structure line are summarized in Figure 40. The fine structure Stark effect is critically important to the spectral analysis of data in Chapter 7.
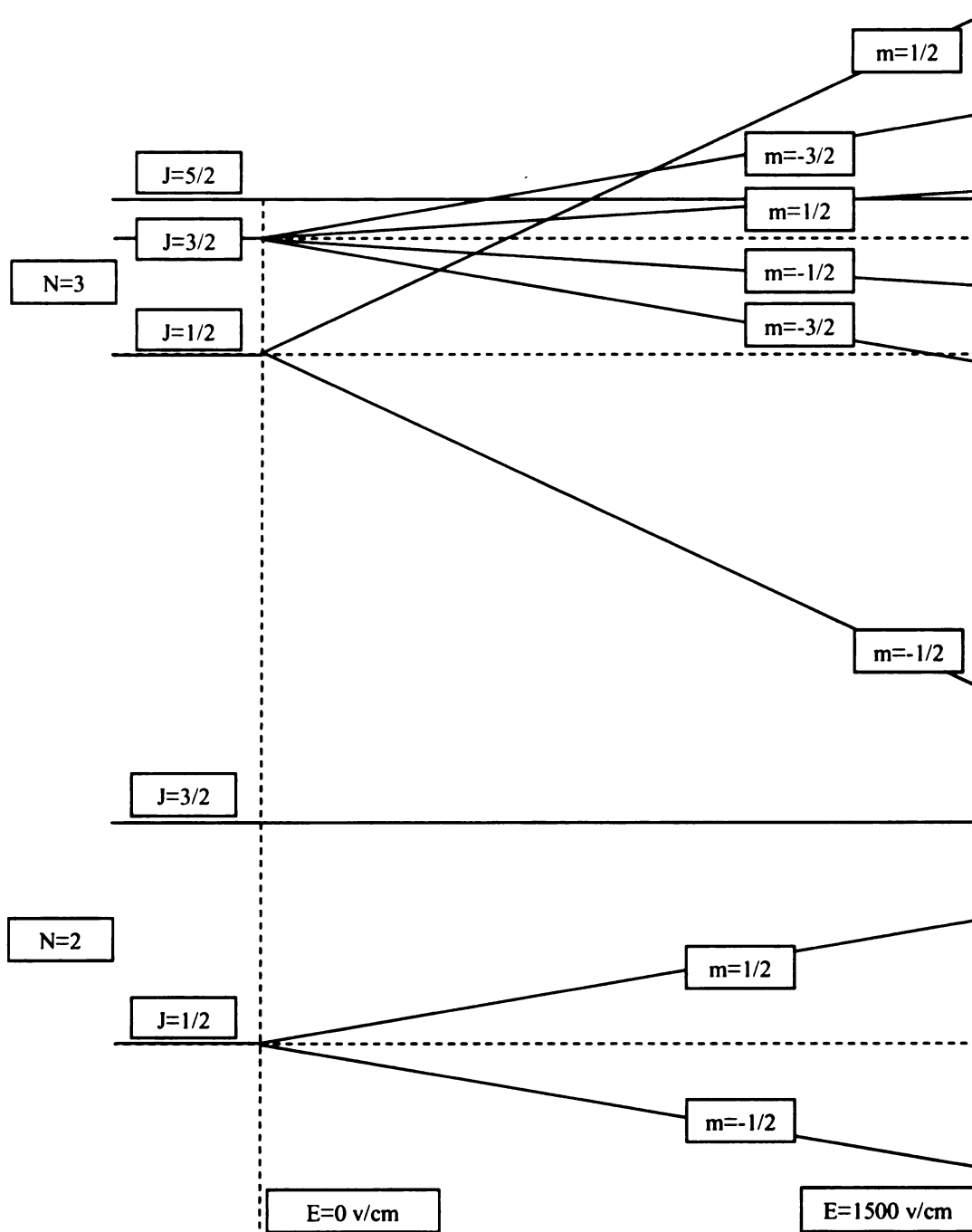
Figure 40 Hα Stark Effect Fine Structure Splitting.

156

6. 4 *Coordinate Transforms*

Connecting spherical and parabolic coordinates requires the development in section 6.2.2, which generates two uncoupled, commuting angular momenta that are operators for the coulombic central force problem in *any* coordinate system in which R_z is separable, given stationary L_z. Consequently, spherical and parabolic coordinates are connected by ladder operators that follow in form the ladder operators developed for angular momentum in section 5.2.1.1.

In the next sections, the ladder operators in parabolic coordinates are developed; then, the ladder operators are shown as the connection between parabolic and spherical coordinates, generating the associated Clebsch-Gordan coefficients [71]. Finally, semi-parabolic coordinates are used to represent the angular momentum operators found in parabolic coordinates as two coupled, two dimensional harmonic oscillators (Schwinger) acting in three dimensional Lorentz space SO(2,1), for constant L_z [60]; that is, oscillators composing angular momenta on the hyperboloid surfaces described in section 6.2.1.

6.4.1 Parabolic Ladder Operators

The angular momentum operators in parabolic coordinates, and their associated properties, are developed in section 6.2.2, and given in Equation 6.25. With the additional constraint of Equation 6.35,

157

$$J_i^2 \mid j_i m_i >= j_i(j_i + 1) \mid j_i m_i >= \frac{1}{2}(n-1)(n+1) \mid j_i m_i >$$

$$J_{z,i} \mid j_i m_i >= m_i \mid j_i m_i >$$

(6.49)

$$-j_i \leq m_i \leq j_i$$

$$n = n_1 + n_2 + m + 1$$

Where u is replaced by 1, and v is replaced by 2 in the last equation to match the angular momenta notation. Now, the angular momentum operators in parabolic coordinates exactly mirror the angular momentum operator developed in section 5.2.2.1. Consequently, ladder operators in parabolic coordinates can be composed in an identical way, and the ladder operators themselves, with exception given to the additional constraint of Equation 6.38, yield identical results. That is,

$$J_{1,2}^{\pm} = J_{1,2}^x \pm j J_{1,2}^y$$

(6.50)

And,

$$J_1^{\pm} \mid n_1, n_2, m_1, m_2 >= \sqrt{\frac{1}{4}(n^2 - 1) - m_1(m_1 \pm 1)} \mid n_1 \mp 1, n_2, m_1 \pm 1, m_2 >$$

(6.51)

$$J_2^{\pm} \mid n_1, n_2, m_1, m_2 >= \sqrt{\frac{1}{4}(n^2 - 1) - m_2(m_2 \pm 1)} \mid n_1, n_2 \mp 1, m_1, m_2 \pm 1 >$$

Where,

$$n = n_1 + n_2 + m + 1$$

(6.52)

$$m = m_1 + m_2$$

But, m_1 and m_2 are arbitrary. Setting them equal, and using Equation 6.28,

$$n_1 = \frac{1}{2}(n-1) - m_1$$

(6.53)

$$n_1 = \frac{1}{2}(n-1) - m_1$$

Which results in the following ladder operators in parabolic coordinates [72],

$$J_1^+ \mid n,n_1,n_2,m >= \sqrt{n_1(n-n_1)} \mid n,n_1-1,n_2,m+1 >$$

$$J_1^- \mid n,n_1,n_2,m >= \sqrt{(n_1+1)[n-(n_1+1)]} \mid n,n_1+1,n_2,m-1 >$$

(6.54)

$$J_2^+ \mid n,n_1,n_2,m >= \sqrt{n_2(n-n_2)} \mid n,n_1,n_2-1,m+1 >$$

$$J_2^- \mid n,n_1,n_2,m >= \sqrt{(n_2+1)[n-(n_2+1)]} \mid n,n_1,n_2+1,m-1 >$$

By symmetry, the operators H, L_z, and A_z commute in parabolic coordinates. Consequently, the Stark perturbation potential can be expressed in terms of the rescaled

Runge-Lenz vector a such that it commutes with H and L_z, and its eigenvalues are equal to the Stark energy level shifts found in Equation 6.35.

$$V_{Stark} = eEz, r \rightarrow \frac{3}{2}na$$

$$\Rightarrow V_{Stark} \mid n, n_1, n_2, m > = \frac{3}{2}eEna_z \mid n, n_1, n_2, m >$$

$$= \frac{3}{2}eEn(J_{1,z} - J_{2,z}) \mid n, n_1, n_2, m > \qquad (6.55)$$

$$= \frac{3}{2}eEn(m_1 - m_2) \mid n, n_1, n_2, m >$$

$$= \frac{3}{2}eEn(n_2 - n_1) \mid n, n_1, n_2, m >$$

Mixing $J_{1,2}$ in SO(3) x SO(3) space generates a single three dimensional angular momentum operator λ in SO(4), defined as follows [60]:

$$\lambda = (\lambda_x, \lambda_y, \lambda_z) = (j_{1,x} - j_{2,x}, j_{1,y} - j_{2,y}, j_{1,z} + j_{2,z})$$

$$[\lambda_i, \lambda_j] = j\varepsilon_{ijk}\lambda_k$$

$$\lambda^2 \mid j_1^2 j_2^2 \lambda^2 \lambda_z > = \lambda(\lambda + 1) \mid j_1^2 j_2^2 \lambda^2 \lambda_z > \qquad (6.56)$$

$$\lambda_z \mid j_1^2 j_2^2 \lambda^2 \lambda_z > = m \mid j_1^2 j_2^2 \lambda^2 \lambda_z >$$

$$-\lambda \leq \lambda_z \leq \lambda$$

Motivation for this transform is given in section 6.2.1. The rotation operator $R_\alpha = e^{j\alpha\lambda x}$ connects ellipses with constant energy (W) but different eccentricity (α), where $\alpha = A/me^2$, as given in section 6.2.2.

6.4.2 Clebsch-Gordan Coefficients

Wave functions in spherical and parabolic coordinates each have exactly one state in which the shared quantum number m is a maximum. That is,

$$| n, l = n-1, m = n-1 >_{spherical} \equiv | n, n_1 = 0, n_2 = 0, m = n-1 >_{parabolic} \qquad (6.57)$$

As a result, these states are identical functions in both coordinate systems. Operating on each side of Equation 6.57 with its prescribed ladder operator L⁻ yields:

$$L^- | n, l = n-1, m = n-1 >_{spherical} = \sqrt{2(n-1)} | n, l = n-1, m = n-2 >_{spherical}$$

$$L^- | n, n_1 = 0, n_2 = 0, m = n-1 >_{parabolic}$$

$$= (J_1^- + J_2^-) | n, n_1 = 0, n_2 = 0, m = n-1 >_{parabolic}$$

$$= \sqrt{n-1} | n, n_1 = 1, n_2 = 0, m = n-2 >_{parabolic}$$

$$+ \sqrt{n-1} | n, n_1 = 0, n_2 = 1, m = n-2 >_{parabolic}$$

$$(6.58)$$

Setting the spherical and parabolic results equal generates the expected Clebsch-Gordan coefficients $\pm 1/\sqrt{2}$, matching results from eigenvalue/eigenvector calculations, and mechanizing the process.

The following tables give Clebsch-Gordan coefficients, transforming from spherical to parabolic coordinates, for constant values of n-m= 2, 3, and 4, respectively [73]-[74]. The rows are defined by parabolic quantum number n_1, the columns by the spherical quantum number t=l-m.

$n - m = 2$:

	0	1
0	$\dfrac{1}{\sqrt{2}}$	$\dfrac{1}{\sqrt{2}}$
1	$\dfrac{1}{\sqrt{2}}$	$\dfrac{-1}{\sqrt{2}}$

$n - m = 3$:

	0	1	2
0	$\sqrt{\dfrac{m+2}{2(2m+3)}}$	$\dfrac{1}{\sqrt{2}}$	$\dfrac{1}{2}\sqrt{\dfrac{m+1}{2(2m+3)}}$
1	$\sqrt{\dfrac{m+1}{2m+3}}$	0	$\sqrt{\dfrac{m+2}{2m+3}}$
2	$\sqrt{\dfrac{m+2}{2(2m+3)}}$	$\dfrac{-1}{\sqrt{2}}$	$\sqrt{\dfrac{m+1}{2(2m+3)}}$

$n - m = 4$:

$$
\begin{array}{c|cccc}
 & 0 & 1 & 2 & 3 \\
\hline
0 & \dfrac{1}{2}\sqrt{\dfrac{m+3}{2m+3}} & \dfrac{1}{2}\sqrt{\dfrac{3m+9}{2m+5}} & \dfrac{1}{2}\sqrt{\dfrac{3m+3}{2m+3}} & \dfrac{1}{2}\sqrt{\dfrac{m+1}{2m+5}} \\[3ex]
1 & \dfrac{1}{2}\sqrt{\dfrac{3m+3}{2m+3}} & \dfrac{1}{2}\sqrt{\dfrac{m+1}{2m+5}} & \dfrac{-1}{2}\sqrt{\dfrac{m+3}{2m+3}} & \dfrac{-1}{2}\sqrt{\dfrac{3m+9}{2m+5}} \\[3ex]
2 & \dfrac{1}{2}\sqrt{\dfrac{3m+3}{2m+3}} & \dfrac{-1}{2}\sqrt{\dfrac{m+1}{2m+5}} & \dfrac{-1}{2}\sqrt{\dfrac{m+3}{2m+3}} & \dfrac{1}{2}\sqrt{\dfrac{3m+9}{2m+5}} \\[3ex]
3 & \dfrac{1}{2}\sqrt{\dfrac{m+3}{2m+3}} & \dfrac{-1}{2}\sqrt{\dfrac{3m+9}{2m+5}} & \dfrac{1}{2}\sqrt{\dfrac{3m+3}{2m+3}} & \dfrac{-1}{2}\sqrt{\dfrac{m+1}{2m+5}}
\end{array}
\tag{6.59}
$$

Such that:

$$
\phi_{n_1,n_2,m} = \sum_{l=|m|}^{n_1+n_2} C^{l,m}_{j_1,m_1,j_2,m_2} \, \psi_{n,l,m}
\tag{6.60}
$$

Where ϕ and Ψ are the parabolic and spherical wave functions, respectively.

6.4.3 Semi-Parabolic Coordinates

Returning to the original parabolic transform given in Equations 6.10 and 6.11, the Schroedinger equation for a central coulombic potential can be written:

$$
\frac{1}{2}\left[\frac{1}{\xi\eta(\xi^2+\eta^2)}\left\{ \frac{\partial}{\partial\xi}\left(\xi\eta\frac{\partial}{\partial\xi}\right) + \frac{\partial}{\partial\eta}\left(\xi\eta\frac{\partial}{\partial\eta}\right) \right\} + \frac{1}{\xi^2\eta^2}\frac{\partial^2}{\partial\theta^2} \right]\psi
$$
$$
+ \left[W + \frac{2}{(\xi^2+\eta^2)} \right]\psi = 0
\tag{6.61}
$$

And is easily separable, for constant $L_z=m$, into the following:

$$\left[\frac{\partial^2}{\partial\xi^2}+\frac{1}{\xi}\frac{\partial}{\partial\xi}-\frac{m^2}{\xi^2}+2W\xi^2+4Z_1\right]F(\xi)=0$$

$$\left[\frac{\partial^2}{\partial\eta^2}+\frac{1}{\eta}\frac{\partial}{\partial\eta}-\frac{m^2}{\eta^2}+2W\eta^2+4Z_2\right]G(\eta)=0 \qquad (6.62)$$

$$Z_1+Z_2=1$$

In units of electron charge and mass, $c=1$. Each differential equation in Equation 6.62 represents a two dimensional oscillator in polar coordinates. The angular momentum (m^2), potential energy (W), and charge fractions ($Z_{1,2}$) connect the two equations. For a harmonic oscillator with unit frequency, operators for the first of the two equations can be written:

$$p=\frac{\partial}{\partial\xi}\xi\equiv D\xi$$

$$V\equiv\xi^2 \qquad (6.63)$$

$$H-V=\frac{1}{\xi}\frac{\partial}{\partial\xi}\xi\frac{\partial}{\partial\xi}-\frac{m^2}{\xi^2}\equiv\frac{1}{\xi^2}\xi D\xi D-\frac{m^2}{\xi^2}$$

Where D is shorthand for the first derivative with respect to ξ. As a result:

$$[p \pm 1, V(H-V)] = 0$$

$$[p \pm 1, V](H-V) = -V[p, H-V]$$

(6.64)

$$[p \pm 1, V] = [\xi D, V] = \xi[D,V] + [\xi,V]D = 2V$$

$$\Rightarrow [p \pm 1, H-V] = -2(H-V)$$

And,

$$[(H-V),V] = \frac{1}{\xi} D\xi D\xi \cdot \xi - \xi \cdot D\xi D\xi \frac{1}{\xi} = (p+1)^2 - (p-1)^2 = 4p \qquad (6.65)$$

Combining Equations 6.64 and 6.65 [75],

$$[p,H] = (-H + 2V) \equiv S_\xi$$

$$[H,(-H+2V)] = 4p \equiv S_\eta \qquad (6.66)$$

$$[(-H+2V),p] = -H \equiv -S_\omega$$

And, identical operators (T_i) can be developed for the second equation in Equation 6.62. Physically, S and T are each angular momentum in SO(2,1) space, fixed to the common hyperboloid $L_z = m$, precessing independently about the common axis $n = \eta$,

perpendicular to the plane of motion. Figure 41 presents this physical interpretation [60]; that is, the orbital mechanics in semi-parabolic coordinates.

Mixing operators S and T in SO(2,1) x SO(2,1) generates a new set of three dimensional operators (W) in SO(3) that commute with L_z, and with λ^2, from Equation 6.56.

$$W \equiv (S_\xi - T_\xi, S_\eta - T_\eta, S_\omega + T_\omega) \tag{6.67}$$

Where (S^2, T^2, W^2, W_z) *all* commute with L_z and λ^2. Consequently, the rotation operator $R_\alpha = e^{j\alpha S_\eta}$, analogous to the rotation operator defined in section 6.4.1, connects ellipses with constant energy but different eccentricity. Physically, mixing operators S and T rotates the normal vector n to n' in Figure 41 [60]; the orbital plane intersecting the hyperboloid. As a result, the operator W represents all elliptical orbital paths in semi-parabolic coordinates, whereas S and T each represented strictly circular paths about the η axis.

Stark and Zeeman splitting can be combined by way of the S and T vectors in semi-parabolic coordinates, and this is necessary for analysis of the fine structure of atomic hydrogen for large applied magnetic fields. For this experiment, Zeeman splitting in the fine structure is negligible [60], due to the relatively low level of the magnetic fields, as determined from the rotational spectrum of molecular hydrogen.
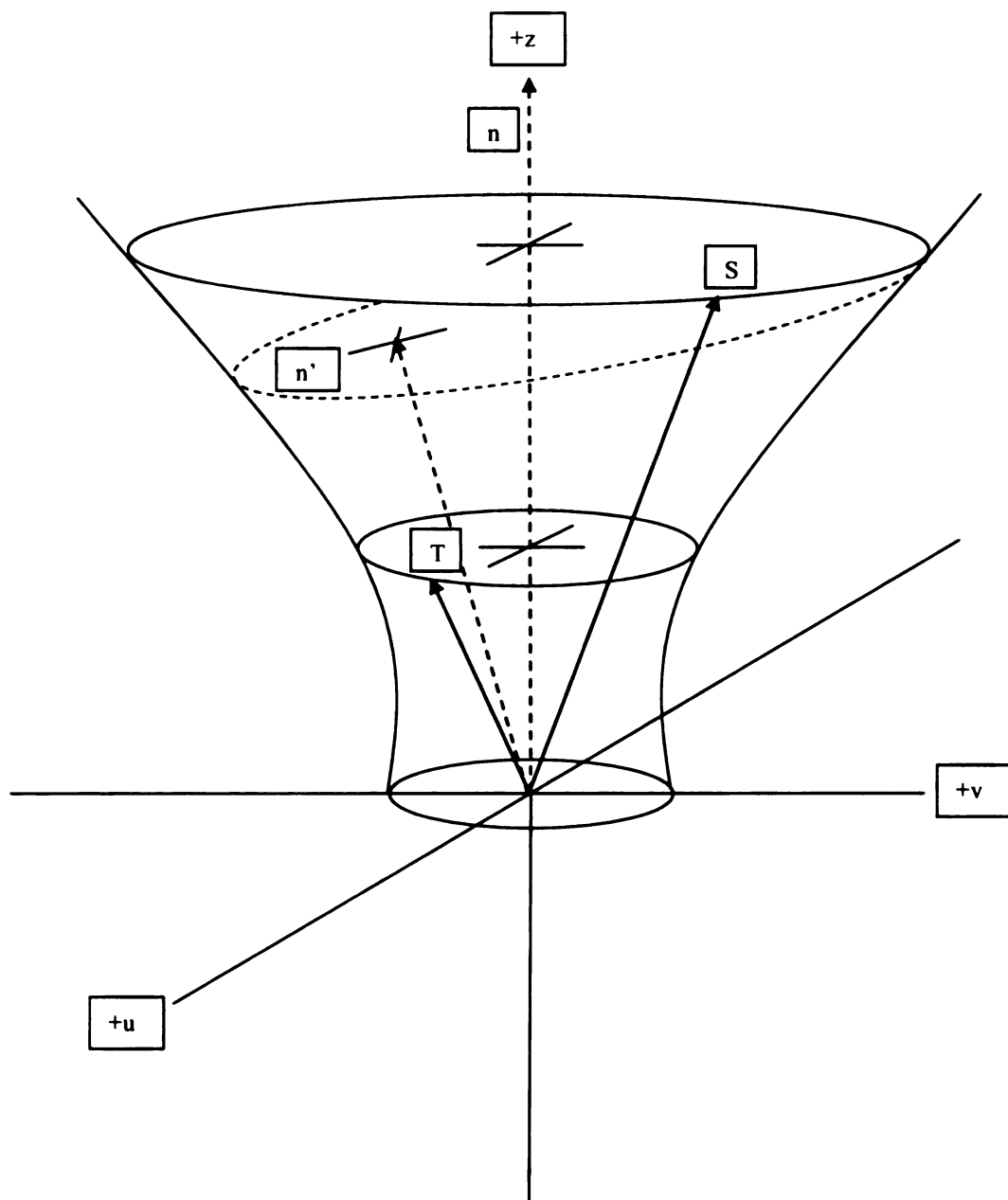
Figure 41 Semi-Parabolic Coordinate Representation of Stark, Zeeman Effect [60].

167

Chapter 7 Results

Results concentrate on matching the spectroscopy readings with theory presented in the previous three chapters. The first section gives spectrometer set-up background, critical in assembling high-resolution scans with as low signal-to-noise ratio as possible. The next section ties the spectrometer readings from Argon to the electron density for Argon, and determines how accurately the measurements for Argon fit the global model presented in Chapter 4.

The final sections examine both diatomic and atomic hydrogen spectroscopy results. The spectroscopy readings are interpreted according to theory presented in Chapter 5 and Chapter 6; calculations are made as to the temperature, electron density, and electric and magnetic field strengths of the hydrogen plasma. From these calculations, conclusions are drawn in the final chapter, Chapter 8, as to the nature of the hydrogen plasma contraction, which begins to occur at pressures as low as 5 Torr.

7. 1 *Spectrometer Set-Up*

Initially, thirteen 1 mm diameter fiber optic channels were focused on the plasma center and available to project the plasma emission through the spectrometer slit. Focusing multiple channels to the spectrometer slit increased the signal to the spectrometer, but drastically reduced the resolution.

Next, one fiber optic channel was set less than 0.25 mm from the slit. Steadily increasing the distance from the slit had the predictable result of reducing signal-to-noise and increasing resolution. Maximum spectrometer resolution of 0.3 A (FWHM) was

reached at a distance of 8 mm, nearly matching the manufacturers specification for a light cone of ratio 9:1.

Accelerating voltage was adjusted to increase signal-to-noise. Figure 42 shows the spectrometer step response to accelerating voltage supplied to the photomultiplier tube (PMT); each step represents a 100 Volt increase in accelerating voltage, from 0 V to 900 V. Evident is a definite nonlinear response, beginning at approximately 500 V. The noise response of the spectrometer is consistent with an older PMT [76].

The response is extremely sensitive to both accelerating voltage and the time derivative (dI/dt) of the excitation signal. Reducing the accelerating voltage to the point that maximized the PMT nonlinear response magnified dI/dt, and allowed the PMT to effectively operate as a detector.

At low accelerating voltages, signal-to-noise was decreased by the accuracy of the pico-ammeter. The pico-ammeter resolution was specified at 10^{-14} A, but the accuracy – the random signal error- was an order of magnitude worse. As a result, several experiments needed to be run for each test case to determine the best accelerating voltage setting to maximize signal-to-noise.

Even after determining the accelerating voltage, the signal still suffered from undershoot. Consistently, sharp drops (0.2 pA) in signal occurred after consecutive readings with high slope (dI/dt). To determine the fidelity of these responses, it was necessary to slow the spectrometer to the slowest accurate scan rate. Scan rates lower than 1 A/minute produced data with less resolution and more noise than slightly higher scan rates; that is, the motor control for the spectrometer mirror was not as accurate for the lowest scan rates.
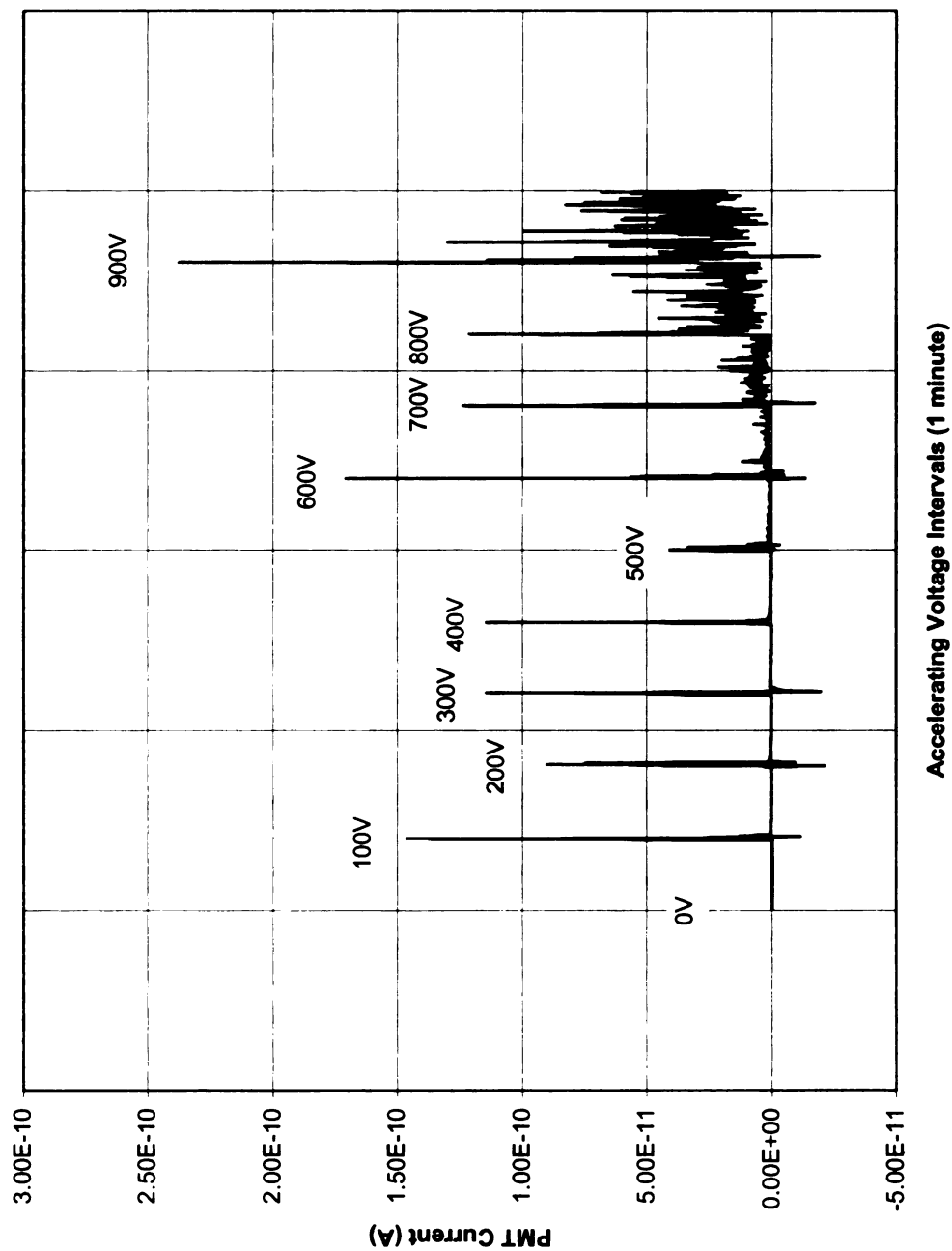
Figure 42 PMT Noise Response.

170

All of the aforementioned adjustments allowed for resolution fine enough to correlate fine structure peaks present in atomic hydrogen spectra, providing a signature for each spectrum. Peaks could be identified that were separated by as little as 0.08 cm^{-1}, approximately 0.04 A. at the H_α line (6562.85 A.) –7.5 times better than the FWHM resolution of the spectrometer. Evidence for resolution of this order is demonstrated in the atomic hydrogen H_α peaks, presented in Section 7.4.1.1.

The line shape of the spectral responses appeared to have first-order decay at the trailing edge; although not universal, often enough for concern. Reducing the accelerating voltage did effect a change, but did not eliminate the decay from the hydrogen rotational band. To determine whether the decay was real or measurement error, all measurements were run forward and backward. In each case, with the reduced accelerating voltages, the forward and backward curves matched exactly; the data was real, and the fine structure peaks were further confirmed.

7.2 Argon Results

The electron density is measured experimentally and compared to the global model predictions for Argon. Gas temperatures for the Argon plasmas in this study are taken from Rogers [77]. The theoretical and experimental data can be expected to diverge at higher pressures (>100 torr), as convective flows begin to dominate diffusion as the major transport mechanism [77].

The first section presents the results from the global model, based on experimental inputs. The next section summarizes the set of experiments run to determine the electron density for the Argon plasma and compares the experimental

171

results for electron density to the global model. The final section suggests an alternative model for electron density based on the line shape of the Argon spectrum at 4300.1 A.

7.2.1 Global Model Results

The global model predicts electron density and electron temperature as a function of input power, pressure, gas concentrations, and plasma geometry. In this case, the global model prediction for electron density will be compared with experimental values. The tables in Tables 1-3 and the plots given in Figures 43-44 summarize the global model results.

7.2.2 Argon Spectroscopy Measurements

Hydrogen was added to the argon plasma at a ratio of 1:25. Stark broadening in the atomic Hydrogen beta (H_β) spectrum was used to determine the electron density for the argon plasma, a result first calculated by Griem [22],[78], and parameterized by Nikolic, et al [79]. The following summarizes the electron density estimate:

$$N_e = \left[3.99x10^8 \bullet \left(\frac{\Delta\lambda_{Stark}}{\alpha} \right) \right]^{\frac{3}{2}} cm^{-3}$$

$$\Delta\lambda_{Stark} = \sqrt{\Delta\lambda^2 - \Delta\lambda_{FS}^2 - \Delta\lambda_{Instrument}^2}$$

$$\alpha = 0.0762 \tag{7.1}$$

$$\Delta\lambda_{FS} = 0.077A$$

$$\Delta\lambda_{Instrument} = 0.30$$

Table 1 Global Model Predictions for Argon Plasmas.

R (mm)	L (mm)	P (torr)	Tg (K)	ng(1/cm3)	Lambda(cm)	P region	HR	hL	Deff(cm)	ngdeff(1/m2)	Te (eV)
5	5	0.001	300	3.22E+13	3.030303	Low	0.425	0.425	0.2941176	9.47059E+16	13
5	5	0.01	300	3.22E+14	0.3030303	Moderate	0.061538462	0.0930069	1.6176475	5.20883E+18	3.5
5	5	0.1	300	3.22E+15	0.030303	Moderate	0.01967081	0.0298871	5.0446069	1.62436E+20	2.1
5	5	1	300	3.22E+16	0.0030303	High	n/a	n/a	0.1263754	4.06929E+19	1.8
5	5	10	493	1.959E+17	0.000303	High	n/a	n/a	0.1263754	2.47624E+20	1.2
5	5	100	493	1.959E+18	3.03E-05	High	n/a	n/a	0.1263754	2.47624E+21	0.75
5	5	200	600	3.22E+18	1.515E-05	High	n/a	n/a	0.1263754	4.06929E+21	0.65
5	5	500	900	5.367E+18	6.061E-06	High	n/a	n/a	0.1263754	6.78215E+21	0.5

R (mm)	L (mm)	P (torr)	Tion (eV)	uB (m/sec)	D (m2/sec)	Aeff (m2,m)	Ecollision (eV)	Etotal (eV)	Pabs (W)	Te (eV)	ne (1/cm3)
5	5	0.001	0.026	5575.6245	n/a	0.0001335	22	115.6	40	13	2.90503E+12
5	5	0.01	0.026	2893.0495	n/a	2.428E-05	40	65.2	40	3.5	5.4596E+13
5	5	0.1	0.026	2240.9465	n/a	7.785E-06	70	85.12	40	2.1	1.68362E+14
5	5	1	0.026	2074.7133	0.5231109	0.0675611	110	122.96	40	1.8	5.75288E+13
5	5	10	0.0427267	1693.9963	0.0272044	0.0675611	200	208.64	40	1.2	6.51937E+14
5	5	100	0.0427267	1339.2217	0.0017003	0.0675611	1000	1005.4	40	0.75	2.16463E+15
5	5	200	0.052	1246.7475	0.0006679	0.0675611	2000	2004.68	40	0.65	2.76381E+15
5	5	500	0.078	1093.4699	0.0001678	0.0675611	4000	4003.6	40	0.5	5.50848E+15

Table 2 Global Model Predictions for Argon Plasmas.

R (mm)	L (mm)	P (torr)	Tg (K)	ng(1/cm3)	Lambda(cm)	P region	HR	hL	deff(cm)	ngdeff(1/m2)	Te (eV)
5	10	0.001	300	3.22E+13	3.030303	Low	0.425	0.425	0.3921569	1.26275E+17	10.2
5	10	0.01	300	3.22E+14	0.3030303	Moderate	0.061538462	0.0663504	2.6395342	8.4993E+18	3.25
5	10	0.1	300	3.22E+15	0.030303	Moderate	0.01967081	0.0211525	8.2652641	2.66142E+20	1.9
5	10	1	300	3.22E+16	0.0030303	High	n/a	n/a	0.1740627	5.60482E+19	1.8
5	10	10	493	1.959E+17	0.000303	High	n/a	n/a	0.1740627	3.41064E+20	1.1
5	10	100	493	1.959E+18	3.03E-05	High	n/a	n/a	0.1740627	3.41064E+21	0.9
5	10	200	600	3.22E+18	1.515E-05	High	n/a	n/a	0.1740627	5.60482E+21	0.7
5	10	500	900	5.367E+18	6.061E-06	High	n/a	n/a	0.1740627	9.34136E+21	0.6

R (mm)	L (mm)	P (torr)	Tion (eV)	uB (m/sec)	D (m2/sec)	Aeff (m2.m)	Ecollision (eV)	Etotal (eV)	Pabs (W)	Te (eV)	ne (1/cm3)
5	10	0.001	0.026	4938.8055	n/a	0.0002003	22	95.44	40	10.2	2.64824E+12
5	10	0.01	0.026	2787.8122	n/a	2.976E-05	40	63.4	40	3.25	4.75363E+13
5	10	0.1	0.026	2131.5653	n/a	9.502E-06	75	88.68	40	2	1.39182E+14
5	10	1	0.026	2074.7133	0.5231109	0.0712264	100	112.96	40	1.9	5.93992E+13
5	10	10	0.0427267	1621.878	0.0249374	0.0712264	185	192.92	40	1.1	7.29576E+14
5	10	100	0.0427267	1467.0439	0.0020403	0.0712264	900	906.48	40	0.9	1.89775E+15
5	10	200	0.052	1293.8111	0.0007192	0.0712264	1500	1505.04	40	0.7	3.24247E+15
5	10	500	0.078	1197.8363	0.0002013	0.0712264	2500	2504.32	40	0.6	6.96093E+15

174

Table 3 Global Model Predictions for Argon Plasmas.

R (mm)	L (mm)	P (torr)	Tg (K)	ng(1/cm3)	Lambda(cm)	P region	HR	hL	deff(cm)	ngdeff(1/m2)	Te (eV)
5	15	0.001	300	3.22E+13	3.030303	Low	0.425	0.425	0.441765	1.42059E+17	10.2
5	15	0.01	300	3.22E+14	0.3030303	Moderate	0.061538462	0.0543369	3.1387024	1.01066E+19	2.3
5	15	0.1	300	3.22E+15	0.030303	Moderate	0.01967081	0.0172762	9.8310872	3.16561E+20	2
5	15	1	300	3.22E+16	0.0030303	High	n/a	n/a	0.1906143	6.13778E+19	1.8
5	15	10	493	1.959E+17	0.000303	High	n/a	n/a	0.1906143	3.73496E+20	1
5	15	100	493	1.959E+18	3.03E-05	High	n/a	n/a	0.1906143	3.73496E+21	0.75
5	15	200	600	3.22E+18	1.515E-05	High	n/a	n/a	0.1906143	6.13778E+21	0.7
5	15	500	900	5.367E+18	6.061E-06	High	n/a	n/a	0.1906143	1.02296E+22	0.65

R (mm)	L (mm)	P (torr)	Tion (eV)	uB (m/sec)	D (m2/sec)	Aeff (m2,m)	Ecollision (eV)	Etotal (eV)	Pabs (W)	Te (eV)	ne (1/cm3)
5	15	0.001	0.026	4938.8055	n/a	0.000267	22	95.44	40	10.2	1.98618E+12
5	15	0.01	0.026	2345.2317	n/a	3.753E-05	65	81.56	40	2.3	3.48214E+13
5	15	0.1	0.026	2186.9399	n/a	1.198E-05	85	99.4	40	2	9.59705E+13
5	15	1	0.026	2074.7133	0.5231109	0.0890908	100	112.96	40	1.8	4.74885E+13
5	15	10	0.0427267	1546.4	0.0226704	0.0890908	800	807.2	40	1	1.53344E+14
5	15	100	0.0427267	1339.2217	0.0017003	0.0890908	1000	1005.4	40	0.75	1.64153E+15
5	15	200	0.052	1293.8111	0.0007192	0.0890908	1500	1505.04	40	0.7	2.5923E+15
5	15	500	0.078	1246.7475	0.0002181	0.0890908	2000	2004.68	40	0.65	6.41739E+15
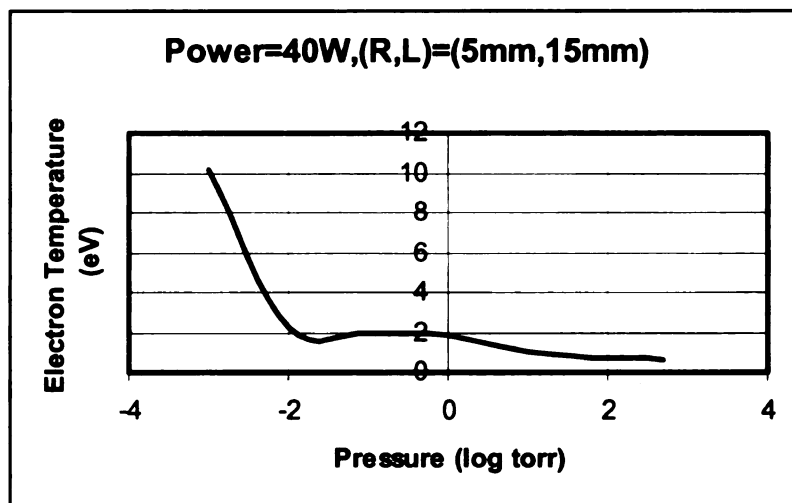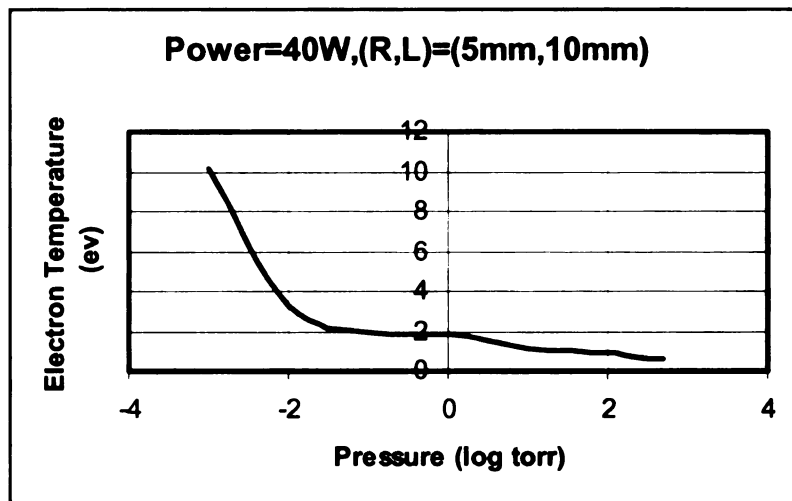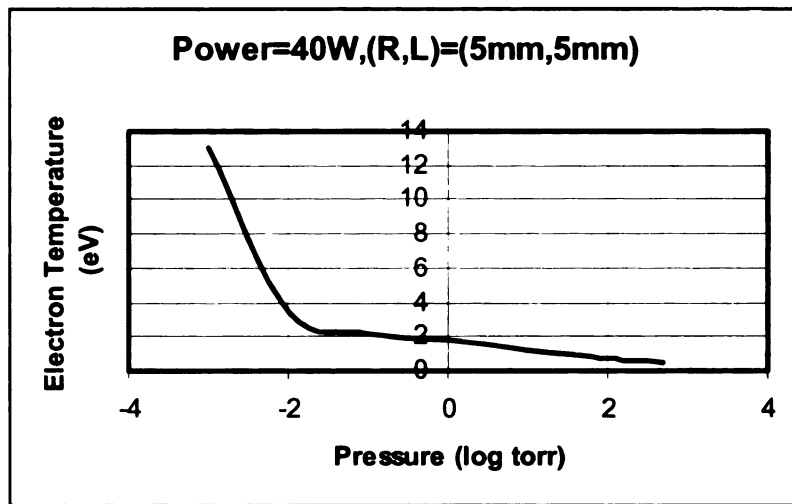
Figure 43 Global Model Predictions for Argon Plasma Electron Temperature.

Power=40W,(R,L)=(5mm,5mm)

Electron Temperature (eV) vs Pressure (log torr)

Power=40W,(R,L)=(5mm,10mm)

Electron Temperature (ev) vs Pressure (log torr)

Power=40W,(R,L)=(5mm,15mm)
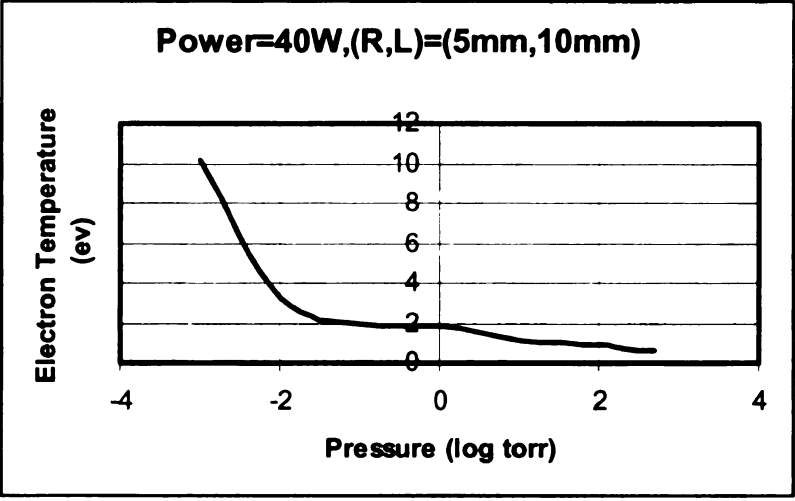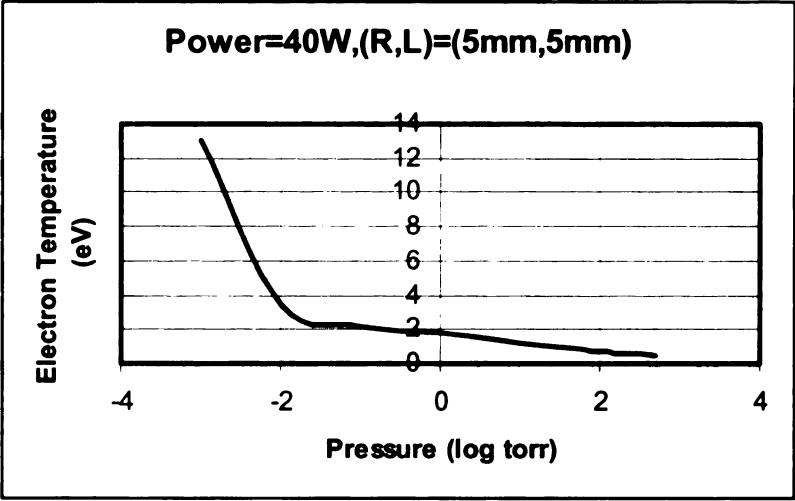
Electron Temperature (eV) vs Pressure (log torr)
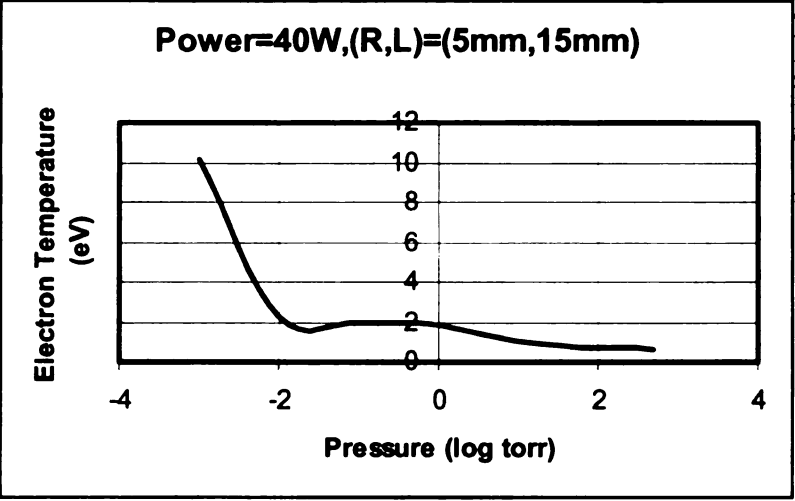
Figure 44 Global Model Predictions for Argon Plasma Electron Density.

Equation 7.1 is specified for the Hydrogen beta (H_β) line in plasmas with approximate electron temperatures of 5000K, and electron densities on the order of 10^{14}-10^{15} cm^{-3}; $\Delta\lambda, \Delta\lambda_{FS}, \Delta\lambda_{Instrumental}$ are full-width half-maximum (FWHM) line widths for the spectrum, fine structure, and spectrometer resolution, respectively. The H_β spectrum is shown in Figure 45 for a pressure of 100 Torr. Figure 46 plots both the Stark broadened electron density from experiment and the global model prediction for pressure ranging from 100 mtorr to 100 Torr.

7.2.3 Argon 4300.1 A Line Shape

Argon spectroscopy concentrated on the Ar*->Ar transition at 4300.1 A. In all readings, accelerating voltage for the photomultiplier tube was set to 300 V. Figure 47 demonstrates the Argon line shape at 4300.1 A, with a pressure of 100 Torr. The wavelength shift from center of the lower (L1) and upper (L2) sidelobes are plotted against pressure in Figures 48-49, as suggested by Milosavljevic, et al [80]. The L1 curve is similar to the theoretical electron density plotted in Figure 46; the L2 curve is similar to the electron density plotted in Figure 46 for experimental data.

7.3 Hydrogen Results: Diatomic Hydrogen

Hydrogen results are divided into two categories: diatomic and atomic hydrogen. First, spectrographic data is used to find the rotational temperature of molecular hydrogen; calculations are made for data both within a single vibration band and within a single rotation band. Then, Zeeman splitting applied to the fine structure of the rotational spectrum is used to estimate the internal magnetic field of the hydrogen plasma.
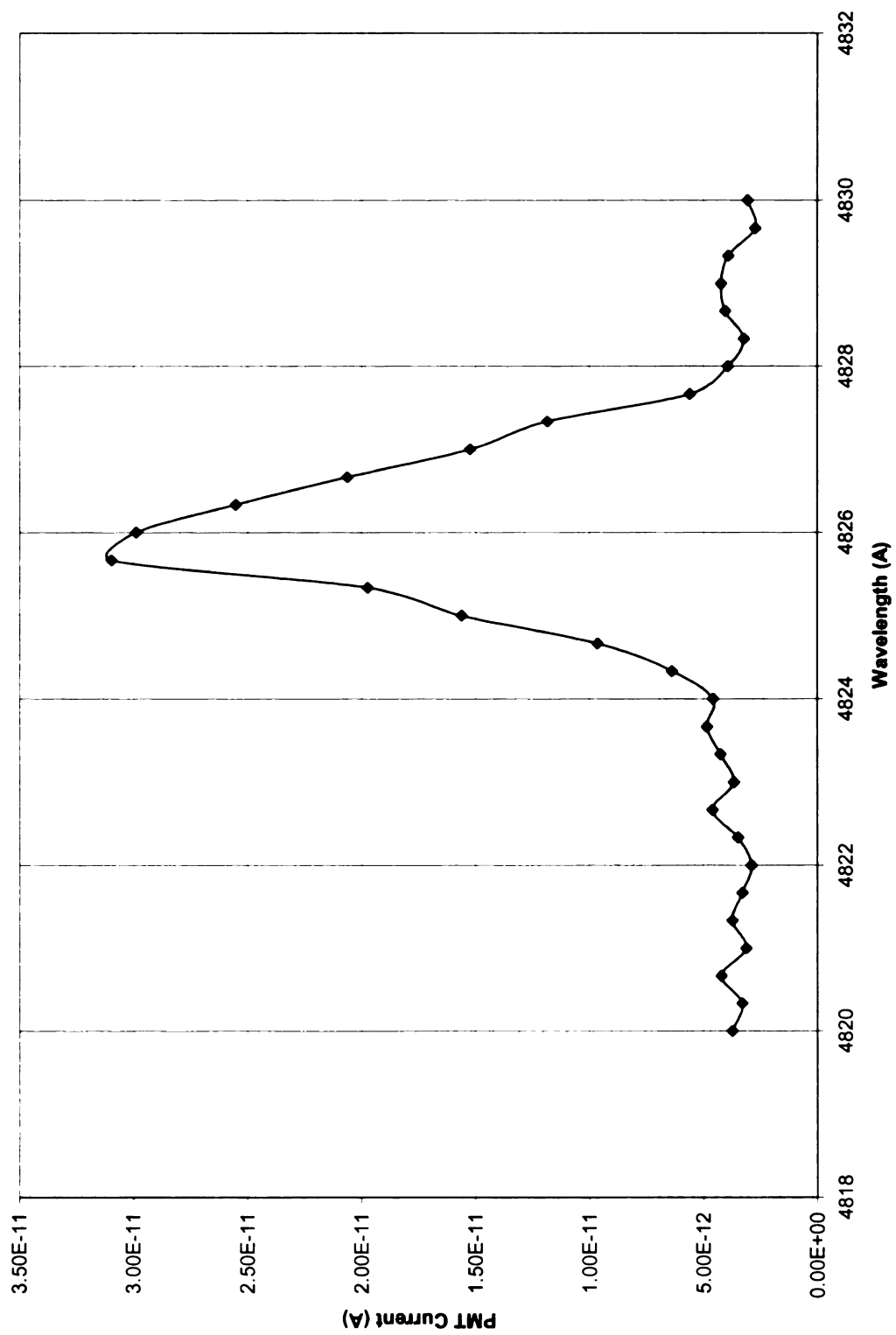
Figure 45 H$_\beta$ Line, P=100 T, 60 W., FWHM=2.025 A.

179
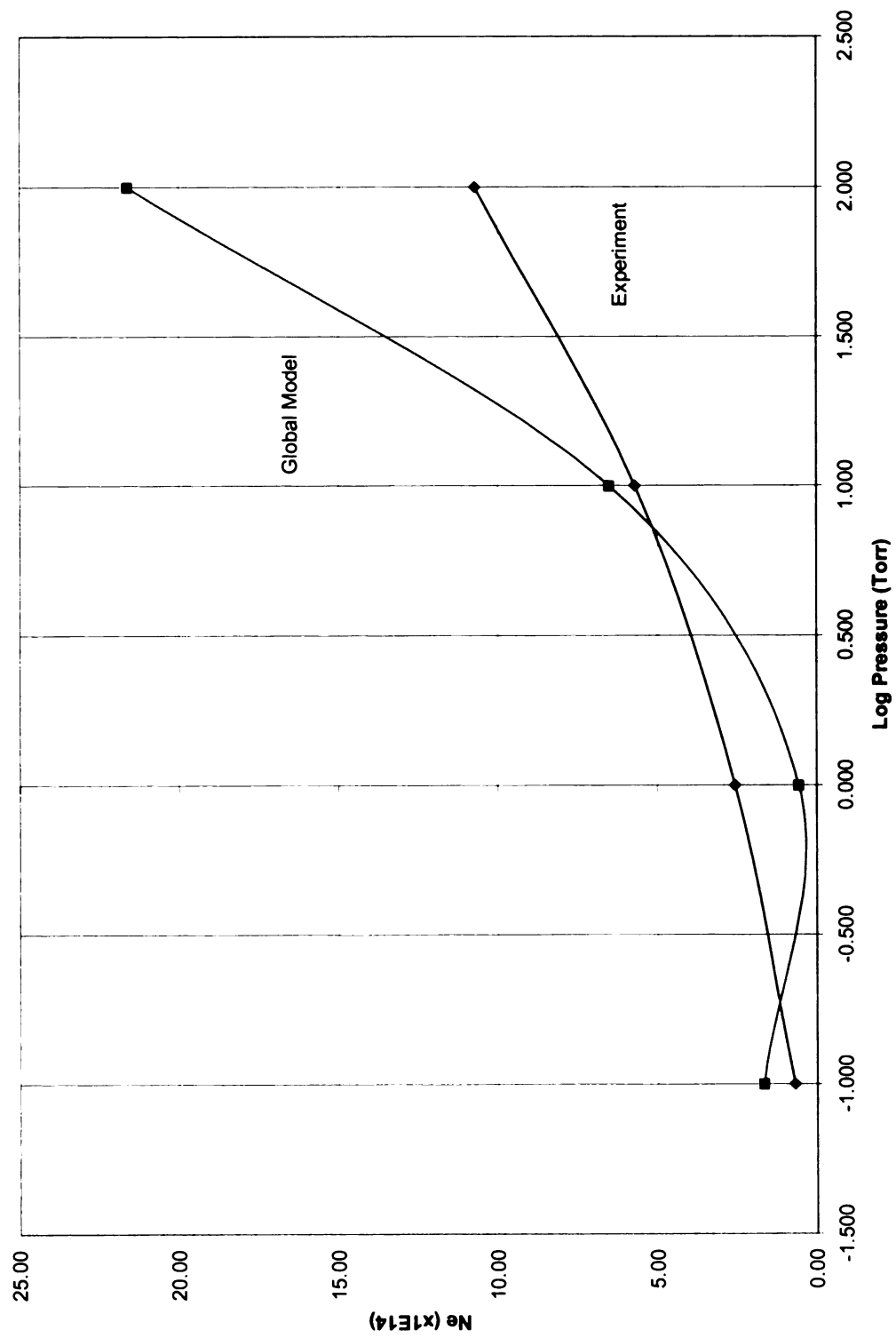
Figure 46 Argon Electron Density (40 W).

180
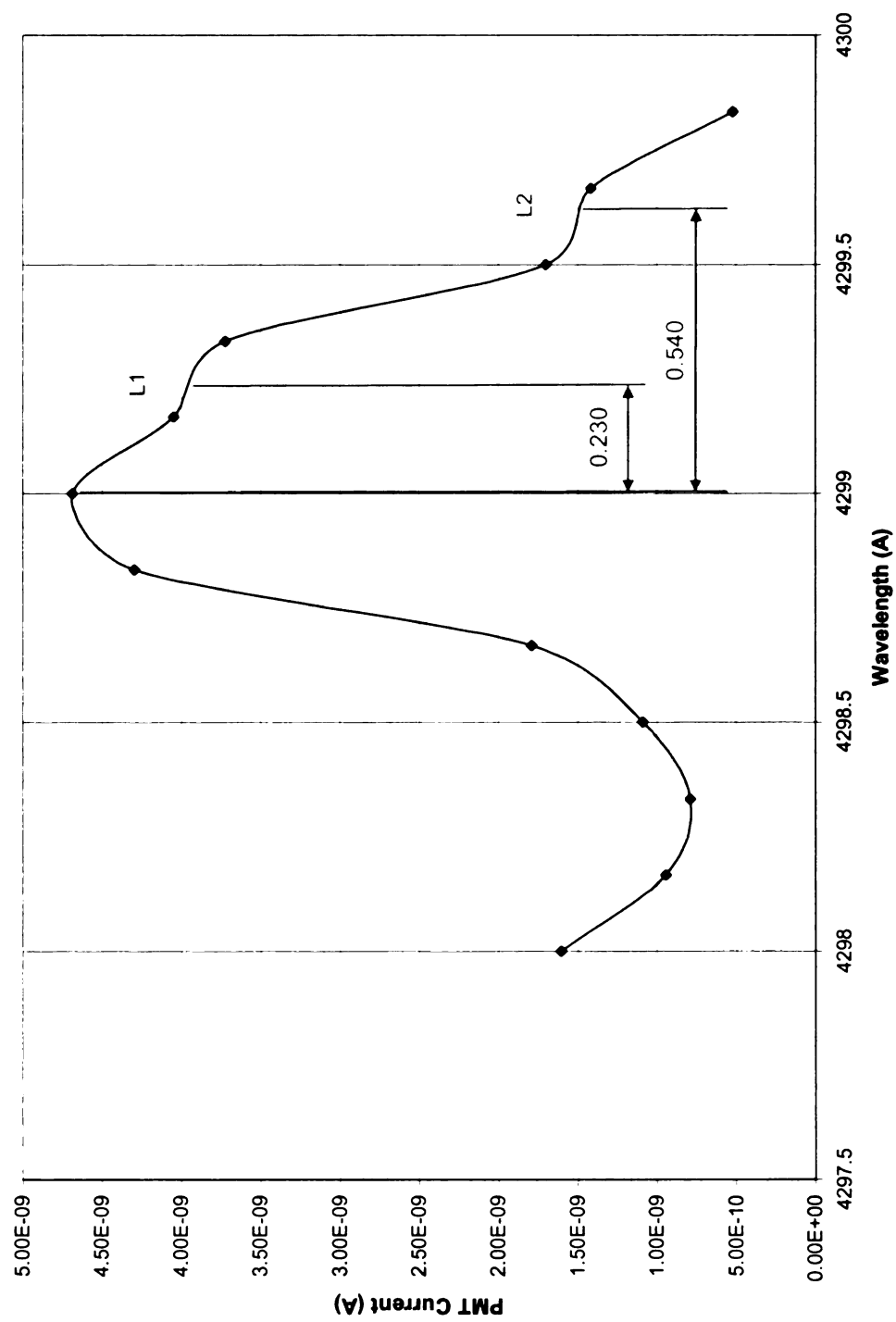
Figure 47 Argon Line Shape, 4300.1 A., 100 Torr.
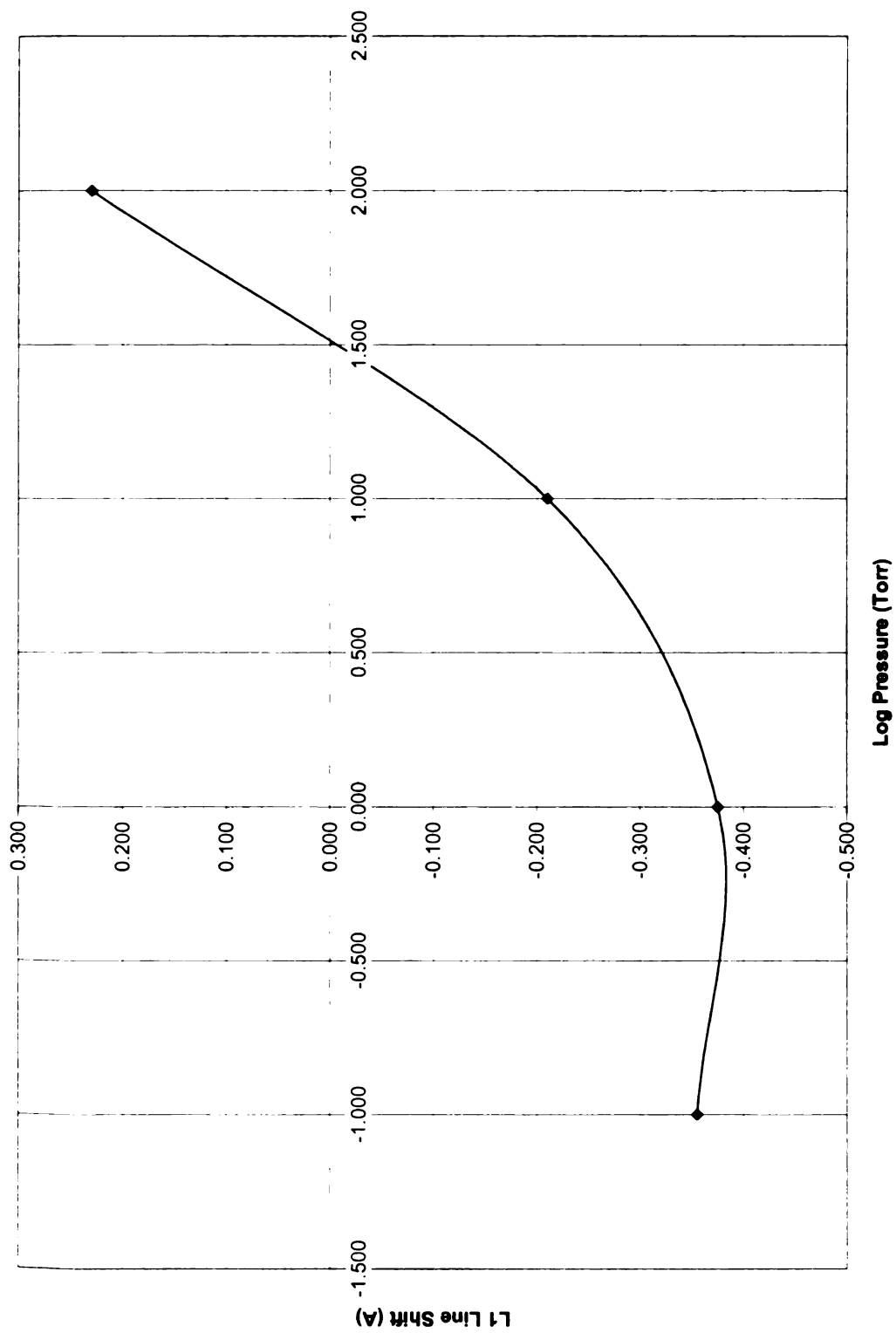
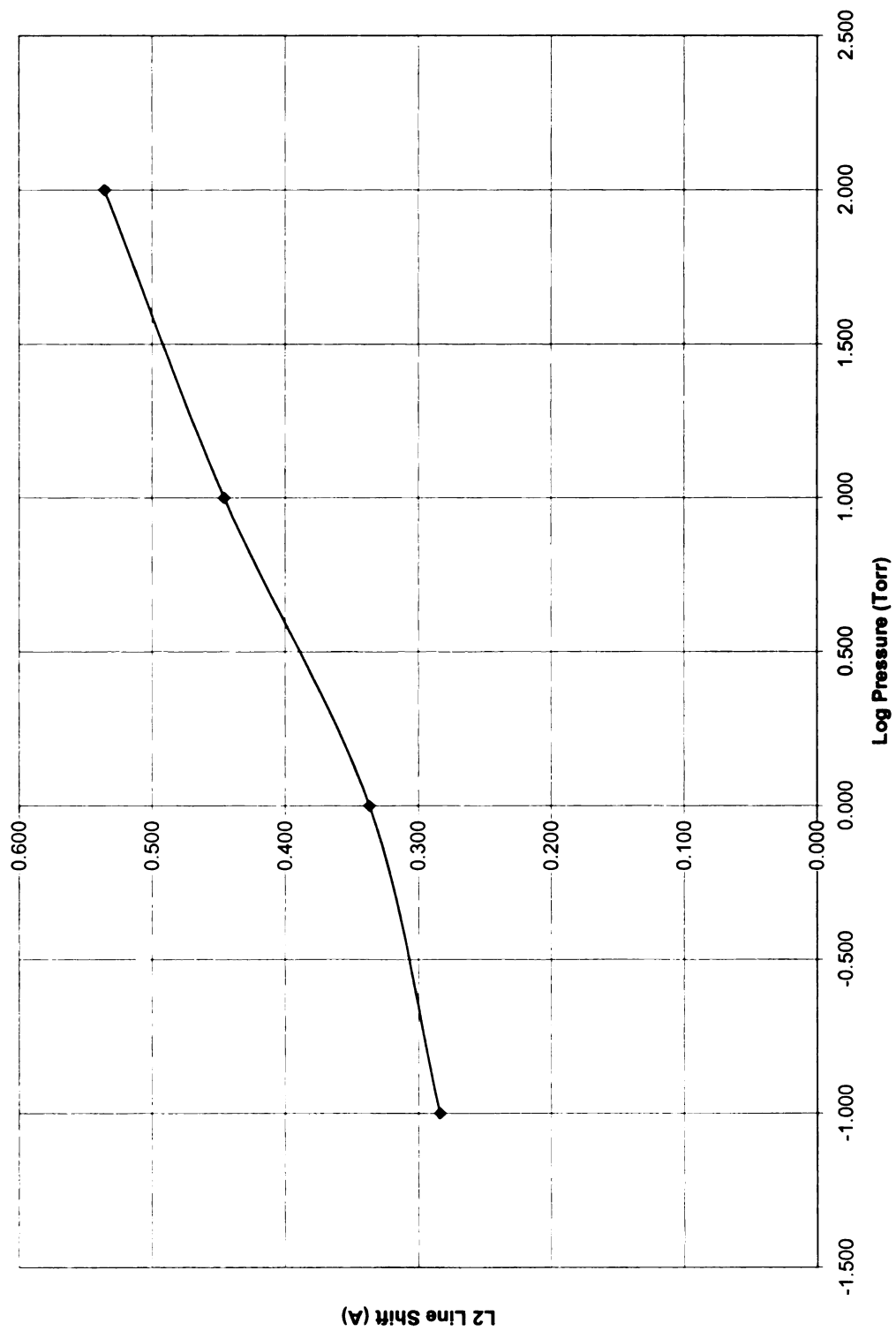181

Figure 48 Argon Line Shape L1.

182

Figure 49 Argon Line Shape L2.

183

7.3.1 Diatomic Hydrogen: Rotational Spectrum

Diatomic hydrogen spectroscopy concentrates on the rotational transitions in the first vibration band of the electronic transition Σ_u-Σ_g; that is, the excited ground state -or 1s state- of H_2 to the ground state of H_2. Transitions in this region emit photons in the visible spectrum, from 4540-4600 A. In this region, the fine structure is simplified, as there is no orbital angular momentum (l=0) intrinsic to the molecule.

First, rotational temperature calculations are made based on the intensity of peaks across the band of rotational transitions (interband transitions). Next, temperature is calculated based on populations in fine structure peaks within a single rotation transition (intraband transitions). Energy differences for fine structure transitions are small, and provide linear temperature curves. Finally, the curves will be compared across the pressure regime.

7.3.1.1 Diatomic Hydrogen Temperature: Interband Transitions

Allowed diatomic hydrogen transitions are prescribed in Figure 27, section 5.7. Relative transition line strengths are a function of the rotational level of the upper vibration band [53]. Relative populations in the upper band (J') are a function of the rotational energy term and rotational inertia of H_2. As a result, the relative line intensity for an approximate Boltzmann distribution is given in the following formula:

$$I \propto (J'+1)e^{-\left(\frac{B_{v'}J'(J'+1)hc}{kT_r}\right)}$$

(7.2)

The H_2 rotational spectrum is very difficult to analyze, as can be seen in Figure 50; it is difficult to identify transition peaks. Table 4 gives a hypothesis set of transition peaks. Transitions that lose one unit of angular momentum (R branch) emit photons of shorter wavelength (higher energy) than the band center; transitions that gain one unit of angular momentum (P branch) emit photons of longer wavelength (lower energy) than the band center.

The lowest energy transition (highest emitted wavelength) in H_2 is not the ground transition. This is due to the rotational inertia increase in H_2 from 20.0 cm^{-1} to 28.4 cm^{-1} in transitions from Σ_u to Σ_g [53]; that is, the excited state electrons, concentrated at the center of the molecule, effectively pull in the protons, reducing the rotational inertia.

In H_2, a nonlinear centrifugal stretching term reduces the rotational energy at low frequencies; that is, the rotational inertia of the protons increases proportional to $J(J+1)$, the rotational energy of the electrons decreases proportional to $J^2(J+1)^2$ [81].

The Fortrat diagram, which plots quantum number as a function of transition energy, is one available test to confirm transition peak identification. The Fortrat diagram is defined by the set of equations given in the following [82]:
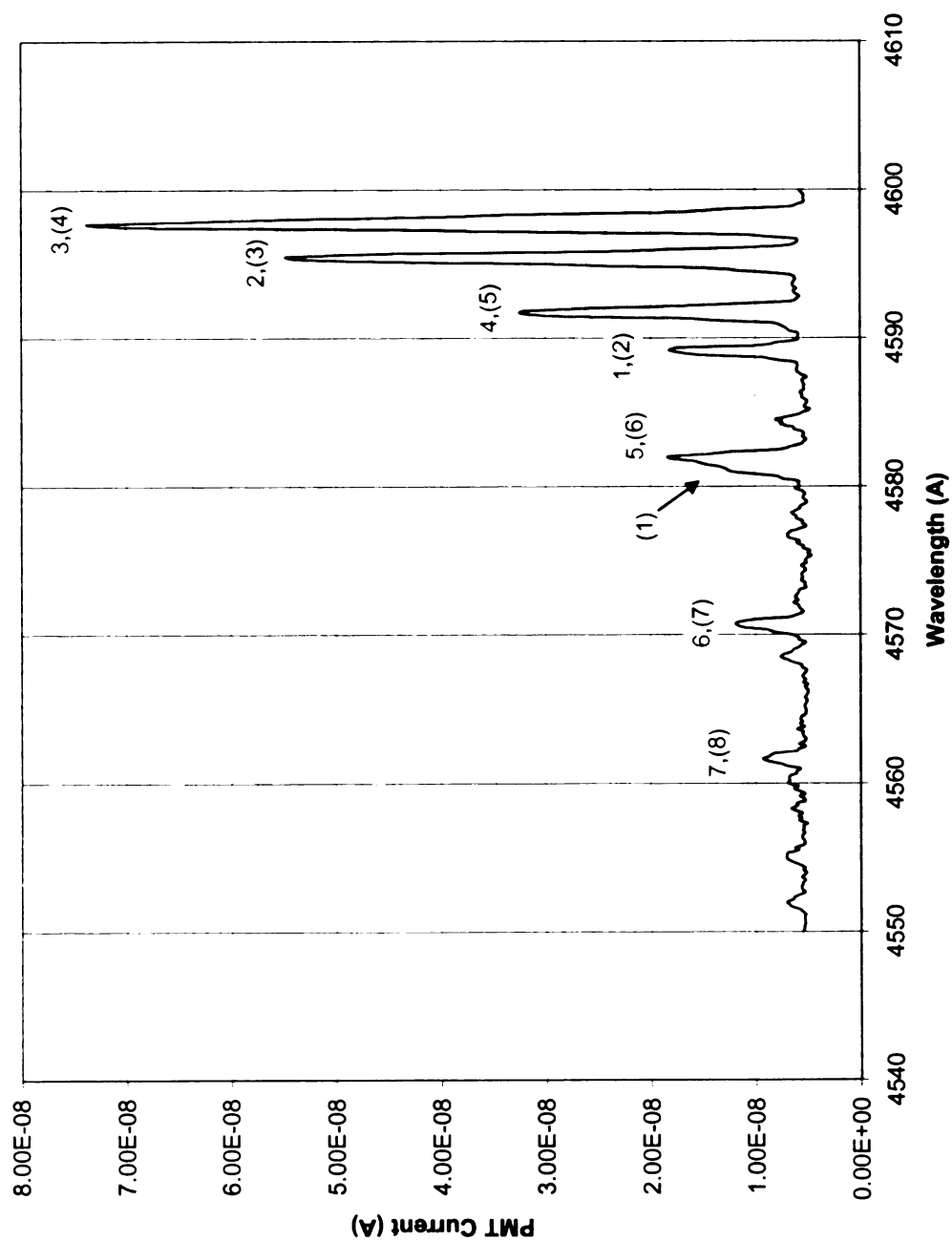
Figure 50 Hydrogen Rotational Spectrum.

186

Table 4 Hydrogen Rotational Transitions.

J R-branch	data λ	I	λcorrected	Fortrat E(1/cm)	m	Fortrat Theory E(1/cm)	M	Temperature m(m+1)	Ln(I/m)
	4583.00	0.000	4627.66	21609.19	0.00	21609.19	0.00		
0.00	4589.16	1.830	4633.82	21580.47	1.00	21567.00	1.00	2.00	0.604
1.00	4595.50	5.470	4640.16	21550.98	2.00	21548.34	2.00	6.00	1.006
2.00	4597.66	7.370	4642.32	21540.95	3.00	21551.56	3.00	12.00	0.899
3.00	4591.66	3.250	4636.32	21568.83	4.00	21573.90	4.00	20.00	-0.208
4.00	4581.83	1.840	4626.49	21614.66	5.00	21611.49	5.00	30.00	-1.000
5.00	4570.83	1.190	4615.49	21666.17	6.00	21659.38	6.00	42.00	-1.618
6.00	4562.00	0.875	4606.66	21707.7	7.00	21711.48	7.00	56.00	-2.079

$$E = E_0 - \left(B'_v + B''_v\right)m - \left(B'_v - B''_v\right)m^2 - \alpha_4\left(\partial B'^2_v - \partial B''^2_v\right)m^2 J^2$$

$$m_{vertex} = -\frac{1}{2}\frac{\left(B'_v + B''_v\right)}{\left(B'_v - B''_v\right)}$$

(7.3)

$$E_{vertex} - E_0 = -\frac{1}{4}\frac{\left(B'_v + B''_v\right)^2}{\left(B'_v - B''_v\right)}$$

$$m = \begin{cases} J + 1; Rbranch \\ \\ -J : Pbranch \end{cases}$$

Figure 51 compares the resulting Fortrat diagram with the R-branch from Table 4. The Fortrat diagram was generated using coefficients from an Origin^R curve fit. Coefficients matched rotational inertia values to within 10%; that is:

$$\left(B'_v + B''_v\right) = 54.24$$

$$\left(B'_v - B''_v\right) = -12.09$$

(7.4)

$$\alpha_4\left(\partial B'^2_v - \partial B''^2_v\right) = -0.046$$

The match should confirm the peak transition identification.

Figure 52 plots from Table 4 the log of the scaled peak intensity vs. the energy of the upper transition band, or rotational energy number, following Equation 7.2. Assuming a Boltzmann energy distribution, the slope of the curve is given as:
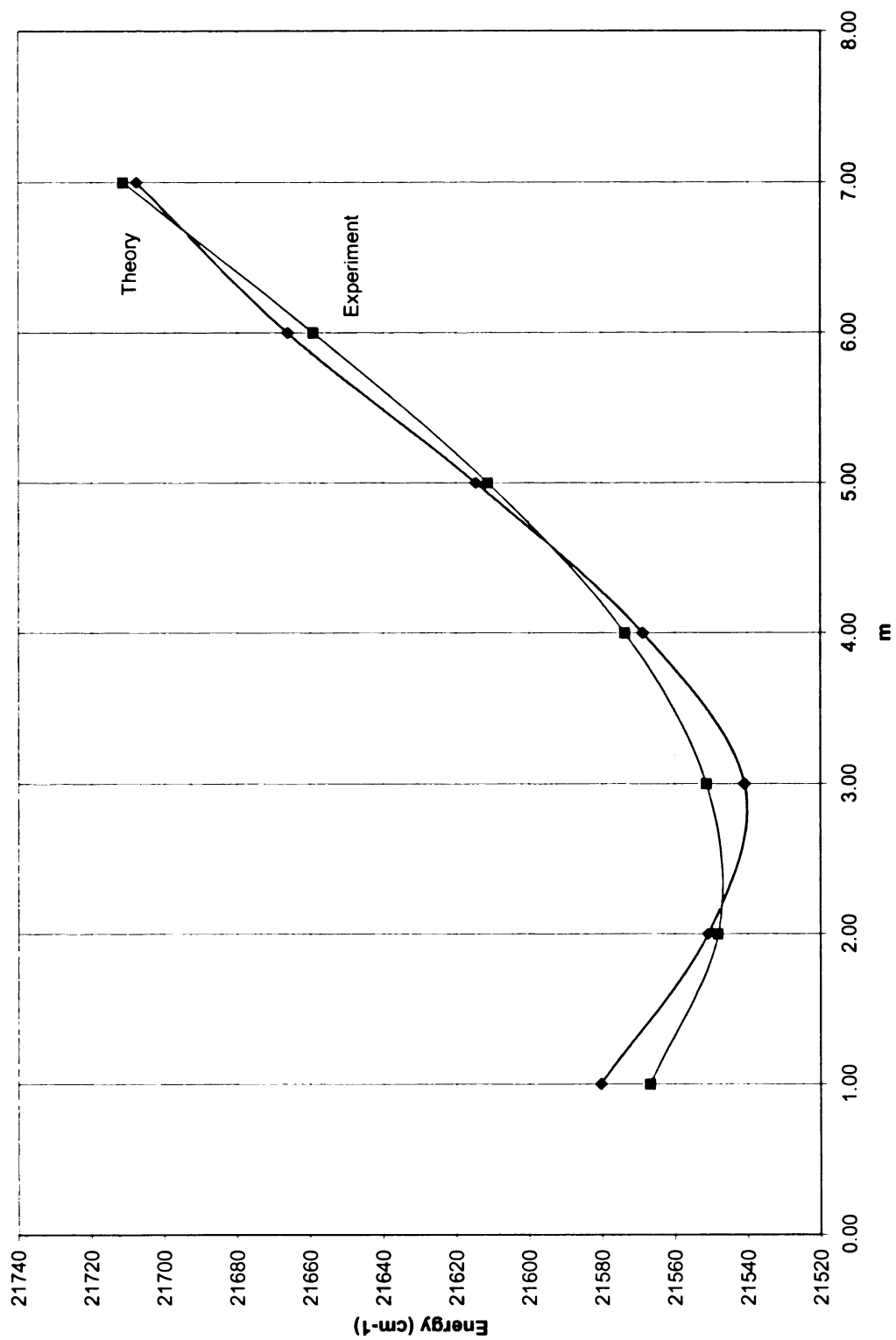
Figure 51 Fortrat Plot.

189
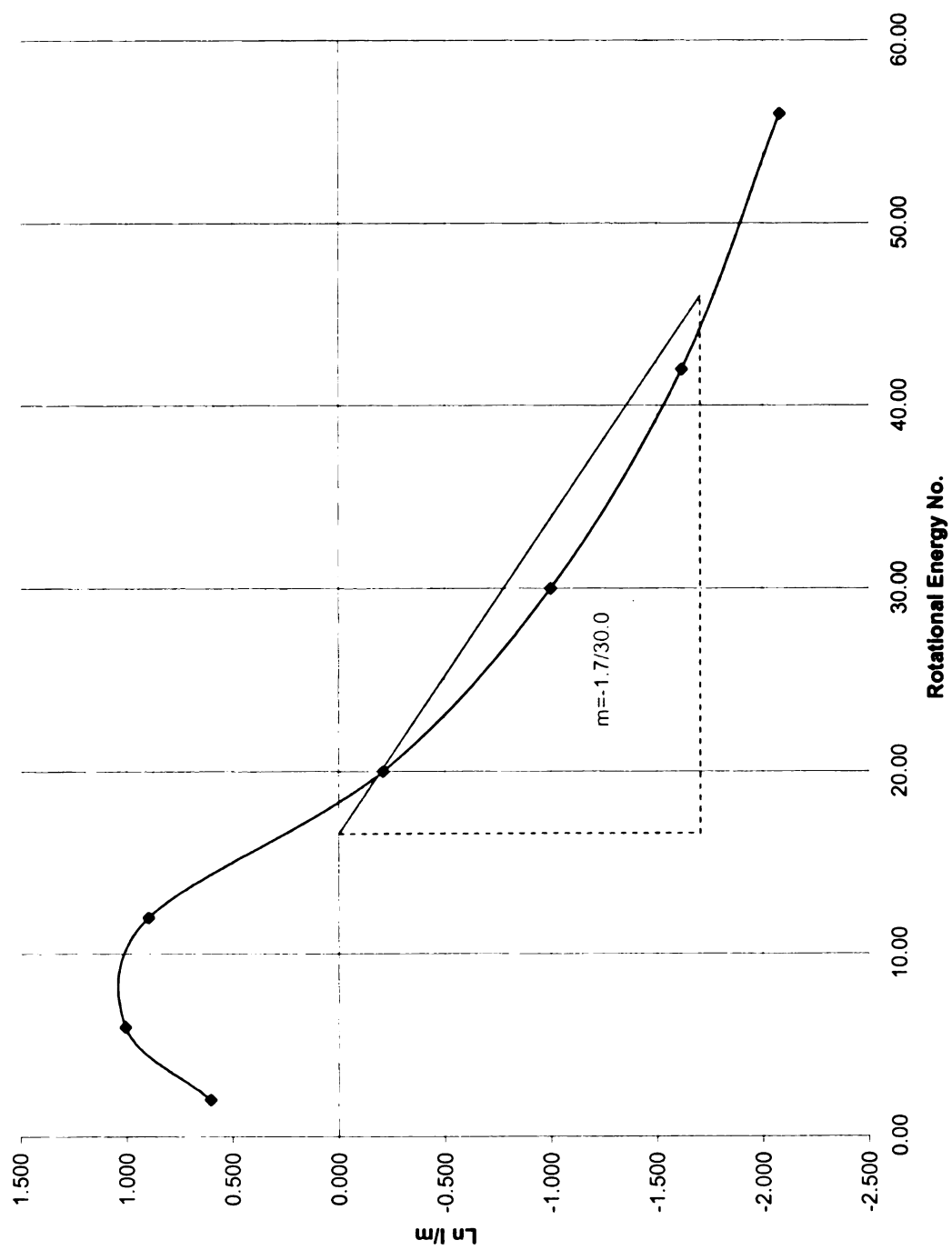
Figure 52 Rotational Energy Transition.

190

$$m_{slope} = -\frac{B'hc}{kT_r} = -\frac{1.7}{30}cm$$

$$(7.4)$$

$$\Rightarrow T_r = -28.8 \bullet \frac{1}{m_{slope(cm^{-1})}} = 508K = 235C$$

Repeating rotational temperature calculations generates the pressure vs. rotational temperature plot of interband rotation transitions given in Figure 53.

7.3.1.2 Diatomic Hydrogen Temperature: Intraband Transitions

As can be seen in Figure 52, the plot of the log of the scaled peak intensity vs. the energy of the upper transition band is not entirely linear. This indicates that either the energy distribution is not a Boltzmann distribution, or the rotation transition peaks are too difficult to identify accurately in H_2. A solution to both of these difficulties is to calculate temperature within one rotation band.

The theory from section 5.6 provides background. Each rotation transition peak in Figure 50 is degenerate; angular momentum is constant, but J_z is not. Application of an electric or magnetic field destroys the spherical symmetry, and removes the degeneracies.

The electric field effect (Stark) is second order –and negligible- for spherically symmetric wavefunctions such as Σ_u and Σ_g; the magnetic field effect (Zeeman) is first order, and causes splitting in Σ_u and Σ_g energy levels, and corresponding peak splitting in transitions.

191
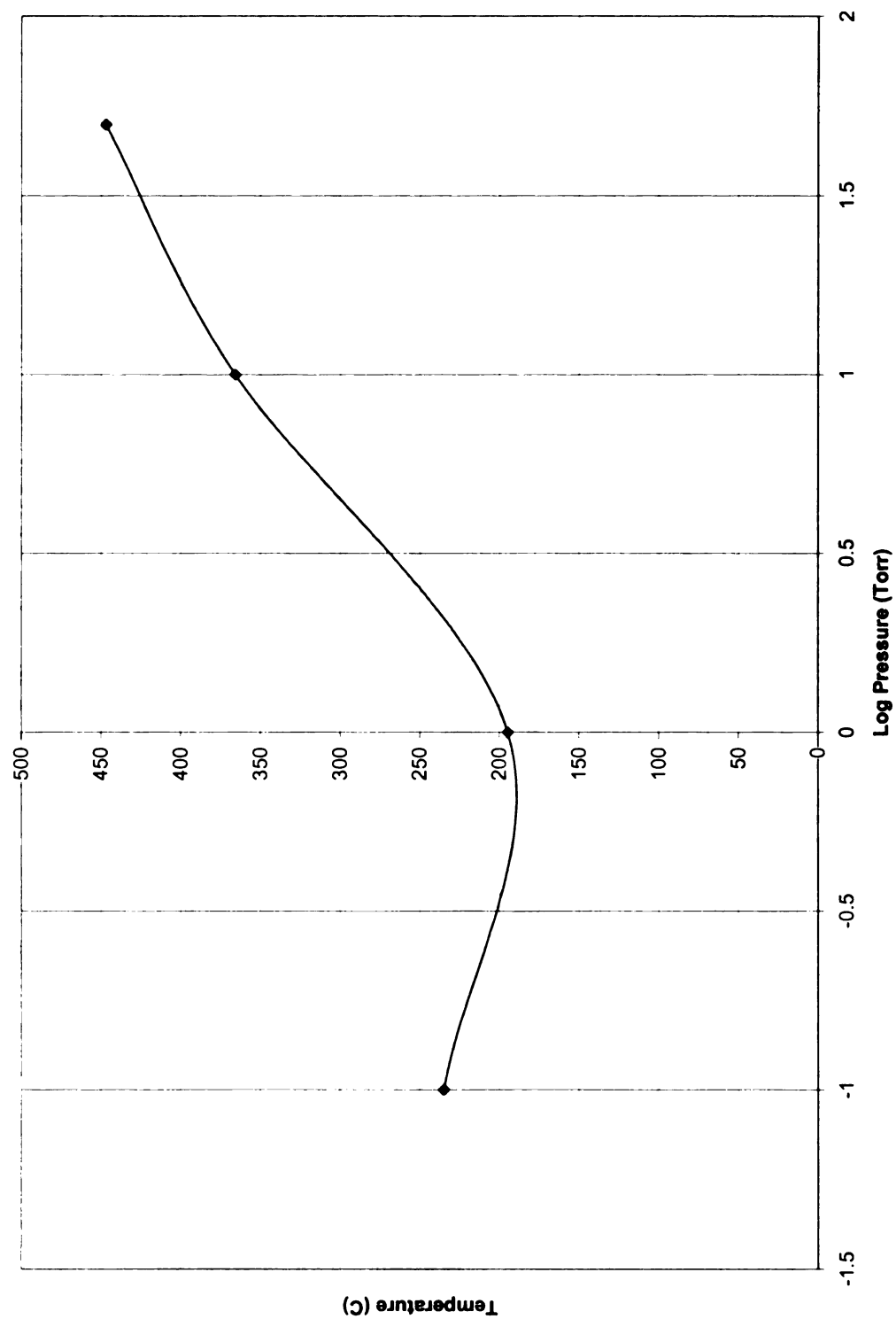
Figure 53 Rotational Temperature vs. Pressure.

192

Figures 54-55 represent a pair of high-resolution images of the peak identified as m=2 (J: 2->2) in the R-branch of the diatomic hydrogen rotation spectrum, taken directly from Figure 50.

Fine structure due to Zeeman splitting is identified. There are fifteen main peaks, corresponding to fifteen transitions within the band. Figure 27 in section 5.7 indicates this peak must represent m=3 (J: 3->2). The bands in Figure 50 were incorrectly assigned; that is, the side lobe at 4581.3 A in Figure 50 is the new m=1 peak, and each assigned m must be incremented by one (parenthetical values). The resulting Fortrat diagram is shifted, but unperturbed.

The magnetic field strength is not strong enough to decouple the orbital angular momentum and spin. Consequently, Clebsch-Gordan coefficients from section 5.4 determine energy levels for both upper and lower bands. Calculations are simplified by concentrating on the orbital angular momentum shifts, the first term in equation 5.73. This term alone is the Larmor precession, or normal Zeeman effect.

$$\Delta_B^1 = -\frac{e\hbar B}{2m_e c}\left(B'n - B''m\right)$$

$$-3 \leq n \leq 3, -2 \leq m \leq 2; m = n \pm 1, n \qquad (7.5)$$

$$B' = 20.0, B'' = 28.4$$
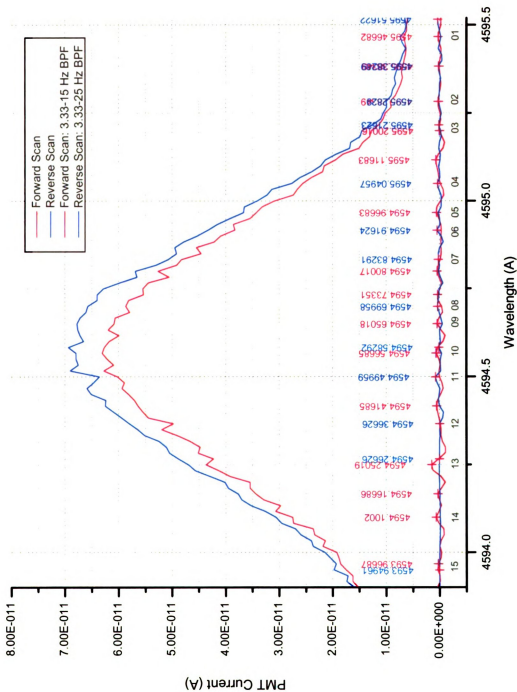
Figure 54 H$_2$ Zeeman Splitting: Tight BPF, 0.5 Torr.

194
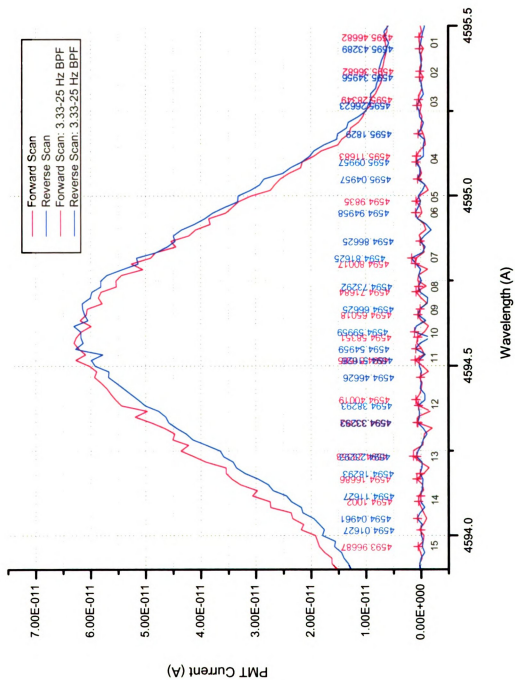
Figure 55 H_2 Zeeman Splitting: Relaxed BPF, 0.5 Torr.

Table 5 fits energy levels from Equation 7.5 onto Figures 54-55, for a given magnetic field strength B. In Table 5, the mean-squared error is minimized for B=35 mT; experimental vs. theoretical magnetic field magnitude is plotted in Figure 56. Figure 57 plots magnetic field strength for pressures from 0.5-50 Torr.

Transition amplitudes come directly from application of the spherical tensor $T_q(k)$. Briefly, the spherical tensor is related to the angular momentum eigenvectors in the following way:

$$[J_z, T_q^{(k)}] = \hbar q T_q^{(k)}$$

$$[J_\pm, T_q^{(k)}] = \hbar \sqrt{(k \mp q)(k \pm q + 1)} T_q^{(k)}$$

(7.6)

And, the spherical tensor is transformed from representation α to α' by a multi-dimensional Clebsch-Gordan rotation, that is:

$$\langle \alpha'; j', m' \mid T_q^{(k)} \mid \alpha; j, m \rangle =$$

(7.7)

$$\langle j, k; m, q \mid j, k; j', m' \rangle \langle \alpha'; j' \mid T_q^{(k)} \mid \alpha; j \rangle \frac{\langle \alpha'; j' \parallel T_q^{(k)} \parallel \alpha; j \rangle}{\sqrt{2j + 1}}$$

Equation 7.7 is the Wigner-Eckart theorem [43]. For $T_q(k)$, an eigenfunction:

$$\int d\Omega Y_l^{m^*} (\vartheta, \phi) Y_{l_1}^{m_1} (\vartheta, \phi) Y_{l_2}^{m_2} (\vartheta, \phi)$$

(7.8)

$$= \sqrt{\frac{(2l_1 + 1)(2l_2 + 1)}{4\pi(2l + 1)}} \langle l_1, l_2; 0, 0 \mid l_1, l_2; l, 0 \rangle \langle l_1, l_2; m_1, m_2 \mid l_1, l_2; lm \rangle$$

196

Table 5 Hydrogen Rotational Energy Levels.

peak: 2>1	Data						R	Plot (B=0.035 T)		Plot (B=0.035 T)	
	B"m-B'n	I(E-11)	λ	λcorrected	E(1/cm)	dE(1/cm)		dE(1/cm)	dE(1/cm)	dE(1/cm)	f(I)
1> 2	36.80		4593.971	4639.413	21554.451	3.4699611		3.469961	3.769976		
0> 1	28.40		4594.114	4639.556	21553.787	2.8056117		2.805612	2.909438		
-1> 0	20.00		4594.268	4639.710	21553.071	2.0902042		2.090204	2.0489		
2> 2	16.80	5.231	4594.346	4639.788	21552.709	1.7278731	0.745	1.727873	1.721076	4.0978	0.020096
-2>-1	11.60		4594.478	4639.920	21552.096	1.1147251		1.114725	1.188362		
1> 1	8.40	6.289	4594.565	4640.007	21551.692	0.7106239	0.943	0.710624	0.860538	2.0489	0.019088
-3>-2	3.20		4594.652	4640.094	21551.288	0.3065379		0.306538	0.327824		
0> 0	0.00	5.868	4594.718	4640.160	21550.981	0	1.000	0	0	0	0.016795
3> 2	-3.20		4594.786	4640.228	21550.665	-0.315818		-0.31582	-0.32782		
-1>-1	-8.40	4.526	4594.899	4640.341	21550.140	-0.840612	0.943	-0.84061	-0.86054	-2.0489	0.013737
2> 1	-11.60		4594.983	4640.425	21549.750	-1.230708		-1.23071	-1.18836		
-2>-2	-16.80	2.211	4595.091	4640.533	21549.249	-1.73224	0.745	-1.73224	-1.72108	-4.0978	0.008494
1> 0	-20.00		4595.167	4640.609	21548.896	-2.085155		-2.08516	-2.0489		
0>-1	-28.40		4595.312	4640.754	21548.223	-2.758449		-2.75845	-2.90944		
-1>-2	-36.80		4595.471	4640.913	21547.484	-3.496702		-3.4967	-3.76998		

peak: 2>1	Data						R	Plot (B=0.0285 T)		Plot (B=0.0285 T)	
	B"m-B'n	I(E-11)	λ	λcorrected	E(1/cm)	dE(1/cm)		dE(1/cm)	dE(1/cm)	dE(1/cm)	f(I)
2> 2	16.80	2.318	4597.133	4639.860	21552.374	1.3934244	0.745	1.393424	1.401448	3.33678	0.020781
1> 1	8.40	2.695	4597.005	4639.988	21551.780	0.7988746	0.943	0.798875	0.700724	1.66839	0.019088
0> 0	0.00	2.375	4596.833	4640.160	21550.981	0	1.000	0	0	0	0.015863
-1>-1	-8.40	1.693	4596.683	4640.310	21550.284	-0.696645	0.943	-0.69664	-0.70072	-1.66839	0.011991
-2>-2	-16.80	0.932	4596.483	4640.510	21549.356	-1.625434	0.745	-1.62543	-1.40145	-3.33678	0.008356

peak: 2>1	Data B"m-B'n	λ	I (E-11)	λcorrected	E(1/cm)	dE(1/cm)	R	Plot (B=0.026 T) dE(1/cm)	dE(1/cm)	Plot (B=0.026 T) dE(1/cm)	f(I)
2> 2	16.80	4595.400	5.842	4639.843	21552.453	1.4723905	0.745	1.472391	1.278514	3.04408	0.021454
1> 1	8.40	4595.583	6.579	4640.026	21551.603	0.622374	0.943	0.622374	0.639257	1.52204	0.019088
0> 0	0.00	4595.717	6.053	4640.160	21550.981	0	1.000	0	0	0	0.016561
-1>-1	-8.40	4595.833	5.003	4640.276	21550.442	-0.538742	0.943	-0.53874	-0.63926	-1.52204	0.014515
-2>-2	-16.80	4596.017	3.211	4640.460	21549.588	-1.393244	0.745	-1.39324	-1.27851	-3.04408	0.011792

198

Figure 56 B Field (B=35 mT).

199
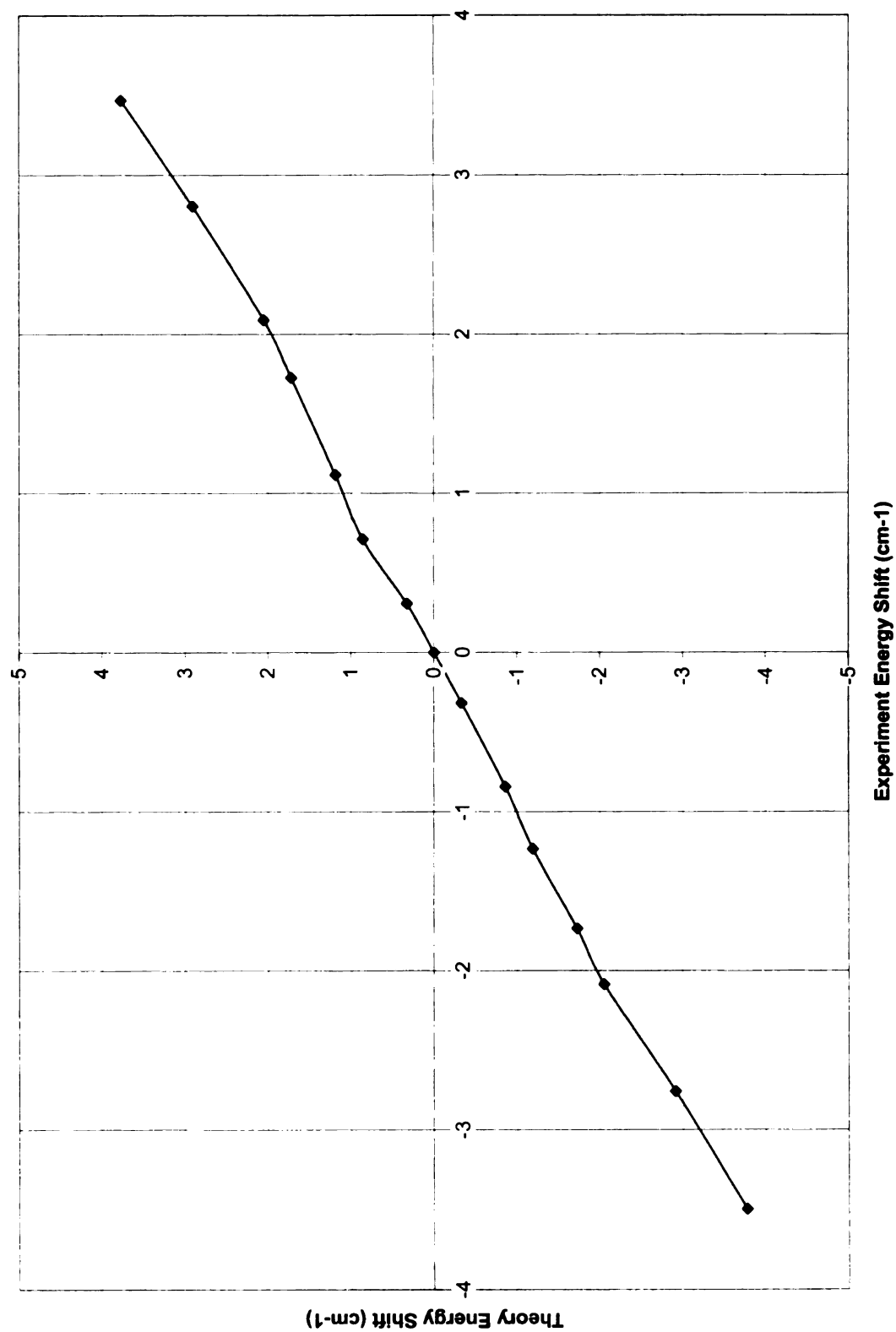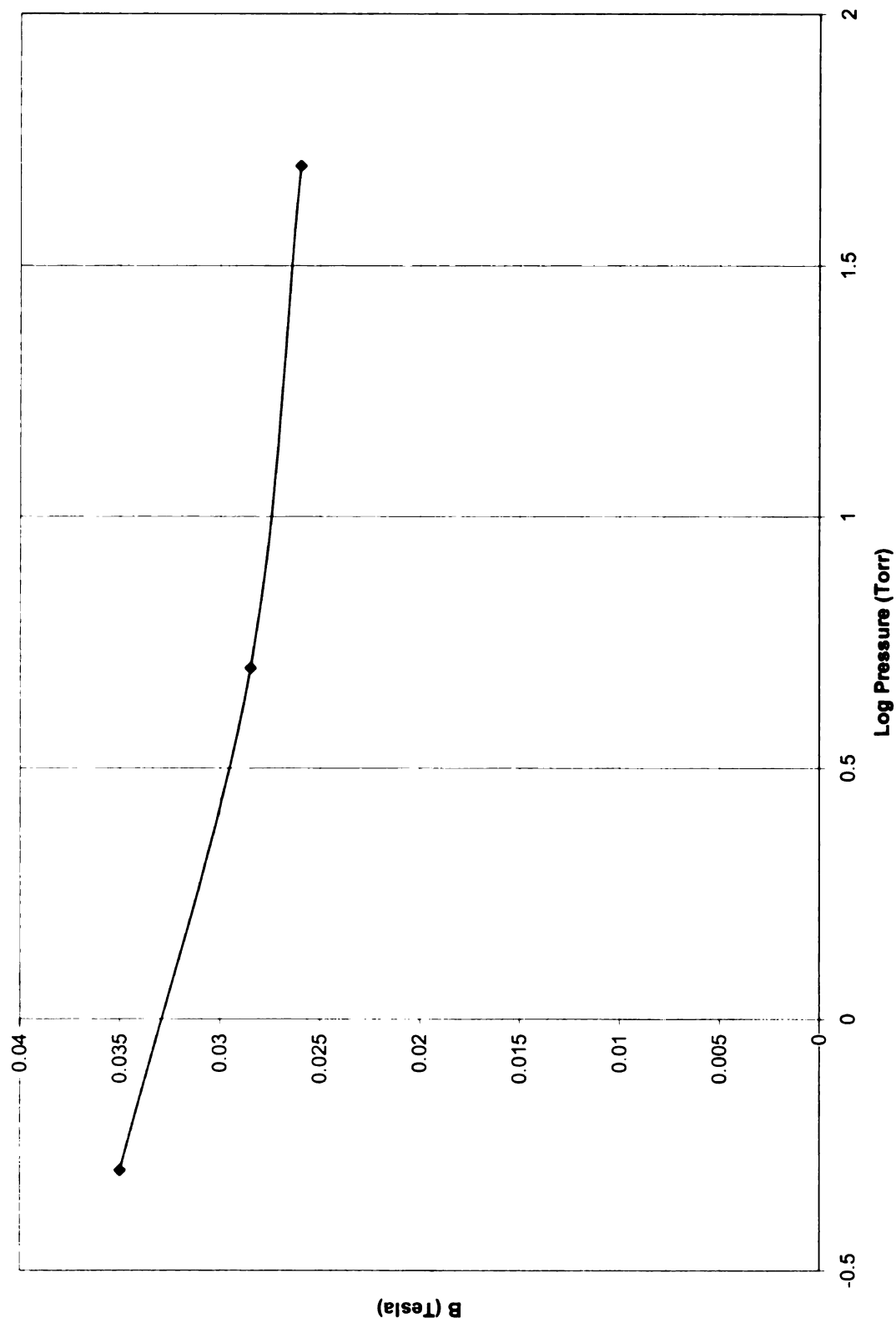
Figure 57 B Field vs. Pressure.

200

Finally, the following three special cases account for dipole transitions:

$$\int d\Omega Y_L^{M^*}(\vartheta,\phi)Y_1^0(\vartheta,\phi)Y_{L+1}^M(\vartheta,\phi) = \sqrt{\frac{3}{4\pi}}\sqrt{\frac{(L+M+1)(L-M+1)}{(2L+1)(2L+3)}}$$

(7.9)

$$\Rightarrow \int d\Omega Y_L^{M^*}(\vartheta,\phi)zY_{L+1}^M(\vartheta,\phi) = \sqrt{\frac{(L+M+1)(L-M+1)}{(2L+1)(2L+3)}}$$

$$\int d\Omega Y_L^{M^*}(\vartheta,\phi)Y_1^1(\vartheta,\phi)Y_{L+1}^{M+1}(\vartheta,\phi) = \sqrt{\frac{3}{8\pi}}\sqrt{\frac{(L+M+1)(L+M+2)}{(2L+1)(2L+3)}}$$

(7.10)

$$\Rightarrow \int d\Omega Y_L^{M^*}(\vartheta,\phi)(x+jy)Y_{L+1}^M(\vartheta,\phi) = -\sqrt{\frac{1}{2}}\sqrt{\frac{(L+M+1)(L+M+2)}{(2L+1)(2L+3)}}$$

$$\int d\Omega Y_L^{M^*}(\vartheta,\phi)Y_1^{-1}(\vartheta,\phi)Y_{L+1}^{M+1}(\vartheta,\phi) = \sqrt{\frac{3}{8\pi}}\sqrt{\frac{(L-M)(L-M-1)}{(2L-1)(2L+1)}}$$

(7.11)

$$\Rightarrow \int d\Omega Y_L^{M^*}(\vartheta,\phi)(x-jy)Y_{L-1}^{M+1}(\vartheta,\phi) = \sqrt{\frac{1}{2}}\sqrt{\frac{(L-M)(L-M-1)}{(2L-1)(2L+1)}}$$

Equation 7.9 accounts for transitions effected by dipoles in the z direction; Equations 7.10 and 7.11 by dipoles rotating about the z-axis. Transition rates from Equation 7.9 are included with peak amplitudes found in Figures 54-55, and charted in Table 5. Transition rates are proportional to the z dipole strength.

Deconvolved transition amplitudes divided by transition probabilities (rates) given in Equation 7.9 are plotted against m_l energy level differences in Figure 58; the slope, calculated in the following, is proportional to rotational temperature, regardless of distribution [54].
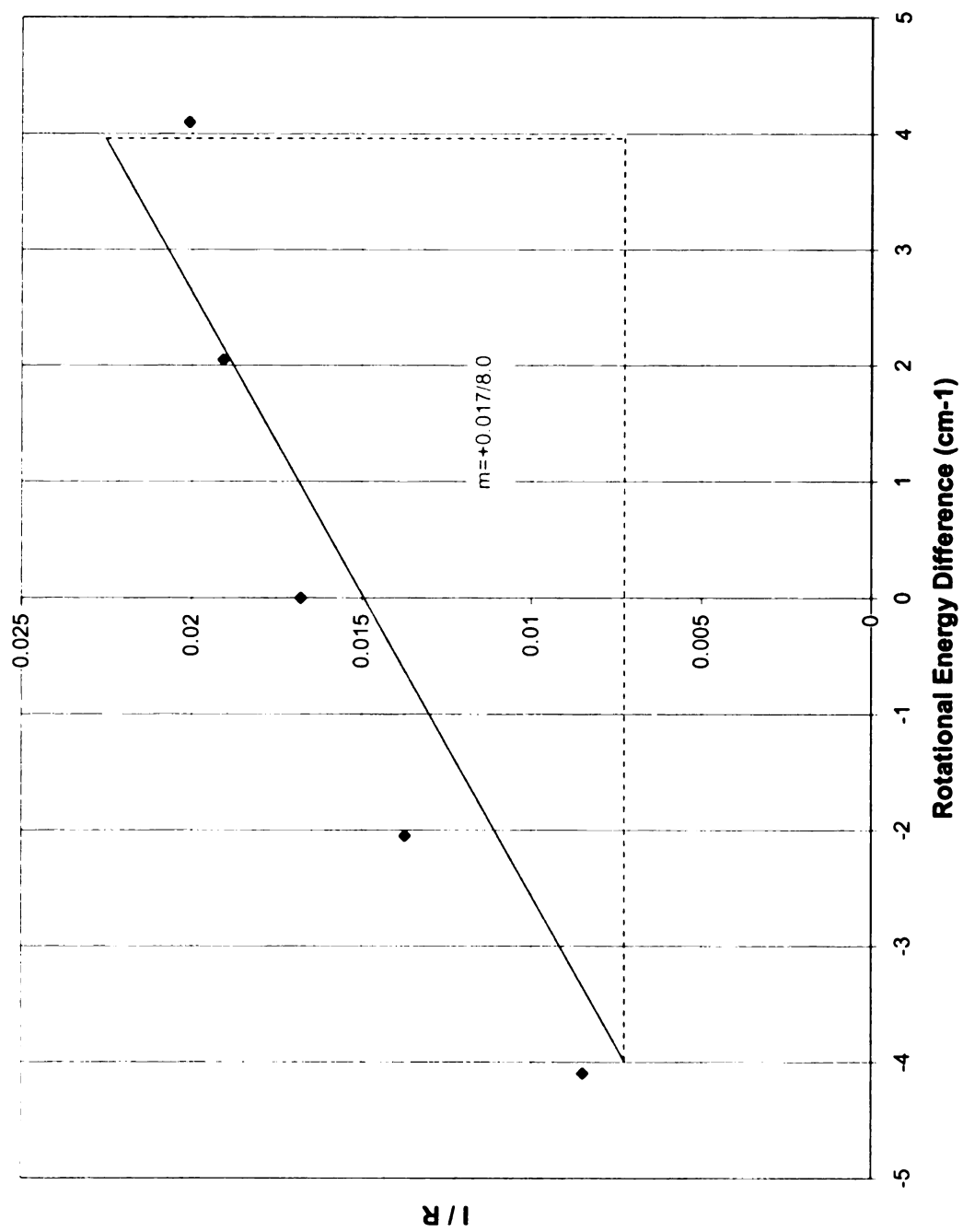
Figure 58 Intraband Energy Distribution.

202

$$m_{slope} = 0.018 \bullet \frac{\partial\left(\dfrac{I/I_0}{R}\right)}{\partial E_B} = \frac{0.017}{8.0} = \frac{hc}{kT_r}\left(1 - \frac{\partial E}{kT_r}\right)cm$$

$$\tag{7.12}$$

$$\Rightarrow T_r = 1.44 \bullet \frac{1}{m_{slope(cm^{-1})}} = 556K = 283C$$

R represents transition probabilities, I the transition amplitudes. The constant 0.018 comes directly from the discrete Gaussian deconvolution of the amplitudes, specifically:

$$0.018 = \frac{\sqrt{2\pi}}{4\pi^2}\frac{1}{\# peaks/\sigma}\frac{\sigma/\sigma_M}{\sqrt{1 - \dfrac{\sigma_M^2}{\sigma}}} \tag{7.13}$$

The deconvolved spectrum is negligibly wider; the second-order energy term on the RHS of Equation 7.12 is not used in this calculation, but accurately depicts the slight parabolic deflection of Figure 58. The accuracy of Equation 7.12 is independent of rotational level distribution. Figure 59 plots intraband rotational temperature vs. pressure.
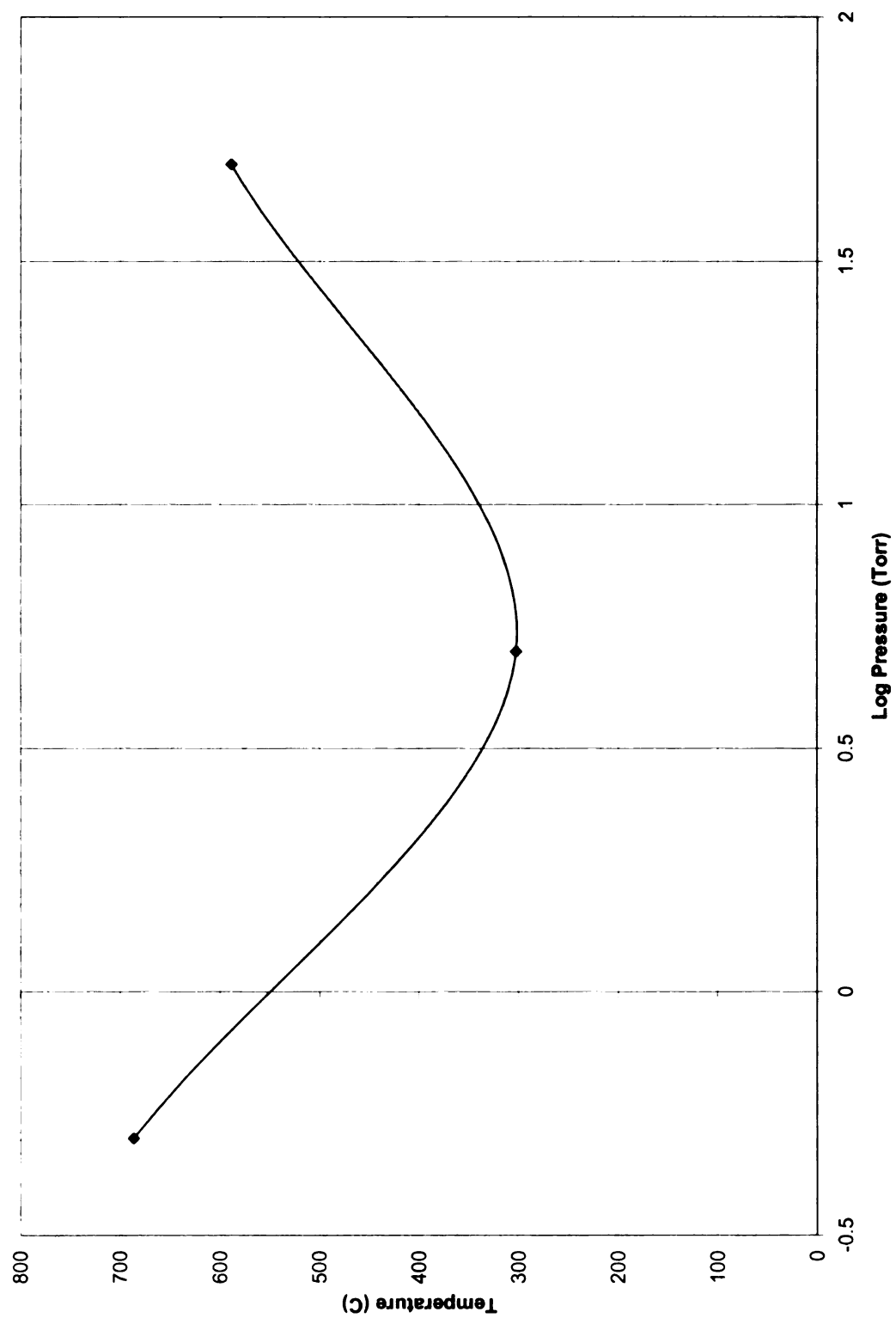
Figure 59 Intraband Temperature vs. Pressure.

204

7.3.2 Diatomic Hydrogen: Zeeman Shift

Peaks for the Zeeman shifted rotation bands were found by deconvolution of a collection of forward and reverse spectral scans. Scans in both directions were necessary to verify peak location, and to avoid increased photomultiplier tube signal-to-noise level evident on the falling edge of the band, as discussed in section 7.1 and demonstrated in Figure 42.

To verify Zeeman peaks, both forward and reverse scans were band-passed filtered to remove modulation at the sampling frequency. The band-pass filter results are given at the baseline of Figures 54-55. The reverse scans are flipped to align with the forward scans. The forward scan amplitudes in Figure 54 are artificially reduced. All spectral readings were taken with the accelerating voltage set to 550 V. The plasma conditions were identical for each reading; the pressure was 0.5 Torr, the gap size 5 mm, the power set to 60 W, and the hydrogen flow rate was 100 sccm. The wavelength of the spectrum served as the time element for the band-pass filter; that is, 1 A = 1 second.

Figures 54-55 attempt to demonstrate the consistency of the spectral data; peaks lined up vertically –as demonstrated by the band-pass filter results- confirm peak location. Peaks are identified by the Origin^R cross-correlation software package.

Band-pass filter results suffer from time shifts, as is expected from broadband finite impulse response (FIR) filters. This is seen in Figure 54; the cut-off frequency on the forward scan is set to 15 Hz. Figure 54 identifies peaks with amplitudes greater than 0.2 E-11 A. Time shifts from the FIR filter are evident. Software peak identification is unreliable for time shifts of this magnitude; as an example, peaks 5-6 should register for both forward and reverse scans, and do not.

Figure 55 examines the same two spectral scans with relaxed band-pass filters (fcut-off=25 Hz) on both forward and reverse scans. Additionally, peak triggers are raised to 0.5 E-11 A. on both forward and reverse scans to counteract the raised noise floor associated with the wider filters. Peaks identified in Figure 55 are cataloged in Table 5 and compared to peaks expected from normal Zeeman splitting for the J: 3->2 band of the Σ_u->Σ_g transition in molecular hydrogen.

A second filtering method combined both inputs in a moving average windowed cross-correlation filter. Results from this filter are shown graphically in Figure 60, with results from Figure 55 given along the baseline for comparison.

Results for both filtering methods (Figure 55, Figure 60) identify peaks consistent with normal Zeeman splitting for hydrogen in the given rotational band, further strengthening the evidence for Zeeman energy shifts in the diatomic hydrogen rotational spectrum.

Figures 61-62 are plots of the H_2 rotational spectrum for pressures of 5.0 Torr and 50 Torr. The five transition peaks identified represent transitions effected by the circumferential electric field. Magnetic field strengths are calculated for the given pressures and included in Table 5 and plotted in Figure 57 in section 7.3.1.2. The magnetic field strengths at 5.0 Torr and 50 Torr are 28 mT and 25 mT, respectively.

7. 4 *Hydrogen Results: Atomic Hydrogen*

J. Balmer described atomic Hydrogen lines, in the visible spectrum, in 1885. N. Bohr first explained the Balmer Series in 1913. The energy differences (E_n) found in the Schrodinger equation with central potential energy match the Balmer series. Three of these lines, H_α, H_β, and H_γ, are investigated in this study.

206
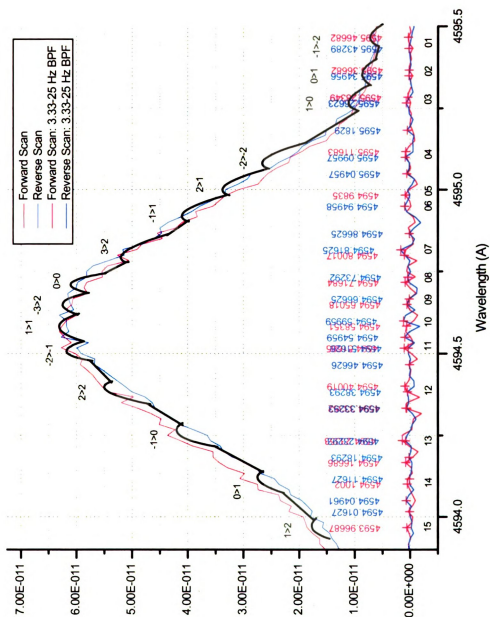
Figure 60 H_2 Zeeman Splitting: Cross-Correlation Filter, 0.5 Torr.
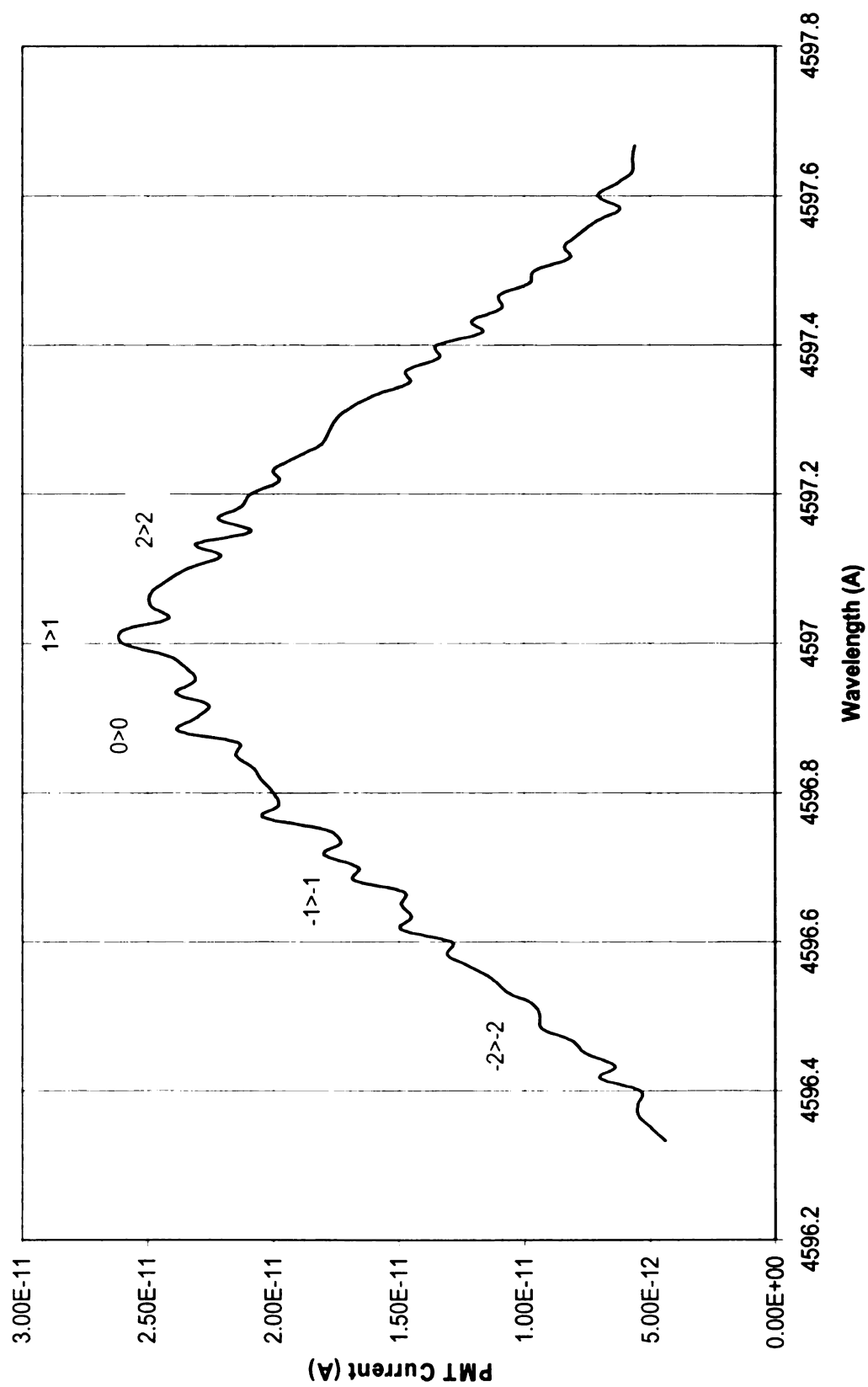
Figure 61 H_2 Zeeman Splitting: 5.0 Torr, 60 W.

208
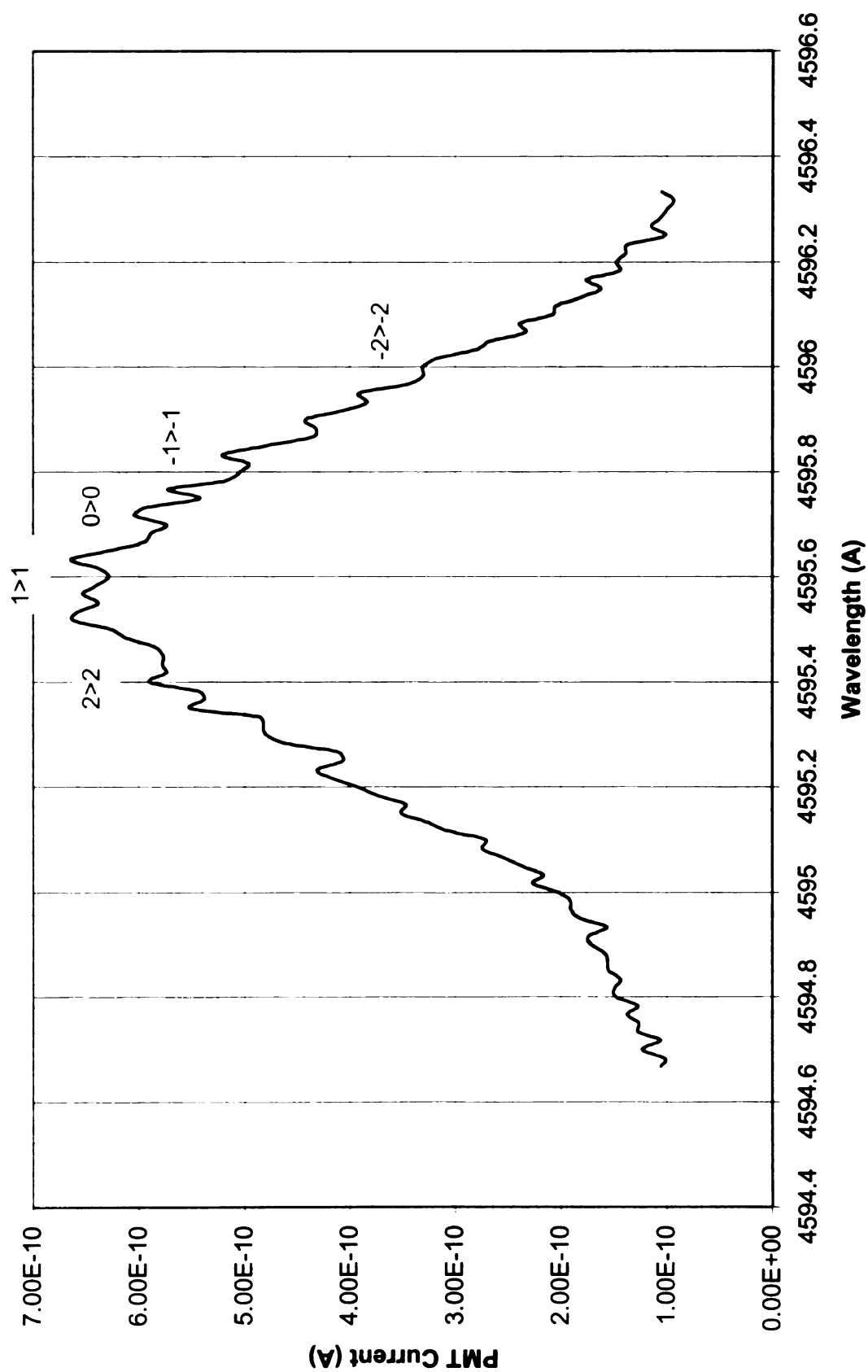
Figure 62 H_2 Zeeman Splitting: 50 Torr, 60 W.

209

Gross and fine structure spectral results from atomic hydrogen lines H_α, H_β, and H_γ are studied in the next section to determine the resident electric field in the hydrogen plasma. In the final section, the Stark broadened H_β line is used to determine the electron density of the plasma.

7.4.1 Atomic Hydrogen: Stark Shift

Section 6.3.1 develops the concepts that govern Stark effect energy shifts and transitions for the atomic hydrogen gross structure. Included are direct calculations for the resulting H_α and H_β energy spectrum shifts (Figures 38-39), and Equations 6.36-6.37 defining relative transition amplitudes. Gross structure splitting is dominant with applied fields on the order of 5000 V/cm [60] and larger.

Section 6.3.2 develops the concepts that govern the Stark effect for the fine structure of atomic hydrogen. Fine structure analysis is in general limited to fields on the order of 1000 V/cm [60]; larger fields mix the fine structure wave functions, complicating the analysis.

Analysis of intermediate fields requires coupling both gross and fine structure effects. For exact solutions, all perturbation potentials must be reformulated in the Schroedinger equation. Accurate approximate solutions have been found up to the field limits, where gross and fine structures mix.

Electric fields in this investigation are anticipated to be on the order of 2000-5000 V/cm (see section 8.1.2) –a consequence of the small electrode gap that was necessary to confine miniature plasmas. Fields at this level effect a uniform distortion in the parabolic orbital wave functions [60]; the outer shell of the wave function retains parabolic symmetry, the wave function core approximates spherical symmetry. The anticipated

spectral response is an interleaving of the gross structure splitting and fine structure splitting. It is anticipated that gross structure spectral shifts and relative amplitudes should follow closely those outlined in section 6.3.1.

Further, it is anticipated that the fine structure splitting should be convolved with the gross structure. The fine structure amplitudes will deviate from the nominal values found in section 5.8 (Figure 30), a result of the relatively high electron density ($N_e \sim 10^{14}$-10^{15} cm^{-3}) of the plasma [60]. The fine structure signature should more closely follow that of experiments at approximately the same electron densities. Figures 31-32 in section 5.8 demonstrate fine structure spectrums from experiments conducted in low-pressure gas discharges under similar conditions.

Even at much higher applied electric fields, the parabolic wave functions do not interact with each other. Instead, each series of components {(n_1,n_2,m), (n_1+1,n_2,m)...} are superimposed, with spacing proportional to $E^{3/4}$ [60].

7.4.1.1 Stark Shift: H_α

Sections 6.3.1-6.3.2 develop the gross structure and fine structure for Stark effect atomic hydrogen transitions from principle quantum numbers n=3 to n=2, the H_α energy spectrum. Figures 38 and 40 give a graphical depiction of the gross and fine structure Stark effect for the H_α spectrum.

Figure 63 [83] gives the H_α transition amplitudes for the parabolic eigenvectors, calculated using Equations 6.36-6.37 in section 6.3.1. Figure 65 and Figures 67-68 are the H_α spectrums from discharge experiments where the pressure was controlled at 50 Torr, 5.0 Torr, and 0.5 Torr, respectively. In each case, discharge conditions were set to

π: linear polarization

σ: circular polarization

-8 -6 -4 -2 0 2 4 6 8
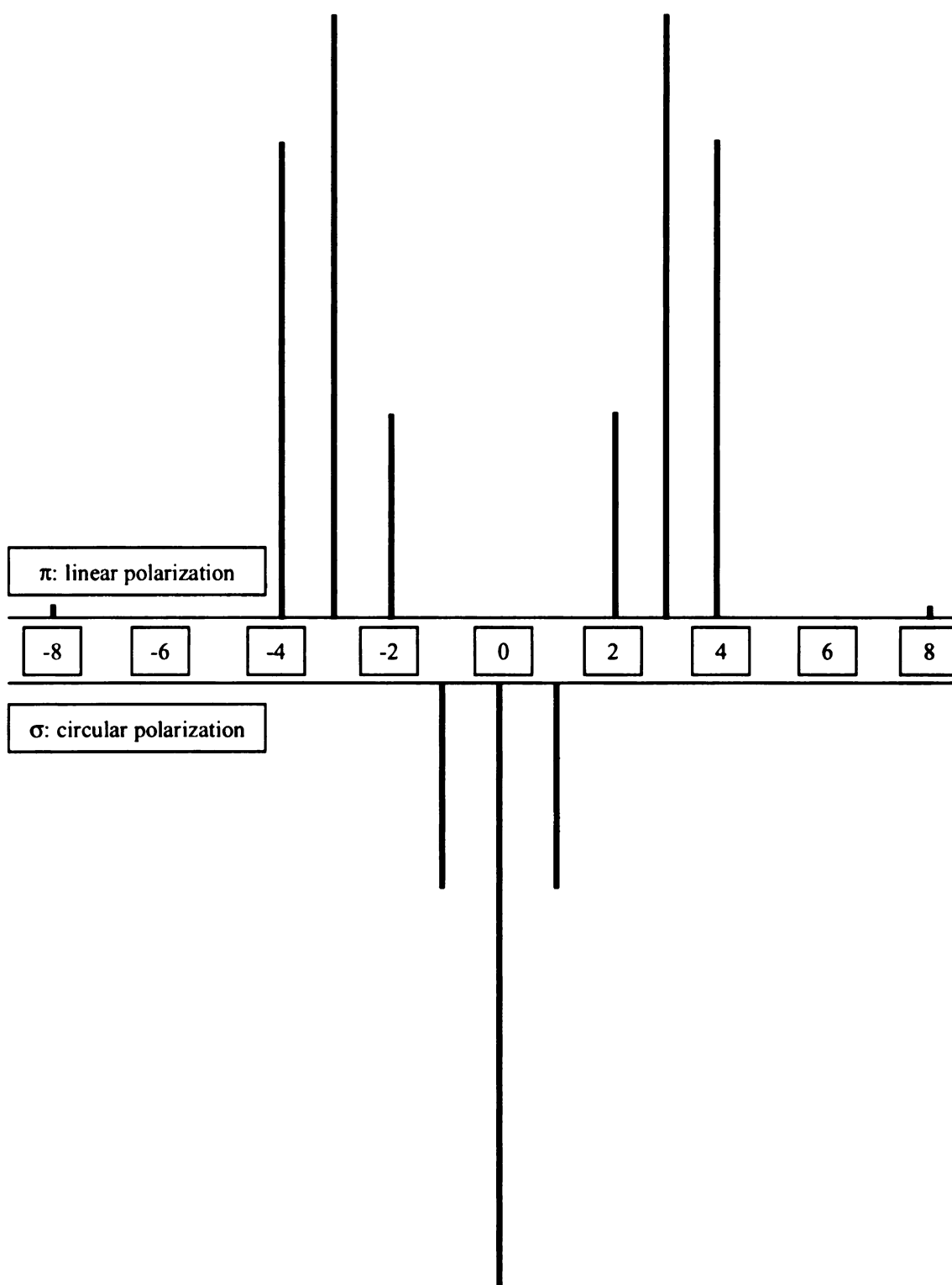
Figure 63 Hα Parabolic Transition Intensities.
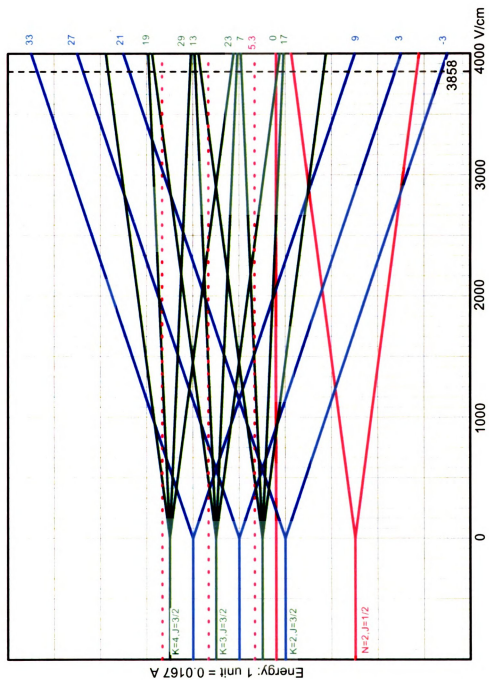
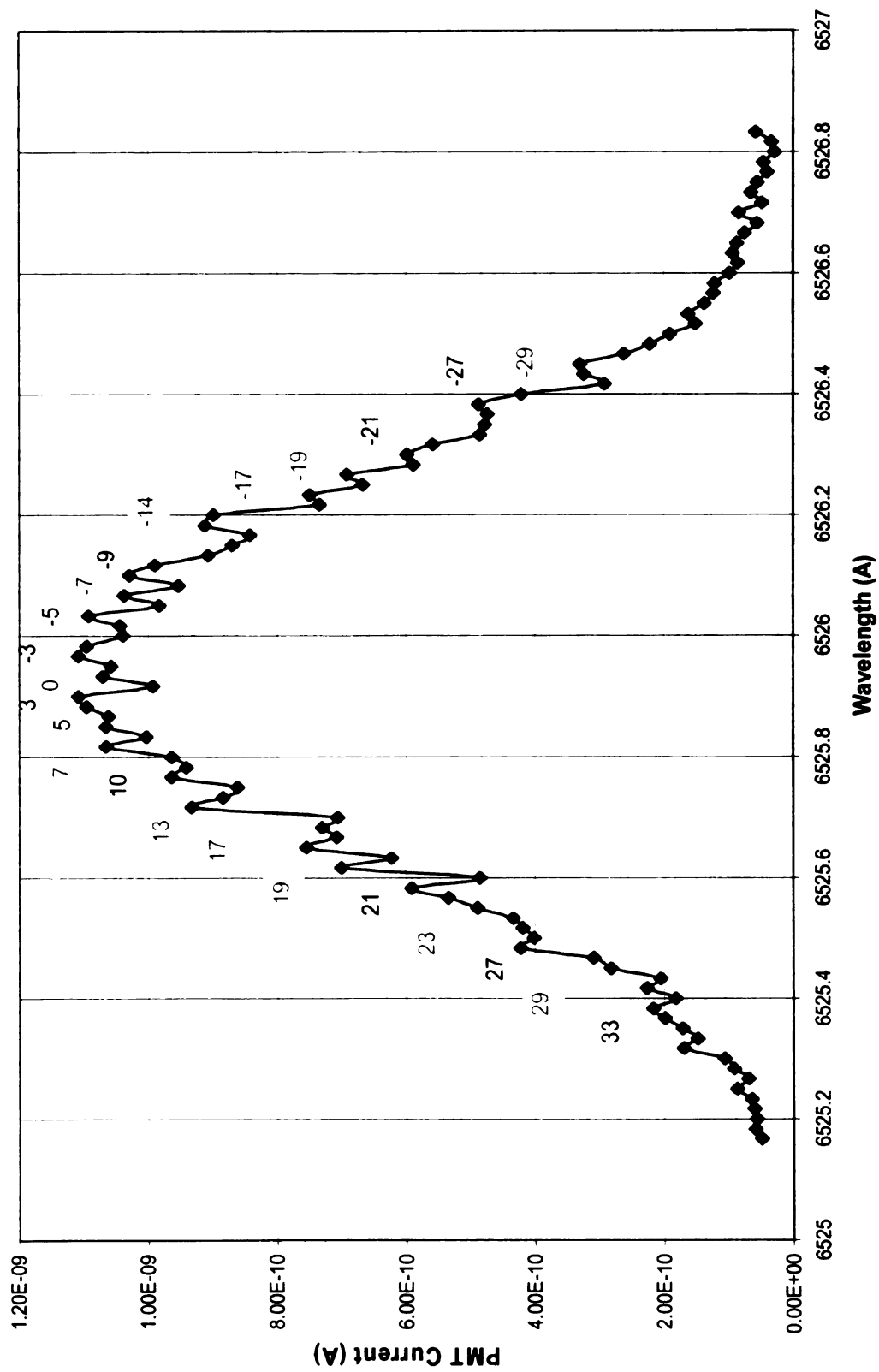**Figure 64** Hα Spectral Response: Gross and Fine Structure, 50 Torr.
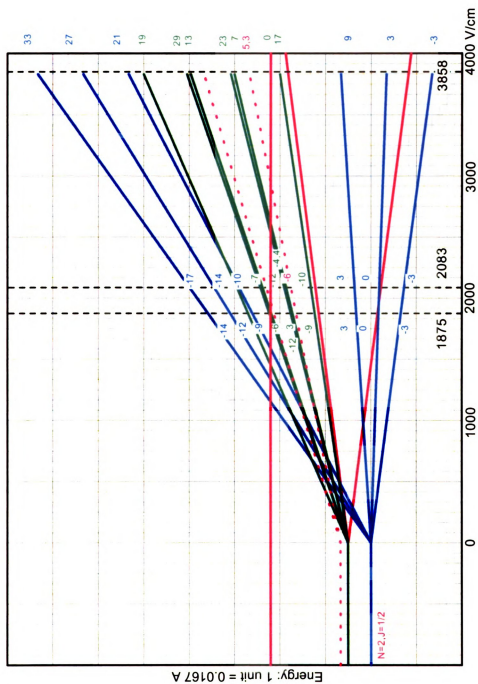
Figure 65 Hα Experimental Spectrum, 50 Torr.

214
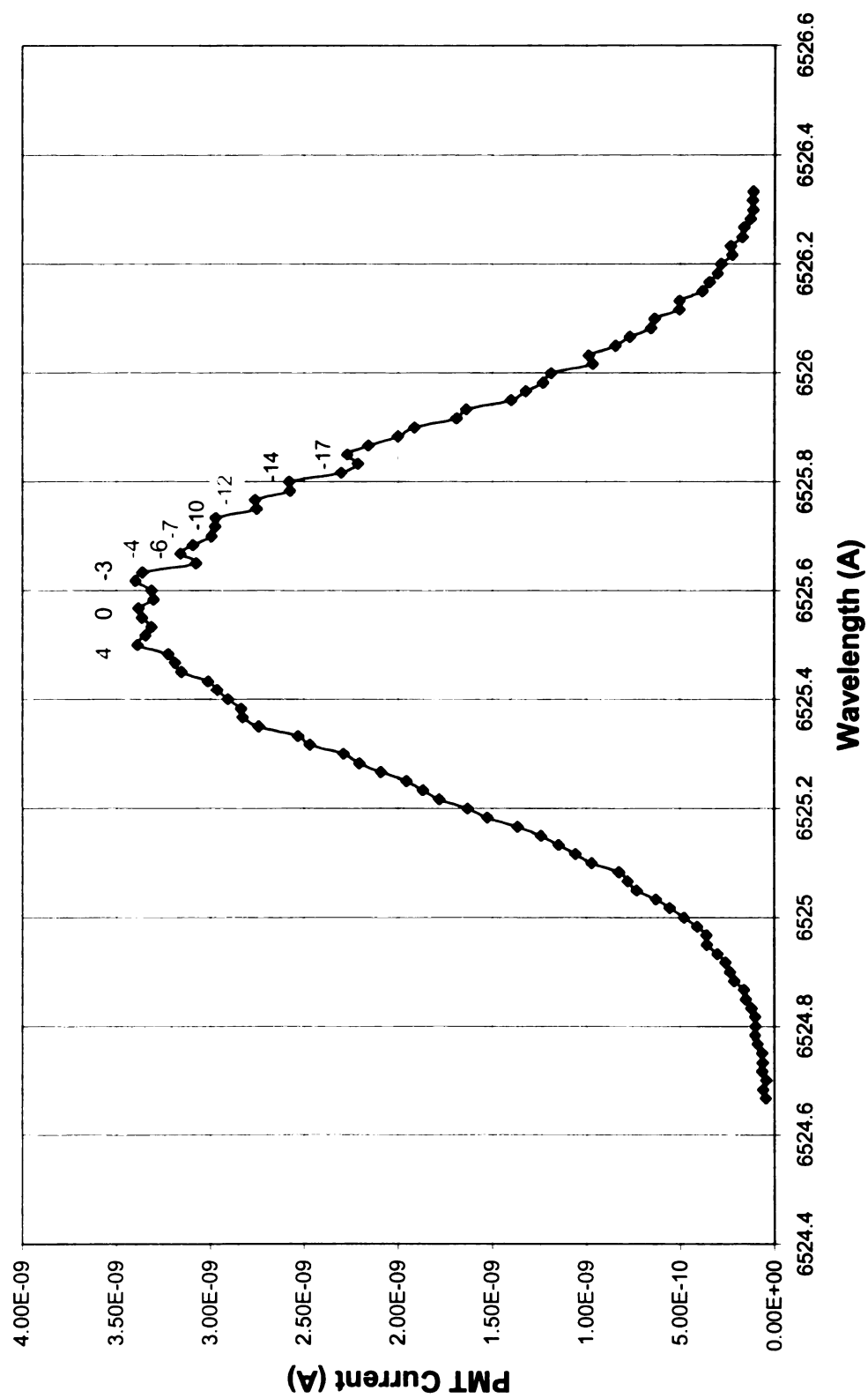
Figure 66 Hα Spectral Response: 0-4000V/cm Continuum.
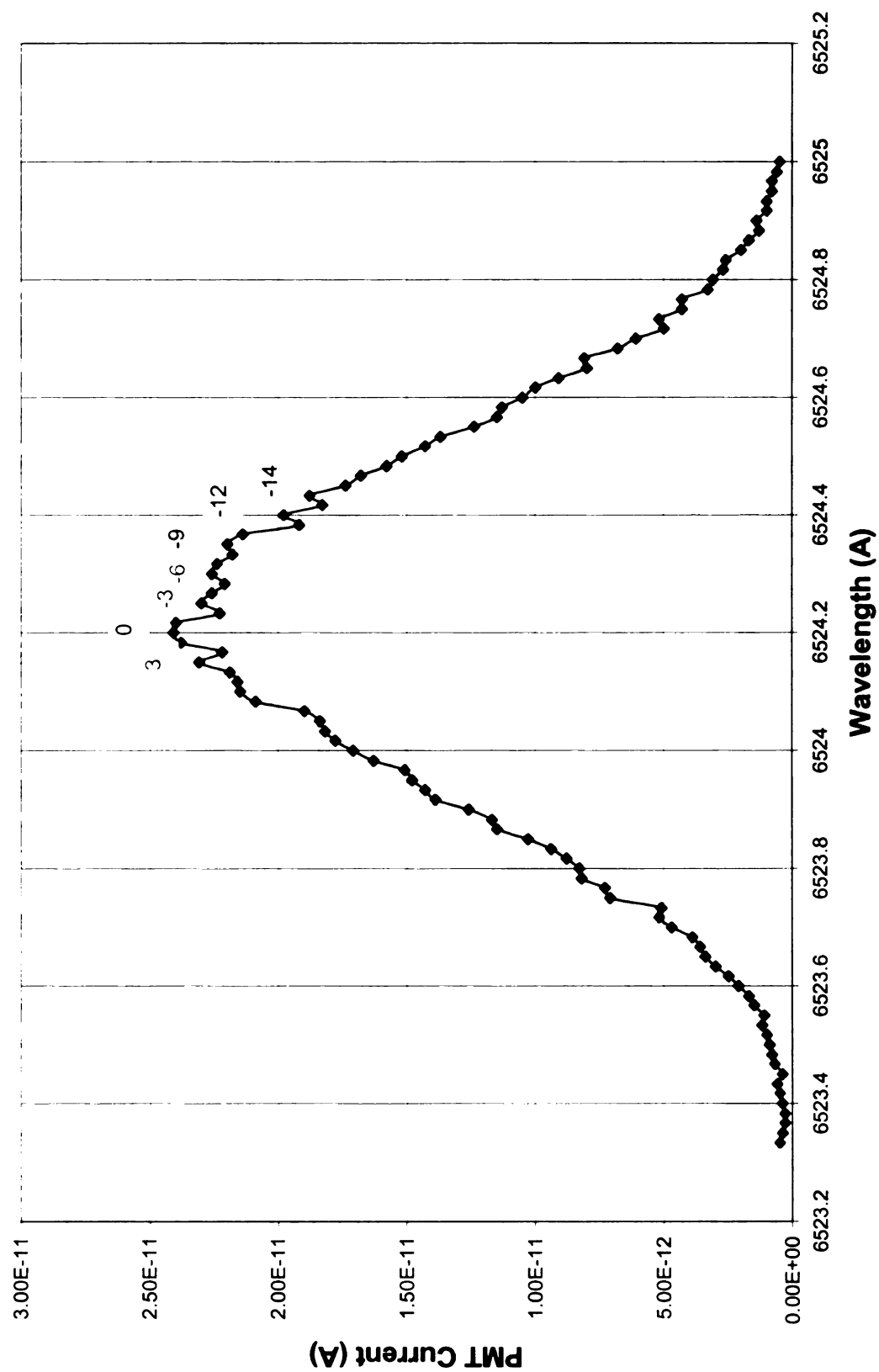
215

Figure 67 Hα Experimental Spectrum, 5.0 Torr.

216

Figure 68 Hα Experimental Spectrum, 0.5 Torr.

maximize power density; the electric probe gap fixed at 5 mm, the input power at the maximum power level of the microwave supply, 60 W. Hydrogen flow meters were set uniformly to 100 sccm. Critical peaks are identified on each of the three figures.

Figure 64 shows graphically the theoretical mixing of gross and fine structures at 50 Torr. The theoretical H_α spectrum given in Figure 64 and the experimental spectrum given in Figure 65 are consistent with an electric field estimate of 3858 V/cm. Critical peaks in Figures 64 and 65 are labeled.

The gross spectrum peaks are separated uniformly by 6 units (0.1 A) in Figure 64, approximately equal to the expected gross structure splitting (~6.40 units=0.1067 A) for the given electric field. The sharp nature of the peaks is unexpected; that is, Doppler broadening is not evident in the fine structure transitions. This point is addressed in Chapter 8 (section 8.1.3).

Figures 67-68, representing pressures of 5 Torr and 0.5 Torr, do not give as much detail. However, peak identification is still possible. Figure 66 gives the theoretical H_α spectrum response for applied electric fields that vary continuously through 4000 V/cm. Figure 66 connects the fine structure with no applied field to the mixing at ~4000 V/cm (3858 V/cm at 50 Torr). The peaks identified in Figure 66 map onto Figures 67-68; the associated electric fields are 2083 V/cm and 1875 V/cm for 5 and 0.5 Torr.

7.4.1.2 Stark Shift: H_β

Sections 5.8 and 6.3.1 develop the fine structure and gross structure for atomic hydrogen transitions from principle quantum numbers n=4 to n=2, the H_β energy spectrum. Figure 29 and Figure 39 give a graphical depiction of the fine and gross H_β

spectrum. Note that the k=0 transition is allowed for H_β (Figure 39), but the composite parabolic functions (1,1,1) and (0,0,1) are orthogonal.

Figure 69 [83] gives the H_β transition amplitudes for the parabolic eigenvectors, calculated using Equations 6.36-6.37 in section 6.3.1. Figure 71 and Figures 73-74 are the H_β spectrums from discharge experiments where the pressure was controlled at 50 Torr, 5.0 Torr, and 0.5 Torr, respectively, and all other operating conditions matched those given in the previous section for H_α experiments. Critical peaks are identified on each of the three figures.

The H_β peaks do not present the striking character of the H_α peaks; the peaks are neither sharp nor is the fine structure as easily unraveled. Gross structure peaks are Doppler broadened. However, it is still very possible to repeat the theoretical spectrum analysis of the previous chapter with fewer points.

Figure 70 shows graphically the theoretical mixing of gross and fine structures at 50 Torr for H_β. Figure 72 connects the fine structure with no applied field to the response at ~4000 V/cm (3890 V/cm at 50 Torr). The peaks identified in Figure 70 and Figure 72 map onto Figures 71 and Figures 73-74, respectively. The associated electric fields are given in Figure 72. As can be seen, the electric field strength of the hydrogen plasma taken from H_α and H_β spectral data, under identical operating conditions, are nearly identical.

In the theoretical H_β spectrum given in Figure 72, the gross spectrum begins to emerge and dominate at fields >4000 V/cm, and it becomes possible to estimate the electric field from gross structure splitting alone. Parabolic wave function energy levels
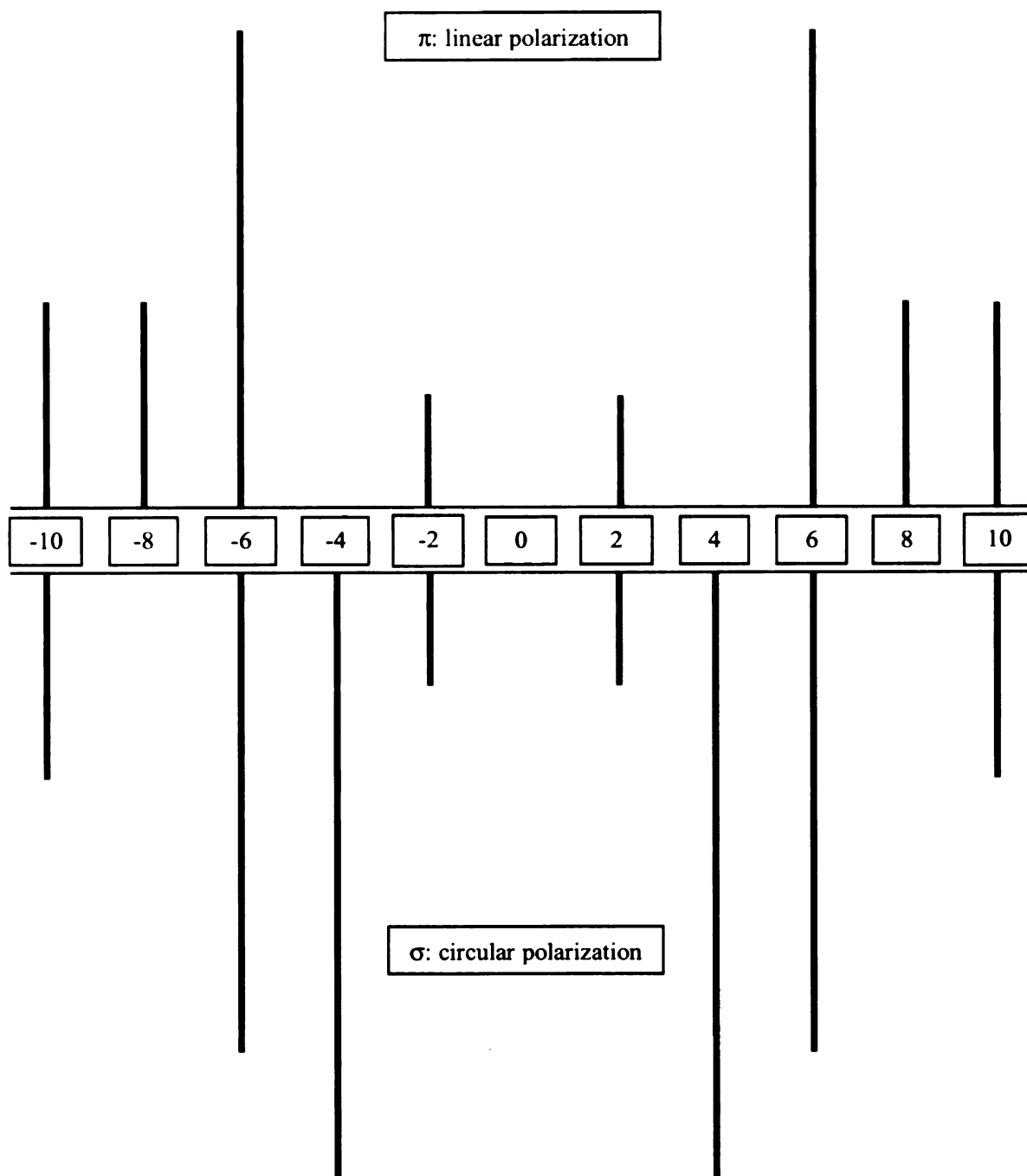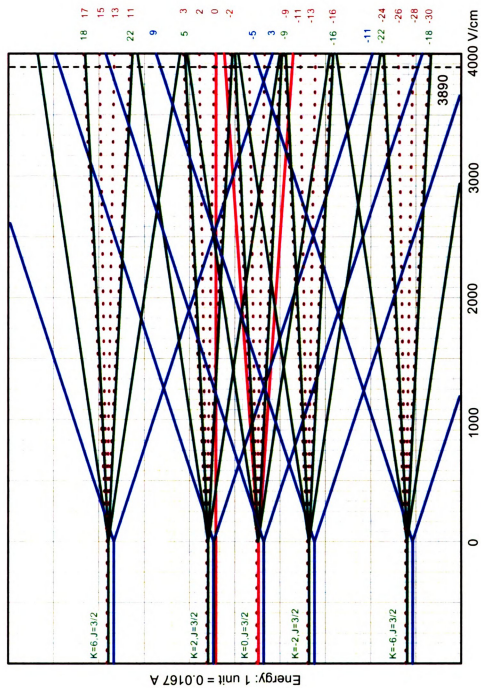
Figure 69 H_β Parabolic Transition Intensities.

220

Figure 70 H$_\beta$ Spectral Response: Gross and Fine Structure, 50 Torr.
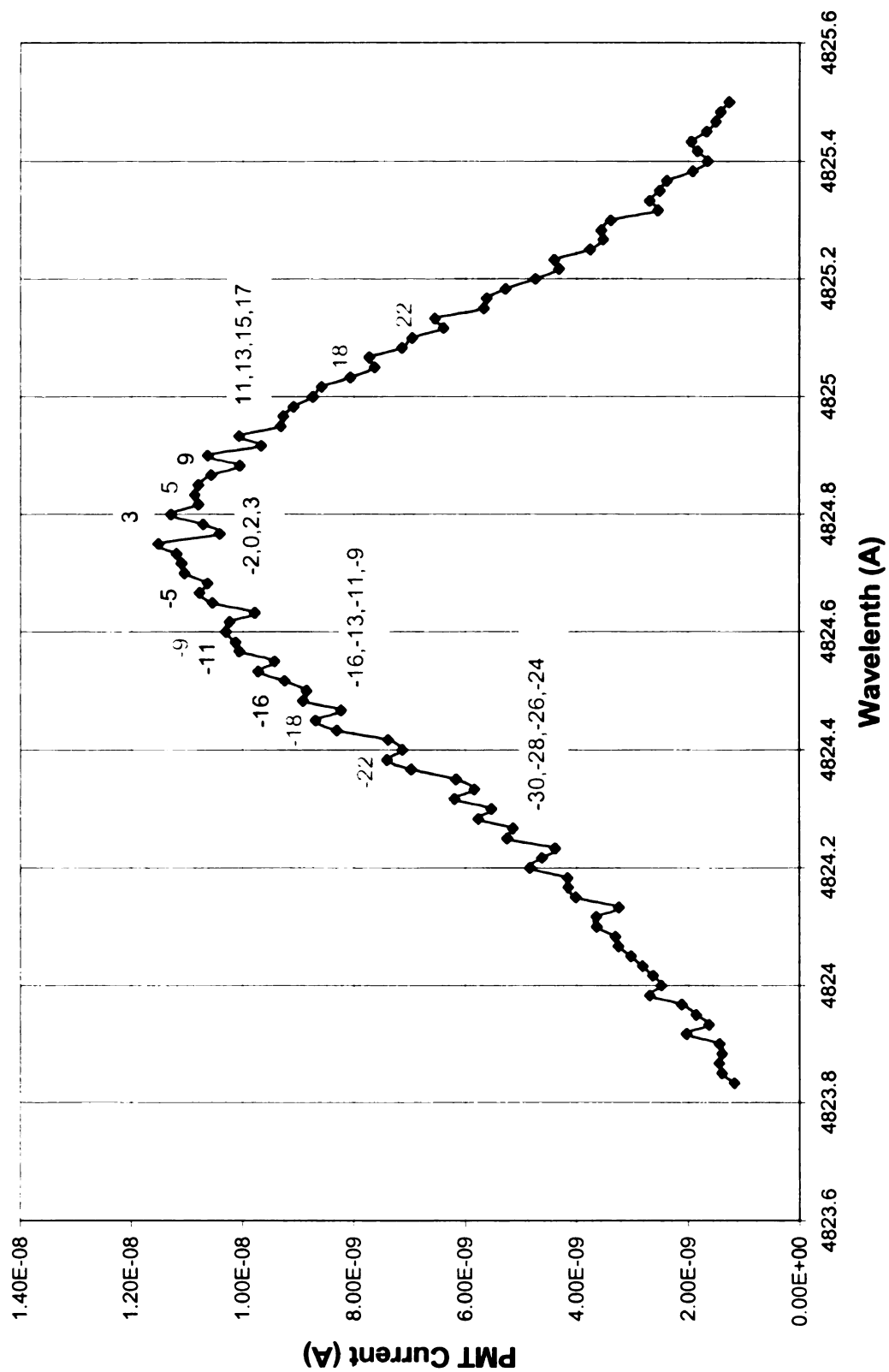
221

Figure 71 H$_\beta$ Experimental Spectrum, 50 Torr.

222
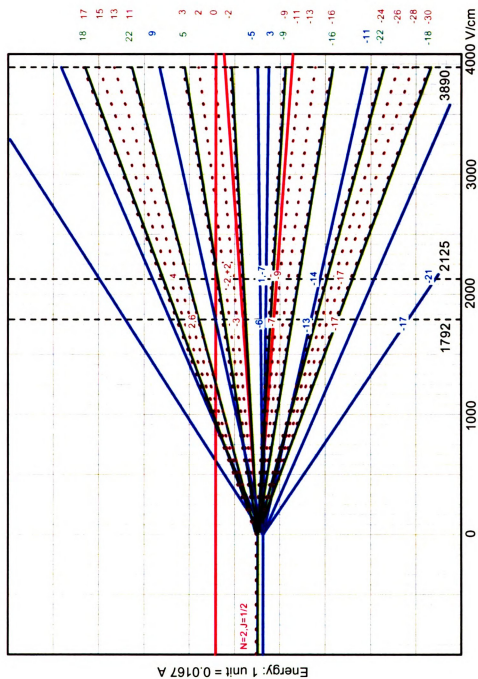
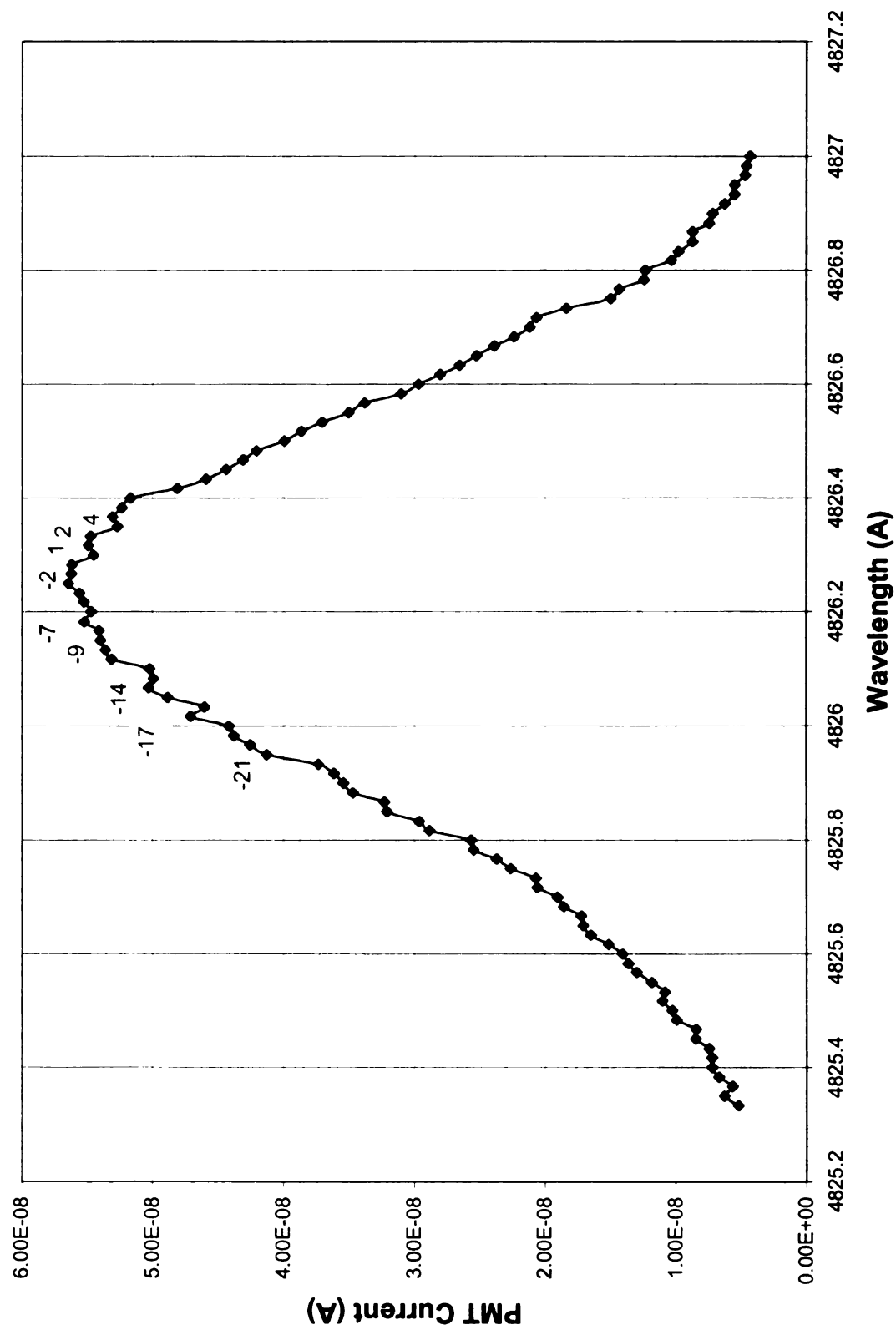**Figure 72** H_β Spectral Response: 0-4000V/cm Continuum.

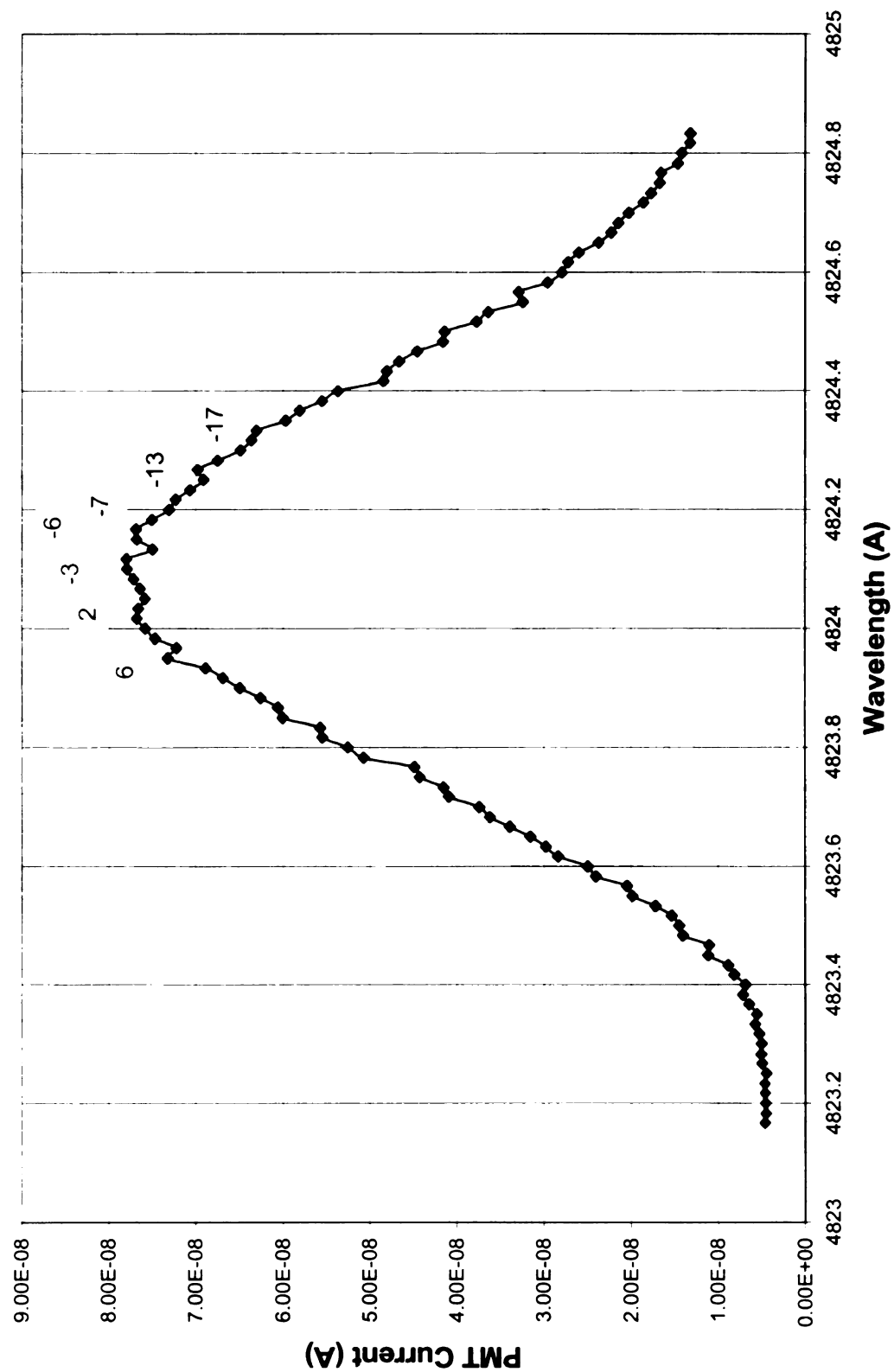**Figure 73** H$_\beta$ Experimental Spectrum, 5.0 Torr.

224

Figure 74 H$_\beta$ Experimental Spectrum, 0.5 Torr.

225

are separated uniformly by 3.3 units, or 0.236 cm⁻¹ (0.056 A). The corresponding electric field can be calculated by the following:

$$\frac{E_\beta}{E_\alpha} = \frac{\Delta W_\beta}{\Delta W_\alpha} = \frac{\dfrac{\Delta \lambda_\beta}{\lambda_\beta^2}}{\dfrac{\Delta \lambda_\alpha}{\lambda_\alpha^2}} = \frac{\dfrac{3.3units}{6.0units}}{\left[\dfrac{4861.33A}{6562.85A}\right]^2} = 1.00$$

(7.14)

$$\Rightarrow E_\beta = 1.00 E_\alpha = 3858 v/cm$$

The electric field estimate for H_β using only the parabolic energy level shifts is nearly the same as the full spectrum estimate, and identical to the electric filed estimate for the H_α band.

7.4.1.3 Stark Shift: H_γ

Figure 75 [83] gives the parabolic transition intensities for both linear and circular electric dipoles. Figure 76 gives the H_γ spectral data for operating conditions identical to those for H_α and H_β, at 50 Torr. Although noisier, it is still relatively easy to see the Doppler broadened gross structure peaks, separated by 2.7 units, or 0.237 cm⁻¹ (0.045 A). Accordingly, the estimated electric field from the H_γ data is:

$$\frac{E_\gamma}{E_\beta} = \frac{\Delta W_\gamma}{\Delta W_\beta} = \frac{\dfrac{\Delta \lambda_\gamma}{\lambda_\gamma^2}}{\dfrac{\Delta \lambda_\beta}{\lambda_\beta^2}} = \frac{\dfrac{2.7units}{3.3units}}{\left[\dfrac{4340.47A}{4861.33A}\right]^2} = 1.03$$

(7.15)

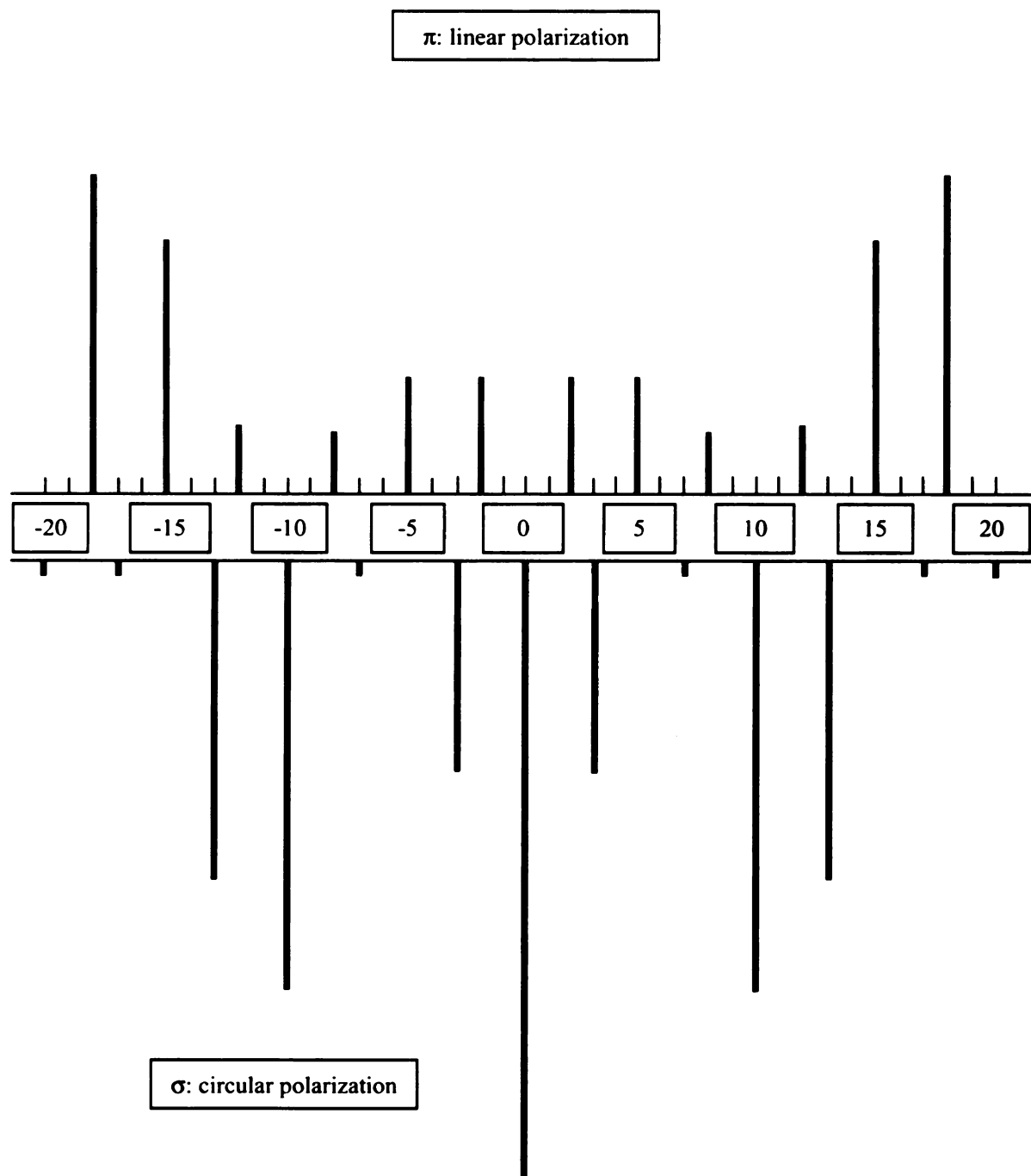$$\Rightarrow E_\gamma = 1.03 E_\beta = 3959 v/cm$$

226

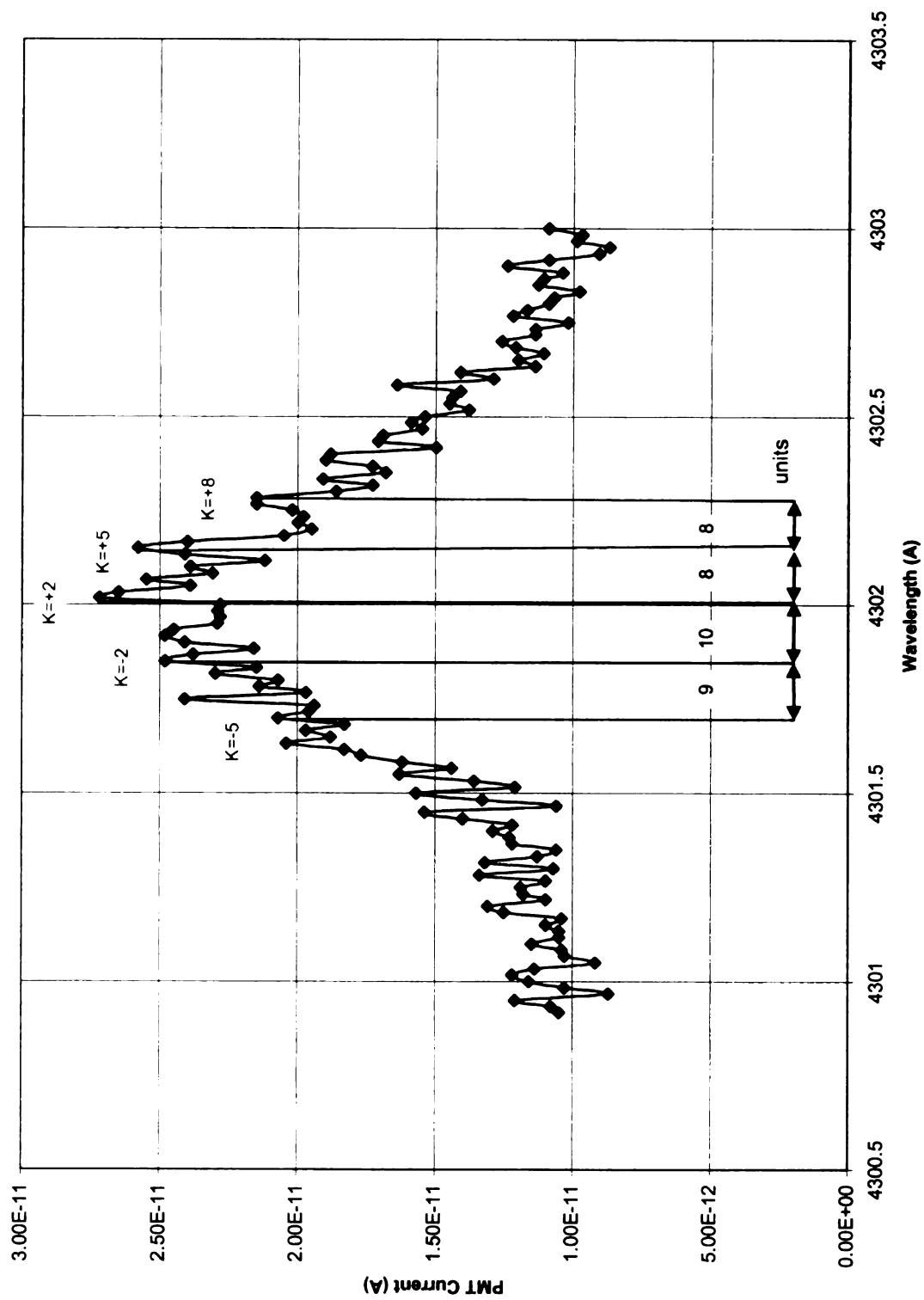**Figure 75** Hγ Parabolic Transition Intensities.

227

Figure 76 Hγ Experimental Spectrum (Gross Structure), 50 Torr.

Therefore, the electric field strength of the hydrogen plasma at 50 Torr, taken independently from H_α, H_β, and H_γ spectral data, agrees to within less than 3%. The electric field is plotted vs. pressure in Figure 77 on the following page. The resulting electric field strength is considerably greater in this set of experiments than that found in previous spectroscopic studies using higher principle quantum numbers (n=14-20) [84].

7.4.2 Electron Density

Stark broadening measurements of H_β lines were carried out in section 7.2.2 to ascertain electron densities for Argon. Stark broadening measurements for hydrogen follow this procedure; a sample H_β line is given at 100 Torr, in Figure 78. Figure 79 plots hydrogen electron density estimates of the hydrogen plasma for pressures from 0.1-100 Torr. For each experiment, the probe separation was set to 5 mm, the flow rate 100 sccm, the power 60 W.
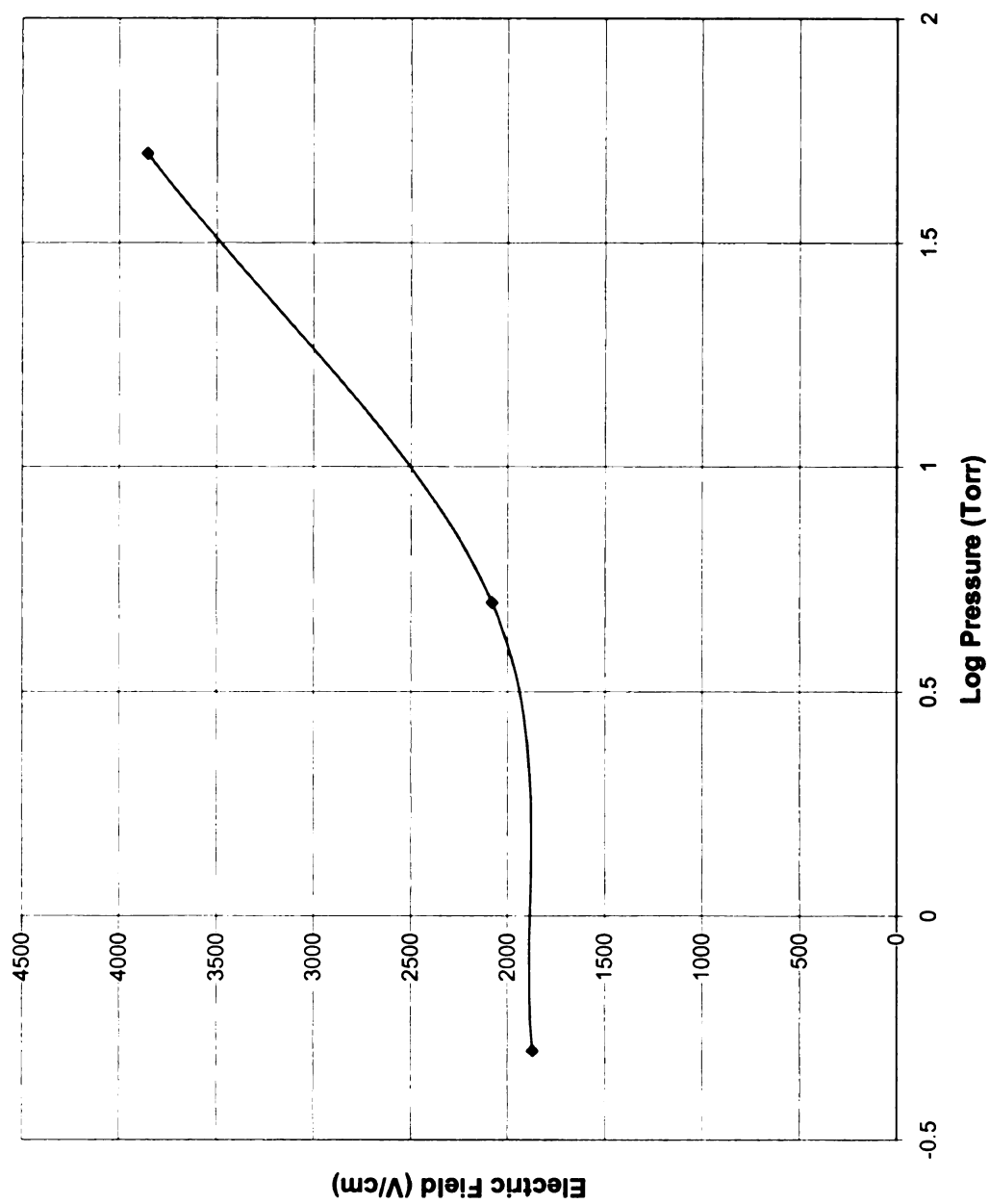
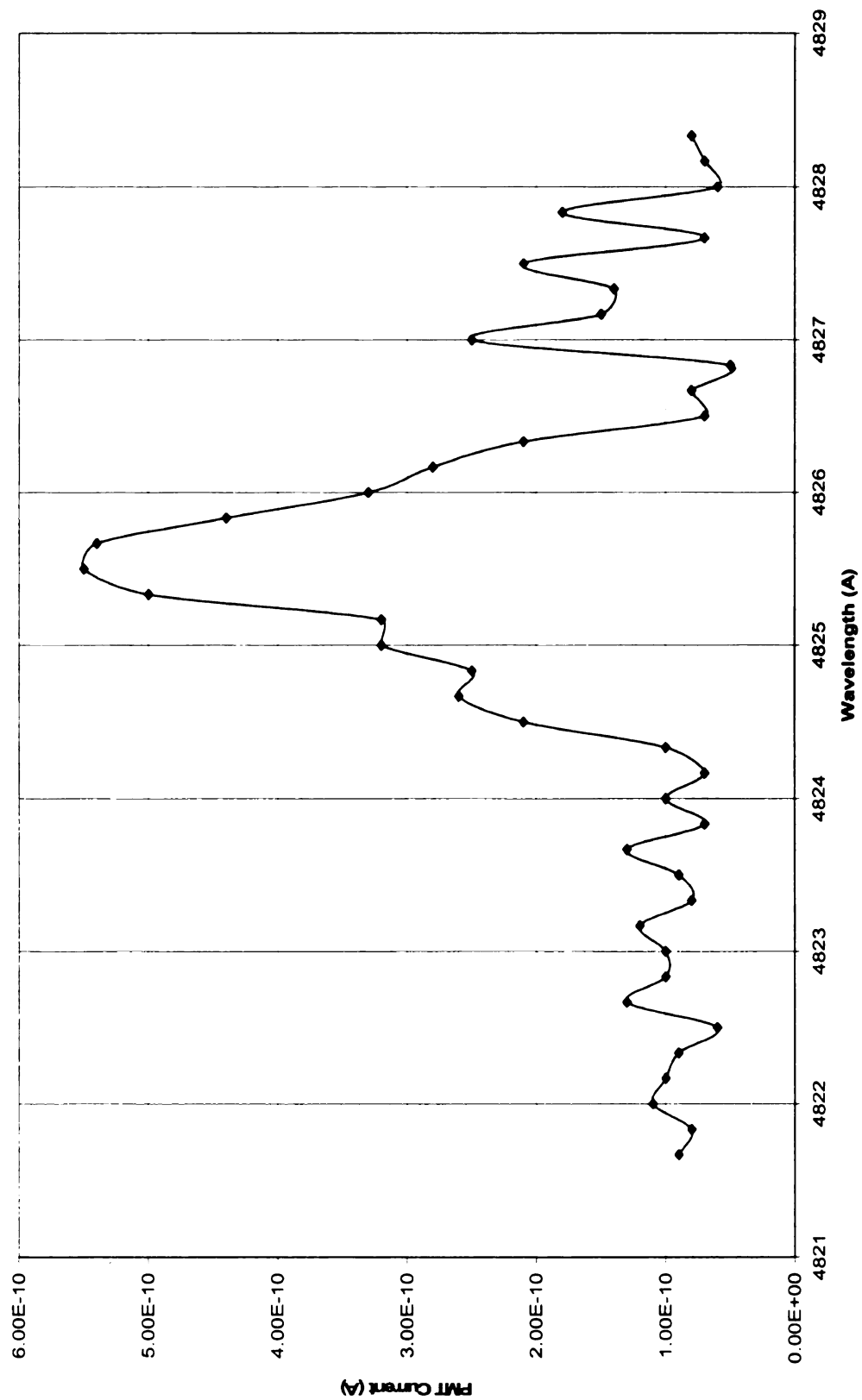**Figure 77** Electric Field vs. Pressure.

230

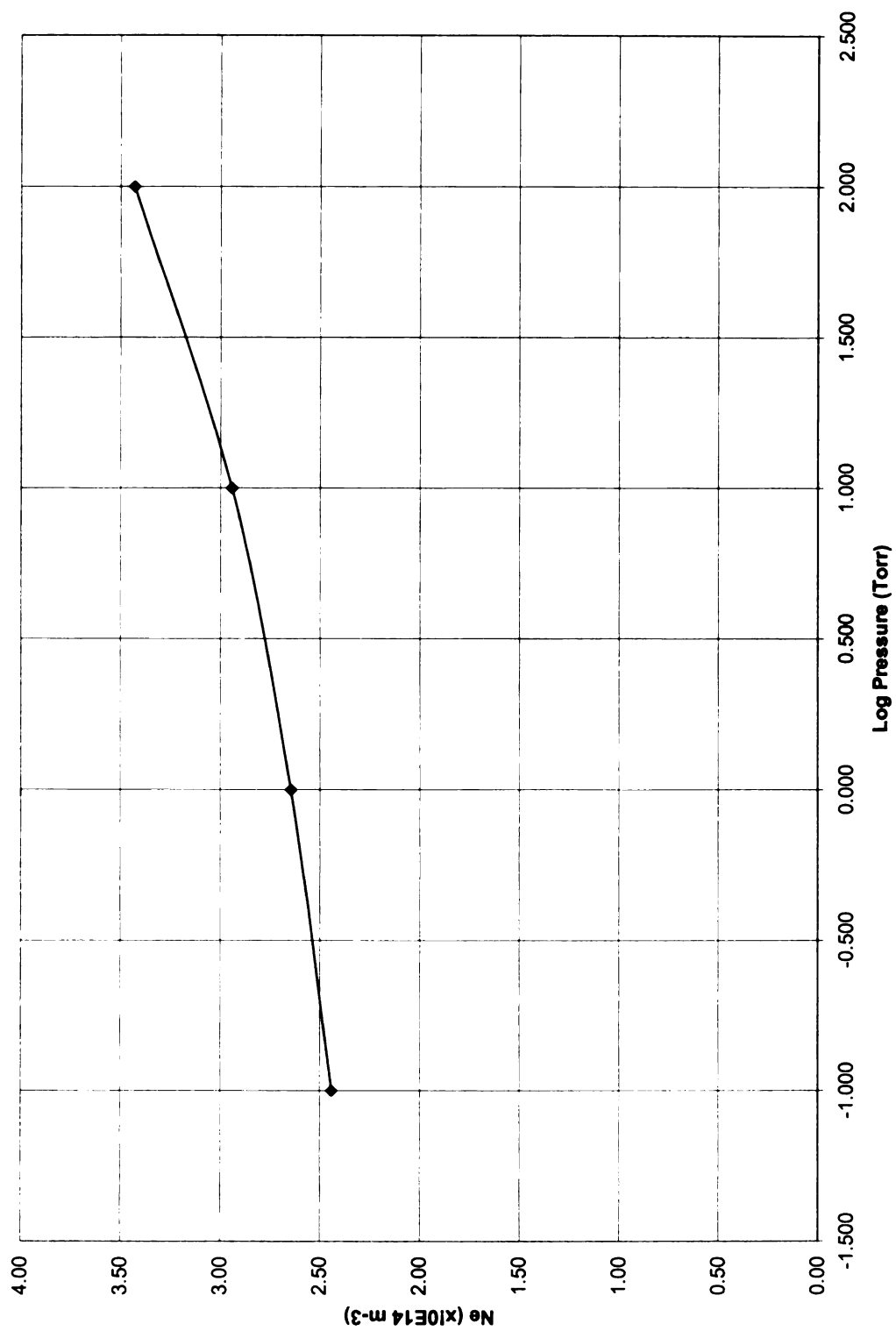**Figure 78** H$_\beta$ Spectrum, 100 Torr, 60 W., FWHM=1.241 A.

231

Figure 79 Hydrogen Electron Density vs. Pressure (60 W).

232

Chapter 8 Conclusion

The purpose of this investigation was to design and build a miniature microwave plasma system and associated diagnostic optics to collect spectroscopic information that would possibly reveal reasons for the plasma behavior as pressures are increased.

To this end, a new plasma system was created as a flexible test bed for experiments. A new optical system was designed and built to bring the collection lens system to within 5 mm of the plasma center. A sophisticated measurement technique was discovered to zero in on some of the fine structure associated with hydrogen and argon lines; taking advantage of nonlinearities in the response of the photomultiplier tube (PMT), the monochromagraph resolution was pushed beyond performance specifications.

The following sections target specific areas where the experimental results appeared contradictory or at odds with what might be expected from the experimental parameters.

8. 1 *Experimental Results*

Results from molecular and atomic hydrogen studies must be consistent with each other, and with each element of the theory that predicts these results. The next few sections examine the consistency of the results with respect to the electric field polarization, electric field magnitude, and atomic hydrogen spectral resolution.

8.1.1 Results: Electric Field Polarization

Assumptions made about the polarization of the electric field resident in the plasma were corroborated by experiments with atomic hydrogen: the absence of a center peak in both H_α and H_γ spectrums eliminates the possibility of a rotating electric field.

233

Further, the solid match of the atomic hydrogen experimental data to the theoretical spectrum verifies the presence of a linearly polarized electric field, a field that changes strength with changing pressure.

The experimental data for molecular hydrogen appears to contradict the absence of a rotating electric field. Zeeman splitting generates fifteen peaks; five peaks result from transitions involving linearly polarized fields, and five each from right and left hand circularly polarized fields.

This apparent contradiction is resolved graphically in Figure 80. The linearly polarized electric field is fixed along the z-axis, connecting the electric probes of a nearly capacitive discharge. In the reference frame of molecular hydrogen spinning about the circumferential axis, the electric field appears to be rotating; molecular orbitals experience a circularly polarized field. In the reference frame of molecular hydrogen spinning about the z-axis, the electric field appears stationary, and linearly polarized. The combination of hydrogen rotations –the molecular hydrogen domains aligned helically around the cylindrical discharge- explain the transitions associated with both linearly polarized and circularly polarized fields.

8.1.2 Results: Electric Field Magnitude

The electric field, calculated from the Stark shift spectral data, approximates an independent electric field calculation that follows from resonance principles. The quality factor can be expressed in two ways; the ratio of the resonant frequency to the full-width half-maximum (FWHM) frequency band, and the ratio of the stored energy to the applied
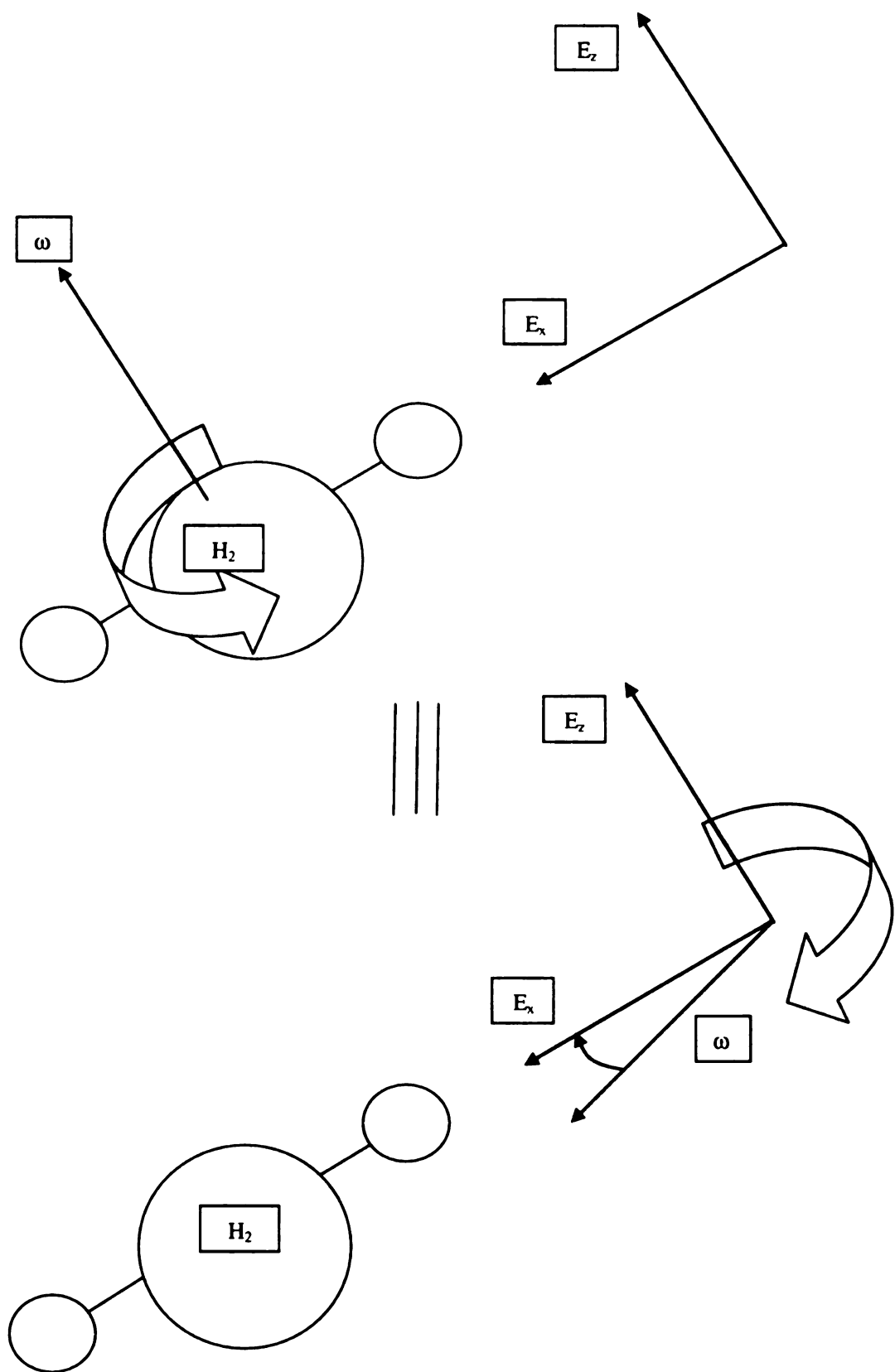
234

Figure 80 Electric Field Polarization for Molecular Hydrogen.

power. The former can be used to find the quality factor while the experiment is running; the latter allows for an approximation of the resident electric field.

The quality factor for the resonant cavity was found for experimental conditions identical to those of the experimental set that was used to find the Stark shift in the hydrogen plasma, with pressure set to 50 Torr. At low power, the input power dropped to half of its original value when the cavity length was increased by approximately 0.5 cm.

As a result,

$$Q = \frac{f_{res}}{\Delta f_{FWHM}}$$

$$\frac{3}{2}\lambda_{res} = \frac{3}{2}\frac{f_{res}}{c} = 18.73cm$$

$$\frac{3}{2}\lambda_{FWHM} = 18.73cm + 0.5cm = 19.23cm \tag{8.1}$$

$$\Delta f_{FWHM} = 2\left[f_{res} - \frac{c}{\lambda_{FWHM}} \right] = 0.220GHz$$

$$Q = \frac{f_{res}}{\Delta f_{FWHM}} = 11.15$$

The transverse electric field in the resonant cavity (E_r) can be approximated by,

$$Q = \frac{\omega_{res}W}{P} = \frac{\sum 2\pi f_{res}\varepsilon_0 E_r^2}{P}\delta Vol$$

$$= \frac{2\pi f_{res}\varepsilon_0 E_r^2}{P}2\pi\frac{3}{2}\lambda_{res}\int RdR\frac{R_0^2}{R^2}$$

$$= \frac{(2\pi)^2 R_0^2\varepsilon_0 E_r^2}{P}\frac{3}{2}c\ln\frac{R}{R_0}$$

(8.2)

$$= 1.063 \times 10^{-3}E_r^2(v/cm)$$

Where R/R_0 is the ratio of the outer to inner coaxial diameters. For gaps (Δd) much less than one-quarter wavelength, the resonant (transverse) field E_r is related to the field between the two probes E_p by,

$$E_p = \frac{\Delta V}{\Delta d} = \frac{1}{\Delta d}\frac{\Delta d}{\frac{1}{4}\lambda_{res}}E_r\int dR\frac{R_0}{R} = \frac{E_r R_0}{\frac{1}{4}\lambda_{res}}\ln\frac{R}{R_0}$$

(8.3)

$$= 0.266E_r(v/cm)$$

Now, the ratio of the electric field at the plasma sheath (E_s) to the electric field between the probes is approximately equal to the ratio of their surface areas. Combining with Equations 8.1-8.3:

$$\gamma_{area} \cong \frac{A_{sheath}}{A_{probe}} \cong \frac{\pi R_{sheath}^2}{\pi R_0^2} = \left(\frac{D_{sheath}}{D_0}\right)^2 = \left(\frac{1.0mm}{10mm}\right)^2 = 0.01$$

$$E_s = \frac{1}{\gamma_{area}} E_p(v/cm) = \frac{0.266}{\gamma_{area}} \sqrt{\frac{Q}{1.063x10^{-3}}} \qquad (8.4)$$

$$\cong 2725(v/cm)$$

The electric field at the sheath is of the same order of magnitude as that found in sections 7.4.1-7.4.3 (3858 V/cm) using the Stark effect shift. Figure 81 illustrates the electric field structure in the resonant cavity.

8.1.3 Results: Atomic Hydrogen Spectral Resolution

The spectral resolution is sharper and the magnitude greater in the set of peaks corresponding to H_α fine structure transitions (n,j)=(3,3/2)>(n,j)=(2,1/2), and to a lesser extent, the other peaks as well. Normally, these peaks are not this sharp, the resolution reduced by instrument broadening and Doppler broadening.

The effects of Instrument broadening were reduced by adjusting the accelerating voltage to push the photo-multiplier tube (PMT) to operate in its nonlinear range (section 7.1, Figure 42). As a result, the slope of each dI/dt response from the PMT that was above the threshold was magnified. The PMT effectively took on characteristics of a detector.

The narrowing of Doppler broadened spectra is more involved. Figure 64, in Section 7.4.1, shows the theoretical interweaving of the Stark effect for both gross and
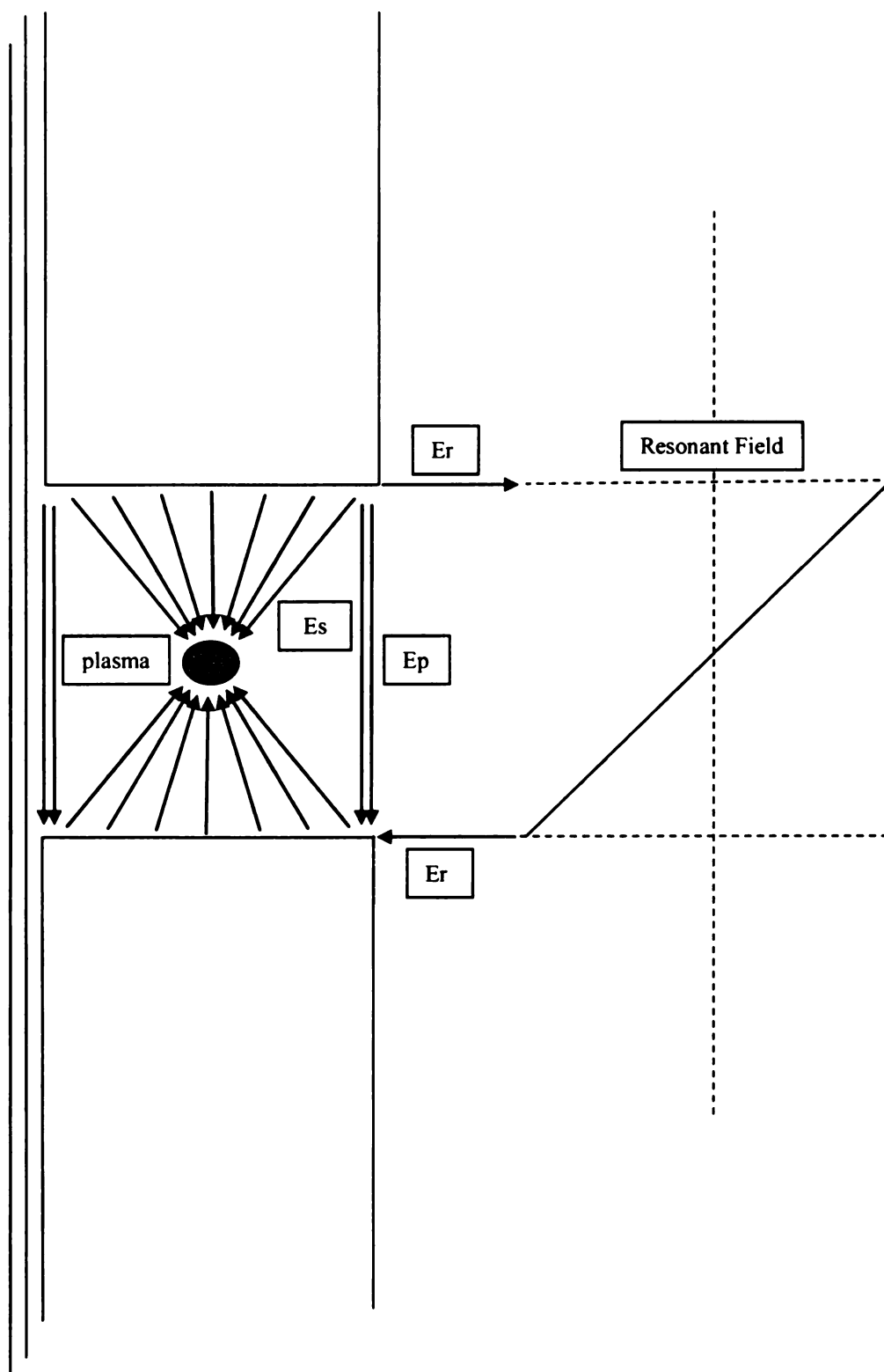
Figure 81 Electric Field in Resonant Reactor Chamber.

239

fine structure in the H_α line. Figure 64 allows for the location of 25 independent transitions, shown graphically on Figure 65. Figure 64 also helps explain why the H_α peaks are much sharper than expected, and why H_β and H_γ peaks are not. The explanation follows.

With an applied field of exactly 3858 V/cm, levels j=3/2 and j=1/2 in n=2 are coupled by the microwave power source at 2.45 GHz. Electrons in the lower level are raised to the upper level by the strong overlap between (n,j)=(3,5/2) and (n,j)=(2,3/2) waveforms.

Now, transitions from (n,j)=(3,5/2) to (n,j)=(2,3/2) and (n,j)=(2,1/2) are recorded by the spectrometer. Additionally, the photon released in these transitions interacts with atomic hydrogen orbitals that are immersed in a strong microwave standing field. This modulates the interaction energy of the photon by +/-2.45 GHz. The new modulated energy of the photon is exactly the amount necessary to raise electrons from the (n,j)=(2,1/2) and (n,j)=(2,3/2) levels into several of the (n,j)=(3,1/2) gross structures. The energy released in the transition of these energy levels to a lower state is modulated, and continues a chain reaction in which each of the upper states are tied to each other through a series of transitions in the optically thick plasma.

The important point is that this chain reaction is initiated by microwave energy absorbed in the lower band [85], and kept going by the same strong microwave source, frequency modulating the photon energy released in upper-to-lower band transitions. To absorb the exact amount of energy, the hydrogen atoms must be relatively stationary with respect to the standing electromagnetic field [86]. Thus, the emission in the visible spectrum will come from atoms with very small velocities, defeating Doppler

broadening. This effect is similar to that found in laser spectroscopy [87], and was only

observed in this set of experiments where the electric field was found to be ~3800 V/cm.

Another explanation for the relative absence in Doppler broadening is that, as the

plasma is optically thick, the only emissions escaping to the PMT are emissions from

atoms along the perimeter of the plasma. Whether confined in motion by the quartz tube,

or confined by the same forces that constrain the plasma, atoms at the perimeter of the

plasma have very low velocity; the edge of the plasma is the turning point for atoms with

velocities less than escape velocity. As a result, the Doppler broadened line width is

narrowed, reflecting the nearly static hydrogen atoms at the plasma edge, in the direction

that the light is emitted.

This condition is *not* related to the constant velocity, or Bohm velocity (u_B), of

hydrogen ions at the plasma sheath (section 4.1.1). Obviously, H^+ ions have no electrons,

and therefore no electronic emission.

One additional point. The gross structure Stark splitting at 3858 V/cm is predicted

to be 0.1067 A, or 6.40 units, from theory. The gross structure splitting on either side of

the centerline is exactly 6.0 units. The gross structure splitting *between* the left and right

side –that is, the energy difference between the k=+2 and k=–2 parabolic energy levels-

does appear to be exactly 6.40 units.

A rigorous explanation for this effect would be very difficult. The gross structure

energy levels are locked to the fine structure transitions by the nonlinear nature of the

interaction between photon and the atomic orbital and spin-orbit coupling, and in this

case the microwave field. This effect, called mode locking, is common place in physics;

from optical scattering in multi-mode fiber, to clock pendulums mounted on a common wall.

8. 2 *Discussion*

Results from this investigation indicate that a constant magnitude magnetic field and a constant magnitude electric field are both sustained by the plasma, evident in the hydrogen spectrum by strong Zeeman and Stark splitting. These fields are not the applied microwave electromagnetic components; the applied microwave components are sinusoidal, and would imprint a continuous spectrum about the center wavelength, which is also evident.

Furthermore, the impressed magnetic and electric field strengths are not related; the magnetic field decreases with pressure, the electric field increases, as shown in Figures 57 (section 7.3.1.2) and 77 (section 7.4.2).

One possible explanation for the constant magnitude magnetic field is the following: the hydrogen molecules spin in the same direction and align in concentric rings around the plasma center under the strong influence of the microwave H field. Hydrogen is diamagnetic, with very small k ($\sim$-0.2x10^{-2}) [53], but the collection of hydrogen molecules forms domains that are circumferential to the plasma.

If this were the case, one would expect very high rotation temperatures at low pressures. Rotation temperatures should first decrease, due to collisions, then increase as the pressure is increased. This is seen in experimental data.

As with domains in ferrous material, the hydrogen magnetic field does not flip until the microwave field has reversed itself hard enough. At that point, the molecular

spin reverses to its maximum value nearly at once. As a result, the H vs. B plot looks like a standard hysterisis curve.

Furthermore, contractions at higher pressures can be seen as a direct interaction of the spinning hydrogen molecules and the magnetic field gradient set up at the edge of the plasma by internal collisions. The Lorentz force imbalance exerted on the current loop defined by the protons rotating about their center axis pushes the plasma to the center of the reactor. At lower pressures, the magnetic field gradient is not present.

The constant electric field is more difficult to understand, and there will be no proposal for its mechanism at this time.

Improvements to the experiment mostly involve equipment. Hydrogen bonding and spin effects could be monitored by infrared and microwave spectroscopy, respectively. In the optical spectrum, higher pressures could be monitored by CCD spectroscopy; the higher frame rates would eliminate the concern for noise jitter due to instabilities in contraction. Further, spatial resolution –multiple optics channels- would provide interesting comparisons between the plasma center and edge, where magnetic field gradients are suspected.

It is uncertain whether higher resolution optical spectroscopy is the answer. The Lummer-Gehrcke plate [88] requires no slit, increasing signal intensity, and provides spectral data accurate to 10^{-4} cm^{-1}. But, the sinusoidal microwave fields may overwhelm the finer structure, and blur out any advantage.

At this point, there are more questions than answers, and almost limitless avenues to pursue in the understanding of the miniature plasma formed by microwave plasma sources.

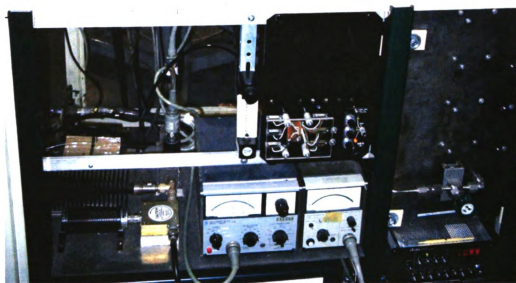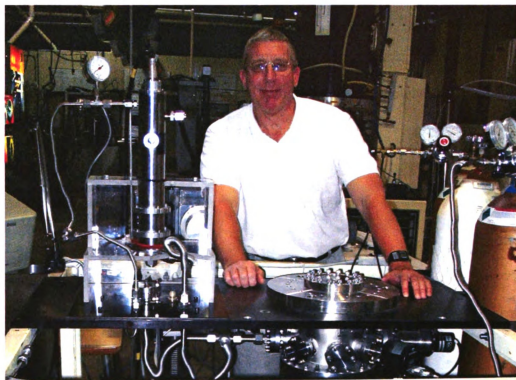# Appendix A   Plasma System and Components
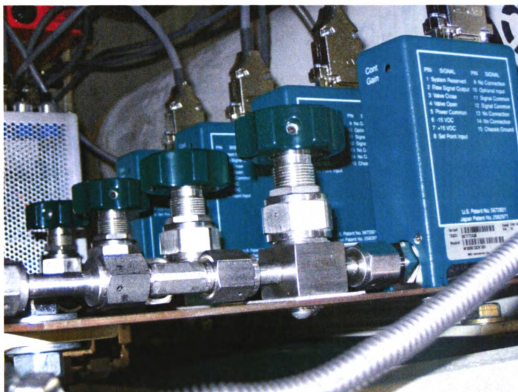

Figure 82 Miniature Microwave Plasma System.

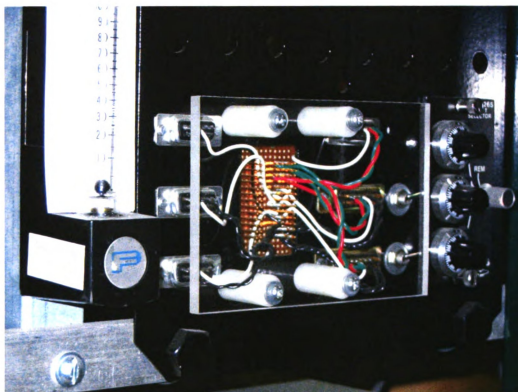**Figure 83** Gas Flow Meter Bank (4 Channel).

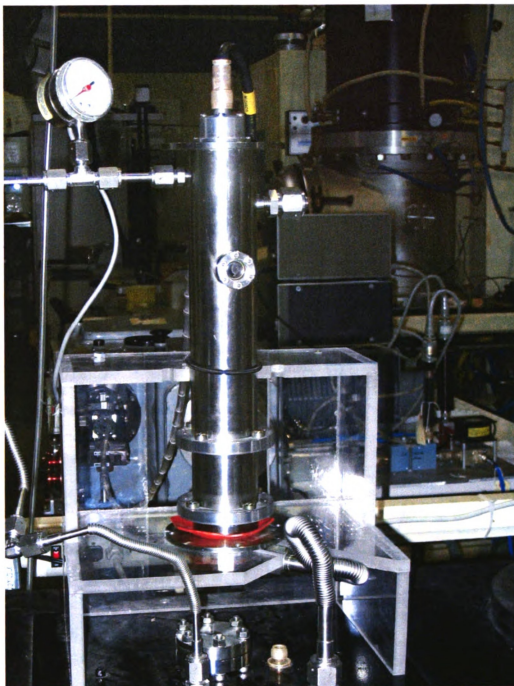
Figure 84 Electronics Control Board.

Figure 85 Plasma Reactor Chamber.
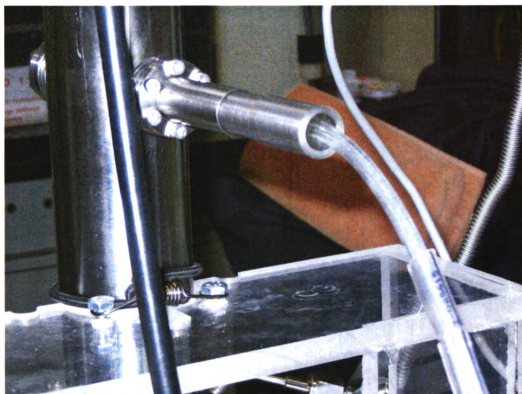
Figure 86 Fiber Optic Feed-Through (13 Channels).
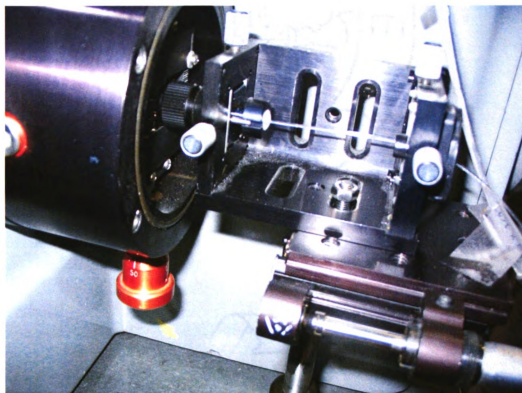

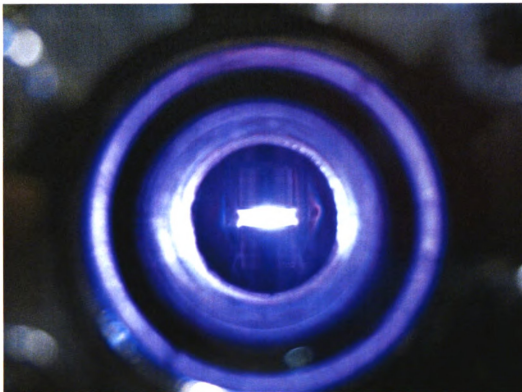**Figure 87** Optical Fiber Micro-Positioner (OES).

247

Figure 88 Hydrogen Plasma; 0.5 Torr, 60 W.
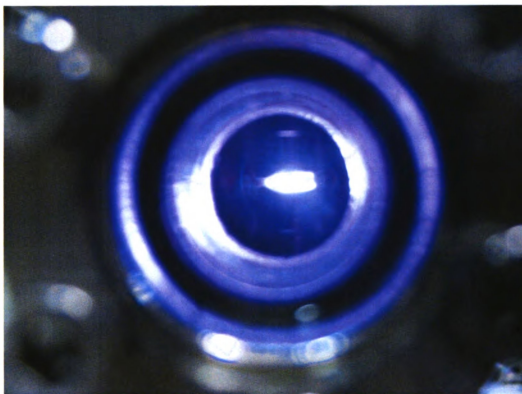

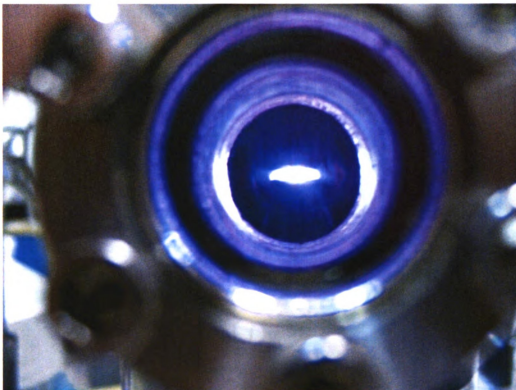**Figure 89** Hydrogen Plasma; 5.0 Torr, 60 W.

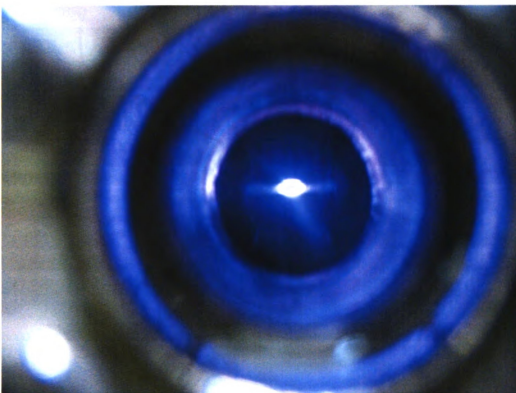**Figure 90** Hydrogen Plasma; 10.0 Torr, 60 W.

Figure 91 Hydrogen Plasma; 50 Torr, 60 W.

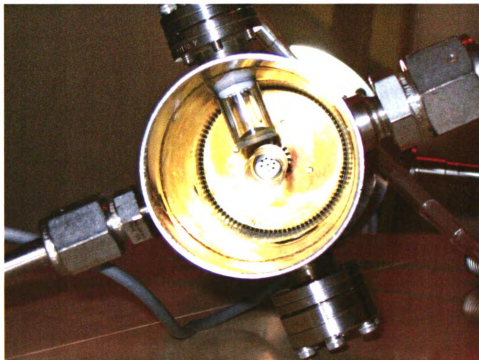# Appendix B   Fiber Optic Feed-Through

Figure 92 Reactor Chamber with Fiber Optic Feed-Through.
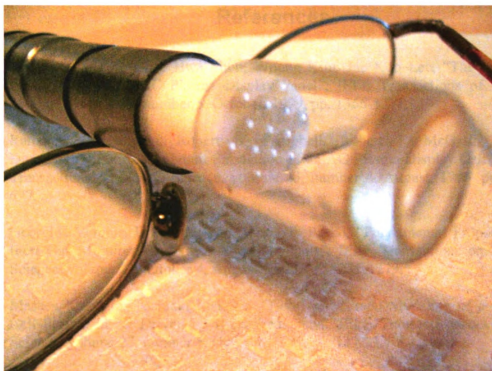

Figure 93 Fiber Optic Feed-Trough.

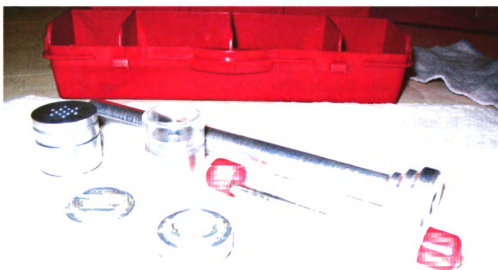**Figure 94** Feed-Trough Micro-Lens System (13 Channels).

Figure 95 Feed-Through Construction Tool Set.

References

[1]   Young Kyo Shin, Chae Hwa Shon, Woong Kim, Jae Koo Lee, "The Voltage-Pulsing Effects in AC Plasma Display Panel", IEEE Transactions of Plasma Science, volume 27, number 5, October, 1999, pp. 1366-1371.

[2]   Ramana Veerasingam, Robert B. Campbell, Robert T. McGrath, "One-Dimensional Fluid and Circuit Simulation of an AC Plasma Display Cell", IEEE Transactions on Plasma Science, volume 23, number 4, August, 1995, pp. 688-697.

[3]   Georgios Veronis, Umran S. Inan, Victor P. Pasko, "Fundamental Properties of Inert Gas Mixtures for Plasma Display Panels", IEEE Transactions on Plasma Science, volume 28, number 4, August, 2000, pp. 1271-1279.

[4]   Masaeu Kurihara, Toshiaki Makabe, "Two-Dimensional Modeling of a Micro-Cell Plasma in Xe Driven by High Frequency", IEEE Transactions on Plasma Science, volume 27, number 5, October, 1999, pp. 1372-1378.

[5]   A.M. Bilgic, U. Engel, E.Voges, M.Kuckelheim, T.A.C. Broekaert, "A New Low-Power Microwave Plasma Source Using Microstrip Technology for Atomic Emission Spectroscopy", Plasma Source Science and Technology, volume 9, 2000, pp. 1-4.

[6]   P. Siebert, G. Petzold, A. Hellenbart, J. Muller, "Surface Microstructure/ Miniature Mass Spectrometer: Processing and Applications", Applied Physics: Materials Science and Processing, A67, 1998, pp. 155-160.

[7]   Yo Yin, Jason Messier, Jeffrey A. Heywood, "Miniaturization of Inductively Coupled Plasma Sources", IEEE Transactions on Plasma Science, volume 27, number 5, October, 1999, pp. 1516-1524.

[8]   V. Kapicka, M. Sicha, M. Klima, Z. Hubicka, J. Tous, A. Brablec, P. Slavicek, J.F. Behnke, M. Tichy, R. Vaculik, "The High Pressure Torch Discharge Plasma Source", Plasma Source Science and Technology, volume 8, 1999, pp. 15-21.

[9]   J. Janca, A. Talsky, "Microwave Torch Combined with Conventional Burner", Journal de Physique IV, volume 8, 1998, pp. 349-365.

[10]   M. Moisan, Z. Zakrzewski, J.C. Rostaing, "Waveguide-Based Single and Multiple Nozzle Plasma Torches: The TIAGO Concept", Plasma Source Science and Technology, volume 10, 2001, pp. 387-394.

[11]   Alexey A. Goncharov, Sergey M. Gubarev, Andrey N. Dobrovolski, Ivan M. Protsenko, Irina V. Litovko, Ian G. Brown, "Moderate Energy Metal Ion Beam

Focusing by a High-Current Plasma Lens", IEEE Transactions on Plasma Science, volume 27, number 4, August, 1999, pp. 1068-1072.

[12]   Alexey A. Goncharov, Irina V. Litovko, "Electron Vortexes in High-Current Plasma Lens", IEEE Transactions on Plasma Science, volume 27, number 4, August, 1999, pp. 1073-1078.

[13]   J. Janca, L. Zajickova, M. Klima, P. Slavicek, "Diagnostics and Application of the High Frequency Plasma Pencil", Plasma Chemistry and Plasma Processing, volume 21, number 4, December, 2001, pp. 565-579.

[14]   Karl H. Schoenbach, Ahmed El-Habachi, Wenhui Shi, Marco Ciocca, "High-Pressure Hollow Cathode Discharges", Plasma Sources Science and Technology, volume 6, 1997, pp. 468-477.

[15]   R.R. Arslanbekov, A.A. Kudryavtsev, R.C. Tobin, "On the Hollow-Cathode Effect: Conventional and Modified Geometry", Plasma Source Science and Technology, volume 7, 1998, pp. 310-322.

[16]   J. Asmussen, D.K. Reinhard, "Diamond Films Handbook", New York, Marcel Dekker, Inc., 2001.

[17]   C.F.M. Borges, M. Moisan, A. Gicquel, "A Novel Technique for Diamond Film Deposition Using Surface-Wave Discharges", Diamond and Related Material, volume 4, 1995, pp. 149-154.

[18]   Meng-Hua Tsai, "Characterization and Modeling of a Compact ECR Plasma Source Designed for Materials Processing", Dissertation for the Degree of Ph.D., Michigan State University, 1999.

[19]   John F. Waymouth, "Chapter 2: Plasma Diagnostics in Electric Discharge Light Sources", Discharge Parameters and Chemistry, New York, Academic Press, Inc., 1989.

[20]   Richard A. Gottscho, Terry A. Miller, "Optical Techniques in Plasma Diagnostics", Pure and Applied Chemistry, volume 56, number 2, 1984, pp. 189-208.

[21]   V. M. Donnelly, "Chapter 1: Optical Diagnostic Techniques for Low Pressure Plasmas and Plasma Processing", Discharge Parameters and Chemistry, New York, Academic Press, Inc., 1989.

[22]   H.R. Griem, "Spectral Line Broadening by Plasmas", New York, Academic Press, 1974.

[23] G. King, "Temperature and Concentration of Ionic and Neutral Species in Resonant Microwave Cavity Plasma Discharges", Dissertation for the Degree of Ph.D., Michigan State University, 1994.

[24] A. Gamero, "Spectroscopic Diagnostics of High Pressure Discharges", Journal de Physique IV, volume 8, 1998, pp. 339-348.

[25] J. Sivagnaname, "Optical Emission Spectroscopy Investigation of Microwave Plasmas", Dissertation for the Degree of M.S., Michigan State University, 1998.

[26] D. Story, "Experimental Investigation of Mini-Microwave Plasma Sources", International Conference on Plasma Pulsed-Power, June, 2001.

[27] G. Goousset, "Modeling of Microwave Reactors: Microwave and Kinetics in Gas Flow Approaches", Journal de Physique IV, volume 8, 1998, pp. 21-32.

[28] V. Rat, J. Aubreton, M.F. Elchinger, P. Fauchais, "Calculation of Combined Diffusion Coefficients from the Simplified theory of Transport Properties", Plasma Chemistry and Plasma Processing, volume 21, number 3, 2001, pp. 355-369.

[29] David J. Smith, Colin J. Whitehead, Robbie Stewart, "Complimentary Optical Diagnostics for Determination of Rate Coefficients and Electron Temperatures in Noble Gas Discharges", Plasma Source Science and Technology, volume 11, 2002, pp. 115-126.

[30] A.A. Matveyev, V.P. Silakov, "Electron Energy Distribution Function in a Moderately Ionized Argon Plasma", Plasma Source Science and Technology, volume 10, 2001, pp. 134-146.

[31] He-Ping Li, Xi Chen, "Three-Dimensional Modeling of the Turbulent Plasma Jet Impinging Upon a Flat Plate and with Transverse Particle and Carrier-Gas Injection", Plasma Chemistry and Plasma Processing, volume 22, number 1, March, 2002, pp. 27-58.

[32] S. Gundermann, R. Winkler, "Microwave Diagnostics in Diffusive and Constricted Medium-Pressure Discharges", Plasma Chemistry and Plasma Processing, volume 20, number 1, 2000, pp. 111-135.

[33] K. Hassouni, T.A. Grotjohn, A. Gicquel, "Self-Consistent Microwave Field and Plasma Discharge Simulations for a Moderate Pressure Hydrogen Discharge Reactor", Journal of Applied Physics, volume 86, number 1, 1 July, 1999, pp. 134-151.

[34] J.A. Bittencourt, "Fundamentals of Plasma Physics", Oxford, Pergamon Press, 1986.

[35]   Michael A. Lieberman, Allan J. Lichtenberg, "Principles of Plasma Discharges and Materials Processing", New York, John Wiley and Sons, Inc., 1994.

[36]   R.J. Goldston, P.H. Rutherford, "Introduction to Plasma Physics", London, Institute of Physics Publishing, 1995.

[37]   R. Byron Bird, Warren E. Stewart, Edwin N. Lightfoot, "Transport Phenomena", John Wiley & Sons, Inc., New York, 1960.

[38]   Francis F. Chen, "Introduction to Plasma Physics", Plenum Press, New York, 1974.

[39]   T. Grotjohn, J. Asmussen, "MSU EE 989A and NTU IC 734-MS Class Notes", Michigan State University, June-August, 1997, lectures 11-12.

[40]   Amnon Yariv, "Quantum Electronics", 3rd Ed., John Wiley & Sons, Inc., New York, 1989.

[41]   Stephen Gasiorowicz, "Quantum Physics", 2nd Ed., John Wiley & Sons, Inc., New York, 1996.

[42]   J.J Sakurai, "Modern Quantum Mechanics", Addison-Wesley Publishing Company, Inc., Redwood City, California, 1985.

[43]   Albert Messiah, "Quantum Mechanics", Dover Publications, Inc., Mineola, New York, 1999.

[44]   E.T. Whittaker, G.N. Watson, "A Course of Modern Analysis", 4th Ed., Cambridge University Press, 1927.

[45]   W. Pauli, "On the Connexion Between the Completion of Electron Groups in an Atom with the Complex Structure of Spectra", Z. Physik, vol. 31, 765ff, 1925.

[46]   "Selection Rules for Electronic Transitions", www.hyperphysics-astr.gsu.edu, undated.

[47]   Istvan Kovacs, "Rotational Structure in the Spectra of Diatomic Molecules", American Elsevier Publishing Company, Inc., New York, 1969.

[48]   "Larmor Precession", www.hyperphysics.phy-astr.gsu.edu, undated.

[49]   A. Blom, C. Jupen, "Parameterization of the Zeeman Effect for Hydrogen-Like Spectra in High-Temperature Plasmas", Plasma Phys. Control. Fusion, vol. 44, 2002, pp. 1229-1241.

[50] Richard Becker, "Electromagnetic Fields and Interactions", Dover Publications, Inc., New York, 1982.

[51] James G. Branson, "Hydrogen Fine Structure", www.hcp.ucsd.edu, November 30, 1998.

[52] Anne P. Thorne, "Spectrophysics", Chapman and Hall Ltd., London, 1974.

[53] Gerhard Herzberg, F.R.S., "Molecular Spectra and Molecular Structure", 6th Ed., D. Van Nostrand Company, Inc., Princeton, N.J., 1959.

[54] Susan B. Piepho, Paul N. Schatz, "Group Theory in Spectroscopy with Application to Magnetic Circular Dichroism", John Wiley & Sons, Inc., New York, 1983.

[55] I.S. Gradshteyn, I.M. Ryzhik, "Table of Integrals, Series, and Products", 6th Ed., Academic Press, San Diego, California, 2000.

[56] L. Pauling, E.B. Wilson, "Introduction to Quantum Mechanics", McGraw-Hill, 1935.

[57] G.J. Tallents, "The Relative Intensities of Hydrogen-Like Fine Structure", J. Phys. B: At. Mol. Phys., vol. 17, no. 18, September 28, 1984, pp. 3677-3691.

[58] G.J. Tallents, "The Relative Intensities of Hydrogen-Like Fine Structure Emitted from Recombining and Steady-State Plasmas", vol. 18, no. 16, August 28, 1985, pp. 3299-3309.

[59] D. Esch, S. Herzog, L. Zhou, V. Helbig, "Modeling of Doppler-Broadened H_α and D_α Spectra Including Fine Structure for Moderate Static Electric Fields", Report to Institute for Experimental and Applied Physics, Kiel University, Germany, undated.

[60] G.W. Series, "The Spectrum of Atomic Hydrogen Advances", World Scientific Publishing Co. Pte. Ltd., Singapore, 1988.

[61] Eric W. Weisstein, "Spherical Harmonic", MathWorld –A Wolfram Web Resource, 1999.

[62] David J. Wright, "The Riemann Sphere – SO(2,1) and Hyperboloids", www.math.okstate.edu, November 24, 2004.

[63] Donald H. Menzel, "Mathematical Physics", Dover Publications, 1961.

[64] Eric W. Weisstein, "Parabolic Coordinates", MathWorld-A Wolfram Web Resource, 1999.

[65]   M.R. Flannery, D. Vrinceanu, "Stark Mixing in Rydberg Atoms by Ultralow Energy Collisions with Ions", International Journal of Mass Spectroscopy, vol. 223-224, 2003, pp. 473-489.

[66]   B. Dietz, M. Lombardi, T.H. Seligman, "Parabolic Manifolds in the Scattering Map and Direct Quantum Processes", J. Phys. A: Math. Gen., vol. 29, no. 5, March 7, 1996, pp. 95-99.

[67]   "Generalized Laguerre Polynomials", www.wikipedia.org, November 24, 2005.

[68]   I. Bersons, A. Kulsh, "Transition Form Factor of the Hydrogen Rydberg Atom", Phys. Review A, March 1997, pp. 1674-1682.

[69]   T. Wujec, H.W. Janus, W. Jelenski, "Spectroscopic Measurements of Electric Field Distributions in Dielectric Barrier Discharges in Hydrogen", J. Phys. D: Appl. Phys., vol. 36, 2003, pp. 868-877.

[70]   H.A. Bethe, E.E. Salpeter, "Quantum Mechanics of One- and Two-Electron Atoms", Springer-Verlag OHG, Berlin, 1957.

[71]   David Park, "Relation Between Parabolic and Spherical Eigenfunctions of Hydrogen", Zeitschrift fur Physik, 1960, pp. 155-157.

[72]   C.E. Burkhardt, J.J. Leventhal, "Raising and Lowering the Parabolic Eigenstates of Hydrogen", Am. J. Phys. (submitted), undated.

[73]   I.V. Lutsenko, G.S. Pogosyan, A.N. Sisakyan, V.M. Ter-Antonyan, "Hydrogen Atom as Indicator of Hidden Symmetry of a Ring-Shaped Potential", Teoreticheskaya I Matematicheskaya Fizika, vol. 83, no. 3, June 1990, pp. 419-427.

[74]   Debabrata Basu, Kurt Bernardo Wolf, "The Clebsch-Gordan Coefficients of the Three-Dimensional Lorentz Algebra in the Parabolic Basis", J. Math. Phys., vol. 24, no. 3, March 1983, pp. 478-500.

[75]   D. Basu, K.B. Wolf, "The Clebsch-Gordan Coefficients of SL(2,R) in the Parabolic Basis", Czech J. Phys. B, vol. 32, 1982.

[76]   Hamamatsu Photonics K.K., Electron Tube Center, "Photon Counting Using Photomultiplier Tubes", Technical Information Manual, April 2001, pp. 1-28.

[77]   J.R. Rogers, "Properties of Steady-State, High Pressure, Argon Microwave Discharges", Dissertation for the Degree of Ph.D., Michigan State University, 1982.

[78]   Hans R. Griem, "Stark Broadening of the Hydrogen Balmer-α Line in Low and High Density Plasmas", Plasma Phys., April 2000.

[79]   D. Nikolic, S. Djurovic, Z. Mijatovic, R. Kobilarov, "Measured Stark Parameters for Ar I 430.01 nm Spectral Line", Report to Ministry of Science, Technology and Development, Republic of Serbia.

[80]   V. milosavljevic, S. Djenize, "Plasma Diagnostics Through Analysis of Two Ar I Line Shape Characteristics", 5th General Conference of the Balkan Phys. Union, August 25-29, 2003.

[81]   D. Papousek, M.R. Aliev, "Molecular Vibrational-Rotational Spectra", Elsevier Scientific Publishing Company, Amsterdam, 1982.

[82]   Jacek Klinowski, "High-resolution Molecular Spectroscopy", Department of Chemistry, University of Cambridge, 2004.

[83]   W. Lochte-Holtgreven, "Plasma Diagnostics", American Institute of Physics Press, Woodbury, New York, 1995.

[84]   D. Luggenholscher, U. Czarnetzki, H.F. Dobele, "Investigations on Electric Field Distributions in a Microwave Discharge in Hydrogen", Report to Ministerium fur Schule, Wissenschaft und Forschung des Landes Nordrhein-Westfalen.

[85]   "The Hydrogen 21-cm Line", www.hyperphysics.phy-astr.gsu.edu, undated.

[86]   Satoru Tanaka, Bingjia Xiao, Kobayashi Kazuki, Makoto Morita, "Hydrogen Molecular Effects on the Ha Spectrum in Low-Temperature Plasmas", Plasma Phys. Control. Fusion, vol. 42, 2000, pp. 1091-1103.

[87]   "Chapter XVII: Optogalvanic and Absorption Spectroscopy Using a Tunable 670 nm Diode Laser", Department of Physics, Middlebury College, Modern Physics Laboratory.

[88]   "Zeeman Effect", University of Cape Town, Department of Physics -Physics 322S.